Mechanisms of telomerase inhibition by oxidized and therapeutic dNTPs

by

Samantha Lynn Sanford

B.S., Carnegie Mellon University, 2008

Submitted to the Graduate Faculty of the

Graduate School of Public Health in partial fulfillment

of the requirements for the degree of

Doctor of Philosophy

University of Pittsburgh

2020

UNIVERSITY OF PITTSBURGH

GRADUATE SCHOOL OF PUBLIC HEALTH

This dissertation was presented

by

Samantha Lynn Sanford

It was defended on

August 12, 2020

and approved by

Velpandi Ayyavoo, Professor, Department of Infectious Disease and Microbiology

Andrea Berman, Associate Professor, Department of Biological Sciences

Jeremy Martinson, Associate Professor, Department of Infectious Diseases and Microbiology

Bennett Van Houten, Professor, Department of Pharmacology and Chemical Biology

Dissertation Director: Patricia Opresko, Professor, Department of Environmental and Occupational Health

Mechanisms of telomerase inhibition by oxidized and therapeutic dNTPs

Samantha Lynn Sanford, PhD

University of Pittsburgh, 2020

Telomeres cap chromosome ends and are essential for genome stability and human health, but they shorten in most human somatic cells with cell division due to the end replication problem. Telomerase a specialized reverse transcriptase that lengthens telomeres by adding GGTTAG repeats to chromosome ends and is upregulated in most human cancers to enable limitless proliferation. Here, we uncover two distinct mechanisms by which naturally occurring oxidized and therapeutic dNTP DNA precursors inhibit telomerase-mediated telomere elongation. We conducted a series of direct telomerase extension assays in the presence of modified dNTPs on various telomeric substrates. We provide direct evidence that telomerase can add the metabolized form of NRTIs, dideoxyadenosine 5' triphosphate (ddITP) and 3'-azido-3'deoxythymidine triphosphate (AZT-TP), to the telomeric end, causing chain termination. In contrast, telomerase continues elongation after inserting oxidized 2-OH-dATP or the therapeutic 6-thioguanine metabolite, 6-thio-dGTP, but insertion disrupts translocation and inhibits further repeat addition. Kinetics reveal that telomerase poorly selects against 6-thio-dGTP, inserting with similar catalytic efficiency as dGTP. Furthermore, telomerase processivity factor POT1-TPP1 fails to restore processive elongation in the presence of inhibitory dNTPs. These findings reveal mechanisms for targeting telomerase with modified dNTPs in cancer therapy.

Table of Contents

List of Tables

.

List of Figures

Preface

Two major themes throughout my life have been running and science. I've realized that running a marathon and obtaining this degree require a very similar mentality. Before you even begin to train, you must have a passion for science and a drive to learn and improve. At the beginning of the race, you'll feel invincible, but it is important to pace yourself. As the race progresses, the miles may feel slower, but you must stay strong as you tackle the challenge and move forward along the course. Most importantly, to help you reach the finish line, it is essential to have a strong support network, including coaches, teammates, and cheerleaders.

First and foremost, I'd like to thank my advisor, Dr. Patricia Opresko, for your endless support and guidance throughout this journey. I am exceptionally grateful to have a mentor who is not only a phenomenal scientist and strong leader in the field, but also someone who is the most down to earth person you'll ever meet. Because of this, your mentoring qualities have fostered a positive learning environment, where you have patiently challenged me to think critically about science, but also allowed me to feel safe to learn and grow from my mistakes. You helped me transition from a research technician to a scholar.

To Dr. Andrea Berman: I'm so fortunate that I was able to be trained by a true telomerase expert. Little did I know during my time as a research technician that telomerase assays would become a large part of my dissertation project, and I am grateful for all of the time you took to mentor me. Thank you also for your continued encouragement and support as I made important decisions so that I could continue this journey. To Dr. Ben Van Houten: Your enthusiasm for science and keen eye for detail have been immensely beneficial throughout this project. Dr. Velpandi Ayyavoo: Your support and commitment to IDM students has been incredibly helpful

throughout my time in the program. Dr. Jeremy Martinson: Your enthusiasm for infectious diseases and epigenetics has shown throughout your course lectures and discussions, through which I have learned so much. To my collaborators, Dr. Bret Freudenthal and Dr. Sua Myong, thank you for giving me the opportunity to expand my knowledge and collaborate with your labs.

To my telomere teammates: Dr. Ryan Barnes, Dr. Elise Fouquerel, Dr. Mariarosaria de Rosa, Ariana Detwiler, Katie Lemon, and Sanjana Thosar: I am incredibly fortunate to work alongside a group of such talented scientists, all of whom I have become close friends. Not only can we critically discuss science, but also throw in some good-natured banter. As a result, we are always smiling throughout the day as we complete our experiments. To my telomerase teammates Griffin Welfer and Samuel Johnson: Thank you for critically reading this dissertation and for your helpful discussions. I'm passing the telomerase baton to you both, and I can't wait to see your results.

Finally, I'd like to thank my cheerleaders. They have been supporting me on the sidelines long before this marathon ever began. They have always been my pacers and show through example that anything is possible with grit, determination, and will power. To Dad: Through microscopes, ham radio, and frog dissection kits, you have always made sure to foster my curiosity about science while growing up. To Mom: Thanks for encouraging my biggest dreams and always letting my basement lab stay messy. To Budgie: Between sister trips, sending endless memes, and frolicking through petunia fields, you always make me laugh. To Grandma: Thanks for our book club chats and making sure that I read some books unrelated to science. To Vinay: Thanks for always being by my side. Either by taking biking trips from Pittsburgh to D.C. or running the last few miles with me during a race, you always manage to partake in the adventure and help me get to the finish line. To Sarah: thanks for your helpful design critiques and for always cheering me

along the way; to Rhiannon for running some of the races with me; and to Haley for her encouragement as I worked on my “magazine article”. And of course, I couldn’t have done this without the clown antics of my dachshunds (Ty, Lucy and Olivia) and cats stuck to my side like a magnet.

1.0 Introduction

1.1 Beginning of the end: A brief history of telomeres

The field of telomere biology emerged in the 1930s from the work of two Nobel Prize winners, Hermann Muller and Barbara McClintock. They independently discovered telomeres first in fruit flies and then in corn. From the behavior of broken chromosomes, these scientists concluded that the natural ends of chromosomes were indistinguishable from induced DNA breaks and must be a specialized structure. Muller discovered that when fruit flies were irradiated with x-rays, the majority of the genome would undergo breakage and fusion, but the very ends of each chromosome were resistant to breaking[1]. He hypothesized that the natural chromosome ends are somehow protected against the repair process, and named the protective structure the "telomere" [1]. McClintock independently discovered a similar phenomenon in irradiated maize chromosomes [2]. She found that ruptured chromosomes formed dicentric chromosomes due to fusion of their ends and that the damaged ends of chromosomes could be restored. She concluded that one of the essential functions of telomeres was to protect chromosome ends from fusing with each other following DNA double strand breaks [2].

In hindsight, the next major advancement in telomere biology was in 1961, when the anatomist Leonard Hayflick demonstrated that fetal cells in culture divided only 40-60 times before halting division and becoming senescent, which is an irreversible arrest of cellular growth followed by serial passages of cultured human fibroblast cells [3]. This concept was termed the Hayflick limit, which stated that aging of a cell parallels the overall physical aging of the human body [3]. However, the molecular basis of the Hayflick limit wouldn't be established for another

decade. The link between the Hayflick limit and telomeres was finally identified in the 1970s, when James Watson and Alexey Olovnikov independently proposed the "end replication problem" [4,5]. The end replication problem states that the unidirectionality of DNA polymerase would prevent the complete replication of a chromosome by lagging strand synthesis [4,5]. However, it was Olovnikov that suggested the end replication problem would cause telomeres to shorten with each round of DNA replication, and that telomere shortening was the mechanism behind the Hayflick limit. As is often the case in science, the answer to one question raised another. If telomeres shorten with each cell division and eventually lead to replicative senescence, then how have organisms with linear chromosomes prevented the total erosion of their DNA over time? Olovnikov predicted that cells capable of indefinite replication must have a special DNA polymerase to maintain their telomeres. Olovnikov's prediction sparked a race to find this protein that would take a decade of research to finally identify.

In the early stage of her research career, Elizabeth Blackburn and her colleague Joseph Gall began to unravel the answer to the end replication problem. They found that the chromosome ends of *Tetrahymena thermophila*, a unicellular ciliate organism, had a six-base sequence TTGGGG which was repeated 20 to 70 times [6]. Choosing *Tetrahymena* as an organism to complete these studies was a key factor to their initial success and following studies because it has thousands of chromosomes, which provide large quantities of telomeric material to analyze. By 1981, Backburn collaborated with Jack Szostak and found that telomeric function from Tetrahymena could be transformed into *Saccharomyces cerevisiae* [7]. This work showed that some feature of the telomeric sequence confers function in multiple organisms. In 1985, Blackburn and her graduate student, Carol Greider, identified an enzyme capable of extending telomeric sequences [8]. They identified a "terminal transferase" activity which they classified as a ribonucleoprotein with essential RNA

and protein components and termed it "telomerase" [8]. The repetitive sequence of telomeric DNA combined with the lack of a template DNA strand led them to the conclusion that the RNA component of telomerase was complimentary to the telomeric repeat sequence, suggesting that it was acting as a template for telomeric repeat addition. In 2009, the Nobel Prize in Physiology or Medicine was awarded to Blackburn, Greider, and Szostak for their discovery of how chromosomes are protected by telomeres and the enzyme telomerase. These initial discoveries paved the way for thousands of studies published on telomeres and telomerase in a multitude of fields, including aging and cancer.

1.2 Telomere structure and function

Telomeres consist of repetitive noncoding DNA, which protect chromosomes from degradation and loss of essential genes. Mammalian telomeric DNA has a variable number of G-rich, non-coding tandem repeats of a double stranded DNA sequence 5'-TTAGGG 3'/ 5'CCCTAA-3', followed by a 3' G rich single stranded overhang. The 3' overhang allows telomeric DNA to form a higher order structure wherein the 3' single-stranded overhang folds back, loops around, and invades the double stranded telomeric DNA, forming a telomeric loop (T-loop) that is stabilized by a displacement loop (D-loop). The T-loop prevents the ends of chromosomes from being recognized as double stranded breaks through the physical sequestering of chromosome ends away from DNA damage response machinery.

Human telomeres are coated by a sequence specific protein complex called shelterin[9]. Shelterin interacts with both double and single stranded telomeric DNA and binds to the DNA in the nucleus [10]. Human shelterin complex (**Figure 1**) consists of six distinct proteins: Protection of

telomeres 1(POT1), Ras-related protein 1 (RAP1), TERF1-interacting nuclear factor 2 (TIN2), tripeptidyl peptidase 1 (TPP1), and Telomeric repeat-binding factor 1 and 2 (TRF1 and TRF2) [9]. TRF1 and TRF2 both bind to TIN2 which tethers the proteins together [10 11]. TIN2 can also bind to TPP1, which in turn binds to POT1. RAP1 binds TRF2, which completes the six-subunit complex [9].

The DNA binding domains in the shelterin complex are well established. TRF1 and TRF2 have Myb/SANT domains which bind to duplex telomeric DNA [12]. The TRFH domain mediates the high affinity binding to DNA, which is dependent on TRF1 and TRF2 forming their own homodimers [13]. The TRF1 and TRF2 homodimers create the double stranded 5'TAGGGTT-3' recognition modules of shelterin. POT1 binds to single stranded telomeric DNA with two N-terminal oligonucleotide binding (OB) folds. POT1 can bind to single stranded 5'-TTAGGGTTAG-3' sites at either the 3' end or at an internal position such as the displaced strand of the D-loop [14]. TPP1 also has an OB fold, but does not interact with DNA [15]. Studies have shown that the shelterin complex binds as independent units to the DNA. In human and mouse cells, TRF1, TRF2, TIN2, and RAP1 are ten times more abundant than POT1 and TPP1, which suggests that the core of shelterin is a complex of the four must abundant subunits and a fraction of the complexes have TPP1 and POT1 [16]. TRF1 and TRF2 are abundant enough to cover all of the telomeric DNA in cells with short telomeres. Cells with long telomeres (LT) are not fully coated with TRF2 but are fully protected [16]. Shelterin can bind to most double stranded TTAGGG repeats, and POT1/TPP1 are in ten-fold excess over its single stranded TTAGGG binding sites, which suggests that most of the telomeric DNA is associated with shelterin proteins [16].

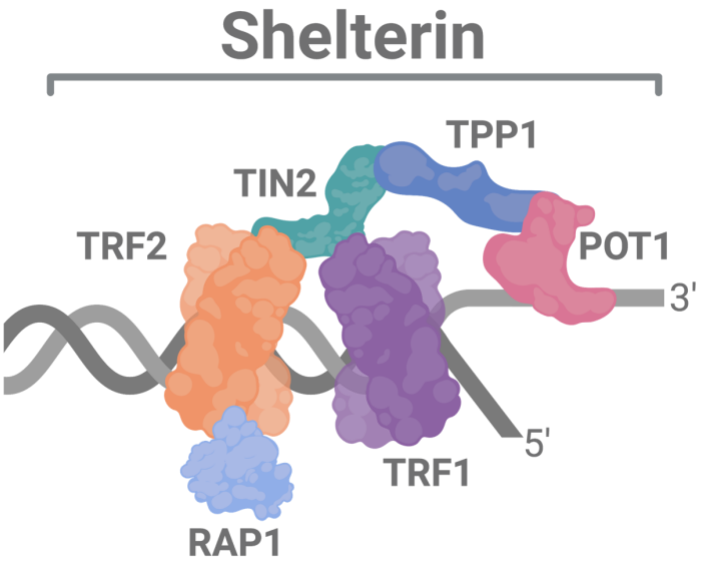

Figure 1. Shelterin complex. Consists of six telomeric proteins: telomere repeat-binding factor 1 and 2 (TRF1 and TRF2), repressor/activator protein 1 (RAP1), TRF1 interacting nuclear protein 2 (TIN2), TIN2-interacting protein 1 (TPP1) and protection of telomeres 1 (POT1). This complex is essential for telomere protection and for regulating telomere elongation.

1.2.1 End replication problem

During each round of chromosome replication, telomeres shorten because of the incomplete replication of linear DNA by the conventional DNA polymerases. DNA polymerases synthesize DNA only in the 5' → 3' direction, and can only extend existing polynucleotide chains. Conventional DNA polymerases cannot synthesize DNA at the 5' ends of a blunt ended DNA molecule. Therefore, the "end replication problem" causes incomplete lagging strand synthesis due to RNA primer removal [5]. To circumvent this loss of telomeric DNA, shelterin functions to recruit a reverse transcriptase, known as telomerase, which can elongate the 3' overhang by adding single stranded telomeric repeats [8].

1.3 Telomerase

Telomerase is a large ribonucleoprotein complex, which processively synthesizes telomeric DNA repeats (5'-GGTTAG-3' in humans) at the 3' ends of linear chromosomes, restoring the DNA lost due to the end replication problem [17]. Telomerase holoenzymes are heterogenous, but the minimally active complex consists of the catalytic protein component telomerase reverse transcriptase (TERT), and an integral telomerase RNA component (TR) and several accessory proteins **(Figure 2)** [18]. TR acts as a template for the synthesis of telomeric DNA, and also aids in the localization, catalysis, and assembly of the telomerase holoenzyme (**Figure 2**).

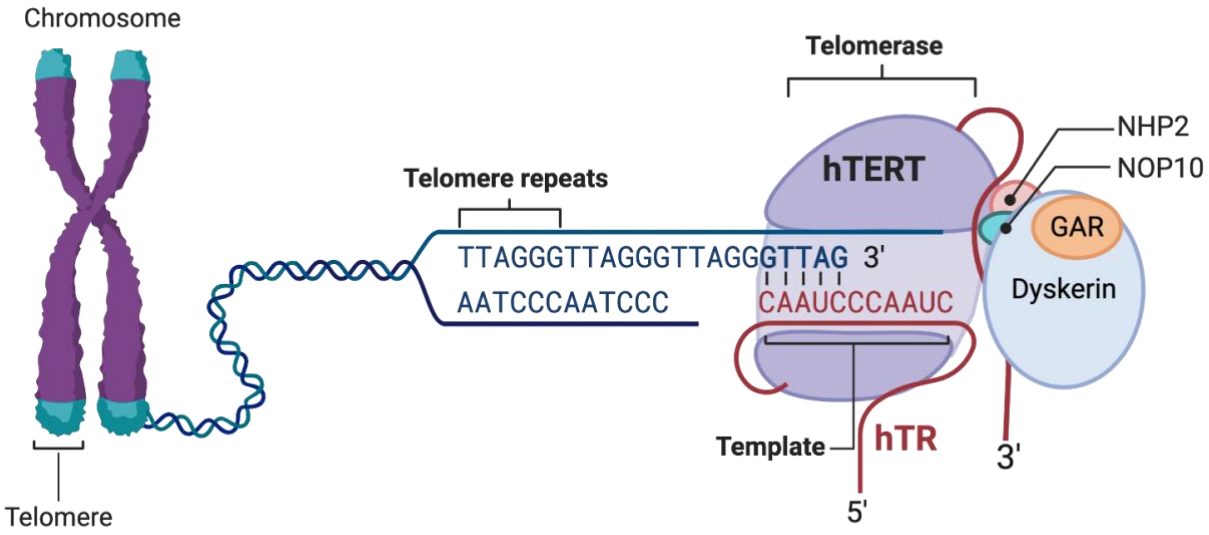

Figure 2. Telomerase at telomeres. Human telomerase consists of telomerase reverse transcriptase (hTERT), telomerase RNA component (hTR), and accessory proteins that are members of the H/ACA small nucleolar ribonucleoprotein family: dyskerin; NHP2 (non-histone protein 2); NOP10 (nucleolar protein 10); GAR1 ribonucleoprotein. Created with Biorender.

1.3.1 Human telomerase RNA subunits

The non-coding hTR (451 nucleotides in humans) is a subunit of telomerase and includes the template for DNA synthesis **(Figure 3)** [18]. hTR is involved at multiple stages of telomerase biogenesis and function. hTR has a template boundary element (TBE) which prevents run on reverse transcription past the end of the template [19]. If the TBE is absent, telomerase can read through past the template to incorporate additional non-telomeric nucleotides [19]. The pseudoknot and triple helix of hTR contribute to catalysis by orienting the primer-template duplex into the enzyme active site [20,21] . TR also contributes to the processivity of telomerase, allowing for multiple rounds of telomeric repeat addition after a single primer binding step [19,22]. hTR can bind to the TERT subunit using the template-pseudoknot domain and the conserved region 4 and 5 (CR4-CR5) domains [23]. In addition to binding to TERT, hTR has important RNA structural and sequence elements which bind to various telomerase accessory proteins. The H/ACA small nucleolar RNAs (snoRNAs) box is located at the 3' end of mammalian hTR, and is associated with the RNA binding proteins dyskerin, NHP2, nucleolar protein 10 (NOP 10), and GAR1 [24]. A Cajal box motif is also located in the 3' domain of mammalian hTR and is bound to the beta transducin (WD repeat) domain protein known as telomerase Cajal Body protein 1 [25]. Localization of hTR in Cajal Bodies (regions in the nucleus enriched with proteins and RNAs involved in mRNA processing) is important, because this is where the RNP is packaged for delivery to telomeres [26]. Once hTR is processed, hTERT controls the exit of hTR from the Cajal bodies [27].

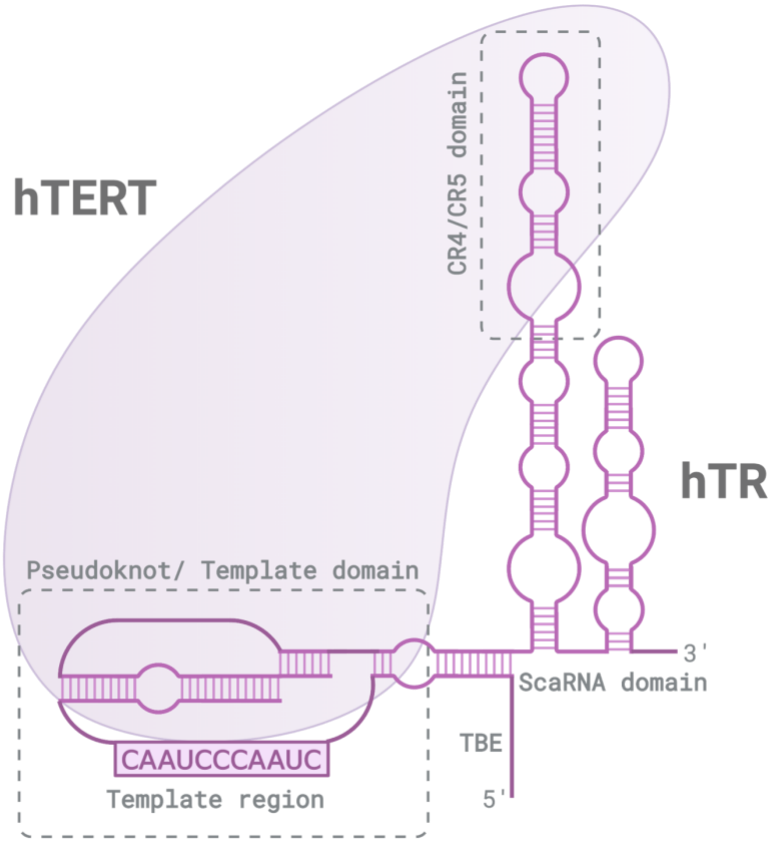

Figure 3. hTR secondary structure. The human telomerase RNA (hTR) contains three major structural and functional domains, the Pseudoknot/template domain, the CR4/CR5 domain, and the H/ACA scaRNA domain. The hTR core and CR4/CR5 domains independently bind to hTERT. Created with Biorender.

1.3.2 TERT subunit

In addition to the RNA subunit described above, telomerase contains the telomerase reverse transciptase component, TERT. hTERT consists of 1132 amino acids and is highly conserved among species [28]. hTERT contains four major domains: the TERT RNA binding domain (TRBD);

the telomerase essential N-terminal (TEN) domain; the reverse transciptase domain, and the C-terminal extension domain (CTE) analogous to a polymerase thumb domain [29].

Due to biophysical limitations such as low copy number and holoenzyme heterogeneity, there is a lack of atomic resolution structural information about human telomerase [30]. Fortunately, the crystal structure of TERT from *Tribolium casteneum*, the red flour beetle, has provided a wealth of atomic resolution information to supplement the subnanometer cryo-EM structure of human telomerase [31]. While tcTERT is highly homologous to hTERT, the RNA component of beetle telomerase has yet to be discovered. This has led to contention in the field of whether or not it is a true telomerase. Importantly, tcTERT contains the T-motif, which is an amino acid sequence preceding the RT motif that is conserved among TERT proteins, but not apparent in other reverse transcriptases [31]. Because beetle telomerase has a T-motif, the beetle structure is believed to be either TERT or a very closely related protein. The beetle structure has revealed close contacts between the TRBD and the thumb subdomain of the RT domain, which results in a closed ring tertiary structure with a large cavity at is center, allowing for binding of the primer-template duplex [32]. A structure of the binary complex containing tcTERT bound to an RNA-DNA hairpin, which mimics the primer-template duplex, confirmed these contacts. The beetle structure shows that the fingers and palm domains of the RT interact with the backbone of the RNA arm of the hairpin in order to properly place the template in the active site. While the fingers and palm grasp the RNA template, the RT thumb binds the DNA primer of the hairpin.

The TEN domain of TERT provides the anchor site which binds the telomeric DNA upstream from the primer-template duplex [33]. For *Tetrahymena thermophila* TERT, the crystal structure of the TEN domain shows a fold with the groove of the surface which is important for DNA-primer binding and telomerase activity. The domain also has a DAT motif, which is involved in

telomerase recruitment [33]. In addition to TR and TERT, there are also several accessory proteins which are involved in telomerase assembly, maturation, recruitment, and activation. hTERT is synthesized in the cytoplasm and associates with chaperones p23 and HSP90 [34]. Assembly of hTR and hTERT into active telomerase is aided by Reptin and Pontin, which belong to the AAA+ ATPase family [35]. Telomerase is then recruited to Cajal bodies by interacting with TCAB, where it stays until it is recruited to telomeres [26].

1.3.3 Telomerase recruitment to telomeres

Since telomerase and its telomeric substrate have very low abundance (approximately 250 telomerase molecules and 184 telomeres in a human cell during late S phase) [36], telomerase is actively recruited to telomeres instead of by simple diffusion. The shelterin component, TPP1, is responsible for telomerase recruitment to telomeres [37]. TPP1 complexes with POT1 to stimulate telomerase repeat addition processivity (RAP) *in vitro* and is a processivity factor [15]. The structure of TPP1 consists of an N-terminal OB-fold domain and is necessary for telomerase recruitment, a central domain that directly binds to POT1, and a C-terminal domain which associates with TIN2 and thereby integrates POT1 and TPP1 into the shelterin complex [38,39]. The TEL patch, which is a patch of amino acids in the OB-fold domain of TPP1, is essential for telomerase recruitment to telomeres *in vivo* and for stimulating telomerase RAP *in vitro* [40]. Studies have shown that the TEL patch directly interacts with telomerase [41]. Although TPP1 is essential for the recruitment of telomerase to mammalian telomeres, this interaction is regulated by the cell cycle because telomerase accumulates at telomeres only during the S phase [36].

1.3.4 Telomerase catalytic cycle

The telomerase catalytic cycle begins with the RNA template 3’ end, which base pairs to the telomeric DNA substrate which primes DNA synthesis **(Figure 4).** After forming an RNA-DNA duplex and addition of a dNTP, the telomerase active site closes to form an elongation conformation. Elongation continues until the template 5’ boundary is reached. When the template 5’ region is in contact with the active site, the RNA template 5’ region is displaced and the RNA-DNA hybrid is disrupted. Next, telomerase translocates along the newly synthesized telomeric repeat to allow the template region to be accessible for the next round of repeat synthesis. After template translocation, a short duplex RNA-DNA duplex is formed. If this duplex is captured into the TERT central cavity by conformational changes necessary for a functional active site, another round of repeat synthesis begins. Alternatively, if the active site cannot be restored, the substrate will dissociate and telomeric synthesis will not occur. The following section describes in more detail several components in the catalytic cycle, including nucleic acid handling, template boundary definition, base pair melting, and DNA product handling.

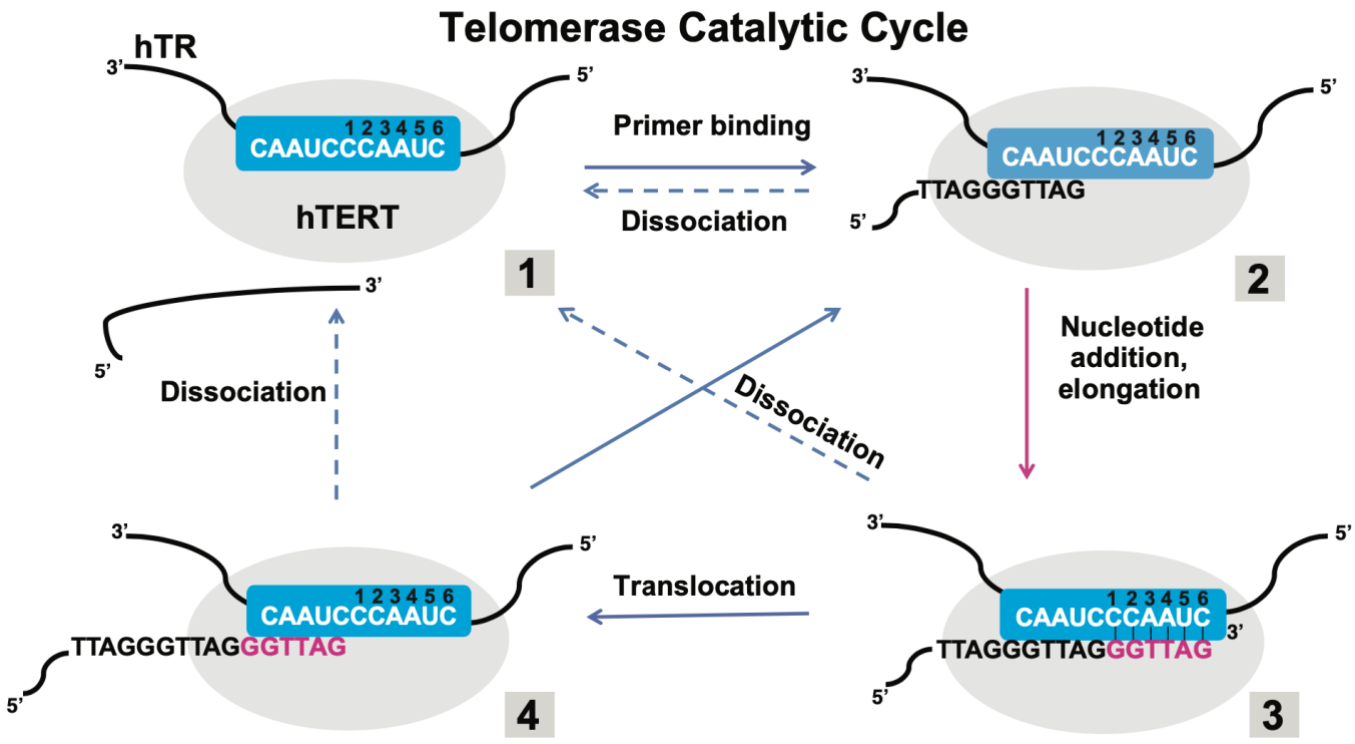

Figure 4. Telomerase catalytic cycle. Blue indicates the telomerase RNA template; black indicates DNA primer; red indicates newly added nucleotides; numbers represent the steps in the cycle.

1.3.4.1 Telomerase nucleic acid handling

Telomerase catalyzes nucleotide addition to a primer 3' hydroxyl group, which forms a product-template duplex similar to many DNA polymerases. Telomerase and other polymerases also share a metal dependent chemistry of nucleotide addition [42]. However, telomerase has several unique properties of nucleic acid handling, which other polymerases lack. Strict template copying boundaries within the telomerase RNA are necessary for accurate telomeric repeat synthesis. Also, telomerase can extend a DNA primer by processive addition of repeats. Repeat addition

processivity (RAP) allows for rearrangement of the product-template duplex without complete substrate dissociation of telomerase from DNA. The template dissociated ssDNA must maintain template independent interactions while the template repositions for base pairing of its 3' end to prime the next telomeric repeat synthesis. The coordination of these events occurs as part of the full catalytic cycle of telomerase repeat synthesis [43].

Telomerase is unique among other reverse transcriptases in its ability to use its internal RNA template for processive addition of multiple telomeric repeats, before dissociating from its DNA substrate [44]. The number of repeats telomerase adds to the chromosome ends depends on both its catalytic activity, which is how fast it can catalyze nucleotide addition, and how many consecutive repeats it can add before dissociating. Repeat addition processivity (RAP) relies on the functional relationship of the specialized hTERT and RNA component. A single telomerase enzyme has the ability to add multiple repeats to the telomeric substrate processively. This has been demonstrated by the synthesis of multiple repeats on an individual telomeric DNA molecule even when the telomeric molecule concentration is present in vast excess relative to the enzyme [45]. With a vast excess of primer, the probability of telomerase engaging with an already elongated primer compared to an unextended primer is low. Partial RAP inhibition in human telomerase by either a chemical inhibitor or a disease associated TERT mutation causes telomere shortening, which suggests that RAP is necessary for telomerase mediated telomere length maintenance [46,47].

1.3.4.2 Template boundary definition

For accurate repeat synthesis, the telomerase active site must only copy a restricted region of TR as the template. In human telomerase, the active site relies on primer-template base pairing,

which allows elongation of an annealed primer-template duplex containing only the remaining template region as single stranded RNA [23]. The first 5 nucleotides of the RNA template bind to the telomeric DNA forming an RNA-DNA duplex. This enables primer alignment at the beginning of the template rather than the end, which is an important feature of internal template use [48]. Template stabilization at the 3' end of the duplex in the active site requires the TEN domain, making it a critical component for RAP. Accurate template use also requires DNA synthesis to halt at the template 5' end [49]. For human telomerase, the template 5' boundary determination mechanism makes less of a contribution than the sequence of the template-product duplex [50].

1.3.4.3 Base pair melting between the product and template.

The product-template duplex must melt for telomerase to dissociate from an elongated chromosome and recycle the RNA template. Several thermodynamic models of duplex melting have been proposed which are covered in this section. Single molecule fluorescence resonance energy transfer (FRET) and biochemical experiments suggest an accordion model in which the TBE and template recognition element expand and contract to allow the template to move during the catalytic cycle [51]. Another model suggests that after synthesis of a telomeric repeat the newly added GT rich DNA loops out into a non-canonical hairpin, while the template translocations to pair with the AG at the 3' end. The incoming dGTP allows the DNA to realign in order for synthesis to proceed [52]. Determining the change in state that is the rate limiting barrier to the product-template unpairing requires more knowledge of the telomerase catalytic cycle.

1.3.4.4 DNA product handling independent of template base pairing.

During strand separation, telomerase must retain the DNA product to avoid complete substrate dissociation. Since the DNA is unpaired from its TR template during this step of the cycle, the enzyme-product interaction is distinct from typical primer-template Watson-Crick base pairing [53]. This interaction defines the telomerase anchor site. The telomerase anchor site allows the enzyme to reposition the unpaired template relative to the active site, which is followed by the formation of a new primer-template duplex. The new duplex can then be re-engaged by the active site for synthesis of the next repeat. Another function of the anchor site may be to control when and how during the catalytic cycle the product DNA is released from the enzyme, however there is no conclusive evidence. Recently, a single molecule telomerase activity assay was developed using high resolution optical tweezers [54]. This assay measured stepwise, processive telomerase activity and monitored conformational dynamics of the product DNA. Telomerase can tightly associate with its DNA substrate, and synthesize multiple telomeric repeats before releasing them in a single step. The rate at which the product is released from the anchor site corresponds to the overall rate of product dissociation from elongating telomerase, which suggests that the anchor site is the main substrate binding site during telomere elongation [54].

1.3.4.5 POT1-TPP1 Stimulation

The addition of both purified POT1 and TPP1 to telomerase reactions result in a two-fold increase in telomerase processivity, whereas addition of TPP1 alone results in a twofold increase in telomerase processivity [55]. POT1-TPP1 is able to increase telomerase repeat processivity by decreasing complete dissociation from the telomere substrate and product and by improving

template translocation. Additionally, only a single POT1-TPP1 DNA interaction is necessary and sufficient to stimulate telomerase processivity, which suggests that once the POT1-TPP1 telomerase complex is bound to the single stranded telomeric DNA, it is maintained throughout the entire telomerase elongation process, independent of additional POT1-DNA binding events [56].

1.4 Telomeres, aging, and cancer

As we age, our telomeres progressively shorten. Age, environmental factors, and lifestyle (diet, smoking, stress) are associated with shortened telomeres. Short telomeres cause an increased risk for an array of aging-related diseases such as cancer, cardiovascular disease, diabetes, neurodegenerative diseases, liver cirrhosis, and hypertension [57-60]. Critically short telomeres trigger a p53 dependent DNA damage response that leads to a state of irreversible cell growth arrest called replicative senescence (Figure 5). At this point, senescence is a critical protective mechanism for the cells to preserve the genome and prevent further proliferation of cells that may have genetic modifications [61-63]. Senescent human fibroblasts have an activated DNA damage response, which includes the protein kinase ataxia-telangiectasia mutated (ATM) and ataxia telangiectasia and Rad3-related protein (ATR) signaling, and nuclear foci containing DNA damage markers including γ-H2AX (phosphorylation of serine 139 on histone H2AX), p53-binding protein 1 (53BP1) and mediator of DNA damage checkpoint protein (MDC1) [64]. The upregulation of p53 and cyclin dependent kinase inhibitors p31 and p16 are additional indicators of an activated DNA damage response. Senescent cells are usually in G1 phase, which is consistent with p53 activation and induction of the CDK inhibitors p21 and p16 [65]. Both the upregulation of p16 and hypo phosphorylation of the tumor suppressor RB can contribute to telomere-induced senescence[66].

Premalignant cells lacking a functional p53 and RB tumor suppressor pathways bypass senescence and continue to divide. At this point, cells have completely eroded their telomeres and their chromosome ends fuse, which can lead to genomic instability, chromosome bridge-breakage-fusion cycles, and eventually apoptosis [67]. The uncapped telomere ends are processed by DNA double strand break pathways which lead to chromosome fusions and instability, killing most cells [68]. The surviving cells undergo malignant transformation, which in most cases, upregulates telomerase or the alternative lengthening of telomeres (ALT) pathway to maintain the shortened telomeres and promote cellular immortalization [69].

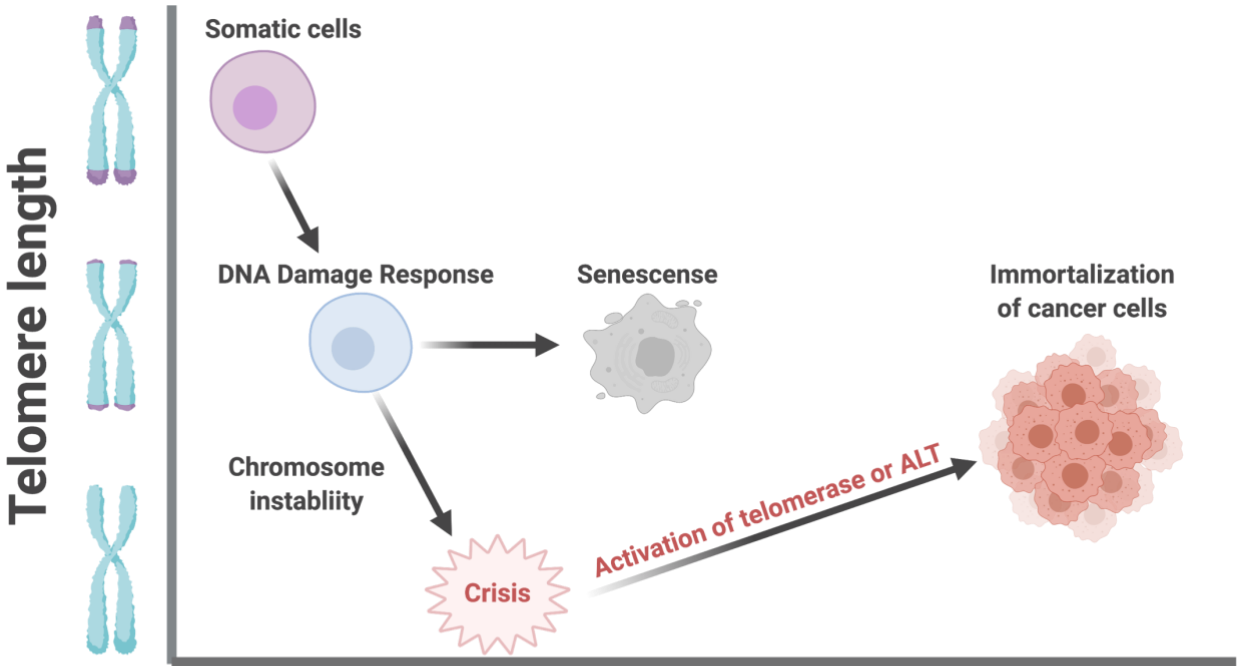

Figure 5. Telomere length vs. number of cell divisions. Somatic cells that do not express telomerase experience telomere shortening with each cell divison. When telomeres become shorter, they induce a signal to enter into senescence (growth arrest). When telomeres have excessive chromosome instability, they enter crisis. Cells are able to survive crisis by activating telomerase or the ALT mechanism to stabilize telomere length, causing malignant transformation. Created with Biorender.

1.4.1 hTERT regulation in cancer

Telomerase upregulation or reactivation occurs in 90% of cancers, and is found in almost all tumor types [70]. In most cancer cases, telomerase activity is present in the tumor and absent in normal cells[71]. Many malignant tumors are characterized by telomerase expression, causing unlimited cell proliferation [72]. Most benign or premalignant tumors are characterized by an absence of telomerase. The most common non coding mutations found across all cancers are somatic mutations to the proximal hTERT promoter. Studies have shown that melanomas, glioblastomas, liposarcomas, and urothelial cancers contain the more frequent hTERT promoter mutations compared to other cancer types [69,73-76]. The hTERT promoter mutations activate telomerase activity by converting the conserved regions in the hTERT promoter to an ETS transcription factor binding site. As a result of this dysregulation, these cancerous cells produce levels of telomerase high enough to enable them to continuously divide without limitation.

1.4.1.1 hTERT promoter mutations

The hTERT promoter is GC rich and lacks a TATA box, which is typically found in the promotor regions of genes that encode proteins found in eukaryotes [77]. The promoter contains multiple binding sites for transcription factors, which suggests that hTERT expression is under many levels of control and may be regulated by multiple factors. The promoter core is a 260 bp proximal region and is responsible for transcriptional activity. It contains five GC boxes (GGGCGG), which bind to the zinc finger transcription factor SP1, which is essential for hTERT promoter activity [78,79]. It has been shown that formation of secondary DNA G-quadruplex structures in the GC boxes masks the SP1 binding site which can also cause hTERT promoter

repression. Therefore, transcriptional up-regulation or reactivation of hTERT is a crucial step in tumorigenesis and there are multiple mechanisms which reactivate hTERT in cancer [78]. These mechanisms include the mutation or deletion of the hTERT promoter, gene amplification, epigenetic alterations, and hTERT gene alterative splicing factors [79].

Recent whole genome sequencing experiments demonstrate that expression of the hTERT gene is reactivated by single nucleotide mutations in the proximal promoter of the hTERT gene [80,81]. These mutations modulate transcriptional regulation without altering the encoding of the hTERT protein. They consist of a cytosine to thymidine transition at the -124bp and 146bp upstream of the translation start site and are very close in proximity to the transcription start site of the hTERT gene. Additionally, they are located in the GC-boxes of the hTERT core promoter [77].

hTERT promoter mutations are less common in lung, breast, esophageal, colon, and prostate cancers because they generate a consensus binding motif (CCGGAA) at the E-twenty-six (ETS) transcription factors [74]. The location of these mutations creates additional binding sites for ETS, which is a novel mechanism of gene activation in cancer, and genomic alteration driver [81]. ETS transcription factor binding to the motifs created by the hTERT mutations cause recruitment of a multimeric ETS family member, the GA-binding protein alpha subunit (GABPA) that activates hTERT transcription [82]. GABPA has been identified as the binding factor in most cancer cells with TERT promoter mutations [79]. Because these mutations are prevalent in many cancer types, hTERT is an attractive therapeutic target to halt the proliferation of cancer cells.

1.5 Roles of oxidative stress in telomere length homeostasis

1.5.1 Reactive oxygen species

Oxidative stress is caused by an excess of reactive oxygen species (ROS), caused by exogenous (UV, ionizing radiation, chemicals) and endogenous sources. Inflammation and mitochondrial dysfunction are the main endogenous ROS sources. Mitochondrial ROS arise from incomplete reduction of O_2 during oxidative phosphorylation to produce superoxide radical O_2-, rather than completely reduced to water [58]. If the cell cannot remove ROS by its antioxidant enzymes, the ROS can damage different cellular components through aberrant oxidation of nucleic acids, lipids, and proteins. Oxidative damage causes the majority of DNA damage in human cells, appearing as an oxidized base, sugar modification, DNA or protein crosslink, or DNA strand break [83]. Guanine is the most susceptible of the DNA bases to oxidation because it has the lowest oxidation potential. This results in the oxidation of guanine to form 8-oxoguanine [84], which is the most abundant oxidized base that arises from ROS exposure [85]. 8-oxoguanine is a highly mutagenic base because the presence of an unrepaired oxidized base in the DNA can be bypassed by DNA polymerases, which typically introduce dAMP opposite 8-oxoG instead of the canonical dCMP. Thus, inducing a G:C-T:A transversion mutation results in genomic instability [86]. The oxidation of guanine also occurs in the free dNTP pool which are the precursors for DNA synthesis. DNA polymerase incorporation of 8-oxodGTP opposite dC or dA on the template strand can induce a A:T-C:G transversion during subsequent replication. Oxidative stress inducing base modifications and single strand breaks can interfere with the replication machinery and are able to activate the DNA damage response [87].

While telomeres only make up a small percentage of the genome, they are highly susceptible to oxidative damage because they are rich in guanine. Numerous studies have shown that oxidative stress leads to accelerated telomere shortening [88]. Not only does ROS induced damage interfere with replication of telomeric DNA [89], but also the oxidatively damaged DNA and free oxidized dNTPs used for telomere synthesis can interfere with telomerase activity [90]. The Opresko lab and others have previously shown that 8-oxo-dGTP is used by human telomerase as a substrate and following incorporation into the DNA it functions as a chain terminator [91,92].

1.5.1.1 Protecting telomeres from ROS

There are several enzymatic pathways that protect telomeres from ROS. Nucleotide pool sanitation enzymes help eliminate oxidized dNTPs and work in parallel with the DNA repair machinery to maintain genome integrity. The most common sanitation enzymes are the nucleoside diphosphate linked with some moiety X (Nudix) hydrolase family [93]. These enzymes work by catalyzing the hydrolysis of nucleoside-like di- or triphosphates to their respective monophosphates. The core residues of the enzyme's catalytic domain are required for divalent cation coordination, which is essential for catalysis, however they do not discriminate or direct the nucleobases, which suggests there is a flexibility within the super family.

The most studied sanitation enzyme today is NUDT1 (Nudix type 1), also known as MutT homolog 1 (MTH1). MTH1 hydrolyses oxidized nucleotides 8-Oxo-7,8-dihydro-2'-deoxyguanosine 5'-triphosphate, 2-Hydroxy-2'-deoxyadenosine-5'-triphosphate, and 8-Hydroxy-2'-deoxyadenosine-5'-triphosphate (8-oxo-dGTP, 2-OH-dATP, and 8-oxo-dATP respectively) to monophosphates (dNMP), thereby avoiding their incorporation into DNA by DNA polymerases **(Figure 6)** [86,94-97]. MTH1 is an important enzyme in maintaining genomic integrity and replicative

potential in cultured fibroblasts and oncogenic Ras transformed cells [98-100]. MTH1 is also a promising drug target in cancer cells, where a dysfunctional redox environment can lead to a dependency on oxidized nucleotide sanitation for cell survival [101-103]. The Opresko lab and others previously reported that MTH1 depletion inhibits telomere maintenance and telomerase activity in cancer cells grown under oxidative stress conditions, and that telomerase insertion of 8-oxo-dGTP terminates further telomere elongation *in vitro* [91,92,104]. However, since MTH1 also removes oxidized dATPs, whether these damaged nucleotides can inhibit telomerase activity, similar to 8-oxo-dGTP, and contribute to telomere shortening had been unknown until my work on this topic.

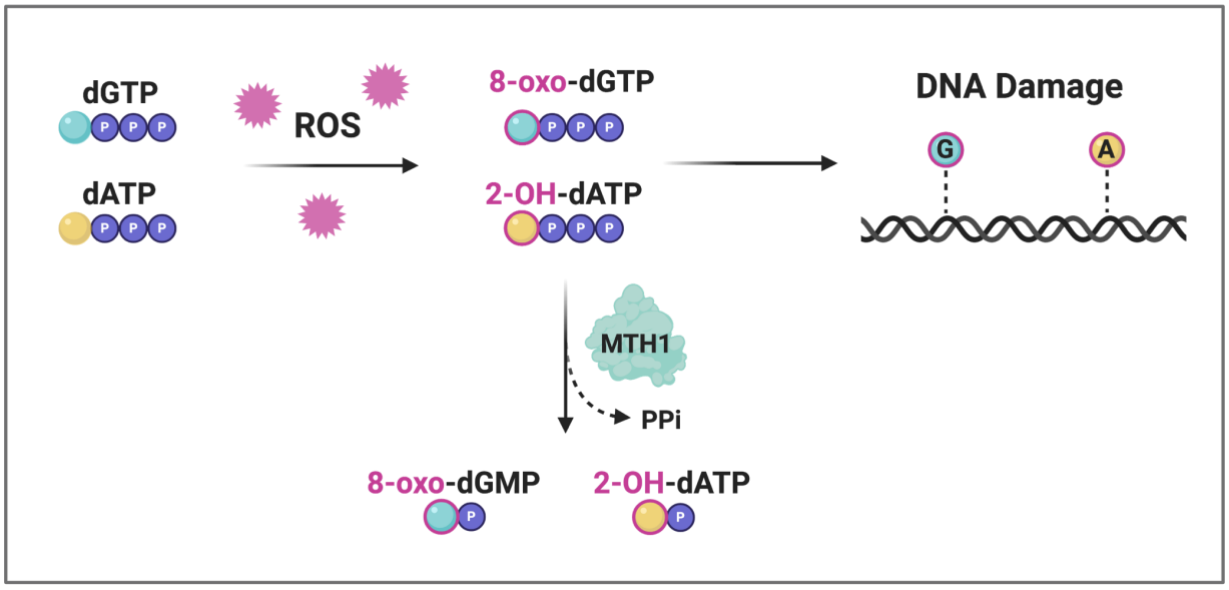

Figure 6. MTH1 pathway. ROS oxidizes the free physiological nucletides dGTP and dATP into 8-oxo-dGTP and 2-OH-dATP. MTH1 hydrolyzes the oxidized dNTPs into 8-oxo-dGMP and 2-OH-dAMP so that they cannot be incorporated into DNA. Oxidized nucleotides incorporated into the DNA cause DNA damage.

1.6 Telomerase inhibitors

Telomerase is a prime target for effective cancer therapeutics since it is expressed in over 90% of cancers. Cancer cells have short telomeres because they have gone through extensive telomere shortening before emerging from crisis, then telomerase can maintain their telomeres at shortened lengths [105]. Non-cancer cells, including stem cells, have lower telomerase activity and normally maintain telomeres at longer lengths than cancer cells. This is advantageous because it suggests telomerase inhibition should deplete telomeres more rapidly in highly proliferating cancer cells with short telomeres, while reducing the risk for extensive telomere shortening in non-cancer cells. In most cancer cases, telomerase activity is present in the tumors and absent in telomerase silent normal cells. Since telomerase is activated due to mutations in the non-coding hTERT promoter region, the goal of anti-telomerase therapeutics is to selectively induce apoptosis and cell death in cancer cells but minimize the effects on non-cancer cells [105]. There are several types of therapeutic telomerase inhibitors including vaccines using a telomerase specific peptide which causes an anti-telomerase immune response, antisense oligonucleotides, modified dNTPs, and small molecule inhibitors of hTERT or hTR.

The most extensively studied telomerase inhibitors to date are Imetelstat (GRN163L) and the BIBR1532 compound. Imetelstat, which is a 13-mer thiophosphoramidate oligonucleotide, binds with high affinity to hTR template of telomerase, resulting in direct, competitive inhibition of telomerase in a dose dependent manner [106]. In several cancer cell lines, Imetelstat induced growth arrest and caused telomere shortening [107,108]. Clinical studies on patients with advanced non-small cell lung cancer showed limited improvement, and for pediatric patients with brain cancer, the drug could only be administered for two weeks before the toxicity levels became intolerable [108]. Unfortunately, the long period of time required for Imetelstat to shorten the

telomere length in patients caused hematologic and hepatotoxic dose-limited side effects [109]. When patients took time off from drug, due to the toxicities, they had reestablishment of their telomere length in their tumors and continued cell growth [110]. One report showed that 2 weeks after termination of Imetelstat, A549-Luc cells (lung carcinoma), were able to reform colonies at the same rate as before treatment with the drug [106].

BIBR1532 is a non-nucleotidic synthetic small molecule drug and has been shown to be a selective inhibitor of telomerase [111]. BIBR1532 acts as a mixed-type noncompetitive inhibitor and interacts with the hydrophobic pocket of the thumb domain of telomerase, which reduces telomerase processivity. BIBR1532 can induce apoptosis in various breast cancer cell lines. The molecular mechanism of BIB1532 inhibition remains to be understood in more detail, and it suppresses cell survival and further activates apoptotic associated factors such as p73, caspase-3, and Bax/Bcl-2 [112]. According to clinicaltrials.gov, there are no ongoing clinical trials of BIBR1532, likely due to tissue toxicities in normal cells [112].

Table 1. Comparison of HIV-1 and Telomerase

	HIV-1 reverse transcriptase	**Telomerase**
Organism	HIV-1 Virus	Humans
Structure	Fingers, thumb, and palm domains + RNase H	Fingers, thumb, and palm domains
Template	Viral RNA	Telomerase RNA template
Final product	Double stranded DNA used for viral integration into the host DNA	Double stranded TTAGGG repeats at the ends of human chromosomes (telomeres)

1.6.1 Telomerase therapeutics: Nucleoside analogs

Another strategy to target telomerase in cancer cells is to introduce a modified nucleoside so that telomerase can preferentially incorporate the modified dNTP into telomeric DNA in order to halt further telomere elongation. An altered nucleotide which is incorporated into telomeres would not bind to shelterin properly and could cause telomere dysfunction and rapid cell death. Nucleoside analogs are commonly used in a wide range of antiviral therapies to prevent viral replication in infected cells. Once they are incorporated into DNA, they are chain terminators and stop the viral polymerase from extending the chain of DNA. Several nucleoside analogs have also been tested as cancer therapeutics, which will be discussed in the next several sections.

1.6.2 Nucleoside reverse transcriptase inhibitors

Nucleoside reverse transcriptase inhibitors (NRTIs) block the reverse transcription of HIV-1 viral RNA. In their phosphorylated form, NRTIs compete with natural dNTPs for insertion by HIV-1 RT, and act as chain terminators [113]. The catalytic core of TERT is structurally homologous to the HIV-1 RT domain (**Table 1**) [114], and telomerase inhibition has been proposed to contribute to premature aging observed in HIV patients undergoing long term NRTI therapy [115,116]. While previous studies have confirmed that treatments with various NRTIs cause telomere shortening and inhibit telomerase *in vitro* [117-119], whether telomerase can insert these chain terminating analogs during telomere synthesis had not been tested until this dissertation.

Accumulation of mitochondrial DNA mutations, increased mitochondrial oxidative stress, and a decrease in mitochondrial energy metabolisms contribute to aging[120]. NRTIs not only act as HIV chain terminators but can also inhibit mitochondrial DNA (mtDNA) polymerase γ (pol γ),

which disrupts mitochondrial DNA replication and induces mitochondria dysfunction **(Figure 7)** [121]. Inhibition of pol γ leads to the depletion of mtDNA, and subsequent depletion of mtRNA and of mitochondria encoded polypeptides involved in oxidative phosphorylation. This discovery led to the theory of NRTI-induced toxicity known as the "polymerase γ theory" [120]. When NRTIs cause a decrease in mtDNA, the electron transport chain proteins are depleted, causing changes in respiration rate, decreased ATP production, diminished mitochondria membrane potential, and an increase in ROS production. NRTIs can also obstruct base excision repair and proof-reading capabilities of pol γ. Studies showed that mice with impaired pol γ proofreading had accumulation of mtDNA mutations which led to disrupted mitochondrial function, several aging phenotypes, and cell death [122]. NRTI mediated increase in ROS via mitochondrial dysfunction has the potential to lead to oxidative damage to dNTP pools.

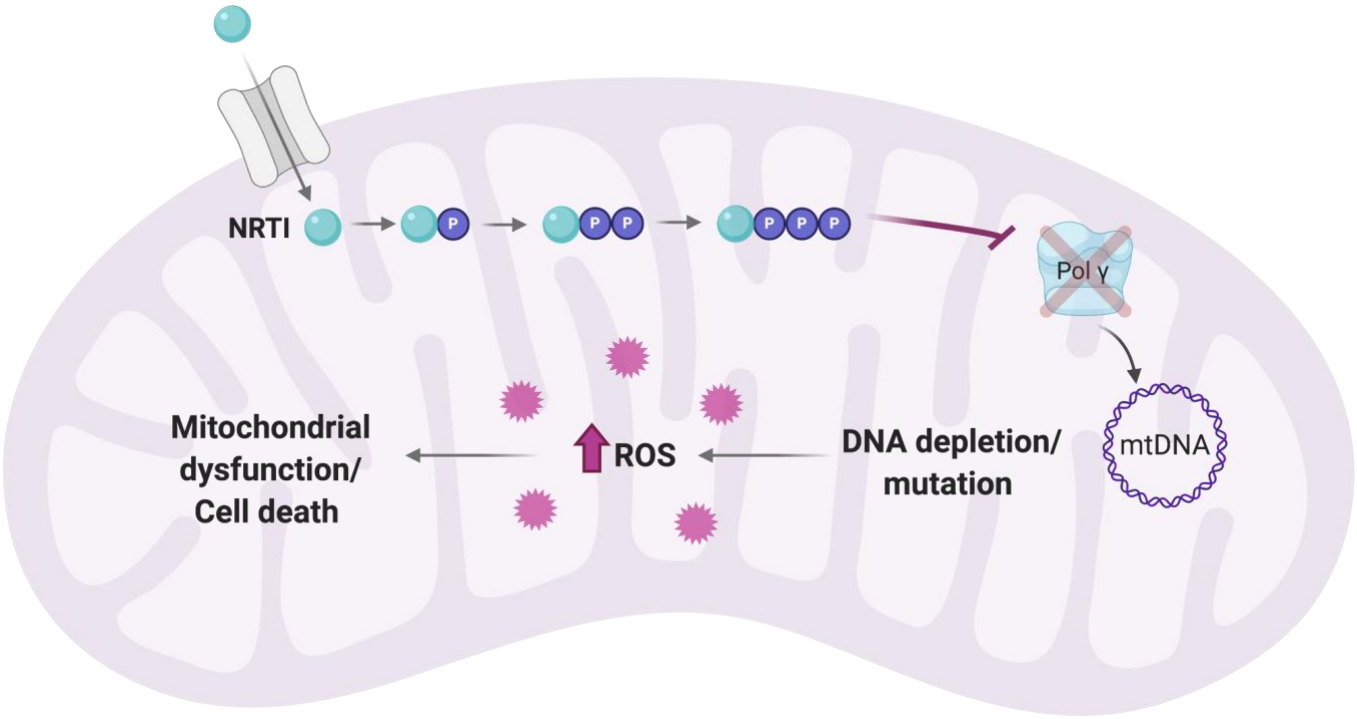

Figure 7. NRTI induced mitochondrial toxicity. The dNTP form of NRTIs inhibits mitochondrial DNA polymerase gamma, which is a polymerase necessary for the normal replication of mitochondrial DNA. Mitochondrial DNA depletion causes elevated levels of ROS which can cause mitochondrial dysfunction and cell death. Created with Biorender.

1.6.3 AZT as a potential cancer therapeutic

3-Azido-2, 3-dideoxythymidine (AZT), clinically referred to as Zidovudine, is a thymidine analog synthesized in the 1960s as a potential anti-cancer agent, however at the time, it failed to be an effective cancer therapeutic [123]. When HIV was discovered in the 1980s, AZT was one of the first drugs shown to be a potent inhibitor of retroviruses. AZT is phosphorylated intracellularly to AZT-triphosphate (AZT-TP) by thymidine kinase, and is then integrated into viral DNA, causing chain termination.

When telomerase was discovered, questions were raised asking if AZT could be a cancer therapeutic. In 1994, Strahl and Blackburn demonstrated that AZT can preferentially incorporate into telomeric DNA of *Tetrahymena*, and cause telomere shortening [117]. During the same year, another group demonstrated strong links between telomerase activity and cancer [70]. AZT-TP can be incorporated into eukaryotic DNA in place of thymidine, although it has low affinity for DNA polymerases α, β and γ, but a high affinity for reverse transcriptases [124]. These two studies led to the hypothesis that AZT could inhibit telomerase in cancer cells. Strahl and Blackburn later demonstrated that AZT could inhibit telomerase and reduce telomere length in two immortalized human lymphoid cell lines [118]. They found that passaging the cells with 100 μM AZT caused progressive telomere shortening in most of the lymphoid cultures, but the treatment did not change the cell growth rates, suggesting that AZT was preferentially being incorporated by telomerase rather than by replicative polymerases. [118]. In immortal mouse fibroblast cultures, AZT induced senescence [125].

In 2001, the effects of chronic *in vitro* AZT treatment on mouse mammary carcinoma cell lines showed that AZT treatment for over 30 passages inhibited telomerase activity, caused progressive telomere shortening, and led to cellular senescence and apoptosis [46,126]. This study demonstrated for the first time that AZT-treated tumor cells had reduced tumorigenicity in BALB/c mice. Tumors volumes were reduced and survival was longer in animals inoculated with AZT-treated tumor cells compared to the control. Additional studies showed that AZT reduced tumor growth in parathyroid cancer cells and hepatocellular carcinoma in rats [127]. AZT is currently used for the treatment of several virus associated human cancers, including Epstein-Barr-associated lymphoma, AIDS-related Kaposi sarcoma, primary central nervous system lymphoma, Kaposi sarcoma-associated primary effusion lymphoma, and adult T cell leukemia [123]. According to

clincialtrials.gov, there are five ongoing phase I and II clinical trials investigating AZT treatment alone or a combination with other drugs in the treatment of breast cancers and lymphomas.

1.6.4 Thiopurines

Thiopurines are a class of therapeutic nucleoside analogs that cause telomere shortening [128], and are currently used in clinical practice as antileukemic, anti-inflammatory, and immunosuppressive agents [129]. Their uses for cancer therapy have been limited to leukemia and some pediatric cancers due high levels of toxicity. In cells, thiopurines are first metabolized to 6-thioguanosine monophosphate and then further metabolized to 6-thio-2'deoxyguanosine-5'triphosphate (6-thio-dGTP). This molecule can then be incorporated into DNA during replication [130]. 6-thio-dGTP is also readily incorporated into mitochondrial DNA, where it is rapidly oxidized [131]. Accumulation of oxidized 6-thioguanine is associated with pol γ inhibition, reduced mtDNA transcription, decline in mitochondrial protein levels, and loss of mitochondrial function. Both of these instances may generate high levels of ROS, which can cause additional damage to the DNA and block cellular replication [132].

Recently, a nucleoside analog of 6-thioguanine, 6-thio-2'deoxyguanosine, (6-thio-dG) was designed with the hypothesis that it may be preferentially recognized by telomerase and be incorporated into telomeric DNA [128]. Because telomeres are G rich, the O6 sulfur moiety in the 6-thio-groups mimic guanines, but they result in an altered chemical structure, and the Shay lab reasoned that if the drug can be incorporated into telomeric DNA, it may impede the function of the shelterin complex. If the shelterin protein, TRF2, is compromised, telomeres may be falsely recognized as DNA double strand breaks and acquire DNA-damage signals which can be detected using immunofluorescence techniques [133]. The damage signals are telomere associated, and

referred to as telomere dysfunction-induced foci (TIF). TIFs can be visualized by the colocalization of DNA damage response factors such as 53BP1 and the histone family member, γ -H2AX [134]. Compared to cancer cells treated with 6-thioguanine, after 72 hours, 6-thio-dG caused 7.8 times more TIFs [128]. When added at equal concentrations to non-cancer cells, 6-thio-dG is significantly less toxic to the cells than 6-thioguanine [128]. Compared to other telomerase inhibitors, 6-thio-dG decreases the lag period in telomere shortening. It also does not have a significant effect on telomerase deficient cells [128].

Clinically relevant studies have shown that 6-thio-dG can control the progression of disease for longer periods in pre-clinical models of melanoma that were resistant to targeted therapies or immunotherapies [135]. The studies analyzed 6-thio-dG in combination with targeted therapies using BRAF inhibitors or as a monotherapy with BIBR1532. When 6-thio-dG was used as a monotherapy, it was more effective than BIBR1532 in causing anti-proliferation of BRAF mutant melanoma cell lines and did not cause any hematological or hepatotoxicities in mice. Importantly, 6-thio-dG was similar to the BRAF inhibitor, PLX4720, and halted tumor growth in xenograft models. Additional pre-clinical studies have shown that 6-thio-dG could overcome chemotherapy resistance in both lung cancers and therapy resistant pediatric brain cancer [136,137].

The previous reports demonstrated that 6-thio-dGTP promotes cell death in telomerase positive cancer cells, and decreases tumor growth in mouse xenograft studies [128]. 6-thio-dG treatment causes telomere shortening and telomere dysfunction, but the mechanism is unclear because extracts from treated cells do not show reduced telomerase activity [128].

1.6.5 Recent FDA approved cancer therapeutic dNTPs

5-flouro-2'deoxyuridine (5-FDU) is an FDA approved agent used for the treatment of metastatic colon and liver cancers. 5-FdU causes a similar cytotoxicity as 5-floururacil (5-FU) after administration *in vivo* [138]. The metabolites from the drug inhibit thymidylate synthase to deplete cellular deoxythymidine pools, which impairs DNA replication and repair. In the cell, the metabolites are converted into nucleotides, which are then misincorporated into DNA and RNA to cause cytotoxic effects. A recent study demonstrated that when several modified nucleotide analogs, including 5-FdU, were replaced with the natural form of the analog, telomerase activity was inhibited [137]. When 5-FdU was substituted into the telomere DNA sequence, POT1-TPP1 binding to the DNA substrate was impaired. 5-FdU is cytotoxic to telomerase positive cancer cells and promotes telomerase inhibition, without initiating cytotoxic mechanisms with selectively low doses of the drug, suggesting that the dosing regimen is highly selective for telomerase positive cancers and has minimal effects on somatic cell populations [137]. The Taylor group also indicated that the cytotoxicity of 5-FdU is telomerase dependent and that its incorporation into telomeric DNA caused a DNA-damage response resulting in cell death within a few days *in vitro* [137]. This study expanded our understanding of how the anti-cancer drug 5-FdU, as well as several other pyrimidines with modifications at the 5-position of the nucleobase could limit telomerase activity in vitro and was cytotoxic in telomerase positive cancer cells.

The Taylor group also screened several indollyll-2'deoxynucleotide analogs with different chemical modifications to determine if they could be incorporated into telomeres [137]. The analogs were designed to mimic the structure of dATP, but had various functional groups introduced at the 5 or 6 position of the indole ring to modulate biophysical features such as hydrophobicity, size variation, shape, and election density. Additionally, these modified analogs disrupted proper

Watson-Crick base pairing with the telomerase RNA template. They found that the nucleotide 5-methycarboxyl-indoly-2'deoxyriboside 5'-triphosphate (5-MeCITP) inhibited telomerase activity *in vitro*. Using structural studies, they determined that the analog binds to the TERT active site when the nucleobase was inverted so that the methyl carboxyl modification interacted with the telomerase specific hydrophobic pocket adjacent to the TERT active site. When they administered a permeable form of 5-MeCITP, they found evidence for telomerase dependent telomere shortening in cancer cells. When compared to AZT-TP, administration of 5-MeCITP inhibits telomerase activity with a similar potency. Compared to AZT, 5-MeCIdR was better tolerated by normal telomerase deficient cells and had minimal changes in cell viability. Their data suggested that 5-MeCIdR treatment was better tolerated by cells than AZT, perhaps due to higher selectivity that limits off target effects on metabolic pathways and non-telomerase polymerases [137].

1.6.6 Treatment with therapeutic dNTPs may avoid the ALT pathway

One caveat to traditional non-nucleoside telomerase inhibitors is that following inhibition, cancer cells must undergo multiple population doublings for the telomeres to shorten enough to trigger replicative senescence or crisis [139]. This delay may allow activation of resistance mechanisms, such as the alternative lengthening of telomeres (ALT) pathway, which is telomerase independent and instead relies on homologous recombination events at the telomere to restore telomere lengths [140]. Because telomerase mediated misincorporation of modified nucleosides occurs within a few days, activation of the ALT mechanism may lessen after following chronic administration of telomerase inhibitors. The molecular mechanisms that initiate and maintain ALT are still largely unknown; however, some mechanisms of ALT inhibition have been explored. ATR

inhibitors, such as VE-822 and NVP-BEZ235 have been shown to selectively target and kill ALT positive cells [141]. Therefore, to completely eliminate the ALT pathway, it may be possible to combine both nucleoside and ALT inhibitors as a treatment strategy.

2.0 Specific Aims

2.1 Statement of Gap in Knowledge

Numerous studies have shown that oxidative stress leads to accelerated telomere shortening [67]. The Opresko lab and others previously reported that MTH1 depletion inhibits telomere maintenance and telomerase activity in cancer cells grown under oxidative stress conditions, and that telomerase insertion of 8-oxo-dGTP terminates further telomere elongation *in vitro* [91,92,104]. However, MTH1 also removes oxidized dATPs, and whether these damaged nucleotides can inhibit telomerase activity, similar to 8-oxo-dGTP, and contribute to telomere shortening is unknown. While oxidized dNTPs arise naturally, synthetic modified dNTPs such as NRTIs and thiopurines have a long history of successful use for anti-viral and cancer therapies. While previous studies have confirmed that treatments with various NRTIs cause telomere shortening and inhibit telomerase *in vitro* [117-119], whether telomerase can insert these chain terminating analogs during telomere synthesis had not been tested. Additionally, thiopurine treatment causes telomere shortening and telomere dysfunction, but the mechanism is unclear because extracts from treated cells do not show reduced telomerase activity [128]. In addition, since both NRTIs and thiopurines can elevate ROS by causing mitochondrial dysfunction, they can potentially increase oxidative damage within nucleotide pools [120,131]. Overall, the mechanisms by which these modified dNTPs inhibit telomerase are poorly understood.

Hypothesis and scope: Oxidized and therapeutic dNTPS can inhibit telomerase both directly, and indirectly through elevated ROS induced oxidized dNTPs.

Approach: We isolated telomerase to perform direct telomeric DNA synthesis assays to measure telomerase activity and processivity to address several fundamental questions related to how the modified dNTPs impact the mechanism of telomeric repeat synthesis.

1. **Can telomerase utilize oxidized or therapeutic dNTPs for telomere elongation?** We conducted telomerase assays in which we replaced increasing concentrations of the natural dNTP with the corresponding oxidized or therapeutic dNTP analog in reactions containing the remaining three natural dNTPs. Our data indicated that oxidatively damaged dNTPs and therapeutic dNTPs inhibited telomerase to varying extents.
2. **Can telomerase incorporate oxidized or therapeutic dNTPs into telomeric DNA? If so, is the nucleotide addition chain terminating and/or mutagenic?** We previously showed that 8-oxo-dGTP is a telomerase chain terminator, so we wanted to determine the mechanism by which other oxidized or therapeutic dNTPs inhibited telomerase. We conducted telomerase assays in which we radiolabeled a DNA primer to initiate DNA synthesis opposite various template positions and added increasing concentrations of only a single dNTP. Our data indicate that the NRTIs are telomerase chain terminators, but 6-thio-dGTP and 2-OH-dATP are not and have distinctly different mechanisms of telomerase inhibition.
3. **If modified dNTP incorporation is not chain terminating, how does the incorporation impact the telomerase catalytic cycle?** To better understand how 2-OH-dATP and 6-thio-dGTP inhibit telomerase, we examined whether telomerase could incorporate a naturally occurring dNTP after inserting either 2-OH-dATP or 6-thio-dGTP. We found that 2-OH-

dATP and 6-thio-dGTP interfere with the translocation step during the telomerase reaction and compromise further telomerase extension.

4. **Can POT1-TPP1 overcome telomerase inhibition during telomere synthesis when treated with oxidized or therapeutic dNTPs?** POT1-TPP1 recruit telomerase to telomeres, and greatly increase telomerase processivity. We hypothesized that POT1-TPP1 may be able to overcome inhibition by the modified dNTPs and enhance telomerase processivity. We conducted telomerase assays with radiolabeled primers in the presence of purified POT1-TPP1. Our results showed that POT1-TPP1 stimulation was not able to fully restore telomerase extension in the presence of the modified dNTPs.
5. **Are modified dNTPs able to compete with natural dNTPs for telomerase utilization?** To gain further insight into telomerase selectivity for the modified dNTPs, we titrated increasing amounts of the modified dNTPs in reactions containing all of the natural dNTPs. We calculated the IC_{50} to determine the concentration of modified dNTP that reduces the telomerase processivity in the bulk reactions by half. The modified dNTPs varied in their ability to compete with natural dNTPs for utilization by telomerase, with 6-thio-dGTP having the lowest IC_{50}.

3.0 Materials and Methods

3.1.1 Telomerase preparation

Telomerase was immunopurified as described previously[91] with some modification. HEK-293T (ATCC) cells were grown to 90% confluency in Dulbecco's modified Eagle's medium (Gibco) supplemented with 10% FBS (Hyclone) and 1% penicillin-streptomycin (Corning) at 37°C and 5% CO_2. Cells were transfected with 10 μg of pSUPER-hTR plasmid and 2.5 μg of pVan107 hTERT plasmid diluted in 625 μl of Opti-MEM (Gibco) mixed with 25 μl of Lipofectamine 2000 (ThermoFisher) diluted in 625 μl of Opti-MEM. Cells expressing hTR and 3xFLAG-tagged human hTERT were harvest 48 hr post-transfection, trypsinized and washed with PBS, and then lysed in CHAPS buffer (10 mM Tris-HCl, 1 mM $MgCl_2$, 1 mM EDTA, 0.5% CHAPS, 10% glycerol, 5 mM β-mercaptoethanol, 120 U RNasin Plus (Promega), 1 μg/ml each of pepstatin, aprotinin, leupeptin and chymostatin, and 1 mM AEBSF) for 30 min at 4°C. Cell lysate supernatant was then flash frozen and stored at -80ºC.

80μL of anti-FLAG M2 bead slurry (Sigma) (per T75 flask) was washed three times with 10 volumes of 1x human telomerase buffer (50 mM Tris-HCl, pH 8, 50 mM KCl, 1 mM $MgCl_2$, 1 mM spermidine and 5 mM β-mercaptoethanol) in 30% glycerol and harvested by centrifugation for 1 min at 3500 r.p.m. and 4ºC. The bead slurry was added to the cell lysate and nutated for 4-6 hours at 4ºC. The beads were harvested by 1 min centrifugation at 3500 r.p.m, and washed 3X with 1X human telomerase buffer with 30% glycerol. Telomerase was eluted from the beads with a 2x the bead volume of 250 μg/mL 3X FLAG® peptide (Sigma Aldrich) in 1X telomerase buffer containing 150 mM KCl. The bead slurry was nutated for 30

min at 4ºC. The eluted telomerase was collected using Mini Bio-Spin® Chromatography columns (Bio-Rad). Samples were flash frozen and stored a -80ºC.

3.1.2 Dot blot quantification of telomerase concentration

The concentration of telomerase pseudoknot RNA in the eluted telomerase preparation was measured as described previously[142]. Briefly, a serial dilution of *in-vitro* transcribed pseudoknot region of hTR (**Supplementary Fig. 1**) was prepared as standards for quantification (0.1, 0.5, 1, 5, 10, 50, 100, 250 fmol/μL). An aliquot of each standard and eluted telomerase (10 μl) was added to 90 μl of formamide buffer (90% formamide, 1X TBE). The samples were incubated at 70ºC for 10 minutes and then placed on ice. Positively charged Hybond H+ membranes and Whatman filter papers (GE Healthcare Life Sciences) pre-incubated with 1X TBE were assembled onto the GE manifold dot blot apparatus and the samples were loaded onto the membrane via vacuum blotting. The membrane was air dried and then UV-crosslinked using a Stratagene Stratalinker 1800 with the Auto-Crosslink program. The membrane was prehybridized at 55ºC in 25 ml of Church buffer (1%BSA, 1mM EDTA pH 7.5, 500mM Na_2HPO_4 pH 7.2, 7% SDS) for 30 minutes. A total of $1x10^6$ CPM of ^{32}P labeled hTR oligonucleotide probe (Supplementary Table 1) was added to the hybridization buffer and incubated overnight at 55ºC. The membrane was washed 3X with 0.1xSSC, 0.1xSDS buffer. After vacuum sealing, the membrane was exposed to a phosphorimager screen for 1-3 hours and imaged using a Typhoon scanner. Image quant TL was used to quantify the blot intensities for the standard curve.

3.1.3 ^{32}P-end-labeling of DNA primers

50 pmol of PAGE purified DNA oligonucleotides (IDT) (Supplementary Table 1) was labeled with γ^{32}P ATP (Perkin Elmer) using T4 polynucleotide kinase (NEB) in 1X PNK Buffer (70mM Tris-HCl, pH 7.6, 10mM $MgCL_2$, 5mM DTT) in a 20 μl reaction volume. The reaction was incubated for 1 h at 37ºC followed by heat inactivation at 65ºC for 20 minutes. G-25 spin columns (GE Healthcare) were used to purify the end labeled primer.

3.1.4 Telomerase activity assay with radiolabeled dNTPs

The telomerase assay was as previously described [91]. Reactions (20 μl) contained 1x human telomerase buffer, 1 μM oligonucleotide substrate and dNTP mix as indicated in the figure legends. Reactions with cellular dNTP concentrations contained 24 μM dATP, 29 μM dCTP, 37 μM dTTP, 5.2 μM dGTP and 0.3 μM 3,000Ci/mmol [α-^{32}P]dGTP or [α^{32}P] dTTP (PerkinElmer) as indicated. Reactions containing the modified dNTPs (Trilink Biotechnologies) substituted for their natural dNTP analog are indicated in the figure legends. The reactions were started by the addition of 3 μl (~35 fmol) of immunopurified telomerase eluent, incubated at 37ºC for 1 hour, then terminated with 2 μl of 0.5 mM EDTA and heat inactivated at 65ºC for 20 minutes. ^{32}P-end-labeled 18 mer loading control (8 fmol) was added to the terminated reactions before purification with an Illustra Microspin G-25 column (GE Healthcare). An equal volume of loading buffer (94% formamide, 0.1 × Tris-borate-EDTA [TBE], 0.1% bromophenol blue, 0.1% xylene cyanol) was added to the reaction eluent from the G-25 spin column. The samples were heat denatured for 10 min at 100°C and loaded onto a 14% denaturing polyacrylamide gel (7M urea, 1x TBE) and electrophoresed for 90 min at constant 38W. Samples were imaged using a Typhoon phosphorimager (GE Healthcare).

Gels were quantitated using Image Quant TL. The processivity was calculated as previously described[55].

3.1.5 Telomerase activity assay with end labeled primers

Reactions (20 μl) contained 1x human telomerase buffer, 5 nM of ^{32}P-end-labeled primer and dNTPs as indicated in the figure legends. The reactions were started by the addition of 3 μl of immunopurified telomerase eluent, incubated at 37ºC for 1 hour, then terminated with 2 μl of 0.5mM EDTA and heat inactivated at 65ºC for 20 minutes. An equal volume of loading buffer (94% formamide, 0.1 × Tris-borate-EDTA [TBE], 0.1% bromophenol blue, 0.1% xylene cyanol) was added to the reaction eluent. The samples were heat denatured for 10 min at 100°C and loaded onto a 14% denaturing acrylamide gel (7M urea, 1x TBE) and electrophoresed for 90 min at constant 38W. Samples were imaged using a Typhoon phosphorimager (GE Healthcare). Percent primer extension was calculated with ImageQuant by measuring the intensity of each product band and dividing by the total radioactivity in the lane or total products, as indicated in the figure legends.

3.1.6 Quantitation

All gels were quantitated using Image Quant TL. Repeat processivity from the direct telomerase extension assays was calculated as $R_{1/2}$ (equivalent to the half-time for decay in an exponential time course), which represents the median length of DNA product formed, expressed in terms of number of telomere repeats. First, the total volume counts for each product band extend by one or more telomere repeats were obtained using Image Quant TL. The volume counts were

then normalized by dividing by the number of radiolabeled guanosines incorporated into the extended products based on the number of repeats added, termed corrected volume (corr vol). The "percent left behind" (%LB) was calculated for each product band by summing the counts for that product band and for every product band below (shorter products), divided by the total counts for the lane, and then multiplied by 100. The natural log of (100 - %LB) was calculated and then plotted vs. repeat number for each product length. A linear regression line was fit to the data to determine the slope of the line. The $R_{1/2}$ value was calculated by dividing -ln(2) by the slope of each fitted line ($R_{1/2}$ = -ln(2)/slope).

For the primer extension calculations, the intensity of the products and unextended primer were measured and corrected for background in the no enzyme control (P) reactions. The percent primer extension was calculated as the amount of extended products divided by the total radioactivity in the lane. The percent total product was calculated as the amount the signal intensity of each individual band (nucleotide) divided by the amount of total product extended.

3.1.7 POT1/TPP1 purification

Full-length human POT1 was expressed as a SUMOstar-hexahistine- POT1 fusion protein in baculovirus-infected SF9 cells (Thermo Fisher Scientific), as described[143]. Sf9 insect cells expressing recombinant POT1 were lysed in buffer (25 mM Tris pH 8.0, 500 mM NaCl, 10 mM imidazole) with a protease inhibitor cocktail (Roche Molecular Biochemicals). Subsequent buffers contained protease inhibitors 2 μg ml^{-1} each of aprotinin, leupeptin, chymostatin, and pepstatin, 1 mM AEBSF and 5 mM β-mercaptoethanol. Following sonication, the lysate was centrifuged at 40,000 r.p.m. for 75 min at 4°C. The supernatant was filtered through a 0.2 micron filter and loaded onto a HisTrap FF column (GE LifeSciences), followed by washing and elution with 20 and 200

mM imidazole, respectively, using an ATKA Pure FPLC (GE Healthcare). Fractions containing POT1 were pooled and incubated with SUMOstar protease (Ulp1 variant, LifeSensors) for one hour with gentle mixing by rotation 20 r.p.m. at room temperature to cleave the histidine tag. POT1 was separated from the protease and cleaved tag by size exclusion FPLC chromatography. Samples were loaded on a HiLoad 16/600 Superdex 200 column (GE Healthcare) equilibrated with 25 mM Tris pH 8.0, 150 mM NaCl, 5 mM DTT and protease inhibitors. Eluted fractions containing POT1 were collected and pooled. Purified TPP1-N (amino acids 89-334) protein was obtained from soluble lysates of isopropyl β-d-thiogalactopyranoside-induced BL21(DE3) pLysS cells (Promega) after nickel agarose chromatography, treatment with Ulp1 protease to cleave the Smt3 tag31 and size exclusion chromatography as described[56]. Expression was induced with 0.8 mM IPTG in cells for about 13 hours at 24ºC, and then harvested by centrifugation at 4500 rpm for 20 min. Cell pellets were lysed in buffer (20 mM Tris pH 7.5, 500 mM NaCl, 10 mM imidazole) with a protease inhibitor cocktail (Roche Molecular Biochemicals). Following sonication, the lysate was centrifuged 40,000 rpm for 75 min at 4 °C. The supernatant was filtered through a 0.2 micron filter and loaded onto a HisTrap FF column (GE LifeSciences), followed by washing and elution with 20 and 200 mM imidazole, respectively, using an ATKA Pure FPLC (GE Healthcare). Fractions containing TPP1 were concentrated and exchanged into buffer (25 mM Tris pH 8.0, 150 mM NaCl, 5 mM DTT) using a Centricon-10 device (Amicon). The sample was incubated with SUMO (Ulp1) protease (Invitrogen) overnight at 4ºC with gentle mixing by rotation at 20 r.p.m. to cleave the tag. Samples were then loaded on a HiLoad 16/600 Superdex 200 column (GE Healthcare). Eluted fractions containing TPP1 were collected and pooled. Protein concentration was determined by Bradford Assay (BioRad) and purity was determined by SDS–PAGE and Coomassie staining.

3.1.8 Expression and purification of *tc*TERT

*tc*TERT was expressed and purified as described previously with some modifications [32 144]. An Epiphyte3 LEX bioreactor was used to grow *tc*TERT in BL-21(DE3) pLysS cells at 37 °C until they reached an OD_{600} of 0.6-0.8, after which we induced protein expression with 1 mM Isopropyl β-D-1-thiogalactopyranoside (IPTG) and dropped the temperature to 30 °C for 4-5 hours of protein induction. Cells were harvested via centrifugation at 4000 x g until lysis. For *tc*TERT purification, we used buffers containing 0.75 M KCl and 10% glycerol for the initial purification step on Ni-NTA columns (GE Healthcare). Samples were further purified via cation exchange on a POROS HS column (Thermo Fisher), using a salt gradient of 0.5 M KCl to 1.5 M KCl. Next, the hexahistidine tag was cleaved with Tobacco etch virus (TEV) protease overnight at 4 °C. The cut tag and TEV protease were separated from the protein with an additional Ni-NTA column chromatography step. The final chromatography step was a Sephacryl S-200 16/60, GE Healthcare column using a buffer containing 50 mM Tris-HCl, pH 7.5, 10% glycerol, 0.8 M KCl and 1 mM Tris(2-carboxyethyl)phosphine (TCEP). Resultant *tc*TERT was concentrated down to 18 mg mL-1 and stored at 4°C [32].

3.1.9 Pre-steady-state kinetics of *tc*TERT inserting 6-thio-dGTP

Pre-steady-state kinetic parameters of *tc*TERT were obtained using established pre-steady-state kinetics protocols for DNA polymerases, also known as single turnover kinetics[145,146]. Briefly, we preincubated 2 μM *tc*TERT with 200 nM annealed DNA:RNA hybrid substrate, with a 6-FAM label on the 5’ end of the DNA component. We then used a KinTek RQF-3 (a rapid quench-flow instrument) to mix equal ratios of the incoming nucleotide triphosphate and 10 mM

$MgCl_2$ with the existing mix of *tc*TERT and its DNA:RNA hybrid substrate. Reactions were run at 37°C and quenched at various timepoints with 100 mM EDTA pH 7.5. In each case, the conditions used for each reaction were: 25 mM TRIS pH 7.5, 0.05 mg mL^{-1} Bovine Serum Albumin, 1 mM dithiothreitol, 10% glycerol, 200 mM KCl, 1 μM *tc*TERT, 100 nM annealed DNA:RNA hybrid substrate, and varying concentrations of 6-thio-dGTP. After each reaction, the samples were transferred to a DNA gel loading buffer, containing 100 mM EDTA, 80% deionized formamide, 0.25 mg ml^{-1} bromophenol blue and 0.25 mg ml^{-1} xylene cyanol. These mixes were then incubated at 95°C for 5 mins, and loaded onto a 21% denaturing polyacrylamide gel. These gels were run at 700 V, 60 A, and 30 W at 30°C in order to separate the reaction product from its substrate.

Gels were scanned and imaged using a GE Typhoon FLA 9500 imager, and the ratios of product to substrate were quantified using ImageJ [147]. Means and standard deviations were taken from at least three replicates were calculated, and graphed using KaleidaGraph. Plots of product formation over time were fit to the exponential Equation 1 to determine k_{obs} values:

$$[\mathrm{P}] = \mathrm{A}(1 - \mathrm{e}^{-\mathrm{k_{obs}}t})$$

In which [P] is the concentration of the product, A is the target engagement (amplitude), and t is the reaction time. After k_{obs} values were determined for multiple nucleotide triphosphate concentrations, the data was replot to compare k_{obs} to concentration of nucleotide triphosphate, and fit to Equation 2:

$$\mathrm{k_{obs}} = \frac{\mathrm{k_{pol}}[\mathrm{NTP}]}{\mathrm{K}_d + [\mathrm{NTP}]}$$

With k_{pol} representing the theoretical maximum value of k_{obs}, and [NTP] representing the concentration of the nucleotide of interest.

3.1.10 Polymerase β dGTP run-on assay

40 nM polymerase β, 400 nM primer-template DNA with a 5' 6-FAM labeled primer, were preincubated for 20 minutes. We then used a multi-channel pipette to mix equal ratios of the incoming nucleotide with 1 mM $MgCl_2$ to start the reaction. Reactions were run at 37°C in a LabDoctor™ heating and quenching was accomplished using a solution of DNA gel loading buffer. In each reaction the conditions were: 50 mM TRIS pH 7.5, 0.1 mg/mL Bovine Serum Albumin, 1 mM dithiothreitol, 10% glycerol, 100 mM KCl, 20 nM polymerase β, 200 nM primer template DNA and either 50 μM or 200 μM dGTP or dTTP. These mixes were then incubated at 95°C for 5 mins, and loaded onto a 21% denaturing polyacrylamide gel. These gels were run at 700 V, 60 A, and 30 W at 30°C in order to separate the reaction product from its substrate. Gels were scanned and imaged using a GE Typhoon FLA 9500 imager.

4.0 Results

4.1 Modified dNTPs decrease telomerase processivity

To determine if telomerase can utilize oxidatively damaged 2-OH-dATP and 8-oxo-dATP or therapeutic NRTIs and 6-thio-dGTP (**Figure 8**) for telomere elongation, we conducted direct telomeric repeat addition assays. For NRTIs we selected didanosine (ddITP) and azidothymidine (AZT-TP) based on evidence they promote telomere shortening [118,119,123].The telomerase catalytic cycle starts when the telomeric single strand overhang base pairs with the complementary 3' end of the telomerase RNA template priming DNA synthesis [43]. Upon incorporation of the incoming dNTP, the telomerase active site moves to the next template base and telomere elongation continues until the template 5' boundary is reached for processive nucleotide addition (**Figure 4**, steps 2-3). In human telomerase, the template region is 11 nt (3′-rCAAUCCCAAUC-5′) comprising of an alignment region plus a template sequence, GGTTAG (numbered 1-6 in **Figure 4)**. Then, telomerase can either dissociate or translocate on the DNA product, generating a realigned 5-bp RNA:DNA hybrid for processive repeat addition. The 6-nt RNA template is reverse transcribed for each cycle of repeat addition and template recycling (**Figure 4,** steps 2-4). Nucleotide addition processivity (NAP) is the number of nucleotides added prior to enzyme dissociation from the template, and repeat addition processivity (RAP) is the number of repeats added prior to dissociation.

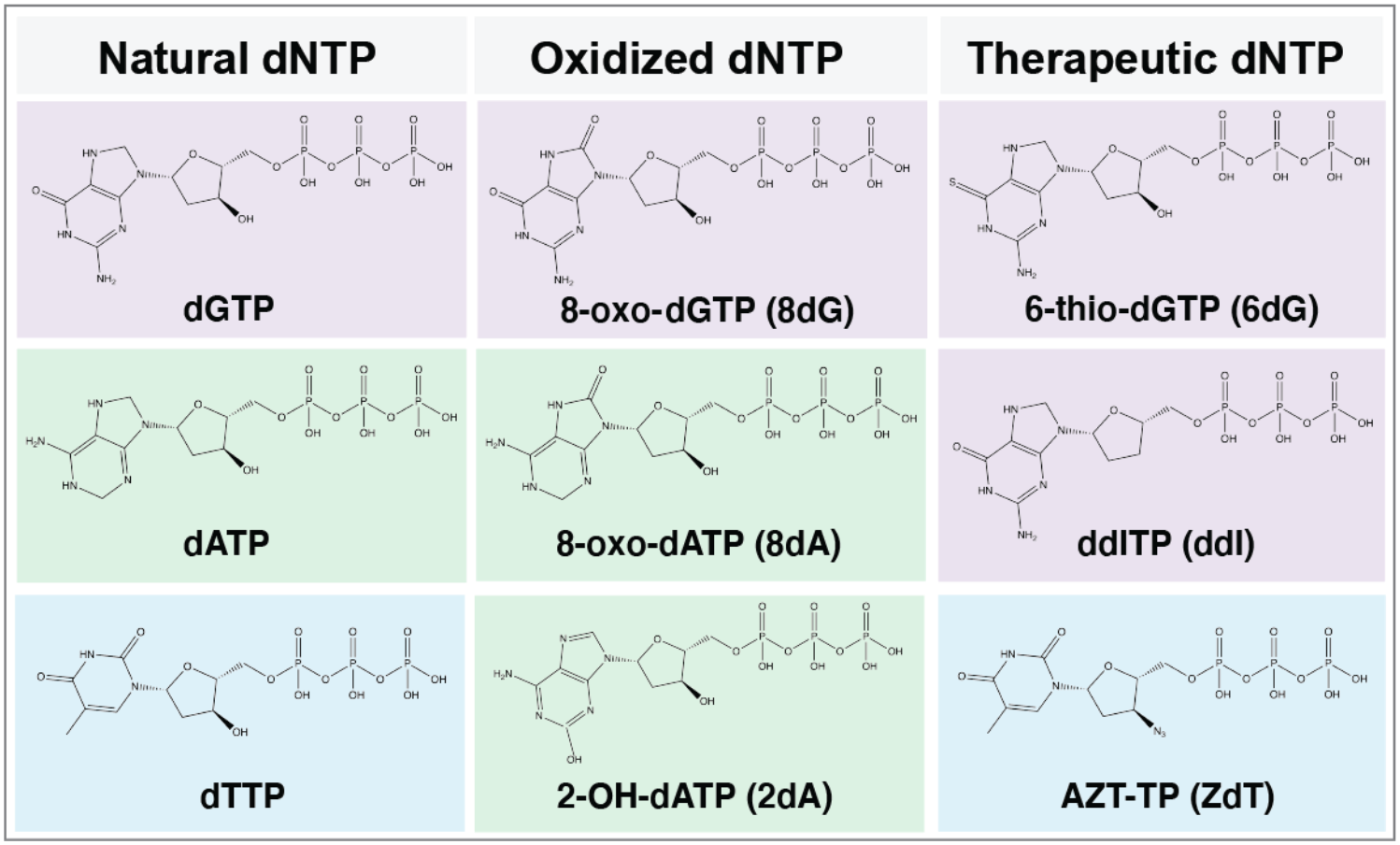

Figure 8. dNTPs used in telomerase reactions. (Chemical structures of dNTP analogs used in this study and the corresponding natural dNTP shown in the same color.

For telomerase reactions, we used the standard substrate of three TTAGGG repeats and immunopurified FLAG-tagged telomerase overexpressed in human HEK 293T cells. This enzyme preparation, termed super telomerase, has kinetic properties similar to endogenous telomerase (**Figure 9**)[36,148,149]. We conducted the reactions with cellular relevant dNTP concentrations (24 μM dATP, 29 μM dCTP, 37 μM dTTP, 5.2 μM dGTP, averaged from multiple studies[150]) since dNTP pool balance can impact telomeric DNA synthesis[150]. We replaced increasing

concentrations of the natural dNTP with the corresponding oxidized or therapeutic dNTP analog (0.5 μM -125 μM) in reactions containing the remaining three natural dNTPs **(Figure 10).** Repeat processivity was measured using the convention of calculating the number of repeats synthesized before half of the DNA substrates dissociate from telomerase[15] (**Supplementary Fig. 2**). 8-oxo-dGTP served as a control since it is an established telomerase chain terminator[91]. As expected, increasing dGTP, dATP or dTTP amounts greatly increased processivity as evidenced by the appearance of longer products (**Figure 11)**. Loss of signal at the highest dGTP concentration was due to dGTP competing with the low radioactive dTTP amounts used to label the products, and was not observed in dATP or dTTP titration reactions containing radio-labeled dGTP **(Figure 11 and Figure 10)**. Similar to 8-oxo-dGTP, 8-oxo-dATP failed to support processive elongation **(Figure 11, a and b)**. In contrast, we observed moderate telomeric synthesis in the presence of 2-OH-dATP, but processivity was lower than control reactions containing the unmodified dATP (**Figure 11b and Figure 10**). These data indicate that oxidatively damaged dATPs inhibit telomerase, although to a different extent depending on the type of modification.

Next, we examined whether telomerase could utilize therapeutic dNTPs for telomere elongation. Reactions with 6-thio-dGTP showed only one repeat added, although at the highest 6-thio-dGTP concentrations telomerase incorporated two additional nucleotides after translocation at the rC_1rC_2 template positions, but not beyond (**Figure 11a, lanes 7 and 8**). This suggests 6-thio-dGTP inhibits both nucleotide and repeat processivity. Although the NRTI didanosine is an adenine analog, when taken orally, it is converted to either ddATP or ddITP, which is an isoguanine[151,152]. When ddITP replaced dGTP in the reaction, we observed no synthesis past the first rC_6 template even with increasing ddITP concentrations (**Figure 11a, lanes 9 and 10**).

Virtually no products were observed in reactions containing AZT-TP, although incorporation opposite the first rA_3 template blocks further extension (**Figure 11c**). In summary, the aborted extension products show substitution of the natural dNTPs with 8-oxo-dNTPs inhibit telomerase activity to a similar extent as substitution with NRTI HIV-RT chain terminators or 6-thio-dGTP. Our data suggest that either telomerase cannot incorporate these modified dNTPs during telomeric DNA synthesis, or following incorporation, they inhibit further elongation of the telomere chain.

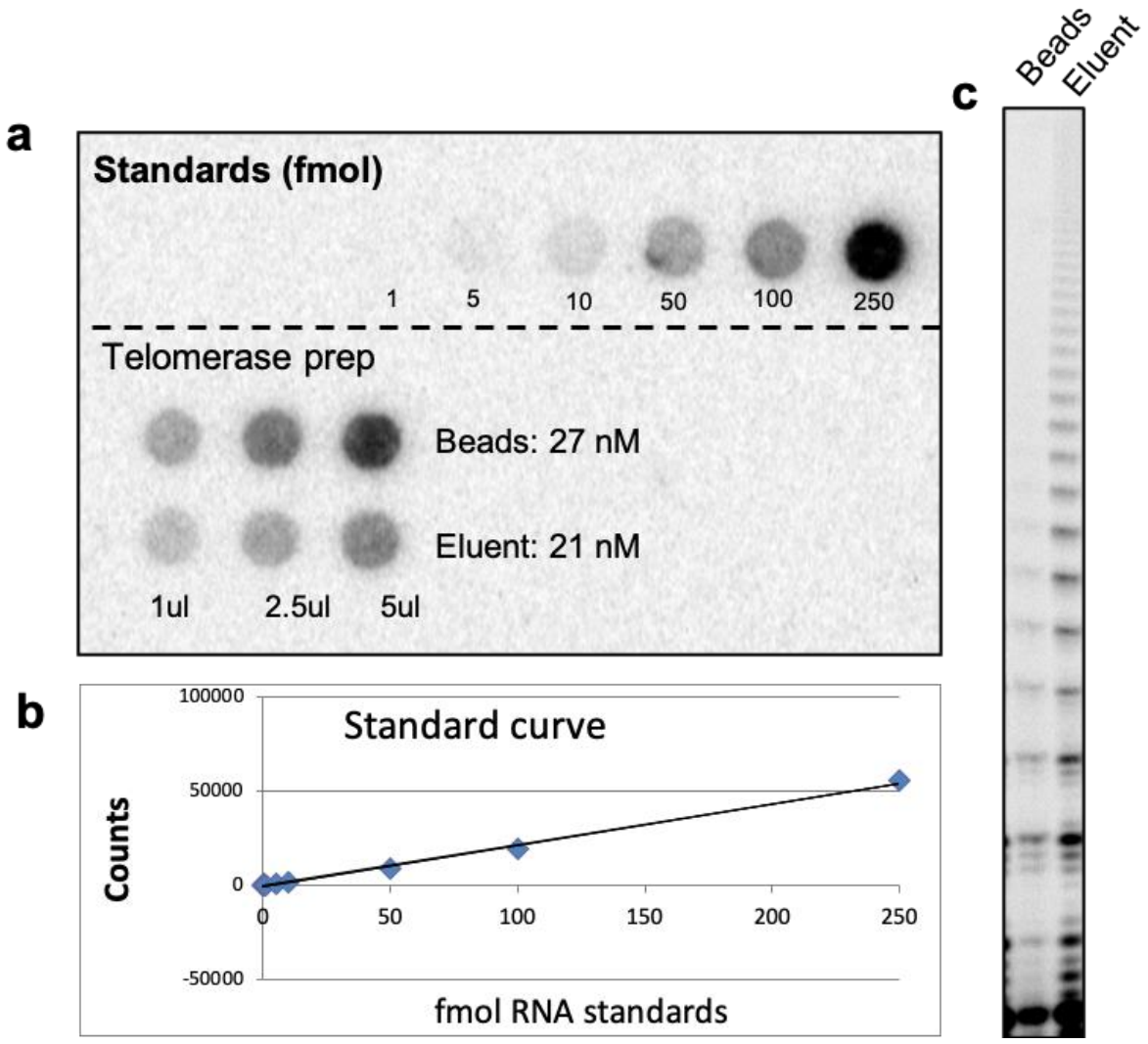

Figure 9. Quantification of immunopurified telomerase-protein-RNA complexes. (a) Telomerase was over expressed in HEK293T cells and immunopurified (IP) using a FLAG tag on the N-terminus of TERT. The beads or eluate from IP reactions were spotted on a blot and probed with a ^{32}P labeled probe against hTR to determine the concentrations of RNA that co-purified with TERT. 1, 2.5, and 5 µL aliquots were compared with *in vitro* transcribed hTR standards from 0.5 to 250 fmol. Concentrations are shown. (b) Standard curve of hTR standards to determine concentration of telomerase. (c) Telomerase primer extension assays. Telomerase activity from beads and eluent preparations were compared using a $(TTAGGG)_3$ primer.

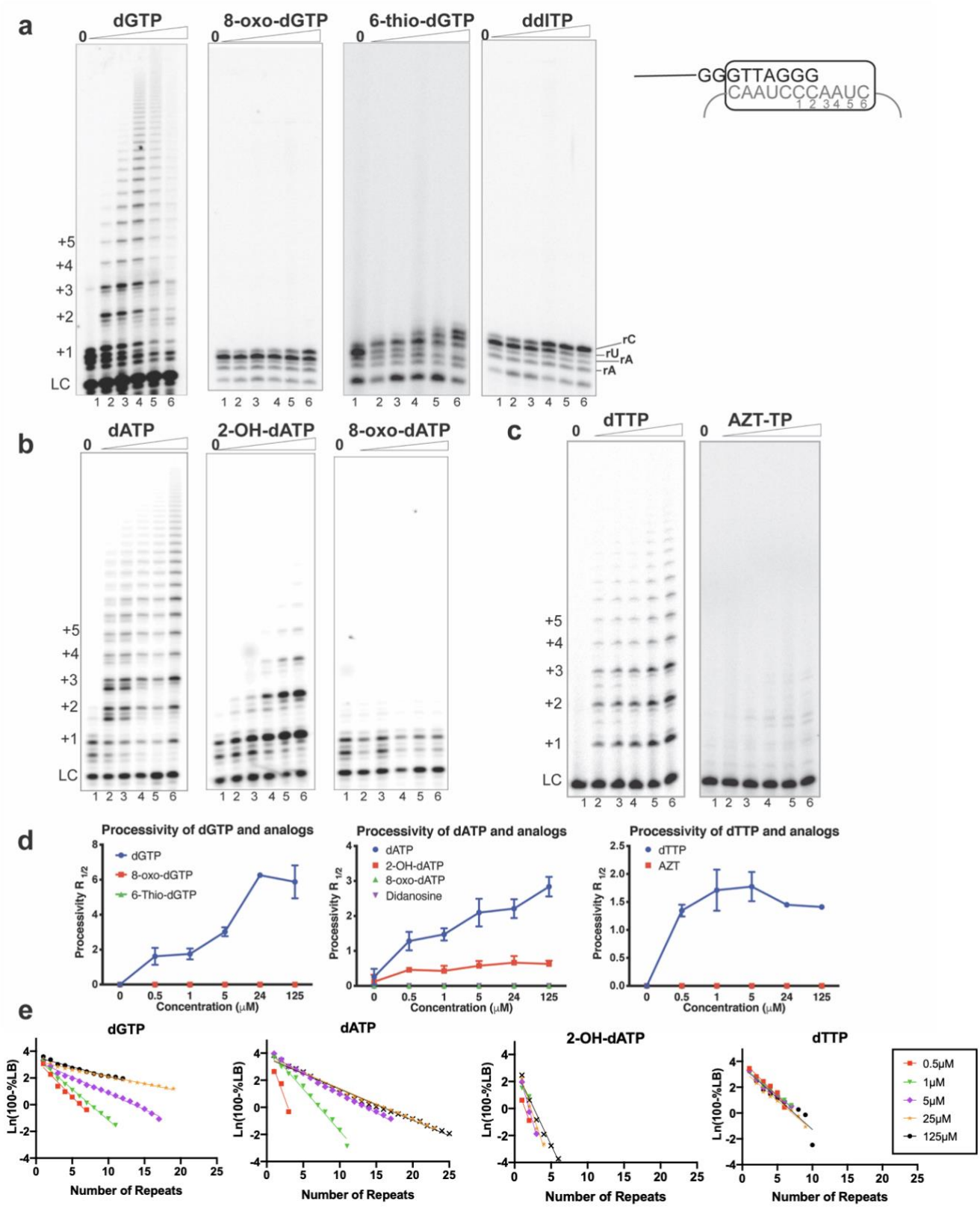
a
dGTP
8-oxo-dGTP
6-thio-dGTP
ddITP
0
GGGTTAGGG
CAAUCCCAAUC
1 2 3 4 5 6
+5
+4
+3
+2
+1
LC
rC
rU
rA
rA
b
dATP
2-OH-dATP
8-oxo-dATP
c
dTTP
AZT-TP
d
Processivity of dGTP and analogs
dGTP
8-oxo-dGTP
6-Thio-dGTP
Processivity R 1/2
Concentration (μM)
Processivity of dATP and analogs
dATP
2-OH-dATP
8-oxo-dATP
Didanosine
Processivity of dTTP and analogs
dTTP
AZT
e
dGTP
dATP
2-OH-dATP
dTTP
Ln(100-%LB)
Number of Repeats
0.5μM
1μM
5μM
25μM
125μM

Figure 10. Modified dNTP titration gels and processivity calculations Telomerase reactions were conducted with $(TTAGGG)_3$ primer 1 and cellular-concentration dNTPs (24 µM dATP, 29 µM dCTP, 37 µM dTTP, 5.2 µM dGTP) except that the indicated natural or modified dNTP was added at increasing concentrations (0, 0.5, 1, 5, 25, and 125 µM) along with either 0.3 µM [α-^{32}P]dTTP (a) or [α-^{32}P] dGTP (b, c). The loading control (LC) was a ^{32}P-end labeled 18-mer. Numbers on the left indicate the number of added repeats. (d) Processivity was calculated as $R_{1/2}$ (see Methods). (e) The natural log of (100-%LB) was plotted vs repeat number. A straight line was fit to the data and the $R_{1/2}$ was calculated by dividing –ln(2) by the slope of each line. Plots shown from one experiment. Images (a-c) and plots (e) are representative of, and data are mean ± s. d. (d) from, three independent

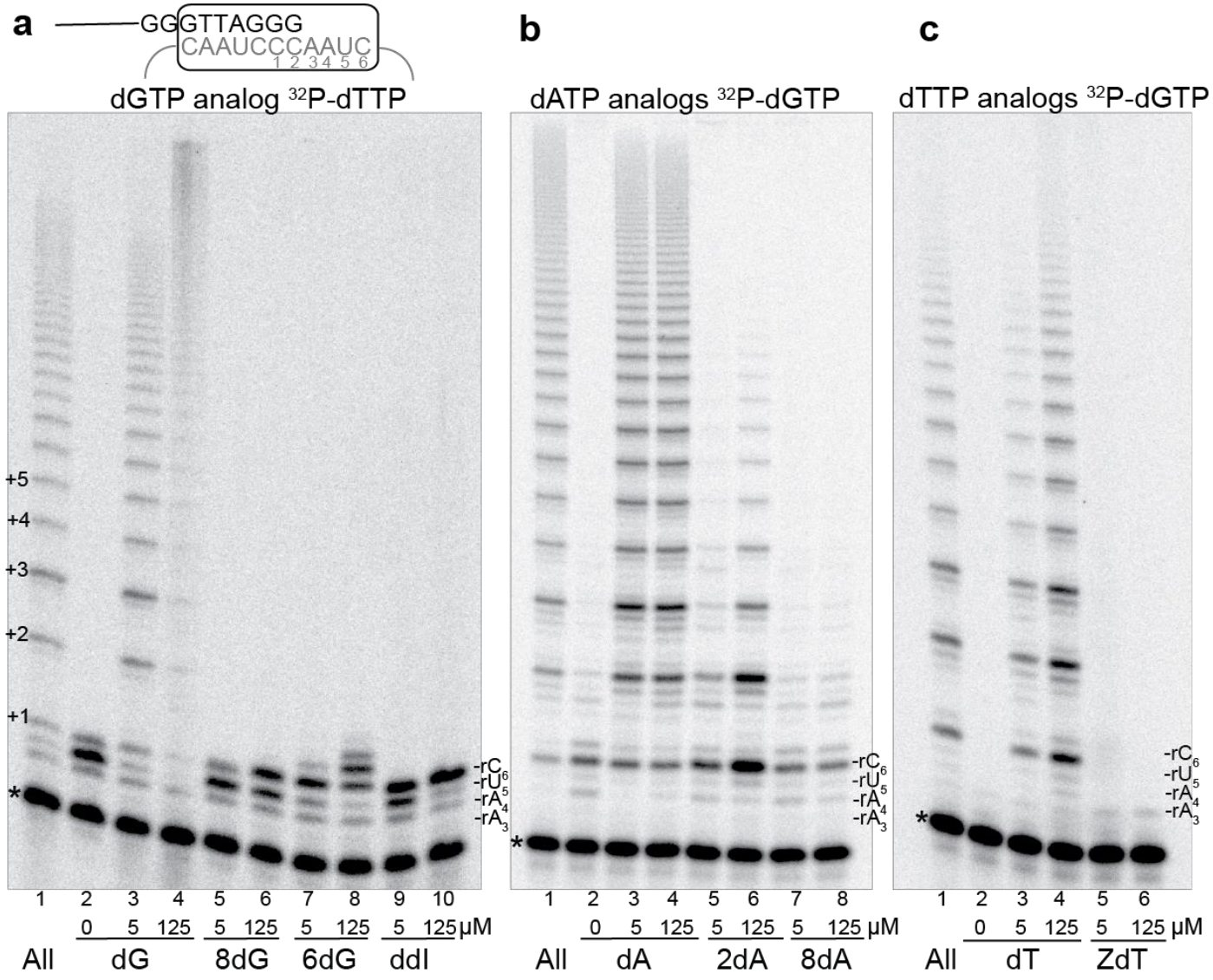

Figure 11. Oxidized and therapeutic dNTPs inhibit telomerase processivity. Telomerase reactions were conducted with $(TTAGGG)_3$ primer (3R) and cellular-concentration dNTPs (24 µM dATP, 29 µM dCTP, 37 µM dTTP, 5.2 µM dGTP) except that the indicated natural or modified dNTP was titrated in at increasing concentrations (0, 5, 125 µM) along with either 0.3 µM [α-^{32}P]dTTP (a) or 0.3 µM [α-^{32}P]dGTP (b, c) to label the products. The loading control (*) was a ^{32}P-end labeled 18-mer oligonucleotide. Numbers on the left indicate the number of added repeats; letters on the right indicate template residue. Images are representative of three independent experiments.

4.2 Telomerase inhibition mechanism depends on the modified dNTP

A chain terminating mechanism of inhibition requires that the enzyme adds the modified dNTP to a growing chain, which then blocks further synthesis. Since we showed previously that 8-oxo-dGTP is a genuine telomerase chain terminator, we used it here as a positive control[91]. To test whether telomerase can incorporate other modified dNTPs, and whether the incorporation is chain terminating and/or mutagenic, we conducted a direct telomerase extension assay in which we radiolabeled the primer and added increasing concentrations (5, 50, and 500 μM) of only a single dNTP (**Figure 14, Figure 15, and Figure 16**). Since modified dNTPs may prefer mispairing, we tested various primers in which the first template base was either rA_3, rC_1, or rU_5 (primer 1, primer 2, and primer 3, respectively), and compared the percent primer extension for each dNTP at the middle 50 μM concentration (**Figure 17**). Primers 1 and 2 initiate synthesis at consecutive rA_3rA_4 or rC_1rC_2 template bases, respectively, so we could examine both incorporation and extension to the next base. However, the telomerase template lacks tandem rU residues.

We first tested incorporation of natural dNTPs at the various template positions as controls. Reactions with a single dNTP type is an established method for determining DNA synthesis fidelity, defined as selectivity for incorporating a correct dNTP versus an incorrect or modified dNTP[153,154]. Interestingly, telomerase extended all three primers in the presence of dGTP, indicating telomerase can incorporate dGTP opposite each template base even at low cellular concentrations (5 μM) (**Figure 12**). However, comparisons at 50 μM dGTP indicates a preference for correct incorporation over misincorporation in order of rC_1 (33%, primer 2) > rA_3 (19%, primer 1) > rU_5 (4%, primer 3) extension (**Figure 17 lanes 2**). We also observed telomerase synthesis of

poly-dG ladders, as reported previously[91], even at early time points and synthesis at a single rC (**Figure 13 a and b**). As a control, reactions with DNA polymerase β showed no evidence of dGTP laddering or misincorporation opposite template A (**Figure 13c** and **d**). Poly-nucleotide ladders were not observed in reactions with any other dNTP (**Figure 17**) or with RNase addition **(Figure 9).** In the presence of dTTP, telomerase preferentially extended primer 1, showing incorporation opposite rA_3 and strong termination after rA_4, as expected, but also minor extension to the subsequent rU_5 (**Figure 17a lanes 3, and Figure 14**). Consistent with this, telomerase could extend primer 3 by misincorporating dTTP opposite rU_5 (**Figure 17c lane 3**). Thus, while telomerase can misinsert dTTP, it strongly prefers correct insertion (41% primer 1 extension versus 9% primer 3 extension). Similarly, telomerase strongly preferred correct insertion of dATP opposite rU_5, elongating primer 3 with minimal extension to the next rC_1, and poor or no extension of primers 1 and 2, respectively (**Figure 17 lane 4**). Finally, telomerase only extended primer 1 in the presence of dCTP, indicating some misincorporation opposite rA_3 (**Figure 17 lane 5, Figure 14**). In summary, these experiments show that telomerase extension was most accurate with primer 2 (template rC_1) and least accurate with primer 1 (template rA_3). Additionally, telomerase incorporation of dGTP is more error prone than the other natural dNTPs, as indicated by the production of poly d(G) ladders.

We next tested whether telomerase can incorporate oxidized dATPs onto the growing telomere chain using the end-labeled primers. Telomerase elongated primer 1 by misinserting 8-oxo-dGTP opposite rA_3 with minimal extension to the next template rA_4, confirming its chain terminating ability (**Figure 17 lanes 6 and Figure 15**)[91]. Telomerase showed little to no extension of primers 2 and 3 with 8-oxo-dGTP, indicating poor incorporation opposite rC_1 or rU_5. In contrast, we detected virtually no extension of any primers with 8-oxo-dATP, except for minimal

misinsertion opposite rA_3 with primer 1 (**Figure 17 lanes 7 and Figure 15**), suggesting 8-oxo-dATP is a very poor substrate for telomerase. However, telomerase readily extended primer 3 by inserting inserting 2-OH-dATP opposite the correct rU_5, generating only 2-fold less product than with dATP (16% versus 30%, respectively), and showed minimal extension to the next incorrect rC_1 position (**Figure 17 lanes 8**). Unlike 8-oxo-dGTP, telomerase insertion of 2-OH-dATP is not mutagenic, showing very low extension of primers 1 and 2 indicative of poor misinsertion opposite rA_3 and rC_1, respectively. The single template rU did not allow us to determine whether 2-OH-dATP insertion is chain terminating. In summary, our data indicate telomerase insertion of oxidized dNTPs follows the order 2-OH-dATP > 8-oxo-dGTP > 8-oxo-dATP opposite their preferred template base.

Analysis of the therapeutic dNTPs demonstrates that telomerase is able to add each of these analogs to a telomere chain Regarding the NRTIs, telomerase inserted ddITP opposite rC_1, extending primer 2 with moderate efficiency (16% extension) compared to reactions with dGTP (33% extension), but did not extend to the next rC_2 (**Figure 17 lanes 10 and Figure 16**). Telomerase extended primer 1 with AZT-TP, showing correct insertion opposite rA_3 with no extension to the next rA_4; yielding 26% extension compared to 41% extension with dTTP (**Figure 17 lanes 11**). These data definitively show that these HIV-1 RT chain terminators are also genuine telomerase chain terminators, and define the inhibition mechanism. Strikingly, telomerase was able to extend all three primers with 6-thio-dGTP, showing a preference for incorporation in order of template rC_1 (45%) > rA_3 (13%) > rU_6 (4%) primer extension (**Figure 17 lanes 9**), at product yields comparable to dGTP incorporation. In reactions with primer 2, telomerase correctly incorporated 6-thio-dGTP opposite rC_1, showing strong termination after insertion opposite the next rC_2. This suggests that, like dGTP, 6-thio-dGTP can bind at the telomerase active site at all

template primer positions, however unlike dGTP, it does not support poly-nucleotide laddering. Our data indicate telomerase insertion of therapeutic dNTPs follows the order 6-thio-dGTP > AZT-TP > ddITP. Unlike the NRTIs and 8-oxo-dGTP, 6-thio-dGTP is not a telomerase chain terminator, indicating the mechanism of inhibition is distinct.

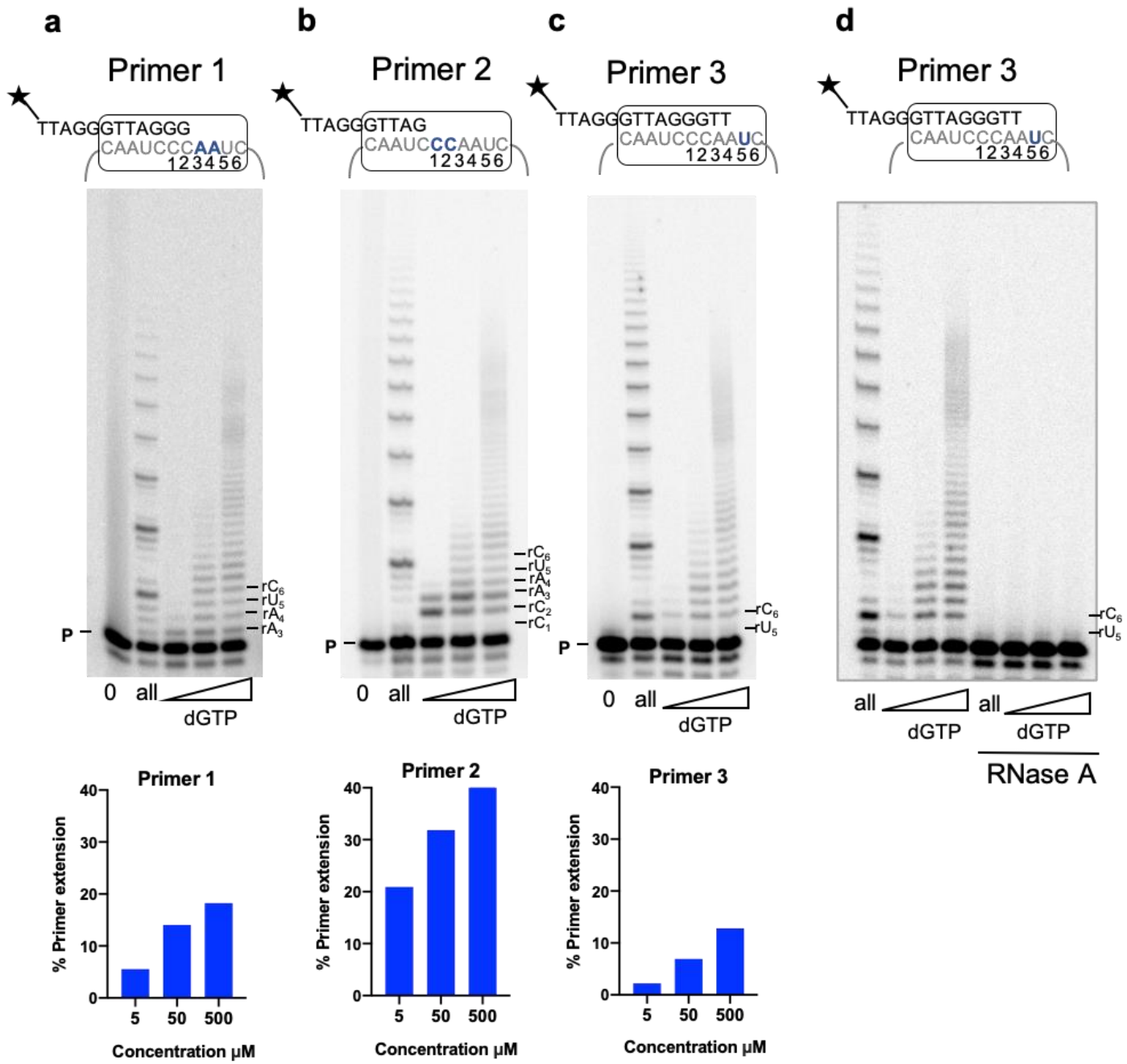

Figure 12. Telomerase extension with dGTP. Direct telomerase assays were conducted with 5 nM ^{32}P-end labeled primer (a) Primer 1 $(TTAGGG)_3$, (b) Primer 2 $(GGTTAG)_3$, or (c and d) Primer 3 $(AGGGTT)_3$. Reactions contained cellular-concentration dNTPs (24 µM dATP, 29 µM dCTP, 37 µM dTTP, 5.2 µM dGTP) (all) or 5, 50, or 500 µM dGTP. In panel (d) reactions contained 3 µg/µl RNase A. Products were separated on denaturing gels. Letters on the right indicate the template base; P indicates unextended primer. Graphs represent the percent of total primers extended for the reactions in panels a – c from one experiment.

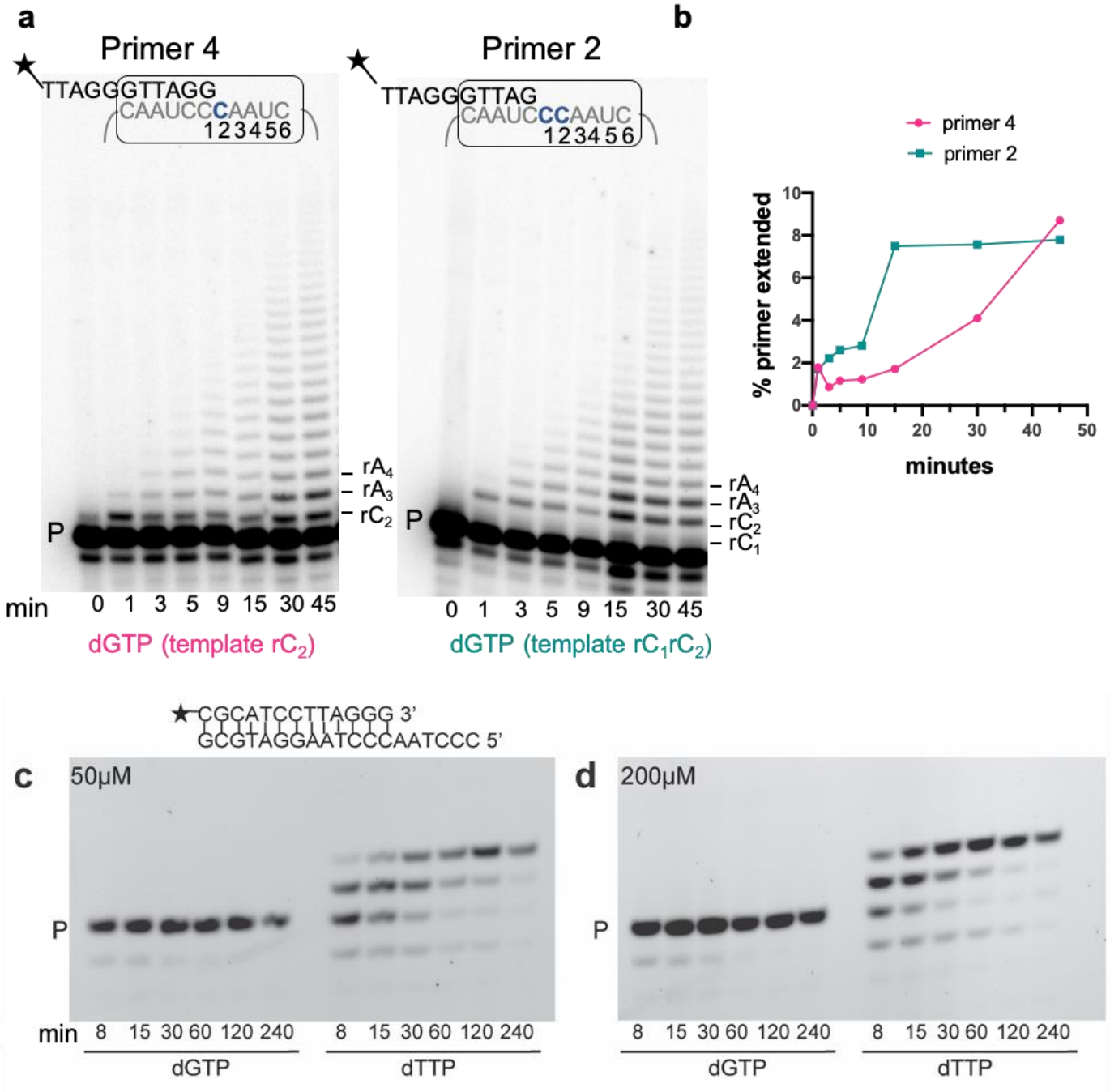

Figure 13. Time course reactions with telomerase or pol β. (a, b) Telomerase reactions were conducted with 5 nM ^{32}P-end labeled primer (a) Primer 4 $(GTTAGG)_3$ or (b) Primer 2 $(GGTTAG)_3$. Reactions contained 50 μM dGTP and were terminated at 0, 1, 3, 5, 9, 15, 30, or 45 minutes as indicated. Products were separated on denaturing gels. Letters on the right indicate the template base; P indicates unextended primer. Graphs represent the percent primer extended for the

reactions in panels a and b from one experiment. (c, d) Primer extension by human polymerase β. The double stranded 6-FAM labeled primer-template and polymerase β were incubated with either 50 μM dGTP or dTTP (c), or 200 μM dGTP or dTTP (d) for time ranging from 8-240 minutes as indicated. The products of the reactions were run on denaturing gels and the gels were imaged using a Typhoon phosphoimager. P indicates unextended primer.

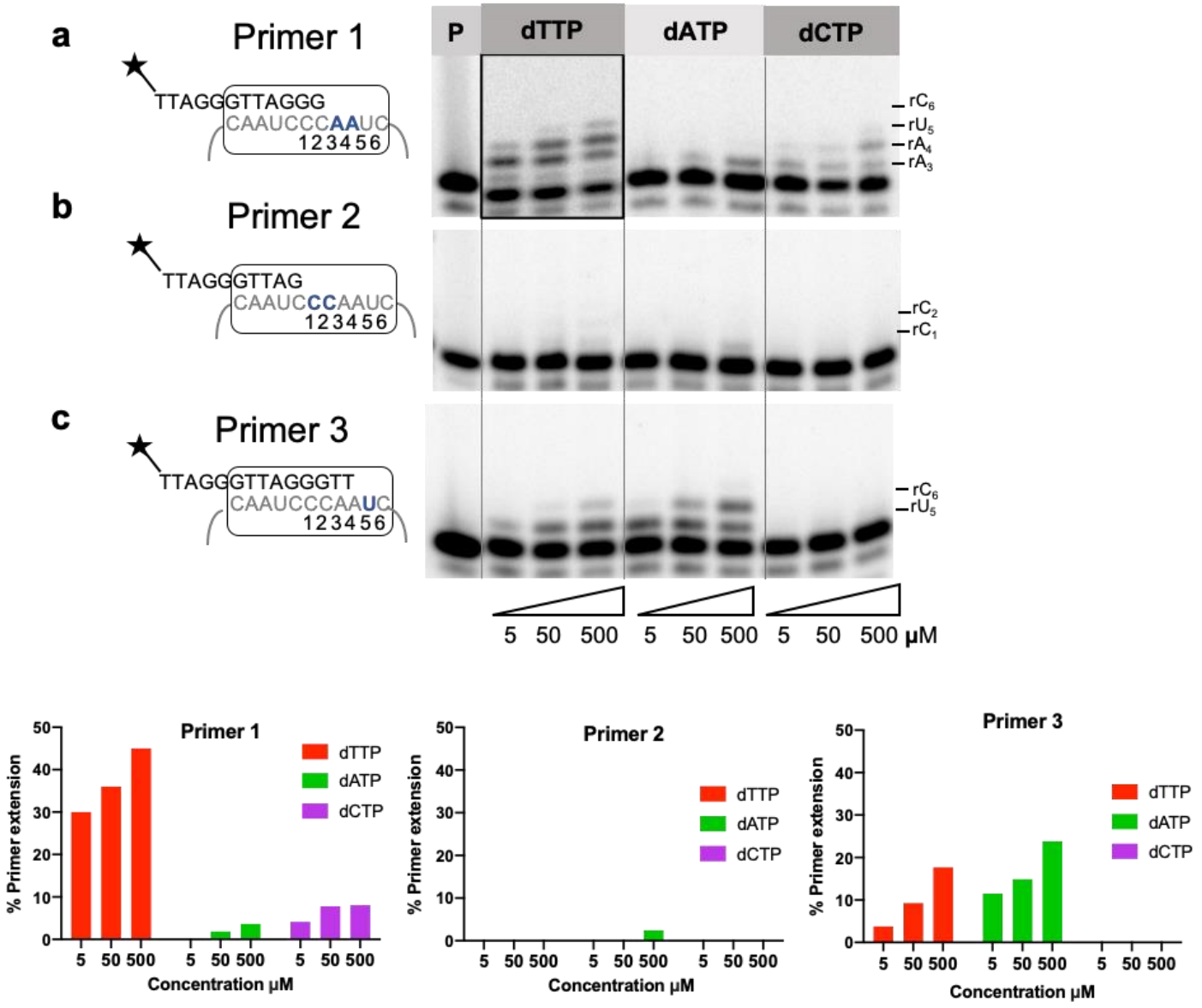

Figure 14. Telomerase extension with natural dNTPs. Direct telomerase assays were conducted with 5 nM ^{32}P-end labeled primer (a) Primer 1 $(TTAGGG)_3$, (the box around dTTP reactions indicates image from a separate gel) (b) Primer 2 $(GGTTAG)_3$, or (c) Primer 3 $(AGGGTT)_3$. Reactions contained 5, 50, and 500 µM dTTP, dATP, or dCTP as indicated. Products were separated on denaturing gels. Letters on the right indicate the template base; P indicates unextended primer. Graphs represent the percent of total primers extended for the reactions in panels a, b, and c from one experiment.

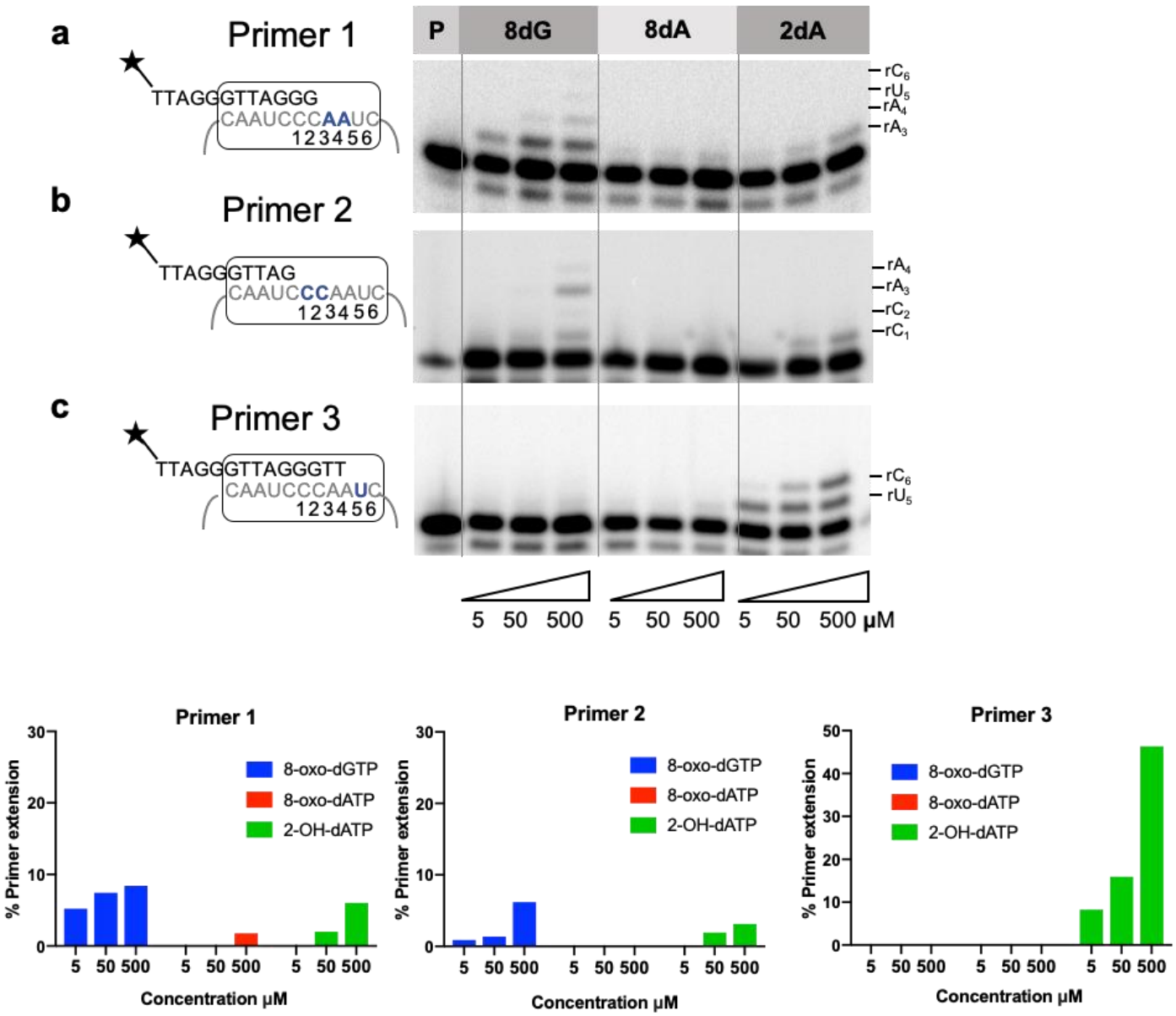

Figure 15. Telomerase extension with oxidized dNTPs. Direct telomerase assays were conducted with 5 nM ^{32}P-end labeled primer (a) Primer 1 $(TTAGGG)_3$, (b) Primer 2 $(GGTTAG)_3$, or (c) Primer 3 $(AGGGTT)_3$. Reactions contained 5, 50, and 500 µM 8-oxo-dGTP (8dG), 8-oxo-dATP (8dA), or 2-OH-dATP (2dA) as indicated. Products were separated on denaturing gels. Letters on the right indicate the template base; P indicates unextended primer. Graphs represent the percent of total primers extended for the reactions in panels a, b, and c from one experiment.

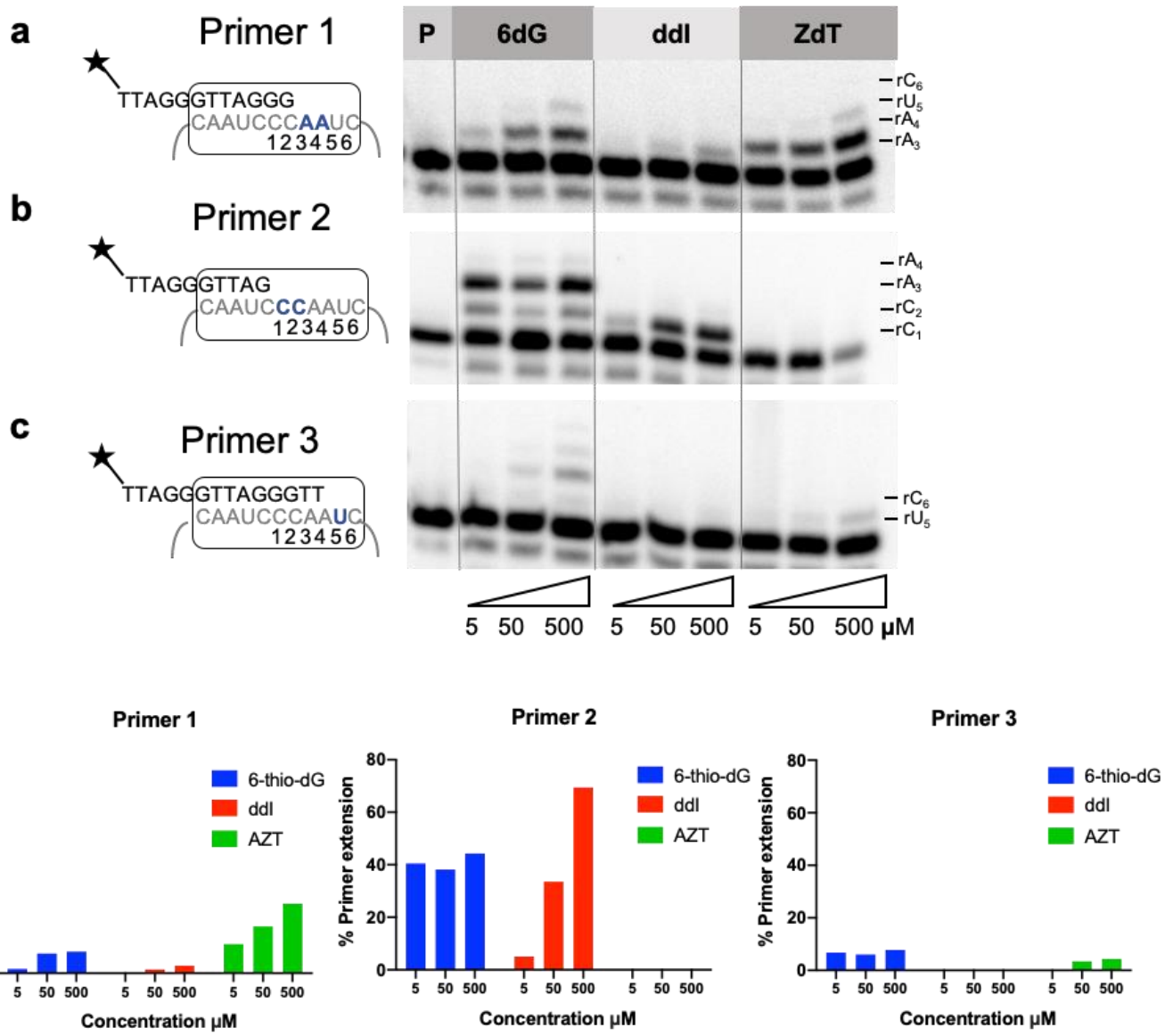

Figure 16. Telomerase extension with therapeutic dNTPs. Direct telomerase assays were conducted with 5 nM ^{32}P-end labeled primer (a) Primer 1 $(TTAGGG)_3$, (b) Primer 2 $(GGTTAG)_3$, or (c) Primer 3 $(AGGGTT)_3$. Reactions contained 5, 50, and 500uM 6dG (6-thio-dGTP), ddI (ddITP) or ZdT (AZT-TP) as indicated. Products were separated on denaturing gels. Letters on the right indicate the template base; P indicates unextended primer. Graphs represent the percent of total primers extended for the reactions in panels a, b, and c from one experiment.

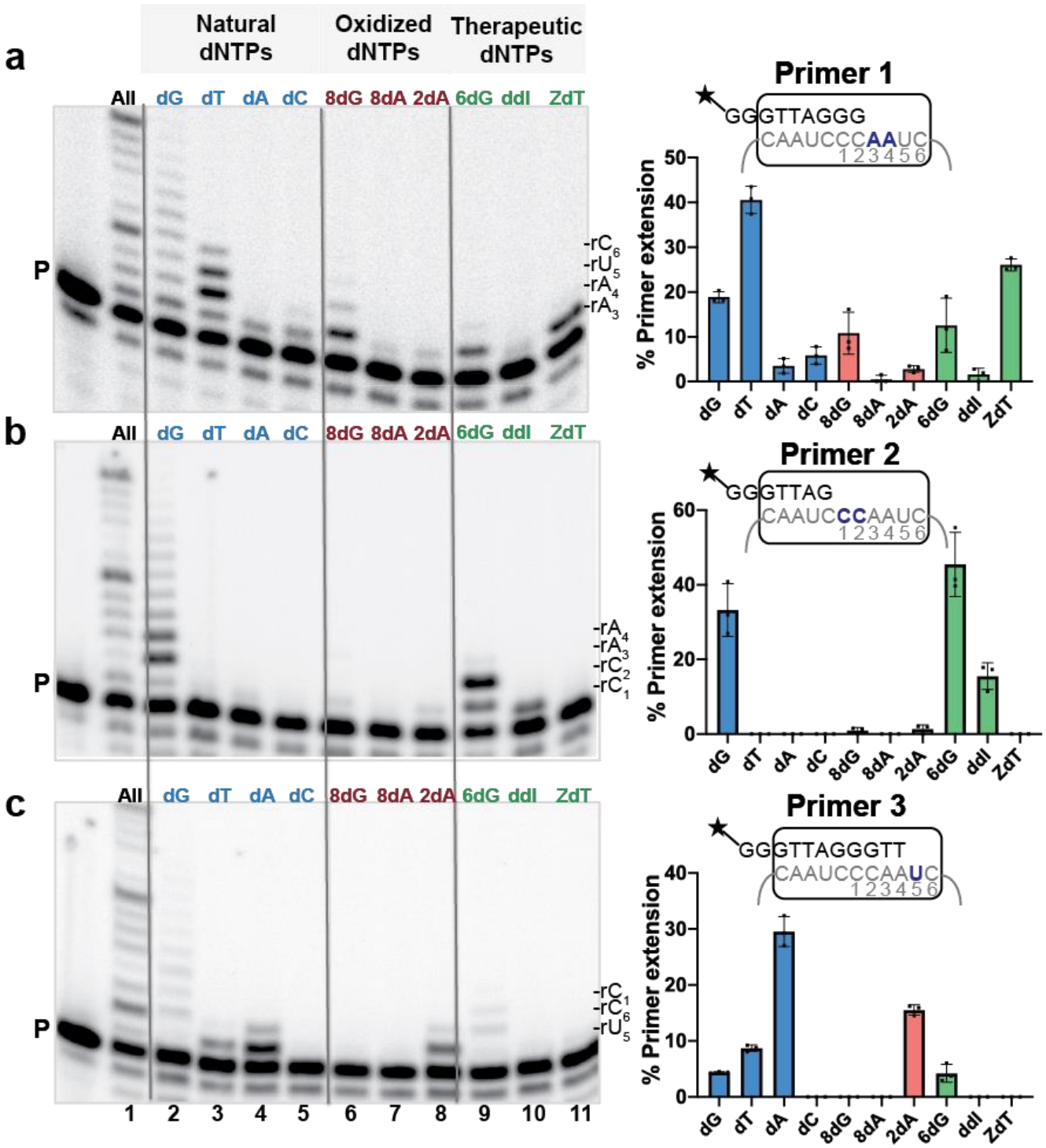
a
Natural dNTPs
Oxidized dNTPs
Therapeutic dNTPs
All dG dT dA dC 8dG 8dA 2dA 6dG ddI ZdT
P
-rC6
-rU5
-rA4
-rA3
Primer 1
GGGTTAGGG
CAAUCCCAAUC
1 2 3 4 5 6
% Primer extension
dG dT dA dC 8dG 8dA 2dA 6dG ddI ZdT
b
All dG dT dA dC 8dG 8dA 2dA 6dG ddI ZdT
P
-rA4
-rA3
-rC2
-rC1
Primer 2
GGGTTAG
CAAUCCCAAUC
1 2 3 4 5 6
% Primer extension
dG dT dA dC 8dG 8dA 2dA 6dG ddI ZdT
c
All dG dT dA dC 8dG 8dA 2dA 6dG ddI ZdT
P
-rC1
-rC6
-rU5
1 2 3 4 5 6 7 8 9 10 11
Primer 3
GGGTTAGGGTT
CAAUCCCAAUC
1 2 3 4 5 6
% Primer extension
dG dT dA dC 8dG 8dA 2dA 6dG ddI ZdT

Figure 17. Telomerase insertion of modified dNTPs. Telomerase reactions were conducted with 5 nM ^{32}P-end labeled primer (a) Primer 1 $(TTAGGG)_3$, (b) Primer 2 $(GGTTAG)_3$, or (c) Primer 3 $(AGGGTT)_3$. Reactions contained cellular-concentration dNTPs (24 µM dATP, 29 µM dCTP, 37 µM dTTP, 5.2 µM dGTP) (lane 1) or 50 µM of indicated natural dNTP (blue, lanes 2-5), oxidized dNTP (red, lanes 6-8), or therapeutic dNTP (green, lanes 9-11). Products were separated on denaturing gels. 8dG (8-oxo-dGTP); 8dA (8-oxo-dATP); 2dA (2-OH-dATP); 6dG (6-thio-dGTP); ddI (ddITP); ZdT (AZT-TP). Letters on the right indicate the template base; P indicates unextended primer. Graphs represent the percent of total primers extended. Data are shown as mean + s.d. from three independent experiments..

4.3 2-OH-dATP and 6-thio-dGTP insertion disrupt telomerase translocation

To better understand how 2-OH-dATP and 6-thio-dGTP inhibit the telomerase catalytic cycle, we examined whether telomerase could incorporate a natural dNTP after adding the modified dNTP. First, we used primer 3 to examine extension after insertion opposite rU_5 in reactions with 50 μM each of dTTP, dGTP and either dATP or 2-OH-dATP. We observed typical processive synthesis with all three natural dNTPs, but replacing dATP with 2-OH-dATP generated a strong termination product after extension to the next base (rC_6), which is the final base prior to translocation (**Figure 18a**). These data indicate that telomerase can extend after insertion of 2-OH-dATP, but translocation to add the next repeat is greatly compromised. Those few reactions that continued after translocation terminated prior to reaching the template end, suggesting 2-OH-dATP disrupts both repeat and nucleotide processivity. Next, we conducted reactions with 50 μM each of dATP, dTTP and either dGTP or 6-thio-dGTP. **Figure 18b-d** show typical processive synthesis with the natural dNTP after initiating synthesis opposite rA_3 (primer 1), rC_1 (primer 2), and rU_5 (primer 3). Next we replaced dGTP with 6-thio-dGTP. Primer 1 reactions show strong termination products after telomerase inserted 6-thio-dGTP opposite rC_6 position (4 nucleotides added) (**Figure 18b**), suggesting dissociation prior to translocation We also observed strong termination products at the next rC_1 (5 nucleotides added), indicating either successful translocation in some reactions followed by dissociation, or template slippage for an additional 6-thio-dGTP incorporation prior to translocation. This result was recapitulated with primer 3. **Figure 18** shows that after telomerase inserted dATP opposite rU_5, the majority of the reactions terminated after 6-thio-dGTP insertion opposite rC_6 or the next rC_1. Finally, reactions with primer 2 show that telomerase incorporates 6-thio-dGTP opposite the first two rC_1rC_2 positions, but

primarily terminates synthesis after extension to rA_3 (three nucleotides added) prior to translocation, despite the availability of natural dNTPs to add another repeat (**Fig. 4c**). Telomerase can also add a natural nucleotide (dTTP opposite rA) after 6-thio-dGTP insertion, confirming 6-thio-dGTP is not a chain terminator. However, termination prior to completing synthesis of the 6-nt repeat indicates that 6-thio-dGTP not only disrupts repeat processivity, but also nucleotide processivity. Our data suggest 6-thio-dGTP and 2-OH-dATP addition interfere with telomerase processivity, and compromise translocation and further telomere extension.

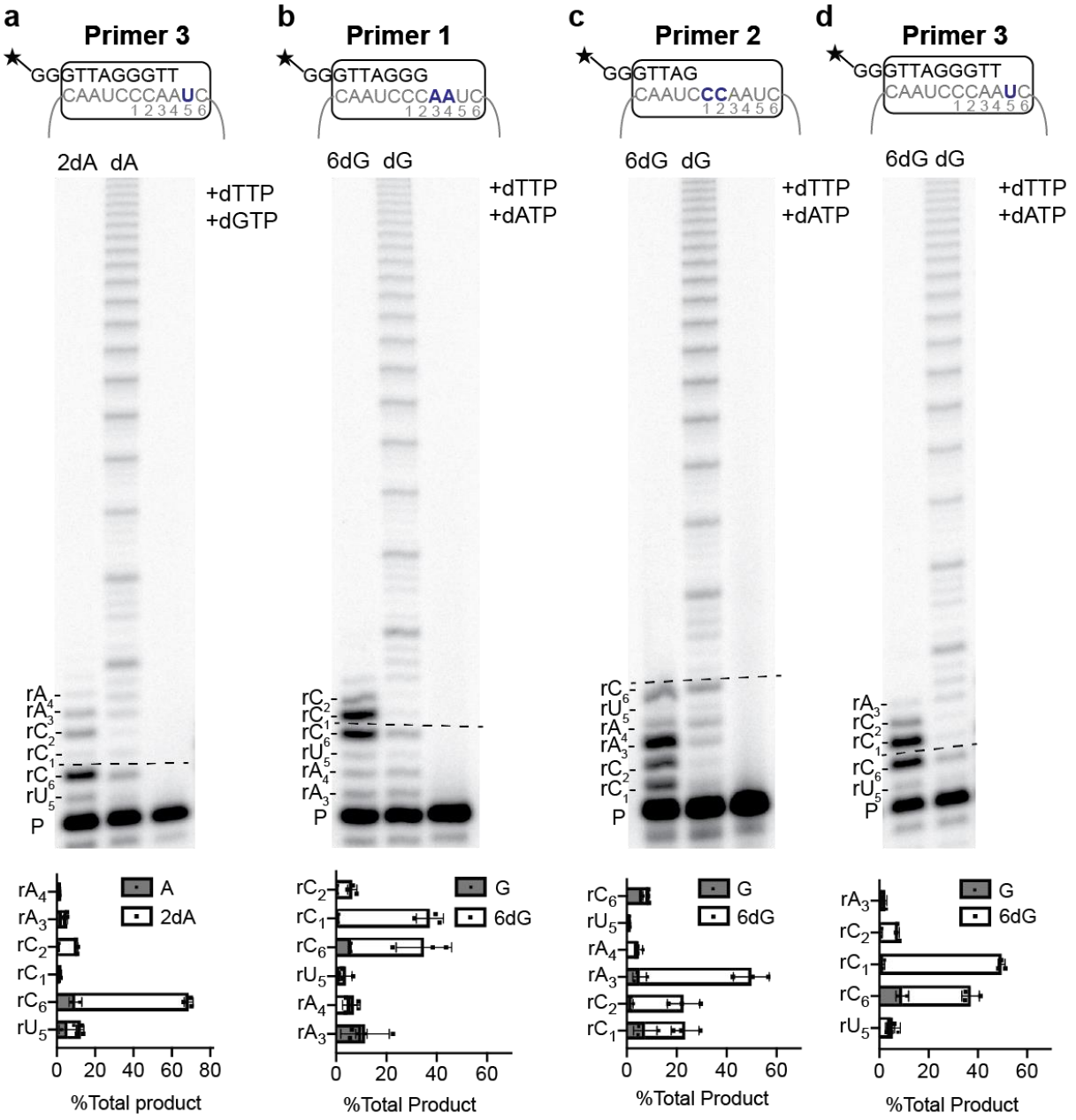

Figure 18. 2-OH-dATP and 6-thio-dGTP insertion disrupt telomerase translocation. Direct telomerase assays were conducted with 5 nM 32P-end labeled primer (a and d) Primer 3 $(AGGGTT)_3$, (b) Primer 1 $(TTAGGG)_3$ or (c) Primer 2 $(AGGGTT)_3$. Reactions contained 50 µM dATP, dTTP and dGTP, except when 2-OH-dATP (2dA) or 6-thio-dGTP (6dG) was substituted for dATP or dGTP, respectively where indicated. Products were separated on denaturing gels. Letters on the right of the graph indicate the template base; P indicates unextended primer. Graphs represent percent of product terminated at each template position as a function of total products. Data are the mean + s.d. from three independent experiments.

4.4 POT1-TPP1 fail to restore telomerase processivity inhibition

Next we tested whether the telomerase processivity factor POT1-TPP1 could modulate modified dNTP inhibition of telomerase. POT1 binds to the telomeric ssDNA overhang, requiring the minimum ssDNA sequence of 5'-TTAGGGTTAG-3'[155]. The inclusion of POT1 binding partner TPP1, increases the binding affinity for telomeric DNA ten-fold compared to POT1 alone[156]. POT1-TPP1 recruits telomerase to telomeres *in vivo*[156], and greatly increases telomerase processivity[15]. Therefore, we reasoned that POT1-TPP1 may be able to overcome inhibition by the modified dNTPs and enhance telomerase processivity. We conducted telomerase extension reactions with radiolabeled primer in the presence of purified POT1-TPP1, and used a primer with a single mutation (TTAGGGTTAGCGTTAGGG; underlined G to C mutation)[55] to ensure the POT1-TPP1 would be positioned at the 5' portion of the DNA primer (**Figure 19**). This provides a homogenous substrate for telomerase extension.

For these reactions, we replaced the natural dNTP with the modified dNTP analog, while the other dNTPs remained at cellular relevant concentrations. As a positive control, we show the addition of POT1-TPP1 to telomerase reactions containing all natural dNTPs significantly increased repeat processivity ($R_{1/2}$) from 2.5 to 4.5, as indicated by the appearance of longer products (**Figure 19 a lanes 1 and 2, and 5c**). $R_{1/2}$ represents the number of repeats added before half of the DNA substrates dissociate from telomerase, meaning nearly half of the bound primers were elongated by roughly 5 repeats in the presence of POT1-TPP1. When dGTP was replaced with 8-oxo-dGTP, addition of POT1-TPP1 was unable to overcome the chain termination (**Figure 19a lanes 3 and 4**). In contrast, for reactions in which 2-OH-dATP replaced dATP, POT1-TPP1 stimulated telomerase extension by enhancing processivity 5-fold from 0.5 to 2.3 (**Figure 19a lanes 7 and 8, and 5c**). This suggests that 2-OH-dATP incorporation may disrupt telomerase

interaction with the primer, which may be partly compensated for by POT1-TPP1. For reactions in which dATP was replaced with 8-oxo-dATP, we observed some POT1-TPP1 stimulation, although processivity was still greatly reduced compared to reactions with all natural dNTPs (**Figure 19a lanes 5 and 6**). However, we suspect this synthesis may have resulted from misincorporation of dGTP or dTTP opposite rU in the absence of dATP (**Figure 17c lanes 2 and 3**), since 8-oxo-dATP is a poor substrate for telomerase. As expected, POT1-TPP1 failed to stimulate telomerase processivity in reactions containing ddITP and AZT-TP, since insertion of ddITP opposite rC and AZT-TP opposite rA halted further synthesis (**Figure 19b lanes 5-8**). However, POT1-TPP1 also failed to stimulate telomerase when dGTP was replaced with 6-thio-dGTP (**Figure 19c lanes 3 and 4**), indicating this analog is also a strong telomerase inhibitor. Overall, these data indicate that POT1-TPP1 is not able to fully restore telomerase extension in the presence inhibitory dNTPs, although these proteins can partly stimulate processivity in reactions containing 2-OH-dATP.

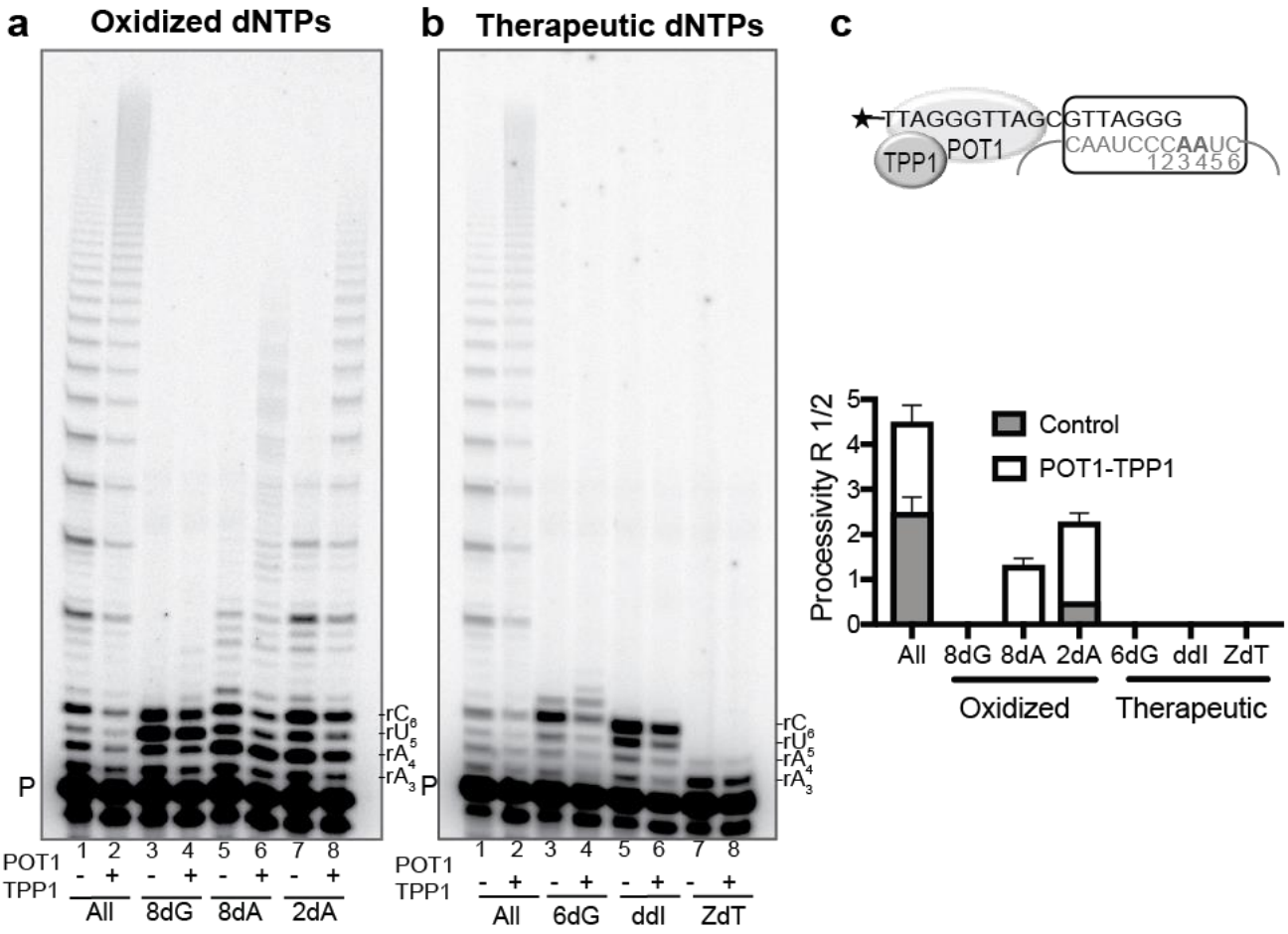

Figure 19. POT1-TPP1 fail to overcome inhibitory dNTPs. Direct telomerase assays were conducted in the absence or presence of 500 nM POT1 and 500 nM TPP1, as indicated, and 5 nM 32P-end labeled primer (TTAGGGTTAGCGTTAGGG) designed to position POT1 at the 10 nt primer 5' end. Reactions contained cellular-concentration dNTPs (24 µM dATP, 29 µM dCTP, 37 µM dTTP, 5.2 µM dGTP) (lanes 1 and 2), except when the natural dNTP was substituted with the oxidized dNTP (a) or therapeutic dNTP (b) analog (lanes 3-8), as indicated. 8dG (8-oxo-dGTP); 8dA (8-oxo-dATP); 2dA (2-OH-dATP); 6dG (6-thio-dGTP); ddI (ddITP); ZdT (AZT-TP). Letters on the left indicate template base; P indicates unextended primer. (c) Processivity calculated on the basis of total products normalized to loading control. Data are shown as mean + standard deviation from three independent experiments.

4.5 Telomerase exhibits poor selectivity against 6-thio-dGTP, ddITP and 2-OH-dATP

In order to gain further insight into the ability of modified dNTPs to compete with natural dNTPs for telomerase utilization, we added modified dNTPs to reactions containing all four natural dNTPs. We conducted reactions with cellular relevant concentrations of natural dNTPs and titrated the modified dNTP from 0 to 10,000 μM to calculate the half maximal inhibitory concentration (IC_{50}) based on telomerase repeat processivity (**Figure 20**). The calculated IC_{50} determines the concentration required to reduce repeat processivity in the bulk reactions by half. However, it is important to note that bulk experiments cannot distinguish effects on individual telomeres, since extended telomeres mask unextended telomeres. Incorporation of a chain terminator during any step will terminate extension of the affected telomere, and just five critically short telomeres are sufficient to trigger senescence[157]. Therefore, repeat processivity IC_{50} values are not necessarily an indicator of the inhibitory potency, but provide information on selectivity for modified dNTPs compared to natural dNTPs. The oxidized dNTPs 8-oxo-dATP and 8-oxo-dGTP had similar IC_{50} values as the genuine chain terminator AZT-TP ranging from 402 to 1690 μM (**Table 2**). However, the therapeutic dNTPs 6-thio-dGTP and ddITP, and oxidized 2-OH-dATP, displayed the lowest IC_{50} values of 5, 61, and 103 μM, respectively. Our data suggest these modified dNTPs, especially 6-thio-dGTP, can effectively compete with the natural dNTPs for binding in the telomerase active site. Given the remarkably low IC_{50} for 6-thio-dGTP, we examined the catalytic efficiency of 6-thio-dGTP incorporation versus dGTP using the *Tribolium castaneum (tc*TERT*)* model of the telomerase catalytic core[32]. The ability to purify sufficient quantities of *tc*TERT enables characterization of the catalytic nucleotide addition by pre-steady-state single turnover kinetics using a defined DNA-RNA primer-template substrate[144]. The catalytic efficiency of incorporating a single dNTP is measured by dividing the observed

nucleotide incorporation rate constant, k_{pol}, by the equilibrium dissociation constant for dNTP binding to the *tc*TERT-primer-template complex (K_d) [158]. The catalytic efficiency of inserting dGTP is only 2-fold higher at 0.034 $\mu M^{-1}s^{-1}$ compared to 6-thio-dGTP at 0.056 $\mu M^{-1}s^{-1}$, indicating poor selectivity against this dNTP analog (**Table 3**). Collectively, these results indicate that modified dNTPs vary in the ability to compete with the natural dNTPs for utilization by telomerase.

Table 2. Telomerase processivity IC50 values

Modified dNTP	**IC_{50} µM** ± SD
8-oxo-dATP	946 ± 49
2-OH-dATP	103± 66
8-oxo-dGTP	1690 ± 172
ddITP	61 ± 23
AZT-TP	402 ± 169
6-thio-dGTP	5 ± 2

Table 3. Single-turnover kinetic values for tcTERT single nucleotide insertion

Incoming Nucleotide	k_{pol} (s^{-1})	K_d (µM)	Catalytic Efficiency (k_{pol}/K_d) ($\mu M^{-1}s^{-1}$)	Fold change
dGTP[a]	1.1 ± 0.03	18.1 ± 3.78	0.058 ± 0.012	1.000
6-thio-dGTP	3.1 ± 0.23	92.4 ± 12.94	0.034 ± 0.005	0.579

[a]Values from [144].

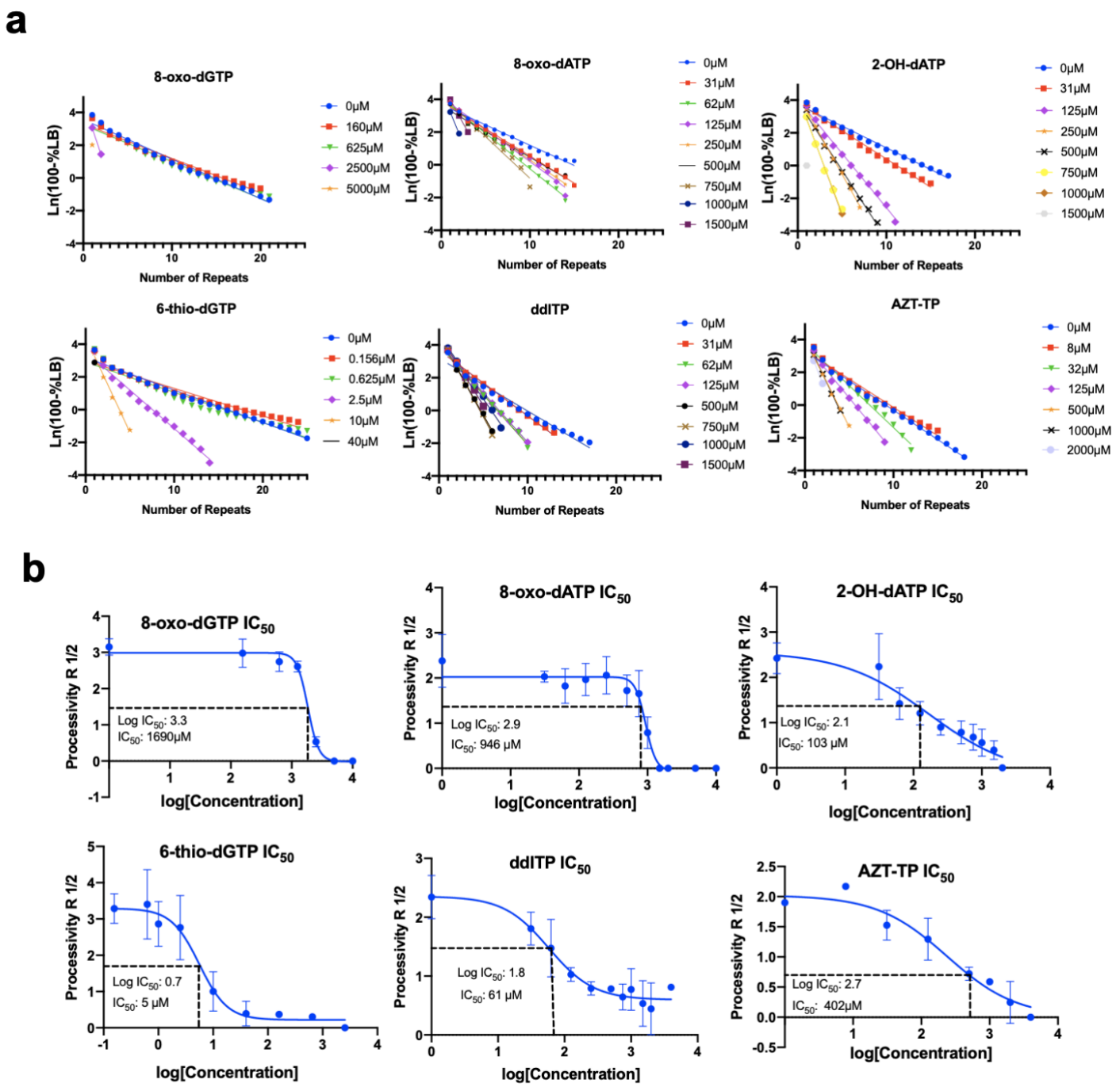

Figure 20. IC_{50} values for telomerase processivity inhibition. Telomerase reactions were conducted with cellular relevant concentrations of all four natural dNTPs and increasing concentrations of the modified dNTP analog from 0 to 10,000 μM to calculate (a) the processivity as R1/2 and (b) the half maximal inhibitory concentration (IC_{50}) based on telomerase processivity. Means and s.d. are from 3-4 independent experiments, and from 2 experiments for the ddITP reactions..

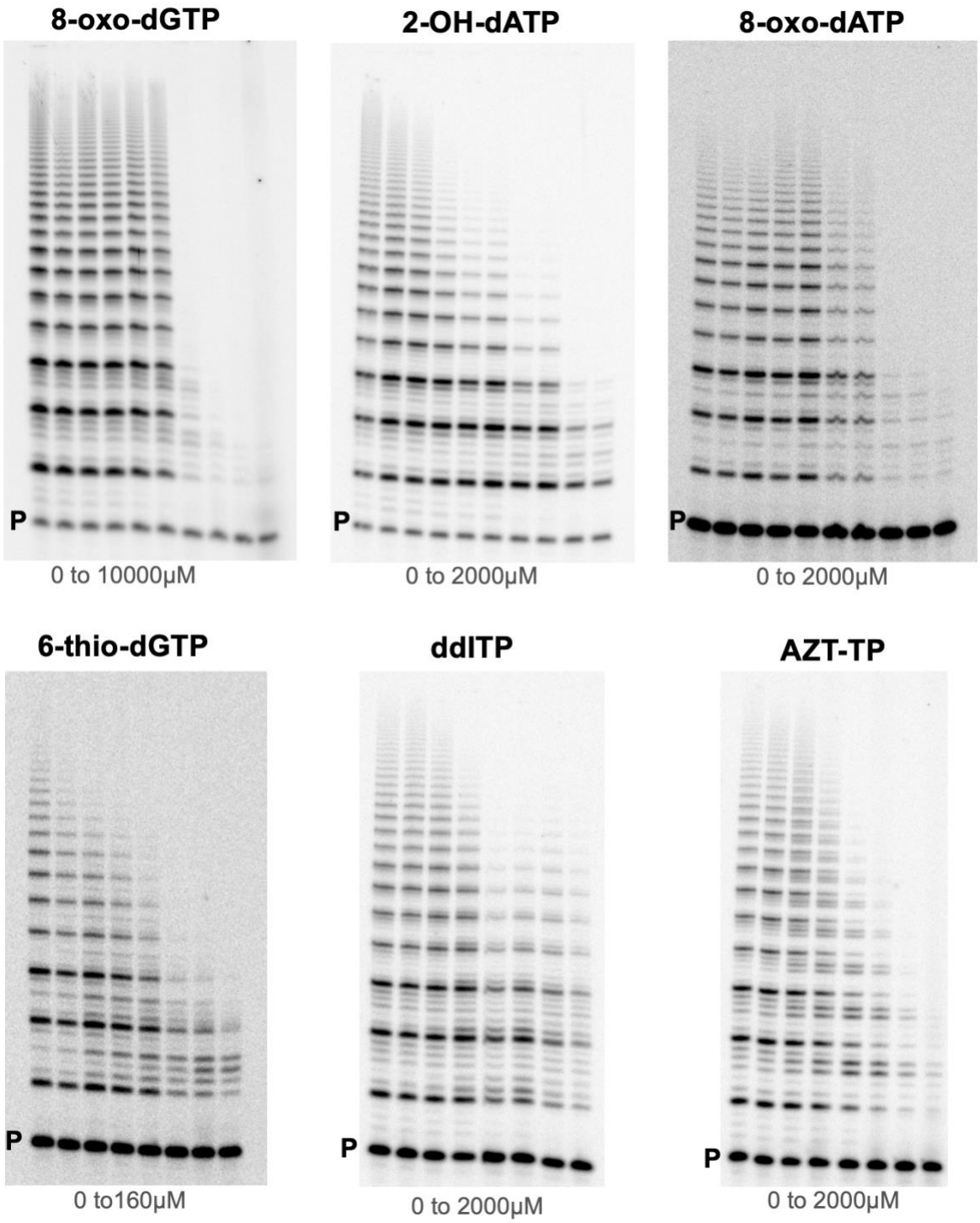

Figure 21. Representative titration gels for IC_{50} values. Telomerase reactions were conducted with cellular relevant concentrations of all four natural dNTPs and increasing concentrations of the modified dNTP analog from 0 to 10,000 μM. Products were separated on denaturing gels; P indicates unextended 18-mer primer. Images are representative from 3-4 independent experiments, and from 2 experiments for AZT-TP reactions.

5.0 Discussion

Previous studies showed that treatments with NRTIs and thiopurines, or the failure to remove oxidized dNTPs, drive telomere shortening in human cells. Here, we report two distinct mechanisms by which oxidized and therapeutic dNTPs inhibit telomerase mediated telomere elongation, either by chain termination or by disrupting translocation and subsequent repeat addition. By using end labeled telomeric primers, we provide direct evidence that telomerase can add the HIV RT inhibitors ddITP and AZT-P to a growing telomere chain, and that incorporation halts further elongation. Unlike the NRTIs and 8-oxo-dGTP, we found that telomerase could continue elongation after inserting a 2-OH-dATP and 6-thio-dGTP, but that addition of these modified dNTPs strongly inhibits repeat addition processivity (RAP), leading to truncated products. We propose a mechanism by which insertion of these RAP inhibitors disrupt stable formation of the RNA:DNA hybrid required for successful translocation and continued repeat addition.

Defining the mechanism of telomerase inhibition requires analysis of whether telomerase can catalyze the addition of the modified dNTP to the telomeric end. Reactions with a single dNTP type also inform about selectivity for inserting a correct dNTP versus an incorrect or modified dNTP during DNA synthesis[158]. Control reactions with natural dNTPs at different template positions revealed several aspects of telomerase fidelity of DNA synthesis. First, we found that telomerase incorporation of dGTP is more error prone than the other natural dNTPs, as indicated by dGTP misincorporation opposite rA and rU even at low 5 μM and the production of poly d(G) ladders. This propensity for telomerase to misinsert dGTP competes with insertion of the low radioactive dTTP amounts used to label the products in **Fig. 2a**, explaining the loss of radiolabeled

products at high dGTP concentrations. In contrast, high dATP or dTTP concentrations did not outcompete insertion of radiolabeled dGTP in **Fig. 2b and c**. However, we observed some dTTP misincorporation opposite template rU even at low 5 μM, and propose that misinsertion of dGTP and dTTP opposite rU likely explains the one repeat addition observed when dATP is absent (**Fig. 2b** lane 2). For reactions containing only dGTP, the poly d(G) ladders appeared at early time points and low percent primer extension (<10%) suggesting they resulted from processive nucleotide addition. Previous reports have also shown that both human and ciliate telomerase can make poly d(G) ladders, and suggest this is due to DNA hairpin-induced slippage of the telomerase product 3' end relative to the template C tract [159,160]. In addition, high dGTP concentrations overcome the template embedded pause site that slows addition of the first dGTP for GGTTAG repeat synthesis[161]. Telomerase has a lower K_m for dGTP incorporation than other dNTPs, which suggests that telomerase has increased dGTP binding affinity[23,154,162], and may explain the higher propensity for dGTP misinsertion and poly d(G) synthesis.

The oxidative stress-induced telomere shortening and loss observed upon MTH1 inhibition has been attributed to telomerase incorporation of 8-oxodGTP which prevents further elongation[91]. Our biochemical results that oxidized dATPs inhibit telomerase indicate that they can also contribute to telomerase inhibition in MTH1 depleted cells. However, unlike 8-oxo-dGTP, 8-oxo-dATP is very poor substrate for telomerase. DNA synthesis accuracy depends on discrimination against base pairs that cannot adopt Watson-Crick like geometry. While polymerase studies of 8-oxo-dATP insertion are lacking, studies with 8-oxodA in the template show mammalian DNA polymerases insert dTTP or dGTP opposite 8-oxodA and accommodate the base pair partly through base tautomerization and interactions with polymerase residues at the active site[163]. Telomerase may lack contacts required to stabilize an 8-oxodA base pair for catalysis. If 8-

oxodATP occupies the active site in a non-productive manner, it may prevent access to natural dNTPs, similar to telomerase inhibitor 5-MeCITP[164]. Alternatively, 8-oxodATP may interact with telomerase elsewhere outside the active site. In contrast, our data indicate the 2-OH-dATP:rU base pair is well tolerated in the telomerase active site, since 2-OH-dATP insertion opposite rU was only 2-fold less efficient than dATP. 2-OH-dATP can pair with thymine or uracil either in an enol tautomeric form with Watson-Crick hydrogen bonding, or in a keto form through wobble base pairing[165,166]. Similarly, HIV-1 and avian myeoblastosis virus RTs also preferentially insert 2-OH-dATP opposite dT or rU, and more efficiently than replicative polymerases α and ε [167,168]. Translesion DNA polymerases typically harbor a larger binding pocket to accommodate lesions, however, not all TLS polymerases can incorporate 2-OH-dATP. Pol η incorporates 2-OH-dATP opposite all template positions except A with an efficiency 2-6% lower than the natural base, whereas Pol ι cannot incorporate 2-OH-dATP at all[169]. Our data indicate that telomerase insertion of 2-OH-dATP more closely resembles other RTs compared to replicative and TLS polymerases, consistent with a similar binding pocket.

Similar to 2-OH-dATP, we found telomerase readily adds 6-thio-dGTP to the telomeric end. Our data indicate that telomerase exhibits very poor discrimination against 6-thio-dGTP. First, dGTP and 6-thio-dGTP yielded similar percent extension of primers initiating synthesis opposite the correct rC and the incorrect rA. Second, although *T. castaneum* telomerase had lower affinity for 6-thio-dGTP, as indicated by a higher K_d than for dGTP, the polymerization rate was faster, yielding similar catalytic efficiencies. Third, 6-thio-dGTP has a very low IC_{50} for telomerase RAP inhibition in bulk biochemical reactions. This is not surprising given that human Pols α, β, δ and γ all insert 6-thio-dGTP with similar efficiencies as dGTP, and structures of Pol β inserting 6-thio-dGTP opposite C, versus dGTP, are nearly identical[170,171]. However, while 6-

thio-dGTP can support DNA synthesis, it reduces primer elongation by mammalian DNA polymerases compared to dGTP[170], and strongly inhibits telomerase processivity. Thus, while the sulfur substitution has a minor effect on catalysis, it has a dramatic effect on telomere elongation. Our results showing 6-thio-dGTP directly inhibits telomerase processivity, provides an explanation for why 6-thio-dG promotes telomere shortening in telomerase positive cells, but not telomerase negative cells[128].

Our results demonstrate that 2-OH-dATP and 6-thio-dGTP are not chain terminators, but rather inhibit telomerase by disrupting the translocation step. While insertion of either modified dNTP did not prevent extension to the next template base, limited synthesis occurred after the first translocation. About 50% of the reactions terminated after 6-thio-dGTP insertion at the last template rC, and the remaining terminated after 6-thio-dGTP insertion at the first template rC following translocation, indicating disruption prior to, or immediately following, translocation. Translocation involves the separation of the DNA:RNA duplex and repositioning of the DNA product to reveal the RNA template and prime additional repeat synthesis. Previous evidence suggests the DNA:RNA duplex separation and realignment occur outside the enzyme active site, followed by binding and repositioning the new DNA:RNA hybrid in the active site after translocation[23,142]. Previous work indicates continuous strand separation maintains the DNA-RNA hybrid at a consistent length during DNA synthesis, and that 5 bp is optimally accommodated in the active site[23]. Protein interactions in the active site are thought to stabilize this very short hybrid, since higher telomerase affinity for the RNA/DNA hybrid correlated with increased RAP. Therefore, any perturbations to the 5 bp hybrid stability, either via reduced melting temperature or protein interactions, could impact translocation. While substitution of 6-thio-dG for guanine in a dG-dC base pair moderately decreases thermal stability of a 17-mer DNA duplex by 10%, kinetic

data indicate the opening rate of a 6-thio-dG-C base pair is 17-fold faster than a dG-dC bp[172]. Structural data indicate that the hydrogen bond is longer with the thio group and dC, compared to with the carbonyl group, in the Pol β active site[171]. Less is known about the impact of 2-OH-dA on bp stability, however, alterations in the bp geometry with rU may impact the telomerase affinity for the RNA:DNA hybrid. Therefore, we proposed minor perturbations could significantly destabilize the already very short thermally unstable 5 bp RNA:DNA, and thereby disrupt translocation.

Results with POT1-TPP1 provide further evidence that 2-OH-dATP and 6-thio-dGTP disrupt translocation. POT1-TPP1 enhance telomerase RAP by decreasing the primer dissociation rate and increasing the translocation efficiency[55]. The result that POT1-TPP1 could partly restore RAP in the presence of 2-OH-ATP, suggests that 2-OH-dA increases the rate of primer dissociation which is rescued partly by POT1-TPP1 increasing primer binding. However, POT1-TPP1 did not increase RAP in the presence of 6-thio-dGTP, suggesting that 6-thio-dG may be more destabilizing than 2-OH-dA. When 6-thio-dGTP replaces dGTP in a reaction, each telomeric repeat will contain three 6-thio-dGs, whereas when 2-OH-dATP replaces 2-OH-dA, each repeat will contain only one 2-OH-dA. We argue insertion of three modified dNTPs disrupts the DNA:RNA hybrid more than a single dNTP, to such an extent that POT1-TPP1 enhancement of telomerase primer binding cannot compensate.

Here, we demonstrate directly that the NRTIs of ddITP and AZT-TP are human telomerase chain terminators by showing the telomerase is able to catalyze the addition of these modified dNTPs to the telomeric end. NRTIs exploit the requirement of DNA polymerases and reverse transcriptases for a 3'OH group on the ribose to catalyze addition of the incoming dNTP to the growing nucleotide chain. NRTIs lack a 3'-OH found in natural dNTPs and therefore block further

elongation after their incorporation into viral DNA, making them efficient inhibitors of HIV-1 RT. While several previous reports provide indirect evidence that AZT-P can be incorporated into telomeric DNA, reduce telomerase products *in vitro*, and cause telomere shortening in cells[118,173,174], our studies provide the first direct evidence that NRTIs are effective telomerase chain terminators. These results have important health implications since the use of AZT has been pursued for anticancer treatments as a telomerase inhibitor[173]. Chronic AZT treatment in mice reduced tumor growth and promoted senescence and apoptosis in mammary carcinoma cells[126]. Furthermore, NRTI inhibition of telomerase has been proposed to promote cellular senescence and features of premature aging in HIV patients under long term treatments[175], and may represent an off target effect of NRTIs in human cells. Diminished cellular renewal capacity contributes to the underlying cause of premature age related co-morbidities in HIV-infected patients[175].

Since most tumors rely on telomerase to enable cellular immortality, one strategy to halt proliferation is to target telomerase with inhibitory nucleosides to prevent telomerase restoration of telomeres after each replication. Several recent reports have shown that oral administration of 6-thio-dG is an effective treatment strategy for melanoma, lung cancer, and glioblastoma in murine models[135,136,176]. These studies also showed that 6-thio-dG treatment led to an increase in telomere dysfunction induced foci[135,136,176]. Here, we uncover the mechanism by which 6-thio-dGTP compromises telomere maintenance via disrupting telomerase translocation. Furthermore, the modified nucleotides used in our study not only inhibit telomerase, but reports show they also inhibit the mitochondrial DNA polymerase γ, leading to mitochondrial dysfunction and elevated ROS which damage dNTP pools[120,131]. Therefore, in conjunction with MTH1 inhibitors, our studies suggest therapeutic NRTIs or thiopurines may deliver a one-two punch to telomerase driven cancers by inhibiting telomerase directly and indirectly through elevated oxidized dNTPs.

In summary, we show that both naturally oxidized dNTPs and therapeutic dNTPs inhibit telomerase activity by distinct mechanisms of either chain termination upon incorporation or disruption of telomerase translocation and subsequent repeat addition. Thus, our studies have important health implications for potential off target effects on long term NRTI treatments, and for therapeutic strategies to target telomerase in cancer **(Figure 22).**

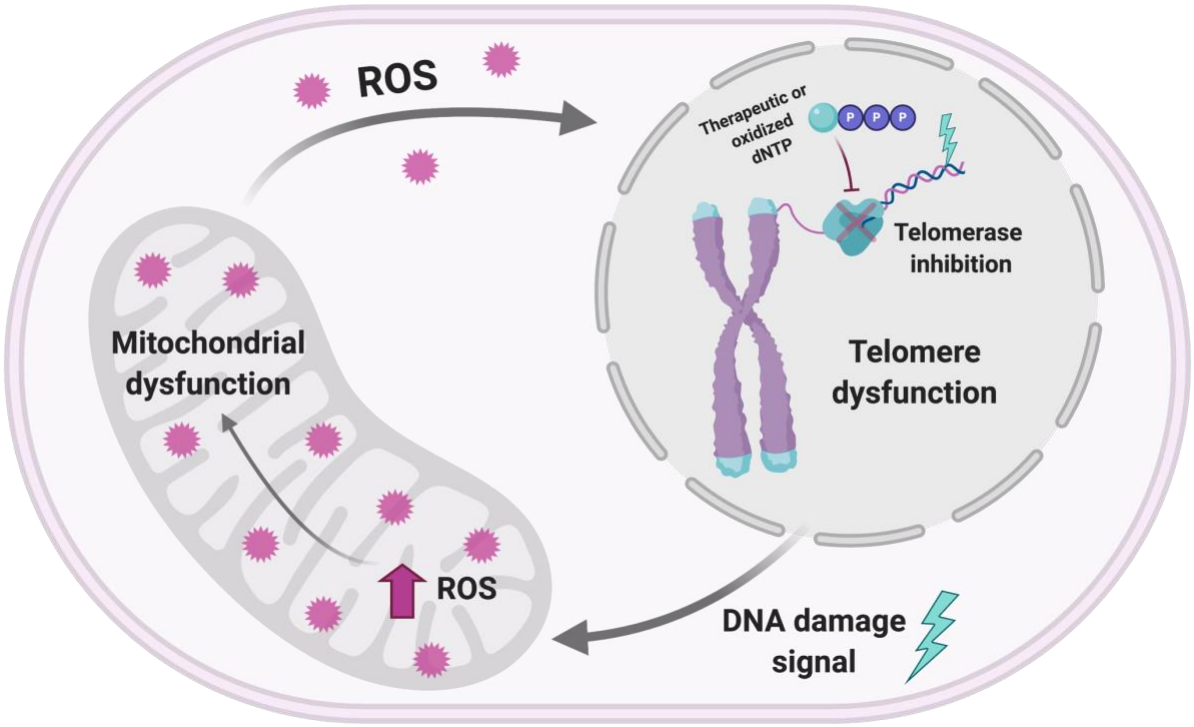

Figure 22. Study model. Treatment with therapeutic dNTPs causes telomerase inhibition which leads to telomere dysfunction. Therapeutic dNTPs inhibit polymerase gamma, which elevates ROS and causes mitochondrial dysfunction. The elevated ROS can damage dNTP pools and be incorporated into telomeric DNA in addition to the therapeutic dNTPs [177]. Created with Biorender.

6.0 Future directions

6.1 6-thio-dGTP at telomeres

Previous reports have demonstrated that 6-thio-dGTP, which forms in cells from 6-thio-dG, promotes cell death and telomere shortening in telomerase positive cancer cells. 6-thio-dG decreases tumor growth in mouse xenograft studies of lung, glioblastoma, melanoma, and colon cancers[128]. 6-thio-dG treatment causes telomere shortening and telomere dysfunction, but the mechanism was unclear because extracts from treated cells do not show reduced telomerase activity[128]. This thesis uncovered the mechanism by which 6-thio-dGTP disrupts translocation during repeat addition processivity during the telomerase catalytic cycle. The following section will address the next steps of this project, which may answer several remaining questions regarding the effects of 6-thio-dG at telomeres.

6.1.1 Can telomerase bind and then extend the growing chain if 6-thio-dGTP is present in the telomeric DNA (primer sequence?)

We will measure thermodynamic and kinetic binding parameters between telomerase and several permutations of the telomeric repeat, as well as rates of nucleotide addition. To determine if telomerase can bind to telomeric DNA containing 6-thio-dG, we will measure the equilibrium binding constant (K_d) , which is the strength of the binding interaction between the telomeric DNA substrates and telomerase. When the K_d value is smaller, it means there is a greater binding affinity of the DNA substrate to telomerase, while a higher K_d value means they are more weakly bound.

To measure the K_d, we will use a well-established telomerase pull down assay [178]. We will use biotinylated 18nt telomeric primers with a site specific 6-thio-dG at various locations on the primer. We will titrate primers at a range of concentrations and incubate them with immunopurified human telomerase as described in section 3.1.1 of this thesis. The DNA substrate and any bound telomerase will be captured by Neutravidin beads, and the amount of unbound telomerase remaining in the supernatant will be quantified by probing dot blots (as described in section 3.1.2 of this thesis) for hTR. The amount of telomerase remaining in the supernatant on the blots will be analyzed using Image Quant TL software. Data will be fitted using the following equation: $y = (B_{max}[S])/(K_d+[S])$, where B_{max} is the maximal level of binding, [S] is the concentration of primer DNA, and K_d is the equilibrium binding constant [178]. We will calculate K_d, because it provides a direct equilibrium measurement of affinity. Primer K_m (the primer concentration at which half maximal telomerase activity is observed) is not always an accurate measure of primer affinity because it is an indirect measurement of affinity derived from activity. Previous groups have determined that the K_m does not accurately reflect primer affinity (K_d) for human telomerase [154].

Since we know that telomerase can incorporate 6-thio-dGTP opposite template rA and rC, our next question is if telomerase can extend telomeric DNA when 6-thio-dG has already been incorporated into the telomere. The Opresko lab and others previously reported that when telomeric DNA is oxidized to form 8-oxoG, telomerase activity is enhanced because secondary G-quadraplex structures are destabilized [91,92]. Telomeric single stranded overhangs in cells have 8-30 repeats and can fold into G-quadraplex structures, which disrupt telomerase loading. We will use direct telomerase assays to test several $(TTAGGG)_3$ (3R) or $(TTAGGG)_4$ (4R) oligonucleotides with a site specific 6-thio-dG modification at various locations on the telomeric

DNA overhang. The 3R substrate will be used because it is unable to form a GQ structure, while the 4R substrate will allow us to test the biologically relevant GQ structure. We will also stimulate telomerase with POT1-TPP1, to determine if the complex can promote improved extension. Based on our previous findings that terminal 8-oxo-dGTP does not impair telomerase loading, we expect that the terminal 6-dG substitution in 3R will minimally affect telomerase processivity. Similarly, we expect that the 4R substrate with 6-thio-dGTP will be poorly extended by telomerase. These experiments will allow us to determine if telomerase can extend telomeres after 6-thio-dGTP has been incorporated, and if 6-thio-dGTP destabilizes secondary G-quadraplex structures.

To determine the mechanism of the enhanced telomerase activity, we will use a single molecule approach with a high molecular resolution to probe the GQ structure with 6-dG. In earlier studies using single molecule fluorescence resonance energy transfer (smFRET), 8oxoG in an oligonucleotide telomeric overhang induces G4 structure dynamics and perturbations which enhance telomerase binding and activity. While telomerase cannot access a tightly folded G4, it binds and extends a G4 when 8oxoG is present at the second T or G repeat, which suggests that a stable G4 in the telomeric overhang can act as a lock which prevents telomerase activity in normal cells, but a single lesion can disrupt the G4 and allow for telomerase extension [179]. A previous study simulated quadraplexes with thioguanine, and showed that primers with multiple thioguanines are unable to form cation-stabilized quadraplex [180]. Although the thio group has a favorable interaction with Na+, it is too bulky and it leads to expulsion of the cations from the channel and collapse of the quadraplex on the nanosecond scale. However, when there is only one thioguanine incorporated into the stem, the structure remains stable, but there are local fluctuations around the thioguanine [180]. These studies examined runs of Gs, however we would like to know if 6-thio-dG can disrupt the otherwise tightly folded telomeric G4. We will collaborate with the Sua

Myong lab to prepare single molecule fluorescence energy transfer (smFRET) of telomeric GQ folding with 6-dG. We will design primers with FRET pair dyes Cy3 and Cy5 attached at both ends of the GQ forming primer with 6dG. Once we have tested the constructs using smFRET, we will use a single molecule pull down (SiMPull) assay with the same primers. The SiMpull assay is a method which applies FLAG tagged telomerase to single molecule slides coated with an anti-FLAG antibody [181]. The primers labeled with Cy3 without biotin will be applied to the telomerase bound surface and a dual excitation detection will be performed to capture both signals from telomerase and the bound DNA substrate. We will calculate the relative binding affinity of each construct for telomerase and normalize it against an unfolded positive control $(TTAGGG)_3$. These studies will allow us to understand the telomerase binding affinity when 6-thio-dG is in the telomeric DNA.

6.1.2 If cells are treated with 6-thio-dG, can telomerase further extend telomeres?

Previous studies have shown that treating cancer cells with 6-thio-dG causes telomere shortening. What remains unknown is if telomerase can extend telomeres when the cancer cells are treated with 6-thio-dG. To determine this, we will use a mutant telomerase cell line that adds a well-tolerated variant telomeric repeat sequence to telomere ends 182. By specifically detecting the addition of these variant repeats, we will be able to directly visualize telomere elongation events in human cells 182. We will express a modified telomerase RNA moiety containing a mutant template (referred to as TSQ1) from a retroviral vector in wildtype and mutant human lox melanoma cell lines. Instead of the normal 5'-TTAGGG-3' telomeric DNA repeats, TSQ1-hTR has a modified template, so that telomerase adds 5'GTTGCG-3' repeats to the 3' ends of telomeres 104. We will treat the cell lines with 1 µmol/L or 10 µmol/L of 6-thio-dG for long as the cells can

tolerate the drug, and collect total DNA at multiple time points. We will look at the incorporation of TSQ1 repeats into telomeric DNA by southern hybridization of total DNA with TSQ1 specific probes. We will normalize the TSQ1 signal to an Alu signal relative to the wild type. We expect that the TSQ1 repeats will rapidly decrease during the duration of 6-thio-dG treatment.

Figure 23. Schematic of wild type and TSQ1 mutant telomerase demonstrates synthesis of TSQ1 (5'-GTTGCG-3')$_n$ telomeric repeats.

6.1.3 Can NUDT15 or MTH1 act on 6-thio-dG? In NUDT15 depleted cells, will 6-thio-dG efficacy increase?

NUDT15 (NUDIX hydrolase 15, also known as MutT homolog (MTH2)) belongs to the NUDIX hydrolase family, which is the same family as MTH1. NUDT15 is capable of hydrolyzing various oxidized nucleotides, however compared to MTH1, it has 40-fold less enzymatic activity toward 8-oxo-dGTP *in vitro* and in cancer cells. NUDT15 can also decap methylated mRNAs, which signifies it has an alternative role in mammalian cells [183]. NUDT15 interacts with the

polymerase clamp PCNA (proliferating cell nuclear antigen), which suggests that sanitation of modified nucleotides could occur at distinct locations, such as the DNA replication fork [184]. When NUDT15 binds to PCNA, it protects the replication fork from degradation, whereas UV irradiation causes dissociation of the NUDT15-PCNA complex and PCNA degradation [184]. Recently, a missense mutation of NUDT15, R139C was discovered in Korean patients with inflammatory bowel disease[185]. It was correlated with thiopurine intolerance in acute lymphoblastic leukemia (ALL) [186,187] and inflammatory bowel disease (IBD) in patients of Asian descent [188].

Finally, NUDT15 is a key enzyme in thiopurine metabolism and decreases the activity of thiopurine drugs by catalyzing hydrolysis of 6-thio-dGTP and 6-thio-GTP. The Helleday laboratory resolved the first crystal structure of NUDT15 in complex with 6-thio-GMP bound in the active site, showing the key determinants for the substrate specificity. *In vivo* studies investigated whether the depletion of the protein increases efficacy of 6-thioguanine in a cellular setting [189]. They depleted NUDT15 in human colon cancer cells (HCT116 and MLH deficient HCT116-3-6) using doxycycline inducible NUDT15 specific shRNA [189]. Clonogenic survival was assessed with increasing doses of 6-thioguanine. Depletion of NUDT15 dramatically increased the sensitivity of HCT116 3-6 cells to 6-thioguanine, showing that NUDT15 reduces the efficacy of 6-thioguanine treatment [189].

Previous studies have demonstrated that 6-thio-dG and 6-thioguanine had similar IC50 values in cancer cells, but 6-thio-dG was less toxic in mouse models, making it an attractive drug for cancer therapy [128]. We predict that if NUDT15 is depleted in cancer cells, 6-thio-dG efficacy will increase, causing more rapid telomere shortening and dysfunction. To complete this study, we will first deplete NUDT15 in HCT116 cells using shRNA to compare cell viability and telomere length between 6-thio-dG and 6-thio guanine treated cells.

Cancer cells with short telomeres are more sensitive to telomerase inhibition than cancer cells with long telomeres, because critically short telomeres require telomerase extension at each cycle for cell viability [190]. We predict that cells with critically short telomeres undergoing 6-thio-dG treatment will be more vulnerable to NUDT15 inhibition, since 6-thio-dG disrupts telomerase translocation and causes rapid telomere shortening. We will deplete NUDT15 by targeting shRNAs in HeLa cells with very short telomeres (HeLa VST) [91] and HeLa cells with long telomeres (HeLa LT) [91] and treat both with 6-thio-dG. We predict that the HeLa VST cells will exhibit inhibited cell proliferation and induced apoptosis. To determine if there is more telomere dysfunction in the NUDT15 depleted cells, we will analyze 53BP1 foci localized at telomeres. 53BP1 is a DNA damage response protein which localizes to dysfunctional telomeres or chromosome breaks [191]. 53BP1 foci at telomeres are referred to as TIFs for telomere dysfunction foci. We will also complete telomere fluorescence *in situ* hybridization (FISH) on metaphase chromosomes to determine if NUDT15 deficiency in addition to 6-thio-dG treatment increases telomere loss and fragile telomeres in both the HeLa VST and LT. Since 6-thio-dGTP will be incorporated into the telomeric DNA, TRF1 will not be able to effectively bind to the DNA, causing telomere fragility. We predict there will be more telomere loss in the HeLa VST, since they will have a higher level of critically short telomeres.

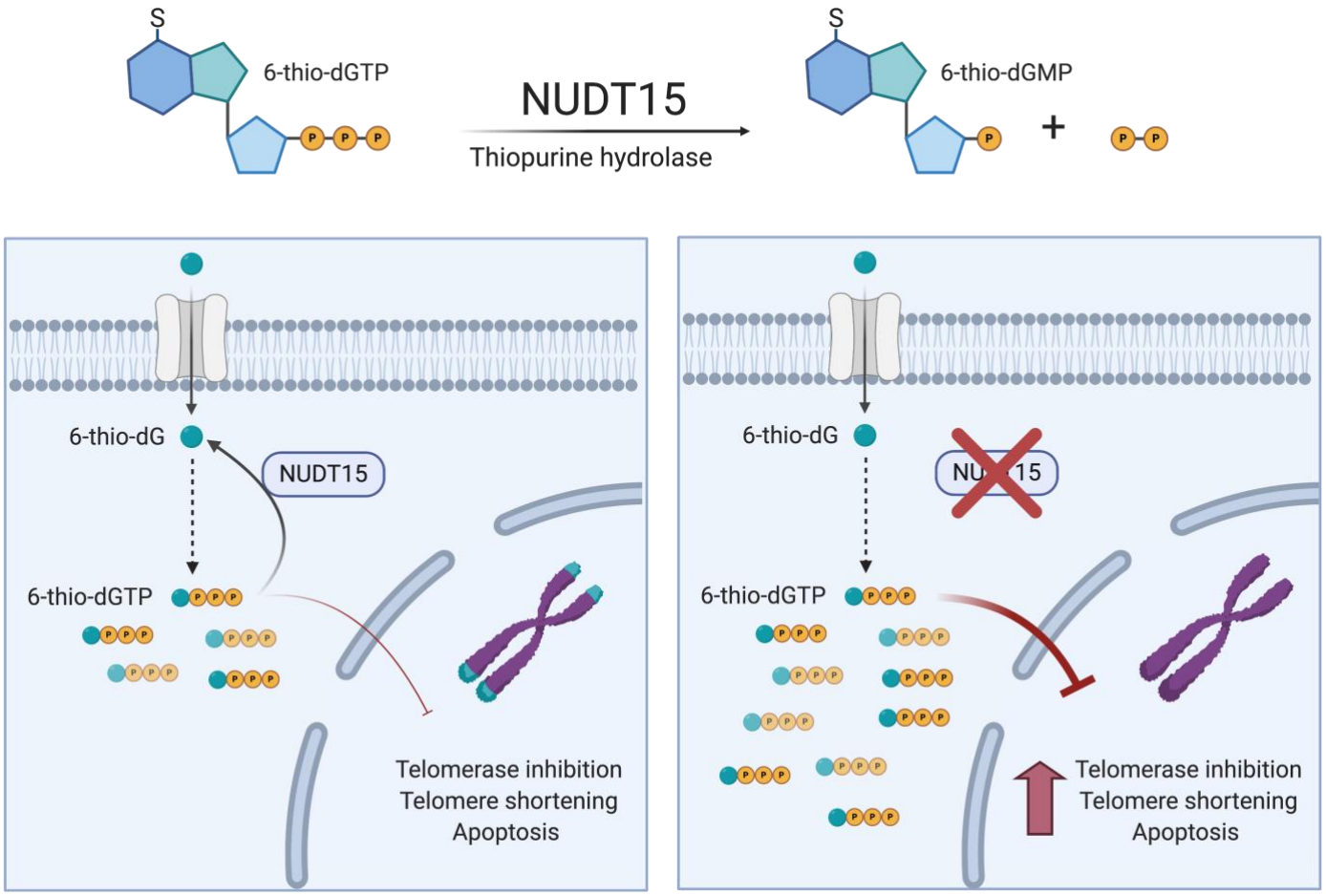

Figure 24. NUDT15 depletion causes elevated telomere dysfunction. NUDT15 is a thiopurine hydrolase which hydrolyses 6-thio-dGTP into 6-thio-dGMP so that it cannot be incorproated into DNA. If NUDT15 is depleted from cells, we predict there will be elevated amount of 6-thio-dGTP in the cell, which would cause rapid telomerase inhibition, shorter telomeres, and apoptosis. Created with Biorender.

6.1.4 Can 6-thio-dG be used as an antiviral treatment for COVID-19 or HIV?

Coronaviruses (CoVs) are genetically diverse positive-sense single stranded RNA viruses which circulate in animals and humans. A novel coronavirus, severe acute respiratory syndrome coronavirus 2 (SARS-COV-2), was first identified in December 2019 as a cause of respiratory

illness designated as coronavirus disease 2019, or Covid-19. According to the most recent data from the John Hopkins COVID-19 resource center, this severe respiratory disease has caused 600,000 global deaths within a span of 6 months. Currently there is no vaccine, and development of an effective vaccine could take 18 months, so it is critical to find an effective therapeutic to decrease the overall death toll from this pandemic. Multiple therapeutic agents have been tested for the treatment of Covid-19, but none are effective because the virus can adaptively overcome negative selective pressure and counteract drugs through the action of a proofreading exoribonuclease.

Remdesivir (RDV) is a prodrug that is intracellularly metabolized to an analog of adenosine triphosphate, which inhibits viral polymerases [192]. Remdesivir has a broad-spectrum activity against members of several viruses, including Ebola and Coronaviruses. Remdesivir (GS-5734) inhibits the viral RNA-dependent, RNA polymerase with inhibitory activity against SARS-CoV and Middle East respiratory syndrome (MERS-CoV). When the viral RNA dependent RNA polymerase (RdPr) incorporates the active metabolite remdesivir triphosphate (RDV-TP), it was more efficient inhibiting RNA transcription than the natural substrate, dATP, and leads to delayed chain termination 3 nt downstream of incorporation.

Remdesivir has been identified as a promising therapeutic candidate for Covid-19 because it can inhibit SARS-CoV-2 *in vitro*. Also, in primate studies, Remdesivir reduced lung virus levels and lung damage 12 hours after inoculation with MERS-CoV [193]. It was recently reported that Remdesivir inhibits SARS-CoV-2 replication in Calu3 human lung cells and in primary human airway epithelial cultures [194]. A comparably lower potency of RDV was detected in established human and monkey cell lines, because they had a lower metabolic capacity to activate the compound. They found that mice infected with a chimeric SARS-CoV encoding the SARS-CoV-

2 RNA dependent RNA polymerase (RdRP) and treated therapeutically with RDV showed decreased viral loads in the lungs and improved pulmonary function, suggesting that RDV is a promising therapeutic candidate for COVID-19 [194].

Remdesivir has recently been used on a compassionate use basis for patients hospitalized with COVID-19, which were receiving oxygen support or mechanical ventilation [195]. Clinical improvement was observed in 68% of the patients, however 60% reported adverse effects of the drug, and 23% reported serious adverse effects such as septic shock, and multiple organ dysfunction syndrome.

Thiopurines have antiviral activity for positive strand RNA viral pathogens such as bovine viral diarrhea virus (BVDV)[196]. Thiopurine metabolism is complex and requires both activation and inactivation reactions. Since 6-thio-dG decreases nonspecific thiopurine toxicity and does not kill non-cancerous cells[128], it could be an effective antiviral treatment for both COVID-19 or HIV-1 with less side effects. It can be rapidly converted into either 6-thio-dGTP or 6-thio-GTP (for RNA insertion) in cells, which could then be incorporated into the viral RNA, blocking COVID-19 transcription similar to the mechanism of Remdesivir.

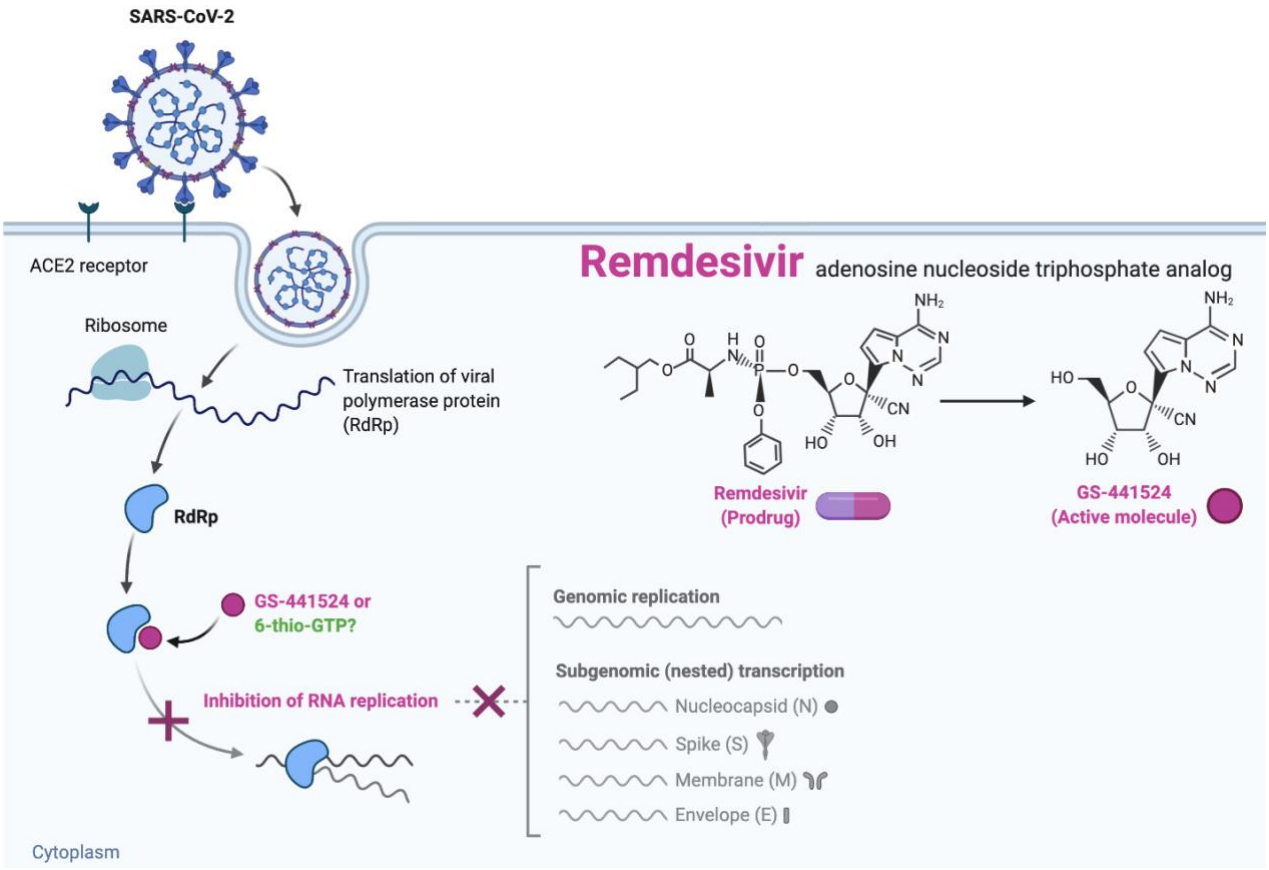

Figure 25. Remdesivir mechanism of action. The active metabolite of Remdesivir, GS-441524, interferes with the action of the RdRP and causes a decrease in viral RNA production. We predict, 6-thio-GTP would have a similar mechanism of action. Created with Biorender template.

6.2 NRTI treatment and aging in HIV patients

In this study, we have shown for the first time that like HIV-RT, NRTIs AZT and ddI directly inhibit telomerase by chain termination. This raises the possibility that, not only is accelerated aging from NRTIs caused by polymerase γ inhibition, but also due to telomere shortening by direct telomerase inhibition. Previous studies[118,173 119] have shown that NRTIs cause

telomere shortening and multiple cell lines, and now we have direct biochemical evidence that NRTIs inhibit telomerase, so the next steps of this project would be to measure telomere length in patients that have been treated with NRTIs for the past thirty years.

6.2.1 Longitudinal study to measure telomere length in patients that have been treated with NRTIs for the past thirty years

We hypothesize that over a thirty-year span, the telomere lengths of patients treated with NRTIs are significantly shorter than their counterparts. Previous studies have shown that highly active retroviral therapy (HAART) decreases telomere length. One study found that after two years of aggressive antiretroviral treatment in thirty patients, mean telomere length was 500 base pairs shorter than healthy controls [197]. Another study followed 27 HIV infected individuals that were approximately 50 years old, for 18 months during HAART. They found telomere length shortened in CD4+ and CD8+ T cells [198]. Another group documented telomere lengths of total peripheral blood mononuclear cells (PBMCs) from HIV-infected individuals for nine years [199]. They found the telomere lengths of the HIV infected individuals shortened 2-fold faster in PBMCs compared to age matched seronegative controls. For the HIV infected patients, the mean telomere restriction fragment (TRF) in the progressors was greater than that in the asymptomatic individuals and both were increased compared to the controls [199]. The studies show that patients treated with HAART therapy have a slight decrease in telomere length during a short duration. However, they failed to complete studies that were longer than two years. Additionally, they have mixed groups of patients, which make it difficult to correlate if the telomere shortening is from normal biological aging or from the retroviral therapy. In order to test this, will complete a thirty-year longitudinal study using the Multi Center AIDs Cohort (MACS).

MACS was initiated in 1983 and investigates the natural history of untreated and treated human immunodeficiency virus (HIV)/AIDS in a cumulative total of 6972 men in four centers [200]. The men in the MACS are followed at 6 month intervals, when they complete a questionnaire which includes medical history, quality of life, and medications including antiretroviral drugs [200]. They also have blood collected, which is divided into serum, plasma, and cells. As of May 2011, the MACS had accumulated 87,000 person-years of follow up in incorporating 8920 variables. This allows MACS to have data and specimens which document the entire natural history of HIV/AIDS from pre-infection, through infection, pre-treatment and treatment, to cause-specific death [200]. The cohort also includes comparison groups of similar risks to those of interest, such as uninfected men. This will allow us to complete a standardized, complete longitudinal study of telomere length in specimens collected uniformly across centers before and after infection and treatment.

To determine if HIV patients undergoing HAART have faster telomere shortening rates than healthy controls, we will perform a longitudinal study by selecting specific criteria from the MACS participants. We will select at least 50 patients who initiated HAART while enrolled in the MACS. Selection criteria will include the following characteristics: an age range of 20-30 years, viral load >50 copies/mL with a successful response to treatment [201]. We will age match MACS participants who have received HAART without NRTIs as a negative control. We will use samples at 5 year intervals. Since the average telomere length decreases by 25 bp per year, length would be difficult to distinguish on a southern blot at less than 5-year intervals. We will extract the DNA from the PBMC samples by a commercially available kit from Qiagen. Contaminants and enzyme inhibitors are removed by salt precipitation, which results in purified DNA that is available for immediate use. The kit can also be used for high-throughput processing of multiple samples, which

makes it useful for this large-scale epidemiological study. After the DNA has been extracted, we will evaluate the DNA integrity using agarose gel electrophoresis, and visualize with SYBR green. We will then digest at least 3μg of genomic DNA with restriction endonucleases Hinf1 and Rsa1 [202]. This allows for a mean telomere length that is longer than 1kb. We will resolve the samples on an agarose gel, and probe with a 5' radiolabeled $(TTAGGG)_3$ oligonucleotide. To measure the final TRF length, we will use ImageQuant TL and adjust for the higher signal intensity obtained from longer TRFs, as the telomere probe hybridizes several times to the fragments [202]. For this epidemiological study, the TRF length will be calculated by integrating the optical density of each telomeric smear and interpolating the mean telomeric length from the molecular weight ladders [202]. To analyze the epidemiology data, multivariable linear regression will be used to identify factors predictive of telomere length at the baseline. Although Southern Blots are optimized in the Opresko lab, there may be challenges with the integrity of the genomic DNA from the MACS. The long term PBMC samples may have degraded which could yield poor quality DNA or less than 3μg necessary for Southern blots. If this occurs, quantitative PCR (qPCR) of mean telomere length can be used. This allows for approximately 50ng of DNA per sample, however only the average telomere length is measured [202]. There may also be selection bias in our analysis due to individuals with aging disorders or environmental factors such as cigarette smoking. Additionally, modeling telomere dynamics may pose a challenge because telomere repeats are proportional to the length of telomeres [203]. Longer telomeres may provide a larger target for free radicals [203].

We expect that telomere length will significantly decrease over time in patients treated with NRTIs versus those not treated with NRTIs **(Figure 26).** This longitudinal analysis will allow us to look at telomere lengths over a 30-year period so we can correlate if NRTIs have a direct effect on aging phenotypes.

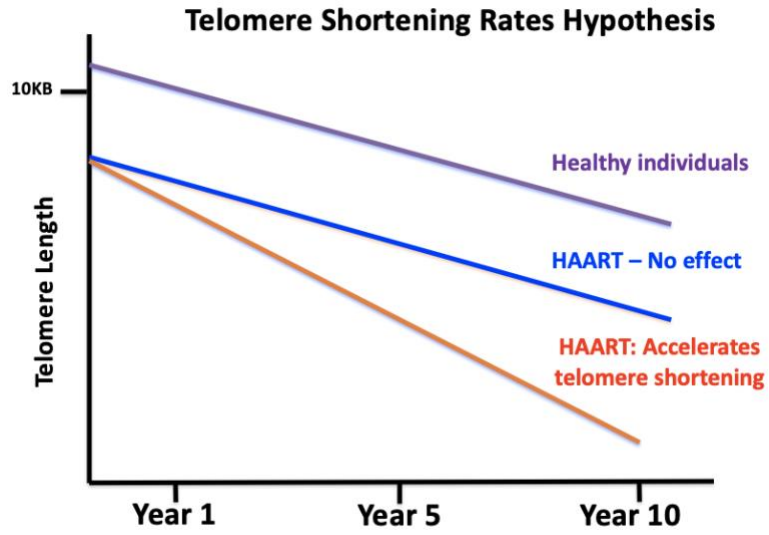

Figure 26. Telomere shortening rates hypothesisWe hypothesize that HIV infected individuals undergoing HAART will have faster rates of telomere shortening than healthy controls. We will select patients from the Multicenter AIDS Cohort Study (MACS) and measuring their telomere length at 5 year intervals.

6.3 Final conclusions

This study deciphers the mechanism by which telomerase can insert oxidized and therapeutic dNTPs into telomeric DNA. 6-thio-dGTP can disrupt telomerase translocation and NRTIs inhibit telomerase by chain termination. Understanding how telomerase incorporates these modified nucleotides paves the way for multiple new projects involving biochemistry, cell biology, and use of clinical samples. Using biochemistry assays such as binding kinetics and smFRET, when the modified dNTPs have already been incorporated into the DNA, we can determine if telomerase can bind to the telomeric DNA. In cells, we can further understand how the modified

dNTPs damage telomeres. A longitudinal cohort study would answer the longstanding question about the rate of telomere shortening in HIV-1 patients undergoing long term HAART. Thus, the future studies and collaborations will have important health implications for potential off target effects on long term NRTI treatments, and for therapeutic strategies to target telomerase in cancer.

7.0 Statement of Public Health Significance

Recent therapeutic strategies for treating HIV and advanced cancer patients have increased their overall survival rate. Both targeted therapies and cancer immunotherapies have allowed these patients to have prolonged remission and improved quality of life. Unfortunately, both HIV and many advanced cancers develop drug resistance. In order to improve patient survival rates, it is necessary to understand the molecular mechanisms in which the virus or tumors develop resistance to existing therapies.

A characteristic of advanced cancers is their ability for continuous cell divisions, which most frequently involves maintaining telomere length by reactivating telomerase. Telomerase is a prime target for effective therapies against cancer, because normal human cells either lack telomerase or have lower telomerase activity and maintain telomeres at longer lengths compared to cancer cells. Fast acting therapeutic agents, such as modified nucleosides, which inhibit telomerase, are highly desirable treatment options. The modified nucleoside could be incorporated into the telomeric DNA, which would cause telomere shortening and rapid cell death. Until this study, the mechanism by which telomerase incorporates these modified nucleotides remains unknown.

Here, we uncover the mechanism by which several modified nucleotides compromise telomere maintenance. The NRTIs (AZT and ddITP) inhibit telomerase by acting as chain terminators. 6-thio-dGTP and 2-OH-dATP disrupt telomerase translocation. Furthermore, the modified nucleotides used in this study not only inhibit telomerase, but reports show they also inhibit the mitochondrial DNA polymerase γ, leading to mitochondrial dysfunction and elevated

ROS which damage dNTP pools [120,131]. Therefore, in conjunction with MTH1 inhibitors, our studies suggest therapeutic NRTIs or thiopurines may deliver a one-two punch to telomerase driven cancers by inhibiting telomerase directly and indirectly through elevated oxidized dNTPs. This study has important health implications for potential off target effects on long term NRTI treatments in HIV patients, and for therapeutic strategies to target telomerase in cancer.

Appendix A Telomerase inhibitors

Table 4. Telomerase inhibitors

Therapeutic approach	Name	Target	Mechanism	Effect in cells	References
Antisense oligonucleotides	GRN163	Telomerase RNA	Targets RNA template of telomerase	Inhibition of tumor cell proliferation. Induction of apoptosis.	204
Small molecule inhibitors	BIBR1532	hTERT	Direct enzyme inhibitor of TERT via active site binding	Inhibition of tumor cell proliferation. Induction of apoptosis.	205
Nucleotide reverse transcriptase inhibitors (NRTIs)	Azidothymidine	hTERT	Nucleotide analog blocks the reverse transcription process by chain termination	Telomere shortening.	119,123,127
	Didanosine	hTERT		Telomere shortening.	119
	Tenofovir	hTERT		Telomere shortening.	119
Modified nucleotides	6-thio-dG	hTERT	Nucleotide analog blocks the reverse transcription process by translocation disruption	Telomere shortening/ telomere dysfunction	128,135,136,176,206,207
	5-FDU	hTERT	Telomerase inhibition	Telomere shortening	137
	MeCITP	hTERT	Binds to hTERT active site	Telomere shortening	164
Immunotherapy	GRNVAC1/2	Dendritic cells	Vaccination/ modified hTERT mRNA	Induction of an immune response	208
	Vx-001	HLA-A	Stimulation of autologous CD4+ cells		209
	GV1001	Multiple HLA classes	Stimulation of autologous CD4+ cells		210
	Recombinant viral vectors	hTERT	Antigen specific immunization. Viral delivery of hTERT to enhance cellular immunity against hTERT		211
Gene therapy	Telomelysin (OBP-301)	Tumor cells with high telomerase activity	hTERT promoter drives the expression of a pro apoptotic suicide gene	Tumor cell lysis	212
	CB1954		TERT promoter expression of an enzyme required for pro drug conversion		213
Natural supplements	Curcumin	Telomerase associated proteins	Inhibits recruitment of hTERT to the nucleus	Down regulation of hTERT expression in cells	214
G-quadruplex stabilizers	BRACO-1910	Telomeric DNA	Stops telomerase from adding further repeats	Induce telomere shorting, block the cell cycle, and induce apoptosis	215

	Telometstatin		Stops telomerase from adding further repeats	Induce telomere shorting, block the cell cycle, and induce apoptosis	[216]
	RHPS4		Telomeres uncapping	Induce telomere shortening, telomerase inhibition, induce apoptosis, activated C-myc.	[217]
	TMPyP4		Telomeres uncapping	Telomere shortening	[218]
	Quarfloxin/CX-3543a		Telomeres uncapping	rRNA biogenesis inhibition	[219]

Appendix B Azidothymidine and 6-thio-dG dosing from pre-clinical or clinical studies

Table 5. Azidothymidine and 6-thio-dG dosing from pre-clinical and clincial studies

Drug	Dose	Study model and cancer type	Study Conclusions	Reference
AZT	Administered in doses of 2, 3, 4, 5.5, 7, 8.5, 10, 12, 15, or 20 g/m^2/day as a continuous infusion over 48 hours. Patients also received fluorouracil plus leucovorin for 24 hours before the start of and during the ZDV infusion.	Fourteen patients (6 women) with solid tumors that were unresponsive to standard therapy received 31 courses of therapy.	Highest doses of the drug were optimal	[220]
AZT + Methotrexate	Treated with weekly oral methotrexate (7.5 mg/M^2 every 6 hours for 6 doses) and continuous oral AZT (200 mg four times daily).	31 patients with adenocarcinoma of the pancreas or hepatocellular carcinoma	One patient achieved a radiographic complete remission and 2 had stable disease. Two-thirds of patients progressed within 2 months of beginning therapy.	[221]
AZT + Cisplatin	AZT was administered as a 72-h infusion on days 1-3 and 14-16 of a 28-day cycle at dose levels from 400 through 14,364 mg/m(2) per day. CDDP at dose levels of 30, 45, or 60 mg/m(2) was administered at hour 36 of each AZT infusion.	61 patients with advanced, histologically confirmed malignancies which were unresponsive to or for which no "standard" chemotherapeutic regimen existed.	Of the 61 patients who completed 125 courses of therapy, 21 had stable disease for a median of four cycles (range two to eight), 33 progressed on therapy, and 7 were not assessable for response. The major observed toxicity was myelosuppression.	[222]
6-thio-dG	2.5 mg/kg of 6-thio-dG every 2 days	Pediatric high-risk group 3 medulloblastoma (tumors were injected into syngeneic (immunocompetent) tumor growth mouse model.	Four of six treated mice had reduced or delayed tumor growth. Two of the six treated mice showed fast tumor growth, most likely due to the tumor aggressive nature and larger tumor volume at the start of 6-thio-dG treatment.	[136]

6-thio-dG	5 mg/kg of 6-thio-dG, for 12 days	Tumor volumes of xenografts of 6 patient or mouse derived cultures of therapy resistant melanoma	6-thio-dG both *in vitro* and *in vivo* that results in telomere dysfunction, leading to apoptosis and cell death in various preclinical models of therapy-resistant melanoma cells.	[135]
6-thio-dG	5 mg/kg of 6-thio-dG, for 14 days	KRAS mutant genetically engineered mouse model ($KRAS^{LA1}$) of lung cancer	66% reduction in tumor volume with 6-thio-dG treatment	[176]
Thiopurine (6-MP)	Remission maintenance chemotherapy for this trial consisted of daily oral 6-MP and weekly oral methotrexate at starting doses of 75 mg/m2 and 20 mg/m2	50 children with ALL who were receiving remission maintenance chemotherapy,	During chronic therapy with 6-MP or azathioprine, patients with low RBC TPMT activities have significantly higher RBC 6-TGN concentrations than do patients with high TPMT activities.	[223,224]
6-thio-DG	Seven days after tumor inoculation (when the tumor volume was 100 mm3), 3 mg/kg 6-thio-dG was administered daily	MC38 (colon cancer) cells injected into mouse models	MC38 tumor cells are sensitive to 6-thio-dG with a half maximal inhibitory concentration (IC50) of 370 nM	[225]

Appendix C Doses of NRTIs and Thiopurines used in the clinic

Table 6. NRTI dosing and combinations for HIV patients from UPToDate Clinician Database

NRTI Combination	Drug Name	Dosage
Lamivudine/Zidovudine	Combivir (COM)	150/300mg tabs
Abacavir/Lamivudine/**Zidovudine**	Trizivir (TZV)	300/150/300mg tabs
Tenofovir/Emitricitabine	Truvada	300/200mg tabs
Abacavir/Lamivudine	Epzicom	600/300mg tabs
Tenofovir/Emtricitabine/Efavirenz	Atripla	300/200/600mg tabs

Table 7. Thioguanine dosing from UpToDate Clinician Database

Disease type	Adult dose	Pediatric dose
Acute myeloid leukemia	Oral: 2 mg/kg once daily for 4 weeks; if no clinical improvement after 4 weeks and ANC and platelet counts are not depressed, may increase dose to 3 mg/kg once daily with careful monitoring.	Delayed intensification treatment phase: Children ≥1 year and Adolescents: Oral: 60 mg/m2/dose once daily for 14 days (Lange 2002; Nachman 1998)
Acute lymphoblastic leukemia	Oral: Late intensification treatment phase: 60 mg/m^2 once daily on days 29 to 42 (in combination with doxorubicin, vincristine, dexamethasone, cyclophosphamide and cytarabine)	Infants and Children <3 years: Oral: 3.3 mg/kg/day divided once or twice daily for 4 days in combination with cytarabine and daunorubicin Children ≥3 years and Adolescents: Oral: 100 mg/m2/day divided once or twice daily for 4 days in combination with cytarabine and daunorubicin
CNS tumors, low grade gliomas	---	Children <10 years: Oral: 30 mg/m2 every 6 hours x 11 doses (from hours 0 to 66) in a 42-day cycle for a total of 8 cycles (in combination with procarbazine, lomustine, and vincristine)

Appendix D Nature Communications Rebuttal

Rebuttal letter submitted to the reviewers of Nature Communications for my first author paper, "Mechanisms of telomerase inhibition by oxidized and therapeutic dNTPs". Currently with assigned reviewers as of July 28, 2020.

We thank the reviewers for their helpful comments and have addressed each in detail as described below. Modifications and additions to the manuscript in response to the reviewers' suggestions are indicated in red text, and we believe strengthen the overall study.

Reviewer #1 (Remarks to the Author):

Approximately 85% human tumors maintain telomeres through telomerase. Disruption of telomerase-mediated telomere repeat addition would affect telomere maintenance and ultimately cancer cell growth. Previously, this group reported that insertion of 8-oxo-dGTP by telomerase terminated telomere elongation in vitro. They demonstrated that depletion of MTH1, which hydrolyzes oxidized dNTPs (e.g. 8-oxo-dGTP), inhibits telomere maintenance in cancer cells grown under oxidative stress conditions. In this study, the authors used the same in vitro telomerase extension assay to investigate the mechanisms by which several modified dNTPs (oxidized and therapeutic dNTPs, including 2-OH-dATP and 6-thio-dGTP) could disrupt telomerase repeat extension and translocation. In addition, they reported that the telomerase processivity factor POT1-TPP1 failed to restore processivity of telomerase in the presence of these inhibitory dNTPs. The in vitro experiments were well conducted. However, the major

weakness of this manuscript is the lack of evidence demonstrating that these modified dNTPs disrupt telomere maintenance and cell survival in human cancer cells.

Although inhibiting telomerase activity is a promising therapeutic strategy to treat many cancers, this approach may disrupt telomere maintenance and viability of human germline cells, stem cells, and progenitor cells. In addition, inserting therapeutic dNTPs in the genome of healthy proliferating cells may occur, which would block DNA replication and lead to genomic instability. Thus, experimental studies that would have enhanced my enthusiasm for the current study would have included testing to determine if these therapeutic dNTPs affected cell growth of healthy and telomerase positive cancer cells differently.

Below we summarized the published studies that have shown oxidized and therapeutic dNTPs particularly impact the growth of telomerase positive cancer cells. We reference this work in our introduction and discussion. Our goal in the current manuscript was to elucidate the mechanism of induced telomere shortening.

We and others previously reported that MTH1 depletion disrupts telomere maintenance and telomerase activity in cancer cells grown under oxidative stress conditions, and that telomerase insertion of 8-oxo-dGTP terminates further telomere elongation *in vitro* [91 92]. Previously studies show that cancer cell lines are more sensitive to MTH1 inhibition compared to normal human cell lines[101]. MTH1 removes other oxidized dNTPs besides 8-oxo-dGTP, including 8-oxo-dATP and 2-OH-dATP, which we tested directly for telomerase inhibition in this manuscript.

In 2001, a study reported that chronic AZT treatment of mouse mammary carcinoma cell lines inhibited telomerase activity, caused progressive telomere shortening, and led to cellular senescence and apoptosis [46]. This study demonstrated for the first time that AZT-treated tumor cells reduced tumorigenicity in BALB/c mice. Additional studies showed that AZT reduced tumor growth in rats with parathyroid cancer cells or hepatocellular carcinomas [123].

The Shay and Wright labs, and collaborators, have published extensive cell and mouse model studies investigating the effects of 6-thio-dG on telomere maintenance, toxicity and tumor growth *in vivo*. They found that 6-thio-dG treatment caused telomere dysfunction, as evidenced by telomere dysfunction induced foci (TIFS), only in telomerase expressing cells, but not in telomerase negative cells [128]. Compared to other telomerase inhibitors, 6-thio-dG caused a faster rate of telomere shortening, and resulted in rapid cell death in numerous cancer cell lines, while normal human fibroblast and epithelial cell lines were largely unaffected. They also found that 6-thio-dG was less toxic to mice compared to equal amounts of 6-thioguanine, but still decreased tumorigenicity of lung tumor xenografts. In other pre-clinical models, 6-thio-dG treatment controlled the spread of a therapy resistant form of melanoma [135]. In xenograft models, 6-thio-dG halted tumor growth [135]. Additional pre-clinical studies have shown that 6-thio-dG induced telomere dysfunction in a telomerase dependent manner in both lung and pediatric brain cancers, resulting in reduced tumor growth [176], [136].

Since multiple previous studies had confirmed that treatments with various oxidized and therapeutic dNTPs cause telomere shortening in telomerase positive human cancer cell lines and

in xenograft tumors, our goal was to elucidate the mechanism of telomere shortening and telomerase inhibition.

Minor comments: As a negative control, please include RNAse A treatment in Supplemental Figure 1.

We included an RNase A control in Supplemental Figure S3 demonstrating that the poly-G laddering and telomerase activity is dependent on the RNA template. However, we inadvertently left out reference to this important control in the original version, and apologize for this omission. We added reference this control on page 6 (1st paragraph).

Reviewer #2 (Remarks to the Author):

The study is clearly presented, and the experiments are well designed and, for the most part, appropriately interpreted. However, there are several points the authors should consider in a revised manuscript, before the paper would be appropriate for publication. Provided the authors can address these concerns, this excellent work will certainly be of interest to the broad readership of Nature Communications.

We thank the reviewer for the positive feedback and helpful comments.

Major points:

1. A major conclusion stated throughout the manuscript is that the action of 6-thio-dG perturbs the translocation step and in turn results in lower repeat addition processivity. However, it is clear in Fig. 4c that the presence of 6-thio-dG causes a major stall mid-way through the first telomere repeat when extending Primer #2. Thus, it is unclear that the effects of this compound and several of the others can be unambiguously linked to specifically the 'translocation' step of the telomerase catalytic cycle. That said, it is clear that the impacts of 2-OH-dA and 6-thio-dG are distinct from traditional chain terminators, which is very interesting indeed. However, the authors should consider revising their paper to tone down the specific link with the translocation step and might consider stating that these nucleotide analogs impact the efficiency of RAP more generally (which might relate to steps other than translocation per se).

We thank the reviewer for pointing this out, and apologize for the lack of clarity. We agree that 2-OH-dATP and 6-thio-dGTP impact more than just the translocation step, since we see effects not only on repeat addition processivity, but also on nucleotide addition processivity. Now, we clearly defined repeat and nucleotide processivity in the text, and the steps involved (pages 3-4, and Figure 1), and clarify throughout the manuscript whether we are referring to repeat or nucleotide processivity. Repeat processivity requires dissociation from the product-template duplex, template repositioning and reannealing to initiate synthesis from the primer 3' end, and active site stabilization of the duplex at the template 3' end to add a telomeric repeat. Nucleotide addition processivity is defined as the number of nucleotides added before the enzyme reaches the 5' template end and dissociates. Therefore, disruption in nucleotide processivity can lead to premature truncation prior to adding the 6 nucleotides to complete synthesis of the GGTTAG repeat. We agree that our data in Figure 4 indicates that 2-OH-dATP

and 6-thio-dGTP are general processivity disrupters, and that they disrupt nucleotide processivity resulting in termination prior to complete repeat synthesis, and repeat processivity resulting in termination after one repeat is added. We added statements to better describe these results, and the effect of these modified dNTP on repeat processivity more generally, on pages 7 and 8 (marked in red).

2. The experiments describing the mixed effects of adding back the telomerase cofactor, POT1-TPP1, appear to be somewhat flawed. While not completely understood, the existing structural and functional data on the interaction of POT1-TPP1 with the telomerase-DNA complex would suggest that the schematic drawn in Fig. 5c is not possible. In other words, using the short 3-repeat DNA primer, one would expect that POT1-TPP1 will not have access to its binding site within the 5' region of the DNA primer until more DNA has been synthesized. In fact, one could interpret the data presented in this figure to suggest that the ability of telomerase to more readily incorporate 8dA and 2dA provides an opportunity for POT1-TPP1 to augment processivity as shown in Fig. 5a. In contrast, since 6dG, ddI, and ZdT do not support addition of more than one repeat, one would not expect POT1-TPP1 to exert any effect on the reaction, as is shown in Fig. 5b. A more informative experiment might be to do the experiment with longer starting primers to determine whether POT1-TPP1 that has access to the 5' end of the DNA can somehow suppress the defects observed in the presence of 6dG. Based upon the data presented in this study, I would expect that the authors interpretation are likely to stand, this additional experiment may not be essential for publication. However, the authors should consider this point when revising their paper.

We considered the possibility that POT1-TPP1 may compete with telomerase for binding at the 3'end of the primer. The schematic in Figure 5c was based on previous published work that showed POT1 binds 10 nt of ssDNA (X-ray crystal structure), which is available in this primer substrate [226], [227]. We used the same substrate (primer a5) shown to be an optimal substrate for POT1-TPP1 stimulation of telomerase [226], [15]. Our data show that when telomerase is stimulated with POT-TPP1, telomerase repeat processivity increases in the presence of 2-OH-dATP. This result supports the conclusion that POT1-TPP1 has access to the 5' end of this substrate, and therefore, we do not expect that a longer starting primer would yield a different result with POT1-TPP1 and 6-thio-dGTP (i.e. we still expect POT1-TPP1 would not be able to overcome the detrimental effects of 6-thio-dG on processivity). With regards to 8-oxo-dATP, in Figure 3 we showed that telomerase very poorly incorporates 8-oxo-dATP opposite any template position. Therefore, in Figure 5a, lanes 5 and 6, telomerase is likely misincorporating dGTP or dTTP opposite template rU, when dATP is absent, which would explain the extension in both lanes.

3. It appears that the structure of 2-OH-dATP is not correct in Fig. 1a, where the authors have shown the OH group appended to the ribose moiety rather than the adenosine base at position 2.

We thank the reviewer for catching this unfortunate error. We have corrected this in the revised Figure 1a.

4. With respect to nomenclature – the authors need to define their shorthand for the various nucleotide analogs used throughout the paper (perhaps doing so in Fig. 1a makes the most sense).

Thank you for this valuable suggestion for improving readability. These abbreviations have been added to Figure 1a.

5. The authors should consider using specific template nucleotide numbering when referring to telomerase RNA template positions rather than rCrC, for example.

Thank you for this suggestion. We defined the template bases $rC_1rC_2rA_3rA_4rU_5rC_6$ in the figures and the text, and found this greatly improved readability. We did not highlight these changes in the text given the abundance.

6. In the discussion the authors claim - "We found that telomerase incorporation of dGTP is more error prone than the other natural dNTPs, as indicated by dGTP misincorporation at low 5 μM." However, this is a bit misleading as the level of misincorporation at low uM concentrations in Fig. S3 is very minimal and only becomes apparent at much high dGTP concentrations.

We agree that the % primer extension is very minimal at 5 μM dGTP across non rC template resides (6% for primer 1 and 2% for primer 3), but we found this noteworthy because at this low physiological concentration we do not see Poly-G laddering. Furthermore, we observed no misincorporation of dGTP even at 200 μM by DNA polymerase β (Supplemental Figure 4d).

On a related note, the authors state, "Interestingly, telomerase extended all three primers in the presence of dGTP, indicating telomerase can incorporate dGTP opposite each template base even at low cellular concentrations (5 μM) (Supplementary Fig. S3)." This result is not very surprising as this G-ladder pattern has been reported previously for both human and cilate telomerase systems (as the authors appropriate cite in the paper). Moreover, it is unclear from these experiments whether or not this ladder pattern in fact is a result of 'misincorporation' across from non 'rC' template nucleotides, or whether this is due to some form of product slippage (as the authors ultimately allude to in the Discussion). The authors should take care to differentiate such a slippage model from actual misincorporation events.

We agree that we cannot rule out that product slippage is a contributor, however, we also cannot rule out that dGTP may be misincorporated as well. Our data in Figure 3 indicate that 50 μM dGTP reactions for insertion opposite template rA (primer 1) yield 20% primer extension, opposite rC (primer 2) show 25% extension, and opposite rU (primer 3) show 5% primer. If extension was due only to non-specific poly-G laddering, then we reason the % primer extension would be the same opposite all starting template positions, which was not the case. Furthermore, we observed comparable % primer extension for dGTP and 6-thio-dGTP with starting template rA (primer 1), yet we observed no evidence for poly 6-thio-dGTP laddering (Figure 3). However, as we noted in the discussion slippage may contribute to misincorporation: "This primer slippage may contribute to dGTP addition opposite non rC residues, although poly d(G) laddering was not observed at low (5 μM) dGTP, suggesting addition by misinsertion". Since we cannot distinguish between these two mechanisms, we altered some of the language (page 5, 11, and 12 from

"indicate" to "suggests"), and to reflect both of these possibilities.

7. Throughout the paper, the authors cite R1/2 values, yet there is no figure included where the data and the associated fits from which they are derived is shown. It would also be a good idea for the authors to clearly articulate how the R1/2 value for processivity is defined, which they appear to be basing on the work from Latrick and Cech. For example, in the text, the authors should not simply state the processivity goes from '2.5 to 4.5', as these numbers are not likely to mean anything to readers if the definition for how this value is determined is not clearly presented.

We agree with this helpful critique and the lack of clarity on the R1/2 values in our original version. We have added the plots from which R1/2 values were derived to the Supplemental figures. We now define in detail how R1/2 was calculated in the methods. Finally, we more clearly explain the meaning of R1/2 in the text on pages 4, and 9. "Repeat processivity was measured using the convention of calculating the number of repeats synthesized before half of the DNA substrates dissociate from telomerase [228]."

8. Late in Results section of the paper, the authors describe pre-steady state kinetics analysis of incorporation by the flour beetle TERT protein using a model hybrid RNA-DNA duplex. The abrupt switch to the tcTERT system appears to come out of nowhere since all prior experiments in the work are done on human telomerase. Moreover, I could not find any description in the Materials and Methods about how this tcTERT was made and what the sequences of the RNA-

DNA hybrid are? The authors should better justify the transition and to this alternative 'telomerase-like' system from Tribolium casteneum.

Thank you for noting this omission from the methods. We have added details of the purification, and sequences used with the tcTERT reactions to the methods section. We have also referenced a very recent publication [144] which further describes in detail the use of this model for comparison with human telomerase catalysis of nucleotide addition. We have also added the following text to page 10, to justify our use of this model.

"We showed previously that the ability to purify sufficient quantities of *tc*TERT enables characterization of the catalytic nucleotide addition by pre-steady-state single turnover kinetics using a defined DNA-RNA primer-template substrate [144]. This analysis measures the catalytic efficiency of incorporating a single dNTP by dividing the observed nucleotide incorporation rate constant, k_{pol}, by the equilibrium dissociation constant for dNTP binding to tcTERT-primer-template complex (K_d) [158].

9. The authors describe an effect of inhibition at high dGTP concentrations of hot-dTTP incorporation (Fig. 2a). This is a bit confusing, because in this figure, lane 4, there appears to be high MW signal that is not being well-resolved? The authors should explain. Also, is a similar inhibition observed at high dGTP when using the 5' end-labeled primer assay? I suppose one would expect the G-ladder pattern to begin to emerge when there is a large excess of dGTP over the other dNTPs.

The reactions in Figure 2a used radiolabeled dTTP and 10μM of cold dTTP. We found that if we added higher concentrations of cold dTTP to the reactions, it would swamp out the signal of the radio-labeled dTTP. The high MW products in lane 4 (Figure 2a) are due to high telomerase processivity when 125 μM of dGTP was added to the reaction. The signal of these products is weak because 1) T makes up of only 30% of each telomeric repeat, and 2) the near 10-fold excess of dGTP (125 μM) over dTTP competes for insertion opposite rA_3. In Supplementary Figure S2 the high MW products are better resolved when the dGTP concentration is lower at 25 μM. When we used radiolabeled dGTP (Figures 2b and 2c), the signal of the high MW products is greater partly because G makes up 50% of the telomeric sequence.

We would not expect to see loss of radioactive signal using a radiolabeled primer, since the product labeling does not depend on insertion of a radio-labeled dNTP. In Figure 4, the reactions were conducted with all the dNTPs, including dGTP, at 50 μM each (see lane 2 of each panel). Here, the higher MW bands appear better resolved with a more even signal for each product.

Reviewer #3 (Remarks to the Author):

I find the paper overall strong, with a well-written, logical flow to the experiments. A limitation of the experiments is the reliance on one (well defined) in vitro assay.

Thank you for the positive feedback. The field as whole has been challenged by developing methods and tools to monitor telomerase-mediated telomeric repeat addition and translocation in cells; partly due to the low expression. But we and others will continue to work on this.

General comments:

The data in figure 2a-c suggests a high tolerance for misincorporation of natural nucleotides (particularly dG). The authors should clarify in the text that in vivo telomerase does not seem to have such a high false incorporation rate for dG. I think that this is needed to put the in vitro data into context.

While we observed misincorporation for dGTP at cellular relevant concentration (5 μM), the misinsertion product opposite rA_3 was minimal (Supplemental Figure 3). Furthermore, we expect that the higher physiological concentrations of dTTP (~37 μM), and the preference for telomerase insertion of dTTP opposite rA_3 (Figure 3, panel a), would outcompete dGTP in a physiological setting. Because the cellular concentration of dGTP is much lower than dTTP, we would not expect to observe high misincorporations of dGTP by telomerase in a cellular context. That said, sequencing data on telomeres from cells is limited, and it is possible that accessory factors improve telomerase fidelity *in vivo*. On page 12 in the discussion we added:

"The lower physiological concentration of dGTP (5 μM), relative to the other dNTPs [150], likely minimizes dGTP misincorporation and laddering *in vivo*. Furthermore, accessory proteins may assist telomerase fidelity."

It would be helpful to educate the reader as early as possible on the physiological nucleotide concentrations to put the assay concentrations into context. This is especially important as, based on the introduction, the focus seems to be on the development of these dNTPs for clinical use.

This is an excellent point, and we included values for the natural dNTPs (24 μM dATP, 29 μM dCTP, 37 μM dTTP, 5.2 μM dGTP, averaged from multiple studies[150]) at the beginning of our results section (page 4).

A few questions come to mind: what are the effects of these modified dNTPs on other polymerases; what are the difficulties already encountered with using modified dNTPs for cancer treatment; and, how may the new information presented in this article circumvent those challenges?

Several studies have shown that the modified dNTPs inhibit mitochondrial DNA (mtDNA) polymerase γ (pol γ), which disrupts mitochondrial DNA replication and induces mitochondria dysfunction [131], [115]. Inhibition of pol γ leads to the depletion of mtDNA, and subsequent depletion of mitochondrial encoded poly peptides involved in oxidative phosphorylation. When the modified dNTPs cause a decrease in mtDNA, the mitochondria protein complex malfunctions, causing changes in respiration rate, decreased ATP production,

diminished mitochondria membrane potential, and an increase in ROS production. The elevated ROS damage natural dNTP pools. We suggest that in conjunction with MTH1 inhibitors, therapeutic NRTIs or thiopurines may deliver a one-two punch to telomerase driven cancers by inhibiting telomerase directly and indirectly through elevated oxidized dNTPs. The new information presented in this article defines the mechanism in which both oxidized and therapeutic dNTPs inhibit telomerase, which has previously not been shown. We comment on these topics in the discussion.

Technical comments:

1. Figure 1 lacks quantification and statistics.

Figure 1 shows chemical structures of the modified dNTPs, and the enzymatic schematic for telomerase. We assume the reviewer is referring to Figure 2. More detailed quantification and statistics for Figure 2 are shown in Supplemental Figure 2.

2. Is there a particular reason why the authors did not test a primer ending on GTTA? I think this could be a good primer to include in figure 3 and 5 as it most effectively tests the effects of 6dG on translocation.

A primer ending in GTTA would be a slight variation of Primer 3 (ending in GGTT). For Primer 3, Figure 4 shows a strong termination product after telomerase incorporated 6-thio-dGTP opposite rC_6, suggesting dissociation prior to translocation. But we also observed a strong

termination product at rC_1, indicating either successful translocation for some reactions followed by dissociation, or template slippage for an additional 6-thio-dGTP prior to translocation. This result was recapitulated with Primer 1. Therefore, we predict the same result if we used a primer ending in GTTA; nearly 50% of the products terminating after insertion opposite rC_6, and the rest terminating after insertion opposite rC_1. Furthermore, since dATP was included in the reactions for Figure 4 and primer 3, the addition of dATP converts the -GGTT ending primer to -GGTTA prior to insertion of 6-thio-dGTP.

3. A key defect of 6dG incorporation is a reduced inability for telomerase translocation. The effect seen is relative and it would be good to corroborate this with an orthogonal (in vivo) assay. The same is true for the lack of stimulation in Figure 5.

We are not aware of any current techniques to measure telomerase translocation directly *in vivo*, although some labs are developing methods for tracking telomerase movement in cells [229], [230]. Notably, even these novel techniques lack the resolution required to visualize telomerase translocation at telomeres in cells. However, we are excited by studies that show 6-thiodG treatment causes telomere shortening in telomerase positive cancer cells in culture, and telomere dysfunction in the tumors. Our purpose for this study was to elucidate the mechanism by which 6-thiodG induces telomere shortening in telomerase expressing cancer cells.

Minor comments:

Citation 22 is a review from 2008 -- is there anything more current?

We have added more recent reviews:

Schmiegelow et al, *J Pedr Hematol Oncol*, 2014

Bradford et al, *World J Gastroenterol*, 2011

Zhang and Shay, *Oncotarget*, 2018

In reference to this sentence, “Previous reports showed that 6-thio-dGTP, which forms in cells from 6-thio-dG, promotes cell death in telomerase positive cancer cells, and decreases tumor growth in mouse xenograft studies23” -- Citation 23 is not the original source for this information. Citation 23’s authors have a patent for 6-thio-dG, and in this article, they are summarizing their past results. Would it be possible to use a different citation for this information?

To our knowledge Citation #23 in the original version of our article (Mender et al, Cancer Discovery, 2015) is the first publication by the Shay/ Wright group we could find in which they report evidence that 6-thio-dG causes telomere dysfunction. The primary data that “6-thio-dG promotes cell death in telomerase positive cancer cells” are shown in Figures 1 and 3, and “decreases tumor growth in mouse xenograft studies” is shown in Figure 5 in this published manuscript.

Appendix E Mechanisms of nucleotide selection by telomerase

Our collaboration with the Freudenthal Lab at University of Kansas Medical center resulted in a research article originally published in eLife [144]. Mechanisms of nucleotide selection by telomerase. Matthew A Schaich, Samantha L Sanford, Griffin A Welfer, Samuel A Johnson, Thu H Khoang, Patricia L Opresko, Bret D Freudenthal. eLife. Jun 5, 2020. DOI: 10.7554/eLife.55438.

RESEARCH ARTICLE

Mechanisms of nucleotide selection by telomerase

Matthew A Schaich[1], Samantha L Sanford[2], Griffin A Welfer[1], Samuel A Johnson[2], Thu H Khoang[1], Patricia L Opresko[2], Bret D Freudenthal[1,3]*

[1]Department of Biochemistry and Molecular Biology, University of Kansas Medical Center, Kansas City, United States; [2]Department of Environmental and Occupational Health, University of Pittsburgh Graduate School of Public Health, and UPMC Hillman Cancer Center, Pittsburgh, United States; [3]Department of Cancer Biology, University of Kansas Medical Center, Kansas City, United States

Abstract Telomerase extends telomere sequences at chromosomal ends to protect genomic DNA. During this process it must select the correct nucleotide from a pool of nucleotides with various sugars and base pairing properties, which is critically important for the proper capping of telomeric sequences by shelterin. Unfortunately, how telomerase selects correct nucleotides is unknown. Here, we determined structures of *Tribolium castaneum* telomerase reverse transcriptase (TERT) throughout its catalytic cycle and mapped the active site residues responsible for nucleoside selection, metal coordination, triphosphate binding, and RNA template stabilization. We found that TERT inserts a mismatch or ribonucleotide ~1 in 10,000 and ~1 in 14,000 insertion events, respectively. At biological ribonucleotide concentrations, these rates translate to ~40 ribonucleotides inserted per 10 kilobases. Human telomerase assays determined a conserved tyrosine steric gate regulates ribonucleotide insertion into telomeres. Cumulatively, our work provides insight into how telomerase selects the proper nucleotide to maintain telomere integrity.

***For correspondence:** bfreudenthal@kumc.edu

Competing interests: The authors declare that no competing interests exist.

Funding: See page 18

Received: 24 January 2020
Accepted: 18 May 2020
Published: 05 June 2020

Reviewing editor: Maria Spies, University of Iowa, United States

Introduction

During every round of eukaryotic cell division, a small amount of DNA is lost from the ends of each chromosome (***Olovnikov, 1973***; ***Watson, 1972***). Termed the end replication problem, this phenomenon is countered by two complementary adaptations. First, repetitive noncoding DNA sequences, known as telomeres, are found at chromosomal ends, preventing the loss of vital genetic information during each cell division (***Blackburn and Gall, 1978***; ***Moyzis et al., 1988***). Second, the ribonucleoprotein telomerase elongates shortened telomeres at chromosomal ends using a reverse transcriptase activity (***Greider and Blackburn, 1987***). Without elongation, telomeres will eventually reach a critically short length, causing cells to undergo apoptosis or become senescent (***Hayflick and Moorhead, 1961***; ***Meyerson, 1998***). Because telomerase plays such a fundamental role in the temporal regulation of cell division, aberrations in telomerase are implicated in numerous human diseases. These include premature aging, idiopathic pulmonary fibrosis (IPF), dyskeratosis congenita, and cancer (***Blasco, 2005***; ***Kim et al., 1994***; ***Nelson and Bertuch, 2012***). In particular,~90% of cancers upregulate telomerase to combat telomere shortening and enable unlimited cell division, as opposed to somatic cells where telomerase is absent (***Jafri et al., 2016***).

The implication of telomerase in multiple human diseases underscores the importance of understanding its catalytic cycle at the molecular level. Although the human telomerase holoenzyme is composed of multiple accessory subunits, catalysis is localized to the telomerase reverse transcriptase (TERT) subunit (***Nguyen et al., 2018***). Historically, biochemical characterization of human TERT (hTERT) has proven challenging, in part because of technical difficulties purifying and reconstituting large quantities of active telomerase (***Ramakrishnan et al., 1997***; ***Schmidt et al., 2016***). As a result,

many fundamental parameters describing the telomerase catalytic cycle have remained undefined. These enzymatic constants are essential for understanding the roles of active site residues, the selection of right from the wrong nucleotides (fidelity), and the prevention of ribonucleotide triphosphate (rNTP) insertion (sugar discrimination). The faithful extension of telomeres by telomerase is critical because aberrations in telomeric sequences prevent shelterin proteins from capping telomeres, thus promoting genomic instability (**de Lange, 2005**; **Nandakumar et al., 2010**). Structural studies of human telomerase have also been historically challenging. Currently, the highest resolution structural snapshot of human telomerase is a cryo-EM structure at 8 Å resolution (**Nguyen et al., 2018**). This structure represents a milestone in telomerase structural biology, revealing details of the telomerase tertiary and secondary structure. However, the positions of amino acids are difficult to distinguish at this resolution, leaving many molecular details of the catalytic cycle ambiguous.

To mitigate the difficulties inherent in the biochemical characterization of human telomerase, several model systems have been established. These include models from yeast, the protazoa *Tetrahymena thermophila* (with which a 5 Å cryo-EM structure was recently determined), and the insect model *Tribolium castaneum* (sequence alignment shown in **Figure 1—figure supplement 1**; **Gillis et al., 2008**; **Jiang et al., 2018**; **Petrova et al., 2018**). For biochemical characterization of TERT, we opted to use *T. castaneum* TERT (*tc*TERT) for the following reasons: first, *tc*TERT readily fit into the cryo-EM density of *h*TERT and aligns well with the recent cryo-EM structure from *T. thermophila*, highlighting the conserved secondary structure (**Figure 1—figure supplement 2**); second, upon alignment with *h*TERT, the active site pocket of *tc*TERT exhibits a high degree of sequence identity (**Supplementary file 1**, Table 1a); third, using a truncated version of the *T. castaneum* telomerase RNA component (TR), we can readily obtain sufficient quantities of isolated, active *tc*TERT for characterization of the telomerase catalytic cycle by pre-steady-state kinetics and X-ray crystallography (**Gillis et al., 2008**; **Nguyen et al., 2018**). Although TERTs have highly conserved active sites, there are significant changes in the domain architecture between human and *tc*TERT. These include *tc*TERT lacking the N-terminal (TEN) domain and missing a portion of the insertion in fingers domain (IFD) (**Supplementary file 1**, Table 1b). These domains are essential for the activity of other telomerase homologs, and have been hypothesized to be particularly important for telomerase ratcheting during translocation (**Steczkiewicz et al., 2011**). Therefore, we kept our *tc*TERT kinetics within a single turnover (i.e. insertion) regime, and, wherever possible, complemented the kinetic results with human telomerase studies to characterize the catalytic cycle of telomerase. Using this combined approach, we have elucidated the role of conserved telomerase active site residues and determined the mechanisms of fidelity and rNTP discrimination.

Results

The TERT subunit of telomerase elongates telomeric DNA using a conserved catalytic cycle as outlined in **Figure 1A**, **Figure 1—figure supplement 3**, and here. First, telomerase anneals its RNA template to the end of telomeric DNA to form a binary complex (TERT:DNA, **Figure 1A**, state A_1). Next, the binary complex binds an incoming dNTP and samples for proper Watson-Crick base pairing to the RNA template (**Figure 1A**, state B_1). The transition between these two states represents the nucleotide binding step, measured as a dissociation constant (K_d). If the resulting ternary complex (TERT:DNA:dNTP) is in the proper orientation, TERT will catalyze the formation of a phosphodiester bond and extend the telomere by one nucleotide (**Figure 1A**, state C_1). The transition between these two states is the chemistry step, and its theoretical maximum rate with saturating nucleotide concentration is described as k_{pol}. Following insertion of the incoming nucleotide, telomerase will shift registry to align the active site with the next templating base (forming state A_2). This core catalytic cycle repeats six times, until a new telomeric repeat is added (**Figure 1A**, state C_6). All 18 telomerase states that are required to add one telomeric repeat are shown in **Figure 1—figure supplement 3** for reference. Importantly, as the telomerase approaches the end of its template, the DNA:RNA duplex at the 5′ end begins to melt, enabling telomerase to either (1) translocate and anneal the RNA component to the newly extended telomeric repeat, thus allowing for additional repeat addition; or (2) dissociate from the telomeric DNA. The number of times that a single telomerase enzyme traverses this catalytic cycle is tightly regulated. It was recently shown telomerase becomes inactive after two repeats, but can be reactivated by the recently discovered intracellular telomerase-activating factors (iTAFs) (**Sayed et al., 2019**).

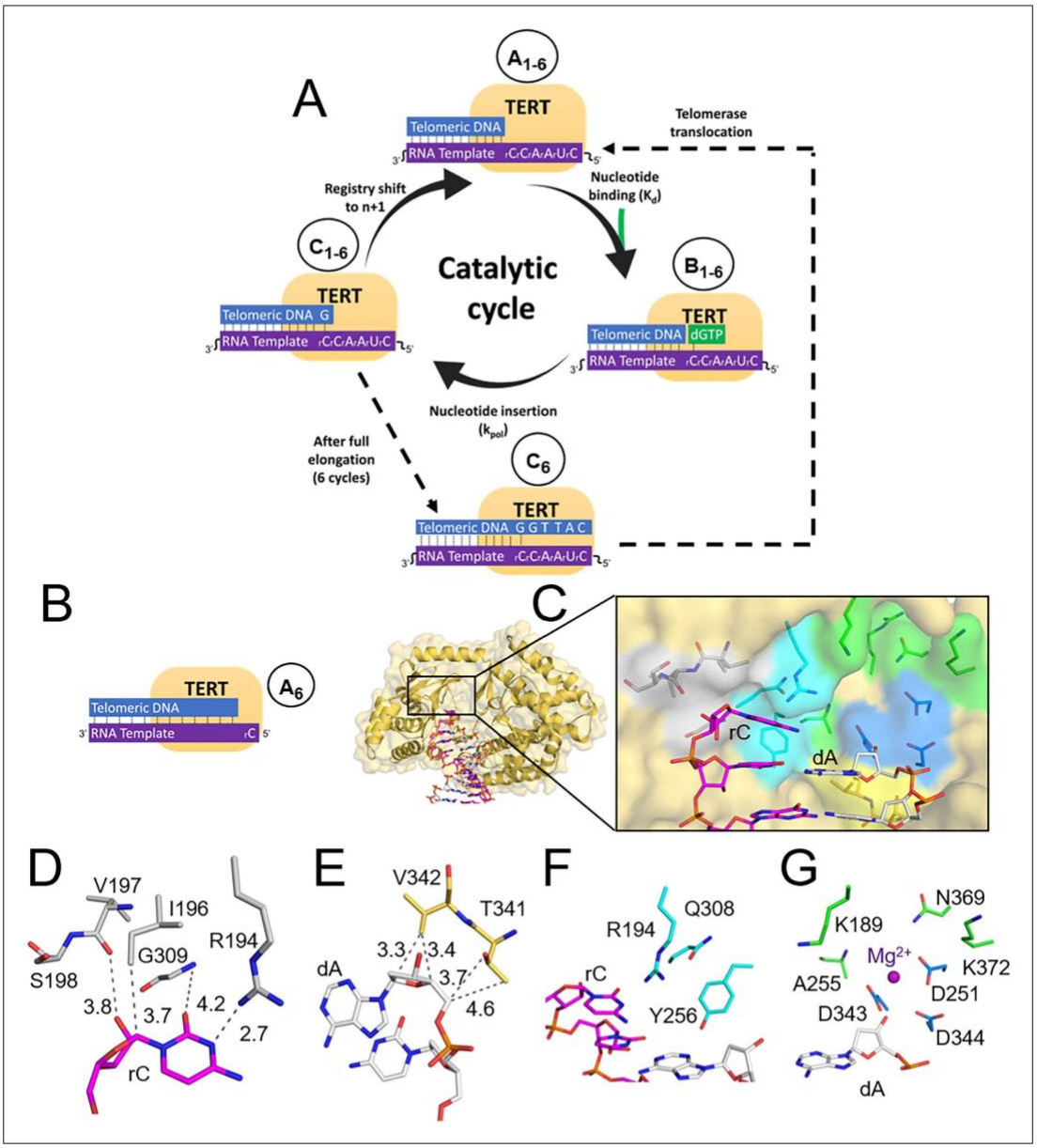

Figure 1. The telomerase catalytic cycle, and its first structural state. (**A**) Overview of the telomerase catalytic cycle. Telomerase forms a prenucleotide bound binary complex (State A_1). Then, it binds the incoming nucleotide triphosphate to form a ternary complex (State B_1), chemically links it to the telomere terminus (State C_1), and then shifting registry to bind the next incoming nucleotide (State A_2). After this cycle completes six times (State C_6), telomerase will either disassociate or undergo translocation (dotted line), which places it back into State A_1. (**B**) The tcTERT prenucleotide binary complex. tcTERT (pale orange cartoon and surface) encircles the DNA (white) and RNA (purple) substrate. (**C**) Active site pocket of the prenucleotide

Figure 1 continued on next page

Figure 1 continued

binary complex. rC binding (gray), dG binding residues (yellow), nucleoside residues (cyan), catalytic residues (blue), and triphosphate binding (green) are shown as sticks. (**D**) Closeup views of the rC binding residues, (**E**) terminal dG binding residues, (**F**) nucleoside binding residues, and (**G**) the tcTERT catalytic residues and triphosphate coordinating residues. A Mg2+ ion is shown as a purple sphere and DNA is presented as white sticks.
The online version of this article includes the following figure supplement(s) for figure 1:

Figure supplement 1. Alignments of several telomerase reverse transcriptase homologs.
Figure supplement 2. Overlay of TERT from *Tribolium castaneum* with other TERT structures.
Figure supplement 3. All 18 structural states involved in the extension of a telomeric repeat.

Observing telomeric extension at the molecular level

Pre-nucleotide binary complex

We determined how TERT engages with telomeric DNA by co-crystallizing *tc*TERT with a 16-mer RNA strand hybridized to its complementary 15-mer DNA strand to form a binary complex. This substrate mimics the initial TERT:RNA complex bound to telomeric DNA (***Figure 1A***, state A_6). In this orientation, an unpaired 5′ cytosine (rC) of the RNA strand acts as the templating base and a 3′ adenosine (dA) of the DNA strand serves as the primer terminus (***Figure 1B,C***). Crystals of this complex grew in a $P3_221$ space group, diffracting to 2.5 Å resolution (***Supplementary file 2***, Table 2a). The resulting structure shows TERT bound as a ring around the end of the RNA:DNA complex, with its active site positioned at the terminus of the DNA strand (***Figure 1B,C***).

Within the TERT active site, the templating RNA strand is stabilized by multiple conserved tcTERT residues (***Supplementary file 1***, Table 1a). Residues I196, V197, S198, G309, and R194 compose a pocket around the templating RNA base (***Figure 1D***). This pocket uses both polar and nonpolar interactions to stabilize the templating rC in a conformation that orients its Watson-Crick edge towards the incoming nucleotide binding site. On the opposite side, the 3′-OH of the primer terminal 3′-dA points towards the catalytic metal binding site, and side chains from T341 and V342 coordinate the deoxyribose sugar moiety of the 3′-dA with nonpolar interactions (***Figure 1E*** and ***Supplementary file 1***, Table 1a). This binary TERT complex also has a cavity in the active site that forms the nucleotide binding pocket. These nucleotide pocket residues can be subdivided into three categories: nucleoside coordinating, catalytic, and triphosphate interacting residues (***Figure 1F and G***). Notably, the residues that compose these three groups are 100% conserved between *h*TERT and *tc*TERT (***Supplementary file 1***, Table 1a). The nucleoside binding group is composed of residues R194, Y256, and Q308 (***Figure 1F***). These residues form a nucleoside shaped cleft directly upstream of the primer terminus of the telomeric DNA and are further characterized below. The catalytic residues include the catalytic triad: D251, D343, and D344. These residues coordinate the divalent metal ions during catalysis (***Figure 1G***). Residues K189, A255, N369, and the backbone of K372 are in position to form interactions with the triphosphate of the incoming nucleotide (***Figure 1G***). Collectively, the active site of *tc*TERT is primed for nucleotide binding, and the residues involved in binding are highly conserved with human telomerase (***Supplementary file 1***, Table 1a).

Nucleotide bound ternary complex

We also determined the structure of TERT after binding an incoming nucleotide, but prior to catalysis (***Figure 1A***, state B_6). To capture the ternary complex, we utilized a non-hydrolyzable nucleotide analog 2′-deoxyguanosine-5′-[(α,β)-methyleno]triphosphate (dGpCpp). dGpCpp is identical to dGTP, except the bridging oxygen between the α and β phosphate is a carbon atom, which prevents catalysis (***Batra et al., 2006***; ***Gleghorn et al., 2011***). Crystals of this complex grew in the same $P3_221$ space group and diffracted to 2.9 Å resolution (***Supplementary file 2***, Table 2a). Comparing this ternary complex to the binary state (RMSD value of 1.52 Å, ***Figure 2A***) indicates minimal structural rearrangements are required for TERT to bind dGpCpp. The active site residues that compose the nucleotide binding pocket of the pre-nucleotide binary complex coordinate the incoming dGpCpp, positioning its Watson-Crick face to hydrogen bond with the templating rC (***Figure 2B,C***). Two Mg^{+2} ions exhibit octahedral coordination to facilitate nucleotide binding. The catalytic metal coordinates residues D251, D343, D344, the 3′-OH of the primer terminus, and the non-bridging oxygen of the dGpCpp α-phosphate (***Figure 2D***). The nucleotide metal coordinates the side chains of D251 and D343, the backbone carbonyl of I252, and a non-bridging oxygen on the α,β, and γ

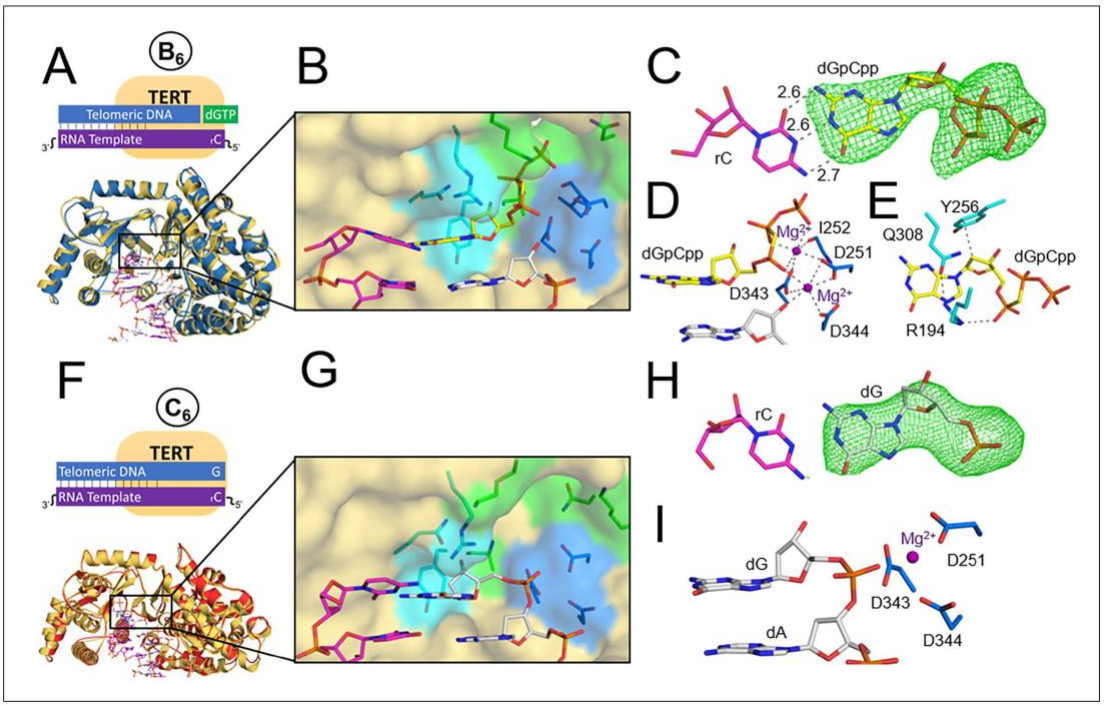

Figure 2. TERT ternary and product structures. (**A**) The tcTERT ternary structure, overlayed with the prenucleotide binary complex. DNA (white), RNA (purple), binary tcTERT (yellow cartoon), and ternary tcTERT (blue cartoon) are shown. (**B**) The tcTERT active site. Nucleoside residues (cyan), triphosphate residues (green), and catalytic residues (blue) are shown. The dGpCpp (yellow), DNA, and RNA are represented as sticks. (**C**) Closeup view of dGpCpp with a polder OMIT map contoured at σ = 3.0 (green mesh). (**D, E**) dGpCpp contacts are shown with Mg2+ (purple), catalytic residues (marine) and nucleoside residues (cyan) indicated. (**F**) The tcTERT product structure (red cartoon), overlaid with the prenucleotide binary complex (yellow cartoon). (**G**) An active site view of the tcTERT product structure. (**H**) A display of a polder OMIT map contoured at σ = 3.3 around the incoming dGpCpp (green mesh). (**I**) Catalytic residues (marine) coordinate the inserted dG (white).

phosphates of the incoming dGpCpp (***Figure 2D***). Nucleoside binding residue R194 remains in a similar position to where it was in the prenucleotide state, but now forms a network of contacts between residue Q308 and the α phosphate of the incoming nucleotide, stabilizing it in an orientation near other nucleoside binding residues. Y256 is positioned near the C2 position of the deoxyribose sugar portion of the nucleoside, and Q308 coordinates the nucleoside component of the dGpCpp (***Figure 2E***). As a whole, the nucleoside binding residues encircle the nucleoside component of the incoming nucleotide, and position it so that the nucleobase can base stack with the primer terminus. Overall, this ternary complex provides insight into nucleotide selection by TERT and the specific roles of active site residues during nucleotide binding.

Product complex

To capture a product complex of telomerase, we crystallized TERT after incubation with its nucleic acid substrate and dGTP, allowing TERT to insert the nucleotide and form the final product stage of the catalytic cycle (***Figure 1A***, state C_6). Both globally and within the active site, we observed minimal structural changes between the prenucleotide binary complex and the product structure (RMSD value of 1.04 Å, ***Figure 2F***). Electron density of the inserted dG indicates its Watson-Crick face hydrogen bonds to the Watson-Crick face of the templating rC (***Figure 2G,H***). The templating rC continues to interact with the residues that coordinated it during the other two structural states

described prior, including I196, V197, S198, G309, and R194. Neither a registry shift nor a translocation step has occurred in this structure; the TERT active site remains aligned to the terminal DNA base (***Figure 2I***). Comparing this structure to structures of the previous stages in the catalytic cycle, we observed that minimal global rearrangements are required to proceed from the binary, ternary, and product states of the catalytic cycle.

Fidelity and sugar selectivity of TERT

Characterization of the telomerase catalytic mechanism was performed using pre-steady-state kinetics of single nucleotide insertion by *tc*TERT (***Figure 3***, ***Figure 3—figure supplement 1***, ***Figure 3—figure supplement 2***, and ***Supplementary file 3***). These experiments determined both the K_d of the

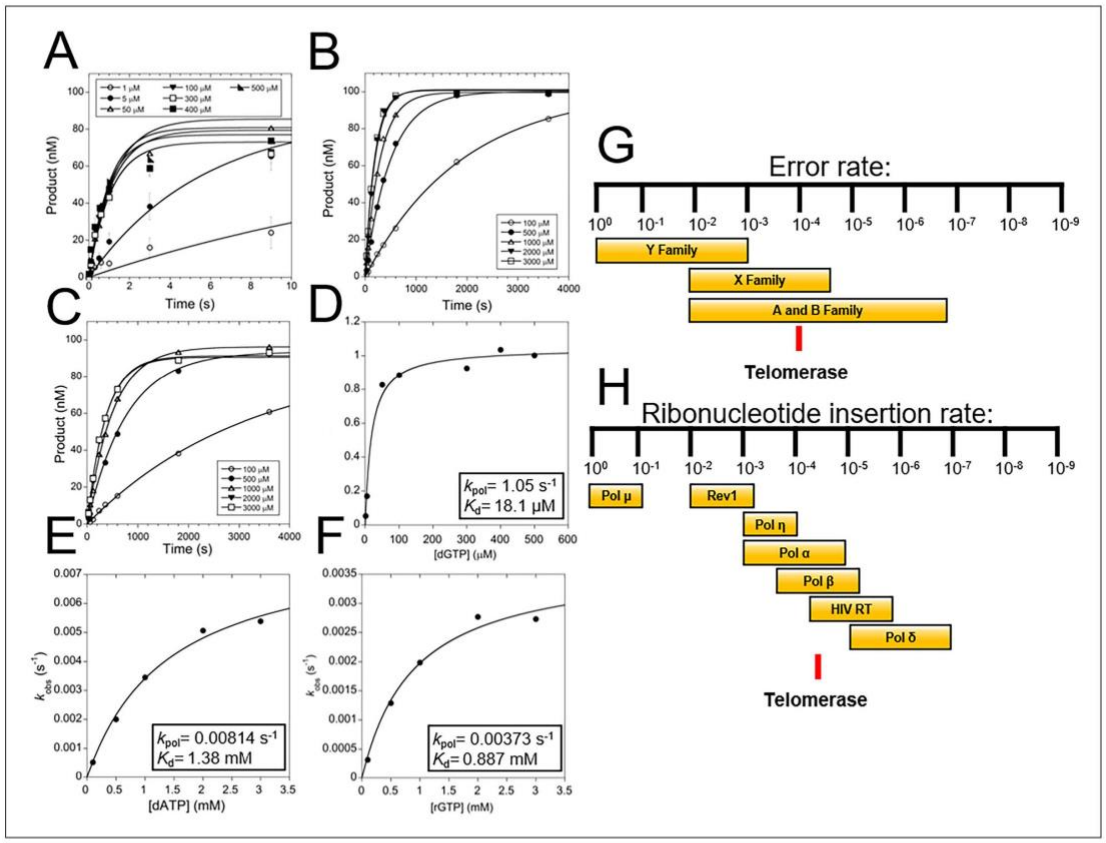

Figure 3. TERT fidelity and sugar discrimination. (**A**) Pre-steady-state kinetics of WT tcTERT inserting dGTP opposite rC. Data was fit to ***Equation 1*** (***Supplementary file 3***, Table 3a and b). Error bars represent the standard deviation of the mean. These experiments were also performed with WT tcTERT inserting dATP across from rC (**B**) and rGTP across from rC (**C**). Replots of the data and fits to ***Equation 2*** were performed for (**D**) dGTP across from rC, (**E**) dATP across from rC, and (**F**) rGTP across from rC. (**G**) A comparison of TERT nucleobase fidelity (red line) compared to other DNA polymerase families. (**H**) TERT's rNTP discrimination rates (red line) compared to select DNA polymerases is shown (***Brown and Suo, 2011***; ***McCulloch and Kunkel, 2008***).

The online version of this article includes the following figure supplement(s) for figure 3:

Figure supplement 1. Pre-steady-state kinetics of additional TERT active site mutants.

Figure supplement 2. Complete graphs of selected TERT pre-steady-state kinetics.

incoming nucleotide and the k_{pol} for nucleotide insertion by *tc*TERT, which have thus far proven unattainable for human telomerase (or any other homolog). TERT inserts the correctly matched dGTP across from a templating rC with a k_{pol} of 1.05 s^{-1} and a K_d for the incoming dGTP of 18.1 μM (***Figure 3A,D***). Both of these values are comparable to other non-replicative DNA polymerases and the TERT K_M values obtained by steady-state kinetics (***Brown et al., 2010***; ***Chen et al., 2018***). We further probed the role of *tc*TERT active site residues R194 and Q308 because their role during catalysis is not clear from the structures alone and both residues protrude into the nucleotide binding pocket (***Figure 1F*** and ***Supplementary file 1***, Table 1a). For TERT R194A, the k_{pol} decreased by 28-fold to 0.0369 s^{-1}, and the K_d for dGTP increased ~5 fold to 93 μM (***Figure 3—figure supplement 2A,C***). With the Q308A variant, the k_{pol} decreased ~60 fold to 0.30 s^{-1} and the K_d for dGTP increased ~2 fold to 45 μM (***Figure 3—figure supplement 2B,D***). Therefore, R194 and Q308 primarily play a role in the chemistry step rather than the nucleotide binding. As the *h*TERT homolog to R194 (R631, ***Supplementary file 1***, Table 1a) is implicated in IPF, we infer that mutations at R631 likely reduce *h*TERT's k_{pol}, contributing to IPF pathologies (***Basel-Vanagaite et al., 2008***; ***Diaz de Leon et al., 2010***).

During telomeric extension, telomerase must select between a variety of nucleic acid substrates in order to properly maintain telomeric integrity. To probe the fidelity of telomerase, we applied pre-steady-state kinetics, assessing the efficiency with which TERT inserts nucleotides during telomeric elongation. Two separate types of nucleotide selection were examined: (1) the selection of a matched dGTP over a mismatched dATP, and (2) the selection of a matched deoxyribonucletide triphosphate (dNTP) over a matched rNTP (***Figure 3B and C***, ***Supplementary file 3***, Table 3a and b). We observed that for the insertion of dATP opposite a templating rC, the catalytic efficiency starkly decreased compared to dGTP insertion, both at the nucleotide binding and chemistry step. For the mismatched insertion, the k_{pol} decreased 129-fold to 0.0081 s^{-1} and the K_d increased 76-fold to 1.3 mM (***Figure 3E***). The resulting catalytic efficiencies (k_{pol}/K_d) for a matched versus mismatched nucleotide insertion indicate telomerase will insert the wrong nucleotide ~1 in 10,000 nucleotide insertion events. This places telomerase at a moderate fidelity of base selection compared to other DNA polymerases (***Figure 3G***). For rNTP discrimination, the k_{pol} for inserting a rGTP decreased 281-fold to 0.0037 s^{-1} and the K_d increased 49-fold to 0.89 mM (***Figure 3F***). This results in a nearly 14,000-fold decrease in the catalytic efficiency for the insertion of a rNTP compared to a dNTP (i.e. sugar discrimination, ***Figure 3H***). Because the cellular concentrations of rNTPs are around 50-fold higher on average than dNTPs, this sugar discrimination indicates telomerase will insert a rNTP ~1 in 280 insertion events in a cellular context (see discussion) (***Traut, 1994***).

The steric gate of telomerase

The high cellular concentration of rNTPs has resulted in most DNA polymerases evolving a structurally conserved active site residue which provides sugar discrimination by reducing the rate of rNTP insertion (***Brown and Suo, 2011***; ***Cavanaugh et al., 2010***; ***Nick McElhinny et al., 2010***). These residues are termed 'steric gates' because they clash with the 2'-OH of the incoming rNTP. Throughout the TERT catalytic cycle, we observed that Y256 rests in the minor groove of the DNA and is in position to clash with the 2'-OH of an incoming rNTP (***Figure 2E***). Therefore, we hypothesized this residue to be the steric gate in telomerase. To test this hypothesis, we performed pre-steady-state kinetics of rNTP insertion with the Y256A variant of TERT (***Figure 4A,B***). Compared to WT TERT, the insertion of a matched rGTP by Y256A showed a 1,490-fold increase in k_{pol} to 5.5 s^{-1} and a 12-fold decrease in K_d to 73 μM (***Figure 4C***). The results for TERT Y256A inserting a matched dGTP were similar to that of the rGTP, with a k_{pol} and K_d of 6.6 s^{-1} and 74 μM, respectively (***Figure 4D***). Thus, the sugar selectivity of TERT dropped from 14,000-fold between rGTP and dGTP for WT TERT to less than 2-fold for the Y256A TERT variant (***Figure 4E***). In other words, a single Y256A substitution increased rGTP insertion efficiency by 18,000-fold, abolishing almost all sugar discrimination. In a cellular environment, where rNTPs are at much higher concentrations than dNTPs, WT TERT would insert rGTP over 100-fold times less efficiently than dGTP. In contrast, TERT Y256A under cellular conditions would insert rGTP 77-fold times more efficiently than dGTP (***Figure 4F***; ***Traut, 1994***).

We next verified that this ablation in sugar discrimination was due to specific changes in the TERT active site rather than global rearrangements of the enzyme. To test for structural rearrangements, we crystallized the pre-nucleotide binary state of TERT Y256A (state A_6), and saw minimal structural differences compared to the WT protein (***Figure 4G–J***). The position of the primer terminus was not

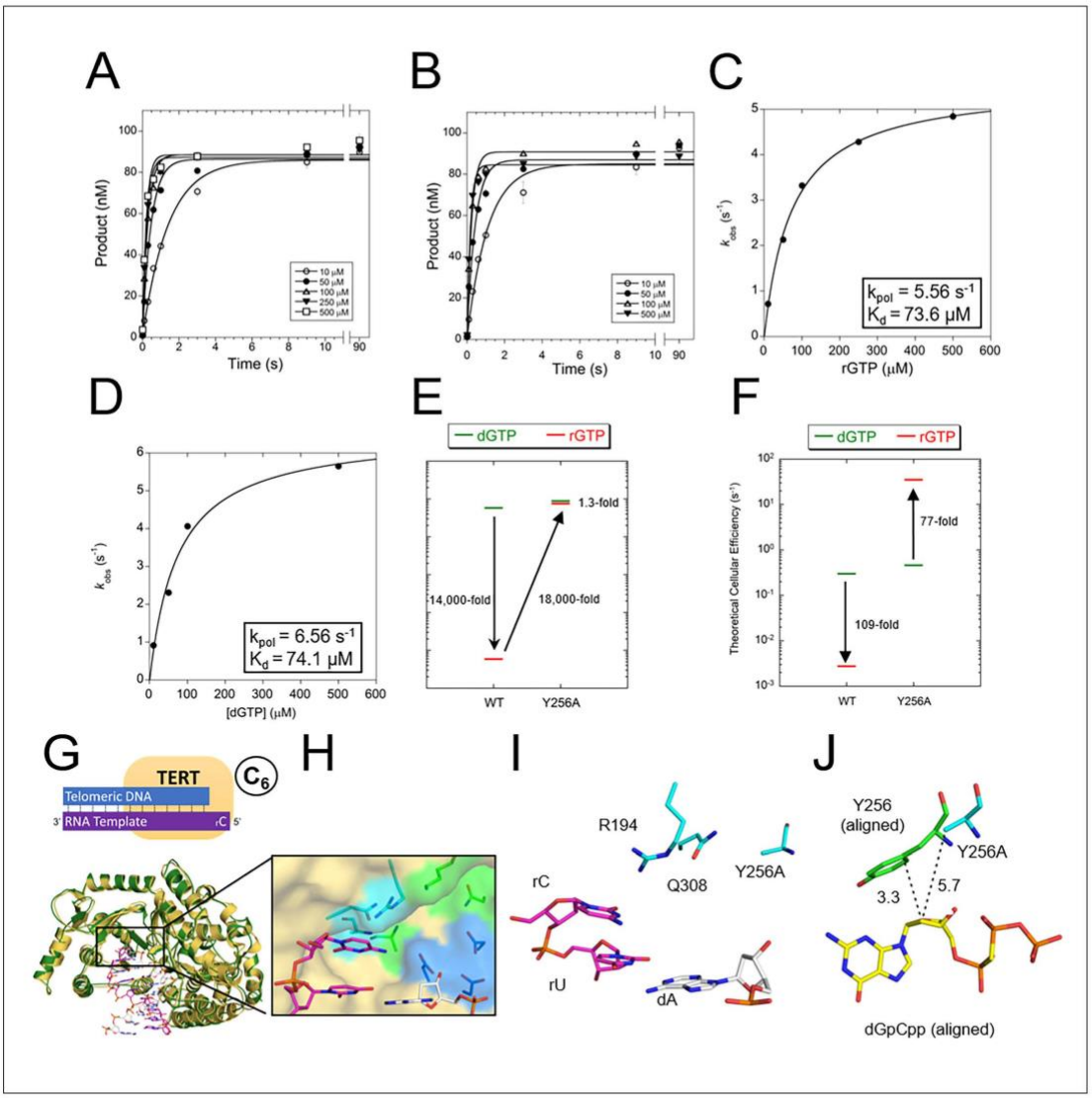

Figure 4. The steric gate of TERT prevents insertion of rNTPs. Pre-steady-state kinetics of tcTERT with its steric gate removed (i.e. Y256A) for both (**A**) rGTP insertion and (**B**) dGTP insertion (***Supplementary file 3***, Table 3a). Error bars represent standard deviation of the mean. These graphs were replotted and fit to ***Equation 2*** for (**C**) tcTERT Y256A inserting rGTP and (**D**) tcTERT Y256A inserting dGTP (**E**) A comparison of catalytic efficiencies (kpol/Kd) of both WT TERT and TERT Y256A for the insertion of dGTP (green) versus rGTP (red). (**F**) A comparison of TERT efficiencies adjusted for cellular nucleotide concentrations. (**G**) The prenucleotide binary complex of TERT Y256A (green) overlaid with the WT TERT prenucleotide binary complex structure (yellow). (**H, I**) The active site pocket of TERT Y256A, with DNA (white), RNA (purple), catalytic residues (blue), and nucleoside coordinating residues (cyan) shown. (**J**) The closest contacts to the C2 position of dGpCpp from the ternary structure (aligned and shown with yellow and green sticks) compared to Y256A tcTERT (cyan).

changed, and catalytic residues D251, D343, and D344 were in position to catalyze the nucleotidyl transferase reaction (***Figure 4H***). Upon closer examination of the active site pocket, the substitution of Y256 with alanine resulted in a more open nucleotide binding pocket (***Figure 4H and I***). The distance from the C2 carbon of the dGpCpp to residue 256 shifted from 3.3 Å in WT TERT to 5.7 Å in TERT Y256A, showing that the TERT Y256A has much more room to accommodate the 2'-OH (***Figure 4J***). Taken as a whole, these results indicate Y256 clashes with the 2'-OH of rNTPs to provide sugar discrimination and is the steric gate in telomerase.

To determine if human telomerase uses a similar mechanism to discriminate against rNTP insertion, we implemented human telomerase activity assays (***Xi and Cech, 2014***). In these assays, 1.5 telomeric repeats with the sequence TTAGGGTTAG were incubated with 50 µM of either all four dNTPs or all four rNTPs and purified 3xFLAG tagged human telomerase overexpressed with hTR. We performed these tests with both WT telomerase and a telomerase Y717A variant, which is the homologous residue to *tc*TERT Y256. WT telomerase showed robust primer extension in the presence of dNTPs, with ~10% of the primer extended into product over the course of 30 min (***Figure 5A,B***). Similarly, with all four dNTPs, the Y717A variant reached ~7% primer extension in the same amount of time (***Figure 5A,B***). In contrast, when we incubated WT telomerase with all four rNTPs rather than dNTPs, we observed very low (<1%) primer extension after 30 min, suggesting that human telomerase discriminates against rNTPs, similar to *tc*TERT (***Figure 5C,D***). When we performed the same telomeric extension assay with the steric gate variant (Y717A), we observed that the primer extension was increased 3-fold compared to WT *h*TERT in the presence of rNTPs (***Figure 5C,D***). These results indicate the conserved residue Y717 in *h*TERT (***Supplementary file 1***, Table 1a) is the steric gate in human telomerase. Interestingly, in both WT and Y717A telomerase, minimal insertion past the first telomeric repeat was observed, which suggests the presence of rNTPs in telomere strands may inhibit the telomerase translocation step (***Figure 5C***).

We next assessed if more subtle alterations in the nucleotide mixture would also cause inhibition of telomerase extension. By substituting one rNTP into the nucleotide mix at a time, we could determine the effects of inserting one, two, or three rNTPs inserted per repeat (with rATP, rUTP, and rGTP, respectively). In each case, telomerase processivity was reduced, with no bands evident past the second telomeric repeat (***Figure 5E***). The inhibitory effect seemed to depend on the number of rNTPs inserted per repeat, with rGTP presence showing the greatest inhibition. For the steric gate Y717A mutant telomerase, the effect of rNTPs on telomerase's processivity were much less pronounced. In the most extreme case of three rNTPs present per repeat, extension products are evident well into the second repeat, in contrast to the WT telomerase which had almost no insertion events (***Figure 5E***). We hypothesize that the rGTP insertion drastically inhibits WT telomerase because the first two insertions in the repeat are templated by rC. Therefore, the first event would need to be a rNTP insertion, followed by another rNTP insertion from a potentially unstable primer terminus. We are unable to decipher if inhibitory effects are due to the number of ribonucleotides per repeat, sequence-dependent inhibition, or a combination of both. In contrast to rGTP, telomerase is able to incorporate multiple repeats when rATP is present, albeit at a reduced efficiency compared to dNTPs (***Figure 5E***).

Within these primer extension activity assays, the effects of rNTP insertions can also be observed at the single nucleotide level. For rATP insertion with WT telomerase, we observed a buildup in substrates one nucleotide shorter than where the rNTP insertion would occur, composing ~60% of the total product formation (***Figure 5F***). This could be explained by the poor catalytic efficiency of telomerase for rATP insertion causing the enzyme to stall directly before the rATP insertion event. In contrast to the WT telomerase, the Y717A variant did not stall at the rATP insertion event. Interestingly, rNTPs inhibited translocation in both Y717A and WT telomerase, implying that telomerase possesses rNTP discrimination mechanisms beyond the level of single nucleotide incorporations (***Figure 5E,F***). The agreement between the results of the *tc*TERT and *h*TERT points towards a universal mechanism of sugar discrimination by any telomerase homolog with a tyrosine in this conserved position (***Supplementary file 1***, Table 1a).

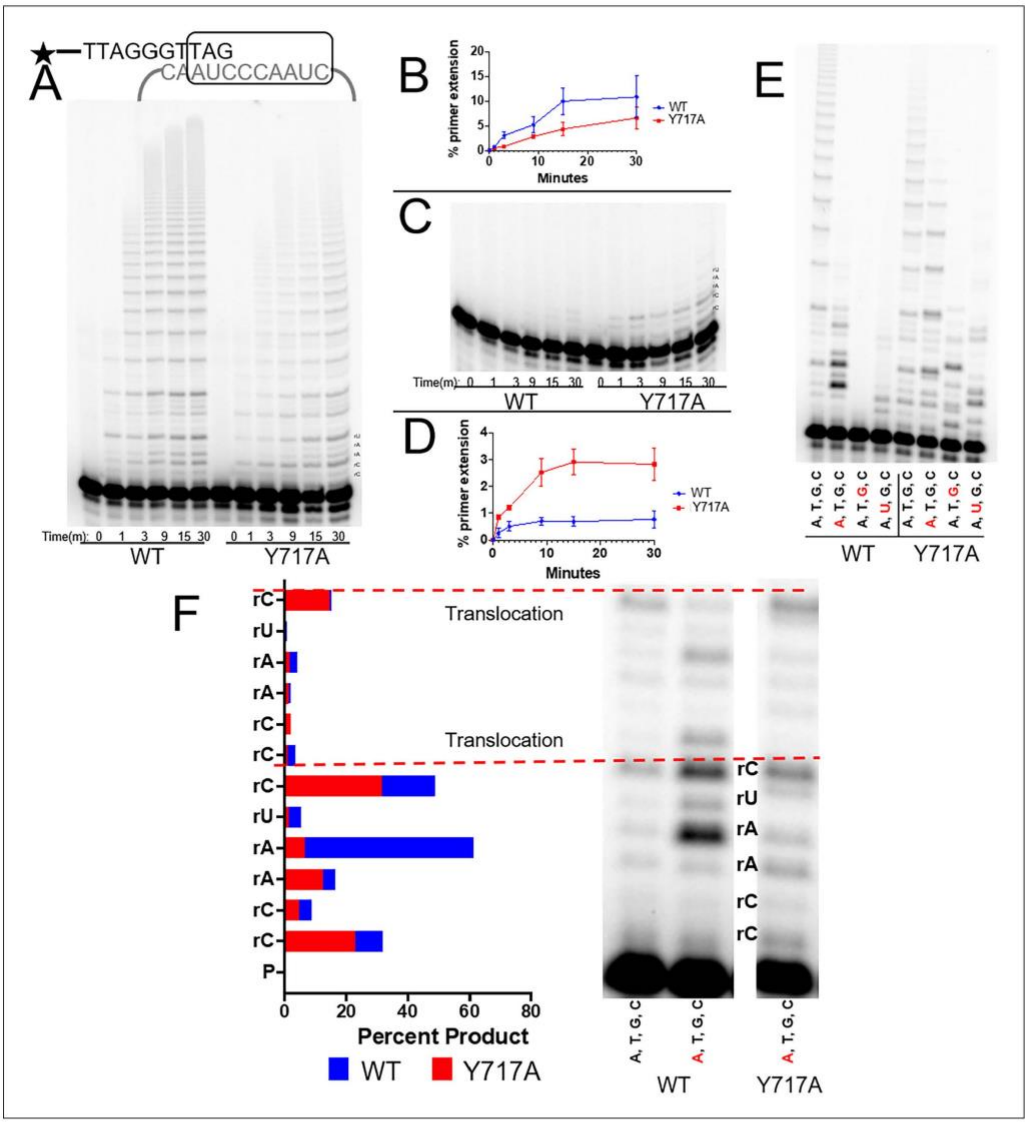

Figure 5. The steric gate of human telomerase. (**A**) Timecourse of primer extension with all four dNTPs by WT (left) and Y717A (right) human telomerase. (**B**) Quantification of percent primer extension, with WT shown as a blue line and the Y717A mutant shown in red. (**C**) Timecourse of primer extension with all four rNTPs for WT telomerase (left) and Y717A telomerase (right). (**D**) Results from the gel in panel C, quantified with the mutant telomerase shown in red and WT telomerase shown in blue. (**E**) Primer extension from both WT (left) and Y717A telomerase. Each lane contains either all four dNTPs, or three dNTP and one dNTP marked in red. (**F**) A close-up view of the first two telomeric repeats from selected lanes in panel E. rNTPs present in the mix are shown in red. Quantifications of each band in terms of percent product are also shown and labeled by the position of the telomerase templating base. The base marked by an asterisk is complementary to the rNTP in the solution. Error bars represent standard deviations of four biological replicates.

Discussion

Telomerase's catalytic cycle and fidelity

In this study, we characterized each step of the TERT catalytic cycle for single nucleotide insertion. We found that, in terms of global protein structure, minimal rearrangement is required to proceed through the catalytic cycle. This lack of rearrangement contrasts many other DNA polymerases and even HIV RT, which have been shown to undergo global shifts from an 'open' to a 'closed' state upon nucleotide binding (**Doublié et al., 1999**; **Sawaya et al., 1994**; **Schmidt et al., 2018**). Although it is unknown why the TERT catalytic core does not open and close, it may be because other complexities necessary for telomerase function limit the opening and closing from occurring, including the translocation step during repeat addition or the extensive interaction with its RNA component. Within the active site, we observed residues that encompass a cavity for the incoming nucleotide prior to binding, which then adjust to coordinate the incoming nucleotide after binding, and continue to stabilize the newly inserted base after its insertion in the product state. Many of the active site residues involved in carrying out the catalytic cycle are in similar positions as other DNA polymerases; a triad of three carboxylate containing residues such as D251, D343, and D344 in *tc*TERT is conserved in many DNA polymerases (**Steitz, 1999**). Interestingly, R194 and Q308 are in a similar structural location to R61 and Q38 of human DNA polymerase η, and both have been shown to be important in its catalytic cycle (**Biertümpfel et al., 2010**).

Our structural snapshots were complemented by kinetic studies, allowing us to understand how telomerase chooses right from wrong nucleotides; that is, selecting canonical dNTPs with correct base pairing compared to noncanonical rNTPs or mismatched base pairing (**Figure 6A**). Our experiments were carried out specifically with a single dGTP insertion using a 4 nucleotide overhang RNA template. While telomerase has been shown to exhibit moderate base and position-specific effects, our results indicate that the telomerase catalytic core generally exhibits moderate base selection fidelity, similar to that of X-family polymerases involved in DNA repair (**Chen et al., 2018**; **McCulloch and Kunkel, 2008**). Based on our kinetic values, we predict that telomerase inserts ~ 1 mismatch per each 10 kb of telomere extension. Because telomerase does not have a proofreading domain, misinsertions created by telomerase will remain as ssDNA during telomere elongation. Upon replication of the complementary strands by a DNA polymerase, the base that was a mismatch (in the context of telomerase) will become a matched base pair, and will not be a substrate for mismatch repair. Therefore, our fidelity measurement is predictive of cellular error rates in telomeric sequences. Accordingly, our predicted error rate agrees with telomeric error rates observed using telomere sequencing (**Lee et al., 2018**). While the downstream consequences of telomeric mismatches have not been studied in a biological context to our knowledge, they likely would disrupt G-quadruplex stability and inhibit shelterin protein binding, as both of these phenomena are dependent on DNA sequence (**Figure 6B**; **Burge et al., 2006**; **de Lange, 2005**).

Telomeric ribonucleotides

DNA polymerases insert millions of rNTPs into the genome during replication, because of a large disparity in nucleotide concentrations (rNTPs are ~50 fold more abundant in cells than dNTPs) (**Traut, 1994**). Telomerase also must select against this disparity; although telomerase is canonically thought to elongate telomeres with only dNTPs, our kinetics imply this is not the case. Instead, we predict that for every 10 kb of telomere extension, telomerase inserts ~ 40 rNTPs, which represents selectivity comparable to DNA polymerase β and DNA polymerase δ (**Brown and Suo, 2011**; **Cavanaugh et al., 2010**; **Nick McElhinny et al., 2010**). However, it is unknown whether ribonucleotides persist in telomeres, their biological consequences, and if they are addressed with ribonucleotide excision repair (RER), similar to other genomic ribonucleotides (**Sparks et al., 2012**). In our experiments with human telomerase, we found that even with increased rates of ribonucleotide insertion at the single nucleotide insertion level, telomere elongation was reduced via an inhibition of the translocation step (**Figure 5E,F**). This reduction was evident even with a single rNTP present in a telomeric repeat. Furthermore, previous studies have found telomeric substrates containing ribonucleotides can prevent or reduce extension of the first repeat depending on the number and position of ribonucleotides present in the DNA template (**Collins and Greider, 1995**). It is possible that telomerase pauses after inserting ribonucleotides to provide an opportunity for an extrinsic

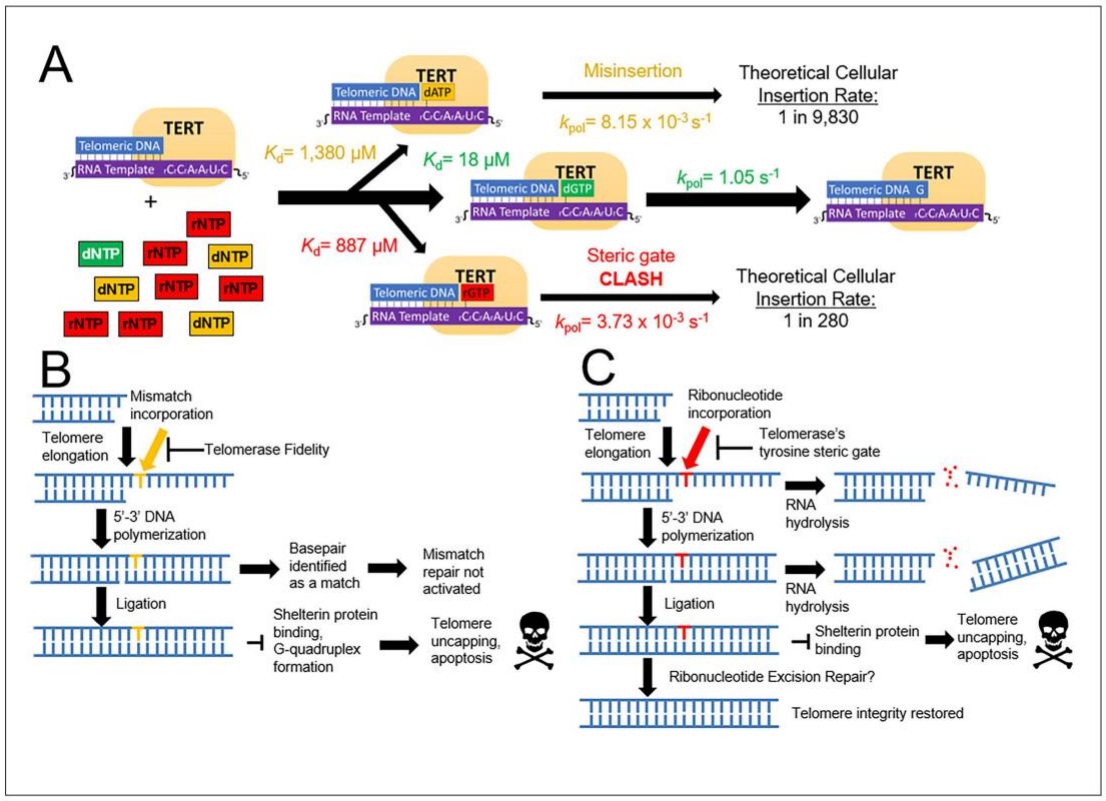

Figure 6. A model for how telomerase preserves telomeric integrity and biological implications. (**A**) The telomerase catalytic cycle, with matched dNTP (green), mismatched dNTPs (orange), and matched rNTPs (red). For each nucleotide path, kinetic parameters are labeled for each step and the insertion probability. (**B**) Downstream consequences of mismatch insertion by telomerase may include evasion of mismatch repair, reduced binding affinity for shelterin proteins, and altered stability of telomeric G quadruplexes. (**C**) Eventual consequences of rNTP insertion by telomerase. After insertion into telomeres, ribonucleotides could cause harsh consequences via hydrolysis, or disrupting telomere capping and stability. Ribonucleotides may also be removed by ribonucleotide excision repair.

proofreader or RER to remove the ribonucleotide before continuing telomeric elongation. Telomerase has previously been observed to halt telomeric extension after the insertion of other noncanonical nucleotides, particularly in the case of 8-oxodeoxyguanine triphosphate (8-oxodGTP) insertion (***Fouquerel et al., 2016***). Therefore, telomerase may stall on noncanonical nucleotides, such as 8-oxodGTP, for similar proofreading reasons.

Telomerase discrimination against rNTP insertion is important because ribonucleotides can cause multiple downstream problems for telomeric stability. These problems can arise from both the direct reduction of telomere length and from altering telomere structure. Because RNA is more vulnerable to hydrolysis than DNA, inserted ribonucleotides are more likely to hydrolyze, which would cause a telomeric single strand break (***Baumann and Cech, 2001***; ***de Lange, 2005***; ***Li and Breaker, 1999***). If the strand break occurred before the complementary strand of the telomere was copied and ligated to the genome, the elongating single strand would be released, and the entire telomere elongation process would need to be restarted (***Figure 6C***). Alternately, the inserted ribonucleotide may not hydrolyze, but instead persist within telomeres. The continued presence of ribonucleotides in telomeres may cause several structural aberrations, including altering G-quadruplex stability and

disrupting shelterin protein binding (**Fay et al., 2017**; **Nowotny et al., 2005**). If shelterin proteins are not able to bind to telomeres, telomere ends may be recognized as DNA damage, activating double strand break repair and causing disastrous biological consequences.

Subtle alterations to the telomeric nucleotides have previously been shown to cause telomeric disruption in a cellular context (**Fouquerel et al., 2016**; **Mender et al., 2015**; **Stefl et al., 2001**). Even changes of only one atom in a nucleotide, including replacing an oxygen of a guanine with a sulfur to form therapeutic 6-thioguanine nucleotides or the adduction of an extra oxygen onto guanine to form 8-oxoguanine nucleotides, have significant biological consequences in the context of telomerase. Therefore, in order to prevent this telomeric disruption, the telomerase active site appears to have evolved a high degree of stringency towards noncanonical nucleotides, including both rNTPs and mismatched dNTPs. This stringency was evident by the reduced telomere elongation efficiency with every variant tested; other mutations could also be identified with this system that show increases in telomere elongation efficiency. Our structural characterization of the telomerase catalytic cycle allowed us to efficiently modify the stringent active site of telomerase, generating a human telomerase variant that readily inserts rNTPs. The applications shown here highlight the potential of combining model TERTs with complementary human telomerase studies to further probe the telomerase catalytic mechanism and screen future telomerase-targeting therapeutics.

Materials and methods

Key resources table

Reagent type (species) or resource	Designation	Source or reference	Identifiers	Additional information
Gene (*Tribolium castaneum*)	tcTERT	GenScript		
Gene (*Homo sapiens*)	hTR	Gift from Dr. Tom Cech		
Gene (*Homo sapiens*)	hTERT	Gift from Dr. Tom Cech		
Strain, strain background (*Escherichia coli*)	One Shot BL21(DE3)pLysS Chemically Competent *E. coli*	Invitrogen	Cat# C606010	
Strain, strain background (*Escherichia coli*)	One Shot TOP10 Chemically Competent *E. coli*	Invitrogen	Cat# C606010	
Cell line (*Homo sapiens*)	HEK 293 T Cells, female	ATCC	RRID:CVCL_0063	Cells were acquired from ATCC, and have not since been tested for mycoplasma, as they were used for protein generation not biological assays
Transfected construct (*Homo sapiens*)	pSUPER-hTR	Gift from Dr. Tom Cech	N/A	
Transfected construct (*Homo sapiens*)	pVan107 3X FLAG hTERT	Gift from Dr. Tom Cech	N/A	
Recombinant DNA reagent	pET-28a(+) with *Tribolium* castaneum TERT	Genscript	N/A	
Sequence-based reagent	Primer for telomerase activity assays	IDT	N/A	5'-GGTCAGGT CAGGTCA-3'

Continued on next page

Continued

Reagent type (species) or resource	Designation	Source or reference	Identifiers	Additional information
Sequence-based reagent	RNA template for *tc*TERT kinetics	IDT	N/A	5′-rCrUrGrArCrCr UrGACCUGACC-3′
Sequence-based reagent	DNA primer for *tc*TERT kinetics	IDT	N/A	5′-/6-FAM/CCAG CCAGGTCAG-3′
Sequence-based reagent	RNA template for *tc*TERT crystallogarphy	IDT	N/A	5′- rUrGrArCrCrUrGr ArCrCrUrGrG rCrUrGrG-3′
Sequence-based reagent	DNA primer for *tc*TERT crystallogarphy	IDT	N/A	5′-GGTTAGGGT TAGGGTTAG-3′
Peptide, recombinant protein	T4 polynucleotide kinase	NEB	Cat# M0201S	
Peptide, recombinant protein	3X FLAG Peptide	Sigma Aldrich	Cat# F4799-4MG	
Chemical compound, drug	2′-deoxyguanosine-5′-[(α,β)-methyleno] triphosphate (dGpCpp)	Jena Biosciences	Cat# NU-431S	
Chemical compound, drug	γ−32P ATP	Perkin-Elmer	Cat# BLU0 02Z250UC	
Chemical compound, drug	2-methyl-2, 4-pentanediol	Hampton Research	Cat# HR2-627	
Software, algorithm	COOT	***Emsley and Cowtan (2004)***	https://www2.mrc-lmb.cam.ac.uk/personal/pemsley/coot/	RRID:SCR_014222
Software, algorithm	Phenix	***Adams et al., 2010***	https://www.phenix-online.org/	RRID:SCR_014224
Software, algorithm	XDS	***Kabsch (2010)***	http://xds.mpimf-heidelberg.mpg.de/	RRID:SCR_015652
Software, algorithm	MolProbity	***Chen et al. (2010)***	http://molprobity.biochem.duke.edu/	RRID:SCR_014226
Software, algorithm	ImageJ	***Schneider et al., 2012***	https://imagej.nih.gov/ij/	RRID:SCR_003070
Software, algorithm	Kaleidagraph	Synergy Software	http://www.synergy.com/wordpress_650164087/kaleidagraph/	RRID:SCR_014980
Software, algorithm	ImageQuant TL v8.1	GE Healthcare Life Sciences	http://www.gelifesciences.com/en/us	RRID:SCR_014246
Software, algorithm	PyMol	Schrödinger LLC	https://pymol.org/2/	RRID:SCR_000305
Other	Large scale expresion (LEX-48) bioreactor	Epiphyte	https://www.epiphyte3.com/LEX	
Other	HisTrap HP 5 mL column	GE healthcare Life Sciences	Cat# 17524801	

Continued on next page

Continued

Reagent type (species) or resource	Designation	Source or reference	Identifiers	Additional information
Other	POROS HS strong cation ion exchange resin	Thermo scientific	Cat# 1335906	
Other	G-25 spin columns	GE Healthcare Life Sciences	Cat #27532501	
Other	Sephacryl 16/60 S-200 HR Size Exclusion Chromatography column	GE Healthcare Life Sciences	Cat # 17116601	
Other	ANTI-FLAG M2 affinity gel agarose beads	Sigma Aldrich	Cat #A2220	

Nucleic acid sequences

To generate crystal structures of the TERT catalytic cycle, the following DNA sequences were utilized for all crystallization experiments: DNA primer of 5'-GGTCAGGTCAGGTCA-3' and the RNA template sequence 5'-rCrUrGrArCrCrUrGACCUGACC-3'. For kinetic studies, we utilized a DNA primer with a 5' label of 6-carboxyfluorescein (6-FAM), and the DNA sequence of 5'- CCAGCCAGGTCAG-3'. The RNA template used in kinetic reactions contained the sequence 5'- rUrGrArCrCrUrGrArCrC rUrGrGrCrUrGrG-3' and was not labeled. In each case, the oligonucleotides were resuspended in molecular biology grade water, and the concentration was calculated from their absorbance at 260 nm as measured on a NanoDrop microvolume spectrophotometer. Nucleic acid substrates for crystallography were annealed at an equimolar ratio, but nucleic acid substrates for our kinetic studies were annealed at a 1:1.2 molar ratio of labeled to unlabeled primer. We used a thermocycler to anneal all nucleic acid substrates, heating them to 90˚C for 2 min before cooling to 4˚C at a rate of 0.1˚C per second.

Expression and purification of *tc*TERT

We used previously published methods for *tc*TERT expression and purification, but implemented several modifications (***Gillis et al., 2008***). Briefly, we grew *tc*TERT in BL-21(DE3)pLysS cells using an Epiphyte3 LEX bioreactor at 37˚C until they reached an OD600 of 0.6–0.8, after which the temperature was dropped to 30˚C for 4–5 hr of protein production. Cells were harvested via centrifugation at 4000 x g until lysis. For TERT purification, we used buffers containing 0.75 M KCl and 10% glycerol for the capture step on Ni-NTA columns (GE Healthcare), and then further purified our sample with cation exchange on a POROS HS column (Thermo Fisher), using a salt gradient of 0.5 M KCl to 1.5 M KCl. Then, we cleaved the hexahistadine tag with Tobacco etch virus protease before purifying the cut tag from the protein with another run on our Ni-NTA columns. Finally, we used a slightly different buffer for the our size exclusion chromatography (Sephacryl S-200 16/60, GE Helathcare), containing 50 mM Tris-HCl, pH 7.5, 10% glycerol, 0.8 M KCl and 1 mM Tris(2-carboxyethyl)phosphine (TCEP). Resultant *tc*TERT was concentrated down to 18 mg mL ^{1} prior to crystallography, and stored at 4˚C (***Gillis et al., 2008***).

Crystallization of *tc*TERT

Prior to crystallization, we complexed *tc*TERT with its nucleic acid substrate by mixing them at a 1:1.2 ratio of protein to DNA. To increase protein solubility, we included 520 mM KCl when preparing to mix *tc*TERT with its nucleic acid substrate. We then used sitting drop vapor diffusion to grow binary complex crystals in conditions containing 11% isopropanol, 0.1 M KCl, 25 mM $MgCl_2$, and 50 mM sodium cacodylate pH 6.5. Volume ratios for the optimal crystal growth were optimized to 2.3 µL *tc*TERT binary complex crystals + 1.7 µL of our crystallization condition, to make 4 µL total. For the ternary complex crystals, we used the same conditions, but included 0.69 mM dGpCpp (Jena Biosciences), the next matched incoming nucleotide in the sequence. Finally, for the product complex, we formed a DNA strand one nucleotide longer by incubating 2.5 mM dGTP with *tc*TERT and

its nucleic acid substrate, allowing the reaction to occur at 22˚C for 30 min prior to setting up crystallization drops. In all cases, crystals were transferred to a cryosolution containing 80% reservoir solution and 20% 2-methyl-2,4-pentanediol by volume before flash cooling them in liquid nitrogen.

Data collection and refinement

All datasets were collected at a wavelength of 1.00 Å, using the 4.2.2 synchrotron beamline at the Advanced Light Source of the Ernest Orlando Lawrence Berkeley National Laboratory. Datasets were indexed and scaled using XDS (RRID:SCR_015652) (**Kabsch, 2010**; **Winn et al., 2011**). Initial models were generated using molecular replacement in PHENIX (RRID:SCR_014224), using a previously published *tc*TERT structure with an alternate substrate, PDB code 3KYL (**Adams et al., 2010**; **Mitchell et al., 2010**). After a solution was found, all DNA and RNA bases were built in the prenucleotide complex, and the resultant structure was then used for further molecular replacements other structures. Model building was accomplished with Coot (RRID:SCR_014222) and validated with MolProbity (RRID:SCR_014226) (**Chen et al., 2010**; **Emsley and Cowtan, 2004**). For structures $\geq$ 3 Å resolution, both secondary structure restraints and torsional restraints from the prenucleotide binary structure were used to prevent overmodeling. All refinements were done using PHENIX, and figures were generated using PyMOL (RRID:SCR_000305, Schrödinger LLC). For each of the structures, Ramachandran analysis revealed a minimum of 100% of non-glycine residues occupied allowed regions and at least 93% occupied favored regions.

Pre-steady-state kinetic characterization of *tc*TERT

Pre-steady-state kinetic parameters of *tc*TERT were obtained using established pre-steady-state kinetics protocols for DNA polymerases, also known as single turnover kinetics (**Beard et al., 2014**; **Powers and Washington, 2017**). Briefly, we preincubated 2 µM *tc*TERT with 200 nM annealed DNA:RNA hybrid substrate, with a 6-FAM label on the 5' end of the DNA component. We then used a KinTek RQF-3 (a rapid quench-flow instrument) to mix equal ratios of the incoming nucleotide triphosphate of interest and 10 mM $MgCl_2$ with the existing mix of *tc*TERT and its DNA:RNA hybrid substrate. Reactions were run at 37˚C and quenched at various timepoints (ranging from 10 ms to 700 s) with 100 mM EDTA pH 7.5. In each case, the conditions used for each reaction were: 25 mM TRIS pH 7.5, 0.05 mg mL ^{1} Bovine Serum Albumin, 1 mM dithiothreitol, 10% glycerol, 200 mM KCl, 1 µM *tc*TERT, 100 nM annealed DNA:RNA hybrid substrate, and varying concentrations of the nucleotide triphosphate of interest. The samples were transferred to a DNA gel loading buffer, containing 100 mM EDTA, 80% deionized formamide, 0.25 mg ml ^{1} bromophenol blue and 0.25 mg ml ^{1} xylene cyanol. For the generation of data sets that had a minimum time point of 12 s or greater, a LabDoctor heating block was used in lieu of the KinTec RQF-3, and quenching was accomplished using a solution of DNA gel loading buffer. These mixes were then incubated at 95˚C for 5 mins and loaded onto a 21% denaturing polyacrylamide gel. These gels were run at 700 V, 60 A, and 30 W at 30˚C in order to separate the reaction product from its substrate.

Gels were scanned and imaged using a GE Typhoon FLA 9500 imager, and the ratios of product to substrate were quantified using ImageJ (RRID:SCR_003070) (**Schneider et al., 2012**). Means and standard deviations were taken from at least three technical replicates were calculated and graphed using KaleidaGraph (RRID:SCR_014980). Plots of product formation over time were fit to the exponential ***Equation 1*** to determine k_{obs} values:

$$[P] = A\left(1 - e^{-k_{obs}t}\right) \quad (1)$$

[P] is the concentration of the product, A is the target engagement (amplitude), and t is the reaction time. After k_{obs} values were determined for multiple nucleotide triphosphate concentrations, the data was replotted to compare k_{obs} to concentration of nucleotide triphosphate, and fit to ***Equation 2***:

$$k_{obs} = \frac{k_{pol}[NTP]}{K_d + [NTP]} \quad (2)$$

k_{pol} represents the theoretical maximum value of k_{obs}, and [NTP] represents the concentration of the nucleotide of interest.

Telomerase expression

HEK293T cells were used to overexpress hTR and 3 × FLAG tagged human telomerase reverse transcriptase (hTERT) genes in pSUPER-hTR and pVan107, respectively. Cells were grown to 90% confluency in Dulbecco's modified Eagle's medium (Gibco) supplemented with 10% High Quality FBS (Hyclone) and 1% penicillin-streptomycin (Corning) at 37˚C and 5% CO2. Cells were transfected with 10 µg of pSUPER-hTR plasmid and 2.5 µg of pVan107 hTERT plasmid diluted in 625 µl of Opti-MEM (Gibco) using 25 µl of Lipofectamine 2000 (ThermoFisher) diluted in 625 µl of Opti-MEM. Cells were cultured for 48 hr post-transfection, and then were trypsinized and washed with phosphate-buffered saline and lysed in CHAPS lysis buffer buffer (10 mM Tris-HCl, 1 mM $MgCl_2$, 1 mM EDTA, 0.5% CHAPS, 10% glycerol, 5 mM β-mercaptoethanol, 120 U RNasin Plus (Promega), 1 µg/ml each of pepstatin, aprotinin, leupeptin and chymostatin, and 1 mM AEBSF) for 30 min at 4˚C. Cell lysate supernatant was then flash frozen and stored at −80˚C.

Telomerase purification

Telomerase was purified via the 3xFLAG tag on hTERT encoded pVan107 using ANTI-FLAG M2 affinity gel agarose beads (Sigma Aldrich), as described previously with some modification (***Fouquerel et al., 2016***). An 80 µL bead slurry (per T75 flask) was washed three times with 10 volumes of 1X human telomerase buffer in 30% glycerol with 1 min centrifugation steps at 3500 r.p.m. at 4˚C. The bead slurry was added to the lysate and nutated for 4–6 hr at 4˚C. The beads were harvest by 1 min centrifugation at 3500 r.p.m, and washed 3X with 1X human telomerase buffer with 30% glycerol. Telomerase was eluted from the beads using 2x the bead volume of 250 µg/mL 3X FLAG peptide (Sigma Aldrich) in 1X telomerase buffer with 150 mM KCl. The bead slurry was nutated for 30 min at 4˚C. The eluted telomerase was collected using Mini Bio-Spin Chromatography columns (Bio-Rad). Samples were flash frozen and stored a −80˚C.

32P-end-labeling of DNA primers

50 pmol of PAGE purified DNA primer GGTTAGGGTTAGGGTTAG (IDT) was labeled with γ−32P ATP (Perkin Elmer) using T4 polynucleotide kinase (NEB) in 1X PNK Buffer (70 mM Tris-HCl, pH 7.6, 10 mM MgCL2, 5 mM DTT) in a 20 uL reaction volume. The reaction was incubated for 1 hr at 37˚C followed by heat inactivation at 65˚C for 20 min. G-25 spin columns (GE Healthcare) were used to purify the end labeled primer.

Telomerase activity assay

The telomerase assay was as previously described. Reactions contained 1x human telomerase buffer, 5 nM of 32P-end-labeled primer and 50 µM dNTP or rNTP mix as indicated in the figure legends. Each reaction was performed with four biological replicates. The reactions were started by the addition of 3 µL of immunopurified telomerase eluent, incubated at 37˚C for a specified time course, then terminated with 2 µL of 0.5 mM EDTA and heat inactivated at 65˚C for 20 min. An equal volume of loading buffer (94% formamide, 0.1 × Tris borate-EDTA [TBE], 0.1% bromophenol blue, 0.1% xylene cyanol) was added to the reaction eluent from the G-25 spin column. The samples were heat denatured for 10 min at 100˚C and loaded onto a 14% denaturing acrylamide gel (7M urea, 1x TBE) and electrophoresed for 90 min at constant 38W. Samples were imaged using a Typhoon phosphorimager (GE Healthcare). Percent primer extension was quantitated using ImageQuant (RRID:SCR_014246).

Crystallographic statistics

Resolution of our crystal structures was determined using correlation coefficients ($CC_{1/2}$), with the highest resolution shell containing a $CC_{1/2}$ value of greater than 0.3 (***Supplementary file 2***, Table 2a). During refinement, the statistics of R_{work} and R_{free}, as calculated by PHENIX, were used to identify a model's fit to electron density. See ***Supplementary file 2***, Table 2a for more details of these parameters for each dataset.

Data resources

Accession numbers for models reported are PDB: 6USO, 6USP, 6USQ, and 6USR.

Acknowledgements

We thank Jay Nix (Molecular Biology Consortium 4.2.2 beamline at Advanced Light Source) for aid in remote data collection and help with data analysis. This research used resources of the Advanced Light Source, which is a Department of Energy Office of Science user facility under Contract DE-AC02-05CH11231. We thank Amy Whitaker (University of Kansas Medical Center) for helpful discussion and assistance with the manuscript preparation, and Scott Lovell (University of Kansas) for his advice and help with crystal optimization. This research was supported by the National Institute of General Medical Science [R35-GM128562 to BDF, MAS, GAW, THK], the National Institute of Environmental Health Sciences [R35-ES030396 to PLO, SLS, SAJ], the Madison and Lila Self Graduate Fellowship [to MAS], and a NIH Clinical and Translational Science Award grant (UL1 TR002366) awarded to the University of Kansas Medical Center.

Additional information

Funding

Funder	Grant reference number	Author
National Institute of General Medical Sciences	R35-ES030396	Patricia L Opresko Samantha L Sanford Samuel A Johnson
National Institute of Environmental Health Sciences	R35-GM128562	Bret D Freudenthal Matthew A Schaich Griffin A Welfer Thu H Khoang
University of Kansas	Madison and Lila Self Graduate Fellowship	Matthew A Schaich

The funders had no role in study design, data collection and interpretation, or the decision to submit the work for publication.

Author contributions

Matthew A Schaich, Conceptualization, Data curation, Formal analysis, Investigation, Writing - original draft, Writing - review and editing; Samantha L Sanford, Griffin A Welfer, Samuel A Johnson, Thu H Khoang, Data curation; Patricia L Opresko, Supervision, Writing - review and editing; Bret D Freudenthal, Conceptualization, Supervision, Funding acquisition, Writing - original draft, Writing - review and editing

Author ORCIDs

Matthew A Schaich https://orcid.org/0000-0001-6771-5623
Bret D Freudenthal https://orcid.org/0000-0003-1449-4710

Decision letter and Author response

Decision letter https://doi.org/10.7554/eLife.55438.sa1
Author response https://doi.org/10.7554/eLife.55438.sa2

Additional files

Supplementary files

- Supplementary file 1. Table 1a. The conservation and function of TERT active site residues. Table 1b. Telomerase architecture of five different TERTs, including *Homo sapiens, Tetrahymena thermophila,Saccharomyces cerevisiae* and *Tribolium castaneum*. Data from this table used from: (***Garforth et al., 2006***; ***Gillis et al., 2008***; ***Jiang et al., 2018***; ***Nguyen et al., 2018***; ***Niederer and Zappulla, 2015***).[1]TR = Telomerase RNA component*TEN = N terminal domain*TRBD = Telomerase RNA binding domain*RT = Reverse transcriptase domain*CTE = C terminal extension*IFD = Insertion in fingers domain[2] This IFD is truncated compared to other TERTs.

- Supplementary file 2. Table 2a. Data collection and refinement statistics for *tc*TERT structures.
- Supplementary file 3. Table 3a. Kinetic parameters and errors for *tc*TERT pre-steady-state kinetics of single nucleotide incorporation. Table 3b. Full kinetic parameters of each curve used to generate K_{obs} and target engagement values in *tc*TERT pre-steady-state kinetics
- Transparent reporting form

Data availability

Diffraction data have been deposited in PDB under the accession code 6USO, 6USP, 6USQ, and 6US.

The following datasets were generated:

Author(s)	Year	Dataset title	Dataset URL	Database and Identifier
Freudenthal BD, Schaich MA	2020	Telomerase Reverse Transcriptase prenucleotide binary complex, TERT:DNA	https://www.rcsb.org/structure/6USO	RCSB Protein Data Bank, 6USO
Freudenthal BD, Schaich MA	2020	Telomerase Reverse Transcriptase ternary complex, TERT:DNA: dGpCpp	https://www.rcsb.org/structure/6USR	RCSB Protein Data Bank, 6USR
Freudenthal BD, Schaich MA	2020	Telomerase Reverse Transcriptase product complex, TERT:DNA	https://www.rcsb.org/structure/6USP	RCSB Protein Data Bank, 6USP
Freudenthal BD, Schaich MA, Khoang TH	2020	Telomerase Reverse Transcriptase binary complex with Y256A mutation, TERT:DNA	https://www.rcsb.org/structure/6USQ	RCSB Protein Data Bank, 6USQ

References

Adams PD, Afonine PV, Bunkóczi G, Chen VB, Davis IW, Echols N, Headd JJ, Hung LW, Kapral GJ, Grosse-Kunstleve RW, McCoy AJ, Moriarty NW, Oeffner R, Read RJ, Richardson DC, Richardson JS, Terwilliger TC, Zwart PH. 2010. *PHENIX*: a comprehensive Python-based system for macromolecular structure solution. *Acta Crystallographica Section D Biological Crystallography* **66**:213–221. DOI: https://doi.org/10.1107/S0907444909052925, PMID: 20124702

Basel-Vanagaite L, Dokal I, Tamary H, Avigdor A, Garty BZ, Volkov A, Vulliamy T. 2008. Expanding the clinical phenotype of autosomal dominant dyskeratosis congenita caused by TERT mutations. *Haematologica* **93**:943–944. DOI: https://doi.org/10.3324/haematol.12317, PMID: 18460650

Batra VK, Beard WA, Shock DD, Krahn JM, Pedersen LC, Wilson SH. 2006. Magnesium-induced assembly of a complete DNA polymerase catalytic complex. *Structure* **14**:757–766. DOI: https://doi.org/10.1016/j.str.2006.01.011, PMID: 16615916

Baumann P, Cech TR. 2001. Pot1, the putative telomere end-binding protein in fission yeast and humans. *Science* **292**:1171–1175. DOI: https://doi.org/10.1126/science.1060036, PMID: 11349150

Beard WA, Shock DD, Batra VK, Prasad R, Wilson SH. 2014. Substrate-induced DNA polymerase β activation. *Journal of Biological Chemistry* **289**:31411–31422. DOI: https://doi.org/10.1074/jbc.M114.607432, PMID: 25261471

Biertümpfel C, Zhao Y, Kondo Y, Ramón-Maiques S, Gregory M, Lee JY, Masutani C, Lehmann AR, Hanaoka F, Yang W. 2010. Structure and mechanism of human DNA polymerase eta. *Nature* **465**:1044–1048. DOI: https://doi.org/10.1038/nature09196, PMID: 20577208

Blackburn EH, Gall JG. 1978. A tandemly repeated sequence at the termini of the extrachromosomal ribosomal RNA genes in Tetrahymena. *Journal of Molecular Biology* **120**:33–53. DOI: https://doi.org/10.1016/0022-2836(78)90294-2, PMID: 642006

Blasco MA. 2005. Telomeres and human disease: ageing, Cancer and beyond. *Nature Reviews Genetics* **6**:611–622. DOI: https://doi.org/10.1038/nrg1656, PMID: 16136653

Brown JA, Zhang L, Sherrer SM, Taylor J-S, Burgers PMJ, Suo Z. 2010. Pre-Steady-State kinetic analysis of truncated and Full-Length *Saccharomyces cerevisiae* DNA polymerase eta. *Journal of Nucleic Acids* **2010**:1–11. DOI: https://doi.org/10.4061/2010/871939

Brown JA, Suo Z. 2011. Unlocking the sugar "steric gate" of DNA polymerases. *Biochemistry* **50**:1135–1142. DOI: https://doi.org/10.1021/bi101915z, PMID: 21226515

Burge S, Parkinson GN, Hazel P, Todd AK, Neidle S. 2006. Quadruplex DNA: sequence, topology and structure. *Nucleic Acids Research* **34**:5402–5415. DOI: https://doi.org/10.1093/nar/gkl655, PMID: 17012276

Cavanaugh NA, Beard WA, Wilson SH. 2010. DNA polymerase beta ribonucleotide discrimination: insertion, misinsertion, extension, and coding. *The Journal of Biological Chemistry* **285**:24457–24465. DOI: https://doi.org/10.1074/jbc.M110.132407, PMID: 20519499

Chen VB, Arendall WB, Headd JJ, Keedy DA, Immormino RM, Kapral GJ, Murray LW, Richardson JS, Richardson DC. 2010. *MolProbity*: all-atom structure validation for macromolecular crystallography. *Acta Crystallographica Section D Biological Crystallography* **66**:12–21. DOI: https://doi.org/10.1107/S0907444909042073, PMID: 20057044

Chen Y, Podlevsky JD, Logeswaran D, Chen JJ. 2018. A single nucleotide incorporation step limits human telomerase repeat addition activity. *The EMBO Journal* **37**:e97953. DOI: https://doi.org/10.15252/embj.201797953, PMID: 29440226

Collins K, Greider CW. 1995. Utilization of ribonucleotides and RNA primers by Tetrahymena telomerase. *The EMBO Journal* **14**:5422–5432. DOI: https://doi.org/10.1002/j.1460-2075.1995.tb00226.x, PMID: 7489731

de Lange T. 2005. Shelterin: the protein complex that shapes and safeguards human telomeres. *Genes & Development* **19**:2100–2110. DOI: https://doi.org/10.1101/gad.1346005, PMID: 16166375

Diaz de Leon A, Cronkhite JT, Katzenstein AL, Godwin JD, Raghu G, Glazer CS, Rosenblatt RL, Girod CE, Garrity ER, Xing C, Garcia CK. 2010. Telomere lengths, pulmonary fibrosis and telomerase (TERT) mutations. *PLOS ONE* **5**:e10680. DOI: https://doi.org/10.1371/journal.pone.0010680, PMID: 20502709

Doublié S, Sawaya MR, Ellenberger T. 1999. An open and closed case for all polymerases. *Structure* **7**:R31–R35. DOI: https://doi.org/10.1016/S0969-2126(99)80017-3, PMID: 10368292

Emsley P, Cowtan K. 2004. *Coot*: model-building tools for molecular graphics. *Acta Crystallographica. Section D, Biological Crystallography* **60**:2126–2132. DOI: https://doi.org/10.1107/S0907444904019158, PMID: 15572765

Fay MM, Lyons SM, Ivanov P. 2017. RNA G-Quadruplexes in biology: principles and molecular mechanisms. *Journal of Molecular Biology* **429**:2127–2147. DOI: https://doi.org/10.1016/j.jmb.2017.05.017, PMID: 28554731

Fouquerel E, Lormand J, Bose A, Lee HT, Kim GS, Li J, Sobol RW, Freudenthal BD, Myong S, Opresko PL. 2016. Oxidative guanine base damage regulates human telomerase activity. *Nature Structural & Molecular Biology* **23**:1092–1100. DOI: https://doi.org/10.1038/nsmb.3319, PMID: 27820808

Garforth SJ, Wu YY, Prasad VR. 2006. Structural features of mouse telomerase RNA are responsible for the lower activity of mouse telomerase versus human telomerase. *Biochemical Journal* **397**:399–406. DOI: https://doi.org/10.1042/BJ20060456, PMID: 16669789

Gillis AJ, Schuller AP, Skordalakes E. 2008. Structure of the tribolium castaneum telomerase catalytic subunit TERT. *Nature* **455**:633–637. DOI: https://doi.org/10.1038/nature07283, PMID: 18758444

Gleghorn ML, Davydova EK, Basu R, Rothman-Denes LB, Murakami KS. 2011. X-ray crystal structures elucidate the nucleotidyl transfer reaction of transcript initiation using two nucleotides. *PNAS* **108**:3566–3571. DOI: https://doi.org/10.1073/pnas.1016691108, PMID: 21321236

Greider CW, Blackburn EH. 1987. The telomere terminal transferase of Tetrahymena is a ribonucleoprotein enzyme with two kinds of primer specificity. *Cell* **51**:887–898. DOI: https://doi.org/10.1016/0092-8674(87)90576-9, PMID: 3319189

Hayflick L, Moorhead PS. 1961. The serial cultivation of human diploid cell strains. *Experimental Cell Research* **25**:585–621. DOI: https://doi.org/10.1016/0014-4827(61)90192-6, PMID: 13905658

Jafri MA, Ansari SA, Alqahtani MH, Shay JW. 2016. Roles of telomeres and telomerase in Cancer, and advances in telomerase-targeted therapies. *Genome Medicine* **8**:69. DOI: https://doi.org/10.1186/s13073-016-0324-x, PMID: 27323951

Jiang J, Wang Y, Sušac L, Chan H, Basu R, Zhou ZH, Feigon J. 2018. Structure of telomerase with telomeric DNA. *Cell* **173**:1179–1190. DOI: https://doi.org/10.1016/j.cell.2018.04.038, PMID: 29775593

Kabsch W. 2010. XDS. *Acta Crystallographica. Section D, Biological Crystallography* **66**:125–132. DOI: https://doi.org/10.1107/S0907444909047337, PMID: 20124692

Kim NW, Piatyszek MA, Prowse KR, Harley CB, West MD, Ho PL, Coviello GM, Wright WE, Weinrich SL, Shay JW. 1994. Specific association of human telomerase activity with immortal cells and Cancer. *Science* **266**:2011–2015. DOI: https://doi.org/10.1126/science.7605428, PMID: 7605428

Lee M, Teber ET, Holmes O, Nones K, Patch AM, Dagg RA, Lau LMS, Lee JH, Napier CE, Arthur JW, Grimmond SM, Hayward NK, Johansson PA, Mann GJ, Scolyer RA, Wilmott JS, Reddel RR, Pearson JV, Waddell N, Pickett HA. 2018. Telomere sequence content can be used to determine ALT activity in tumours. *Nucleic Acids Research* **46**:4903–4918. DOI: https://doi.org/10.1093/nar/gky297, PMID: 29718321

Li Y, Breaker RR. 1999. Kinetics of RNA degradation by specific base catalysis of transesterification involving the 2′-Hydroxyl Group. *Journal of the American Chemical Society* **121**:5364–5372. DOI: https://doi.org/10.1021/ja990592p

McCulloch SD, Kunkel TA. 2008. The fidelity of DNA synthesis by eukaryotic replicative and translesion synthesis polymerases. *Cell Research* **18**:148–161. DOI: https://doi.org/10.1038/cr.2008.4, PMID: 18166979

Mender I, Gryaznov S, Dikmen ZG, Wright WE, Shay JW. 2015. Induction of telomere dysfunction mediated by the telomerase substrate precursor 6-thio-2′-deoxyguanosine. *Cancer Discovery* **5**:82–95. DOI: https://doi.org/10.1158/2159-8290.CD-14-0609, PMID: 25516420

Meyerson M. 1998. Telomerase enzyme activation and human cell immortalization. *Toxicology Letters* **102-103**:41–45. DOI: https://doi.org/10.1016/S0378-4274(98)00278-1, PMID: 10022230

Mitchell M, Gillis A, Futahashi M, Fujiwara H, Skordalakes E. 2010. Structural basis for telomerase catalytic subunit TERT binding to RNA template and telomeric DNA. *Nature Structural & Molecular Biology* **17**:513–518. DOI: https://doi.org/10.1038/nsmb.1777, PMID: 20357774

Moyzis RK, Buckingham JM, Cram LS, Dani M, Deaven LL, Jones MD, Meyne J, Ratliff RL, Wu JR. 1988. A highly conserved repetitive DNA sequence, (TTAGGG)n, present at the telomeres of human chromosomes. *PNAS* **85**:6622–6626. DOI: https://doi.org/10.1073/pnas.85.18.6622, PMID: 3413114

Nandakumar J, Podell ER, Cech TR. 2010. How telomeric protein POT1 avoids RNA to achieve specificity for single-stranded DNA. *PNAS* **107**:651–656. DOI: https://doi.org/10.1073/pnas.0911099107, PMID: 20080730

Nelson ND, Bertuch AA. 2012. Dyskeratosis congenita as a disorder of telomere maintenance. *Mutation Research/Fundamental and Molecular Mechanisms of Mutagenesis* **730**:43–51. DOI: https://doi.org/10.1016/j.mrfmmm.2011.06.008

Nguyen THD, Tam J, Wu RA, Greber BJ, Toso D, Nogales E, Collins K. 2018. Cryo-EM structure of substrate-bound human telomerase holoenzyme. *Nature* **557**:190–195. DOI: https://doi.org/10.1038/s41586-018-0062-x, PMID: 29695869

Nick McElhinny SA, Watts BE, Kumar D, Watt DL, Lundström EB, Burgers PM, Johansson E, Chabes A, Kunkel TA. 2010. Abundant ribonucleotide incorporation into DNA by yeast replicative polymerases. *PNAS* **107**:4949–4954. DOI: https://doi.org/10.1073/pnas.0914857107, PMID: 20194773

Niederer RO, Zappulla DC. 2015. Refined secondary-structure models of the core of yeast and human telomerase RNAs directed by SHAPE. *RNA* **21**:254–261. DOI: https://doi.org/10.1261/rna.048959.114, PMID: 25512567

Nowotny M, Gaidamakov SA, Crouch RJ, Yang W. 2005. Crystal structures of RNase H bound to an RNA/DNA hybrid: substrate specificity and metal-dependent catalysis. *Cell* **121**:1005–1016. DOI: https://doi.org/10.1016/j.cell.2005.04.024, PMID: 15989951

Olovnikov AM. 1973. A theory of marginotomy the incomplete copying of template margin in enzymic synthesis of polynucleotides and biological significance of the phenomenon. *Journal of Theoretical Biology* **41**:181–190. DOI: https://doi.org/10.1016/0022-5193(73)90198-7, PMID: 4754905

Petrova OA, Mantsyzov AB, Rodina EV, Efimov SV, Hackenberg C, Hakanpää J, Klochkov VV, Lebedev AA, Chugunova AA, Malyavko AN, Zatsepin TS, Mishin AV, Zvereva MI, Lamzin VS, Dontsova OA, Polshakov VI. 2018. Structure and function of the N-terminal domain of the yeast telomerase reverse transcriptase. *Nucleic Acids Research* **46**:1525–1540. DOI: https://doi.org/10.1093/nar/gkx1275, PMID: 29294091

Powers KT, Washington MT. 2017. Analyzing the catalytic activities and interactions of eukaryotic translesion synthesis polymerases. *Methods in Enzymology* **592**:329–356. DOI: https://doi.org/10.1016/bs.mie.2017.04.002, PMID: 28668126

Ramakrishnan S, Sharma HW, Farris AD, Kaufman KM, Harley JB, Collins K, Pruijn GJ, van Venrooij WJ, Martin ML, Narayanan R. 1997. Characterization of human telomerase complex. *PNAS* **94**:10075–10079. DOI: https://doi.org/10.1073/pnas.94.19.10075, PMID: 9294165

Sawaya MR, Pelletier H, Kumar A, Wilson SH, Kraut J. 1994. Crystal structure of rat DNA polymerase beta: evidence for a common polymerase mechanism. *Science* **264**:1930–1935. DOI: https://doi.org/10.1126/science.7516581, PMID: 7516581

Sayed ME, Cheng A, Yadav GP, Ludlow AT, Shay JW, Wright WE, Jiang QX. 2019. Catalysis-dependent inactivation of human telomerase and its reactivation by intracellular telomerase-activating factors (iTAFs). *Journal of Biological Chemistry* **294**:11579–11596. DOI: https://doi.org/10.1074/jbc.RA118.007234, PMID: 31186347

Schmidt JC, Zaug AJ, Cech TR. 2016. Live cell imaging reveals the dynamics of telomerase recruitment to telomeres. *Cell* **166**:1188–1197. DOI: https://doi.org/10.1016/j.cell.2016.07.033, PMID: 27523609

Schmidt T, Tian L, Clore GM. 2018. Probing conformational states of the finger and thumb subdomains of HIV-1 reverse transcriptase using double Electron-Electron resonance electron paramagnetic resonance spectroscopy. *Biochemistry* **57**:489–493. DOI: https://doi.org/10.1021/acs.biochem.7b01035, PMID: 29251492

Schneider CA, Rasband WS, Eliceiri KW. 2012. NIH image to ImageJ: 25 years of image analysis. *Nature Methods* **9**:671–675. DOI: https://doi.org/10.1038/nmeth.2089, PMID: 22930834

Sparks JL, Chon H, Cerritelli SM, Kunkel TA, Johansson E, Crouch RJ, Burgers PM. 2012. RNase H2-initiated ribonucleotide excision repair. *Molecular Cell* **47**:980–986. DOI: https://doi.org/10.1016/j.molcel.2012.06.035, PMID: 22864116

Steczkiewicz K, Zimmermann MT, Kurcinski M, Lewis BA, Dobbs D, Kloczkowski A, Jernigan RL, Kolinski A, Ginalski K. 2011. Human telomerase model shows the role of the TEN domain in advancing the double Helix for the next polymerization step. *PNAS* **108**:9443–9448. DOI: https://doi.org/10.1073/pnas.1015399108, PMID: 21606328

Stefl R, Spacková N, Berger I, Koca J, Sponer J. 2001. Molecular dynamics of DNA quadruplex molecules containing inosine, 6-thioguanine and 6-thiopurine. *Biophysical Journal* **80**:455–468. DOI: https://doi.org/10.1016/S0006-3495(01)76028-6, PMID: 11159416

Steitz TA. 1999. DNA polymerases: structural diversity and common mechanisms. *Journal of Biological Chemistry* **274**:17395–17398. DOI: https://doi.org/10.1074/jbc.274.25.17395, PMID: 10364165

Traut TW. 1994. Physiological concentrations of purines and pyrimidines. *Molecular and Cellular Biochemistry* **140**:1–22. DOI: https://doi.org/10.1007/BF00928361, PMID: 7877593

Watson JD. 1972. Origin of concatemeric T7 DNA. *Nature New Biology* **239**:197–201. DOI: https://doi.org/10.1038/newbio239197a0, PMID: 4507727

Winn MD, Ballard CC, Cowtan KD, Dodson EJ, Emsley P, Evans PR, Keegan RM, Krissinel EB, Leslie AG, McCoy A, McNicholas SJ, Murshudov GN, Pannu NS, Potterton EA, Powell HR, Read RJ, Vagin A, Wilson KS. 2011. Overview of the CCP4 suite and current developments. *Acta Crystallographica. Section D, Biological Crystallography* **67**:235–242. DOI: https://doi.org/10.1107/S0907444910045749, PMID: 21460441

Xi L, Cech TR. 2014. Inventory of telomerase components in human cells reveals multiple subpopulations of hTR and hTERT. *Nucleic Acids Research* **42**:8565–8577. DOI: https://doi.org/10.1093/nar/gku560, PMID: 24990373

Appendix F Position-Dependent Effect of Guanine Base Damage and Mutations on Telomeric G-Quadruplex and Telomerase Extension

Our collaboration with the Sua Myong Lab at Johns Hopkins University resulted in a research article originally published in *Biochemistry* [179]. Position-Dependent Effect of Guanine Base Damage and Mutations on Telomeric G-Quadruplex and Telomerase Extension. Hui-Ting Lee, Samantha Sanford, Tapas Paul, Joshua Choe, Arindam Bose, Patricia L. Opresko, and Sua Myong. *Biochemistry*. 2020, 59, 28, 2627–2639. DOI: 10.1021/acs.biochem.0c00434

Biochemistry

pubs.acs.org/biochemistry Article

Position-Dependent Effect of Guanine Base Damage and Mutations on Telomeric G-Quadruplex and Telomerase Extension

Hui-Ting Lee, Samantha Sanford, Tapas Paul, Joshua Choe, Arindam Bose, Patricia L. Opresko, and Sua Myong*

Cite This: https://dx.doi.org/10.1021/acs.biochem.0c00434 Read Online

ACCESS | Metrics & More | Article Recommendations | Supporting Information

ABSTRACT: Telomeres are hot spots for mutagenic oxidative and methylation base damage due to their high guanine content. We used single-molecule fluorescence resonance energy transfer detection and biochemical assays to determine how different positions and types of guanine damage and mutations alter telomeric G-quadruplex structure and telomerase activity. We compared 15 modifications, including 8-oxoguanine (8oxoG), *O*-6-methylguanine (O6mG), and all three possible point mutations (G to A, T, and C) at the 3′ three terminal guanine positions of a telomeric G-quadruplex, which is the critical access point for telomerase. We found that G-quadruplex structural instability was induced in the order C < T < A ≤ 8oxoG < O6mG, with the perturbation caused by O6mG far exceeding the perturbation caused by other base alterations. For all base modifications, the central G position was the most destabilizing among the three terminal guanines. While the structural disruption by 8oxoG and O6mG led to concomitant increases in telomerase binding and extension activity, the structural perturbation by point mutations (A, T, and C) did not, due to disrupted annealing between the telomeric overhang and the telomerase RNA template. Repositioning the same mutations away from the terminal guanines caused both G-quadruplex structural instability and elevated telomerase activity. Our findings demonstrate how a single-base modification drives structural alterations and telomere lengthening in a position-dependent manner. Furthermore, our results suggest a long-term and inheritable effect of telomeric DNA damage that can lead to telomere lengthening, which potentially contributes to oncogenesis.

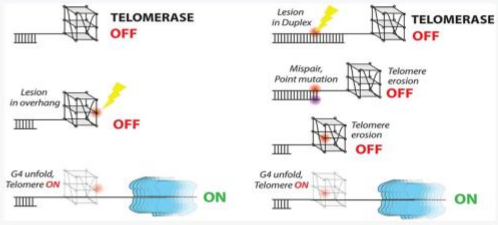

DNA damage has long been linked to cytotoxicity, oncogenesis, and degenerative disorders associated with aging. Many environmental factors and byproducts of cellular metabolism can cause DNA lesions, including base loss, strand breaks, and chemical alterations (reviewed in ref 1). Chemical modification of bases is the most common DNA lesion type[2] that may cause mutations, because many chemically modified bases preferentially pair with an incorrect nucleotide during DNA replication. Therefore, DNA lesions have the potential to alter the local DNA secondary structure either directly or by inducing mutations, if not removed in a timely manner by the DNA repair pathways. Many independent studies reported that 8-oxoguanine (8oxoG), the most common oxidative base lesion, destabilizes the DNA double helix and noncanonical secondary structures.[3−8] 8oxoG mainly induces G to T mutations by mispairing with A, although other mutations have been reported.[9,10] *O*-6-Methylguanine (O6mG), a common base lesion caused by alkylation of the O6 atom of guanine, is highly mutagenic and carcinogenic due to mispairing with T and, thereby, induces high rates of G to A mutations.[11−13] While the impact of DNA lesions on genome replication by DNA polymerases has been extensively studied, far less is known about how lesions affect telomere access and telomere elongation.

Telomeres are specialized structures that cap the ends of linear chromosomes in eukaryotes. Human telomeric DNA consists of TTAGGG tandem repeats in duplex followed by a G-rich 3′ single-stranded overhang.[14] Shelterin proteins associate with telomeric DNA to regulate the structure and length of telomeres and to prevent inappropriate activation of DNA damage signaling and repair pathways.[15−19] Previous work showed that telomeres are prone to oxidative DNA damage due to recurring consecutive guanines in their sequence.[20,21] Other evidence indicates 8oxoG repair is less efficient in telomeres, and the 8-oxoguanine glycosylase (OGG1) repair enzyme does not act on single-stranded DNA.[22] Although the repair efficiency of O6mG at telomeres

Received: May 23, 2020
Revised: June 21, 2020
Published: June 24, 2020

is unknown, this lesion is also mutagenic and carcinogenic[23,24] and can form in G runs of telomeric DNA.

In most somatic cells, telomeres are gradually shortened with rounds of cell division due to the end-replication problem. Exceptions include embryonic stem cells, pluripotent cells, and cancer cells that can replenish telomeres by a special reverse transcriptase called telomerase.[25−28] Telomerase is a ribonucleoprotein complex that binds specifically to the end of the single-stranded telomere overhang and extends it. The RNA component within telomerase functions both in directing telomerase to the telomere and in templating for TTAGGG repeat addition to the 3′ overhang. When sufficiently elongated by the telomerase, a replicative DNA polymerase can then synthesize the C-rich complementary strand, known as C-strand fill in. Shelterin protein POT1 binds to the telomeric single-strand overhang to help regulate telomerase access and activity.[19,29−32]

Single-stranded TTAGGG repeats in the telomeric overhang can fold into G-quadruplexes (G4)[33−35] in which four guanines form a quartet through Hoogsteen hydrogen bonding stabilized by a monovalent cation conjugating with the four neighboring O6 atoms (Figure 1A). The conformation of G4

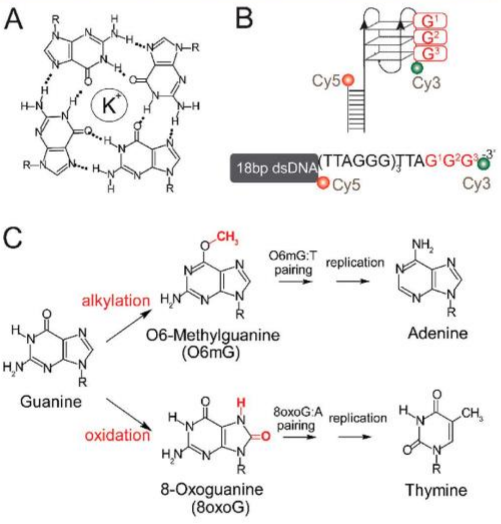

Figure 1. G-Quadruplex and base damage in the telomere terminal repeat. (A) G-Quartet formed by four guanines. (B) DNA construct design and sequence. The three guanines in the 3′ terminal repeat are denoted as G1−G3 in the 5′ to 3′ direction. The Cy5 dye is located at the phosphate group at the 5′ end. (C) 8-Oxoguanine (8oxoG), O6-methylguanine (O6mG), and the major mutations caused by these modified bases after replication.

depends on the loop sequence and solution conditions.[36−38] The mammalian telomere sequence forms a hybrid or parallel G4 conformation at physiological ionic concentrations.[33,39,40] Circular dichroism spectroscopy and ultraviolet (UV) melting experiments show that 8oxoG or O6mG can destabilize and alter telomeric G4 conformations by disrupting the Hoogsteen bonding.[7,41,42] The presence of G4 structure in genomic DNA, including the telomeres, has been well-documented.[43−47] More recently, immunofluorescence-based studies revealed colocalization between telomere binding proteins and the G4-specific antibody, BG4,[48] strongly supporting the formation of G4 at telomeres. The folded structure of G4 can diminish telomerase loading, yet the role of G4 structures in telomere length regulation, aging, or disease development remains elusive.

In earlier studies, using single-molecule fluorescence resonance energy transfer (smFRET) and biochemical analyses, we reported that a single 8oxoG moiety in an oligonucleotide telomeric overhang induces G4 structural dynamics and perturbations, which significantly enhance telomerase binding and activity.[49,50] We also directly compared effects of 8oxoG within the G-quartet versus thymine glycol within the loop, because these are the two most common oxidative lesions. We demonstrated that while telomerase cannot access a tightly folded G4, it binds and extends a G4 when either thymine glycol or 8oxoG is present at the second T or G in the repeat, respectively. This implies that a stable G4 in the telomeric overhang can act as a lock that prevents telomerase activity in normal cells, whereas a single lesion can disrupt the G4 and allow for telomere extension. However, how lesion location determines telomeric structural dynamics and telomerase accessibility is poorly understood.

In this study, we sought to evaluate the structural changes induced by different types and positions of base modifications or mutations. We used smFRET to investigate 15 variants of telomeric G4 that include two types of DNA lesions, 8oxoG and O6mG, and mutations of G to A, C, or T at the three different terminal guanine positions, which serve as an entry access for POT1 and telomerase. By examining the structural changes at a single-molecule level, smFRET allows us to distinguish the different structural dynamics that coexist in all of the individual molecules without having to synchronize. We developed an analytical method to categorize >100000 smFRET trajectories into different classes of dynamic conformational changes induced by various base modifications. Our data reveal that DNA lesions and mutations shift the distribution and dynamics of a series of unfolded, partially folded, or fully folded G4 conformations. Even the base modification located at the most "tolerable" position for G4 formation[7] imparts a significant level of structural dynamics in our study. We correlated the distribution of structural disruption with accessibility by testing for complementary strand annealing, POT1 binding, and telomerase binding and extension activity. Our results indicate that the induced structural dynamics and disruptions, and the resulting accessibility, vary significantly depending on the type and position of the chemical base alteration. Finally, we interpret our results in the context of published G-quadruplex structural data from nuclear magnetic resonance (NMR) and circular dichroism (CD).[5−7,41,42] Taken together, our results have important implications for how DNA damage and mutations at the telomeric end regulate telomerase-mediated telomere lengthening.

■ MATERIALS AND METHODS

DNA Sample Preparation. The single-stranded (ss) DNA oligonucleotides containing 8oxoG or O6mG were purchased from Midland Certified Reagent Company Inc. (Midland, TX). These oligonucleotides were synthesized with a primary amine modification at the designated labeling site and then fluorescently labeled in our laboratory with Cy3-NHS-ester in 100 mM sodium bicarbonate buffer at room temperature as reported earlier.[49,50] Other DNA oligonucleotides were

https://dx.doi.org/10.1021/acs.biochem.0c00434
Biochemistry XXXX, XXX, XXX−XXX

purchased from IDT (Coralville, IA) with or without the corresponding fluorescent dye or biotin conjugation. The sequences of all of the oligonucleotides are listed in Table S1. The partial duplex DNA constructs were prepared by mixing a G-rich ss oligonucleotide with the 18-mer complementary oligonucleotide at a molar ratio of 1:1.2 in a buffer containing 20 mM Tris-HCl (pH 7.5) and 100 mM KCl. The mixtures were incubated in a Bio-Rad C1000 Touch Thermal Cycler with the following program as reported earlier:[49,50] 95 °C for 2 min, slowly cooled to 37 °C at a rate of 2 °C/min, and then cooled to 4 °C.

POT1 Protein and Telomerase Lysate Preparation. Recombinant human POT1 protein was expressed in a baculovirus−insect cell system and purified as previously described.[51,52] FLAG-tagged human telomerase was expressed in HEK-293T cells co-transfected with plasmids expressing hTR and FLAG-tagged hTERT in a 1:3 molar ratio as previously described.[49,50,53] Briefly, the HEK-293T cells were grown in DMEM with 10% FBS and 1% penicillin-streptomycin (Gibco) to 90% confluency. The cells were then transfected using Lipofectamine 2000 Reagent (Invitrogen) and allowed to grow for 48 h. The cells were harvested by trypsin detachment, washed with phosphate-buffered saline (PBS), and lysed with CHAPS lysis buffer [10 mM Tris-HCl, 1 mM $MgCl_2$, 1 mM EDTA, 0.5% CHAPS, 10% glycerol, 5 mM β-mercaptoethanol, 120 units of RNasin plus (Promega), 1 μg/mL pepstatin, 1 μg/mL aprotinin, 1 μg/mL leupeptin, 1 μg/mL chymostatin, and 1 mM AEBSF] for 30 min at 4 °C. The cell lysate was frozen in liquid nitrogen and stored at −80 °C.

Single-Molecule FRET Sample Assembly. Single-molecule FRET (smFRET) data were acquired using a home-built prism-type total internal reflection fluorescence (TIRF) microscope with an electron-multiplying CCD camera (EM-CCD) at room temperature (23 ± 1 °C). The quartz sample slides and glass coverslips were prepared by following a polyethylene glycol (PEG)-mediated surface passivation protocol with a 40:1 mixture of m-PEG-5000-SVA and biotin-m-PEG-5000-SVA (Laysan Bio, Inc.).[49] The imaging chamber formed between the quartz slide and the coverslip slide was coated with 50 μg/mL neutravidin (Thermofisher) in 10 mM Tris-HCl (pH 7.5) and 100 mM KCl for 5 min and then washed with the same buffer. Annealed biotinylated partial duplex DNA carrying both Cy3- and Cy5-labeled strands was immobilized in the PEG-coated imaging chamber via biotin−neutravidin interaction in 10 mM Tris-HCl (pH 7.5) and 100 mM KCl. All of the smFRET experiments were performed in an imaging buffer containing 10 mM Tris-HCl (pH 7.5), 100 mM KCl, 0.5% glucose, 10 mM 6-hydroxy-2,5,7,8-tetramethylchromane-2-carboxylic (Trolox), and 1 mg/mL glucose oxidase and 4 μg/mL catalase to ensure stable G-quadruplex formation and to minimize photobleaching of the fluorophores.

SmFRET Binding Assay. The real-time smFRET binding assay of the complementary strand (C strand) and POT1 was carried out in flow chambers, which have a small plastic reservoir above the hole at one end of the chamber and a syringe pump connected with silicone tubing to the hole at the other end. The DNA labeled with both Cy3 and Cy5 was immobilized in the imaging chamber and imaged alone, and then 100 μL of the C strand (10 nM) or POT1 (100 nM) in imaging buffer was loaded into the reservoir. The C strand stock was stored in 1× TE buffer [1 mM EDTA and 10 mM Tris-HCl (pH 8.0)], diluted to 1 μM in water to prevent secondary structure, and diluted to 10 nM in the imaging buffer right before the experiment. The POT1 stock was stored in storage buffer [25 mM Tris-HCl (pH 8.0) and 150 mM NaCl] and diluted in 10 mM Tris and 100 mM KCl buffer. Right before the binding experiment, POT1 was further diluted to 100 nM in the imaging buffer. The C strand or POT1 solution was passed through the imaging chamber to the silicone tubing, at a rate of 20 μL/s drawing by a Pump 11 Elite syringe pump (Harvard Apparatus, Holliston, MA) equipped with a 1 mL standard disposable plastic syringe. Real-time FRET images were collected during and after sample injection for 5 min at a frame rate of 100 or 150 ms. For the C strand and POT1 binding reactions that reached completion within 5 min of C strand or POT1 flow-in, the binding kinetics were analyzed by monitoring the time from the moment of flow to the moment of the first irreversible FRET decline event as described previously.[50] For the binding reactions that did not reach completion within 5 min, short movies were collected at different time points to generate FRET histograms until the reactions were completed or 2 h had passed.

SmFRET Histograms. A solid state 532 nm green laser (Compass 315M, Coherent) was used to generate an evanescent field of illumination for smFRET detection. Data were recorded with a time resolution of 100 ms, processed by an IDL script, and then analyzed by Matlab scripts. Each FRET histogram was generated from 15−30 independent images containing 250−350 individual molecules per image to ensure the inclusion of more than 5000 molecules. To prevent the donor-only molecules from interfering with low-FRET regions, the molecules containing both the donor and the acceptor were selected through sequential excitation of the donor (Cy3, by a 532 nm green laser) and acceptor (Cy5, by a Coherent cube 641 nm red laser). Donor leakage was corrected on the basis of the FRET value of donor-only molecules. Each corrected and normalized histogram was fitted to Gaussian distributions using Origin 2016. The histograms of DNA alone were fitted with an unrestrained peak center position. The peak center positions were then used to restrain the peak position in the C strand or POT1 bound histograms. The reported histogram fitting results were obtained from averaging two or three trials, each containing more than 6000 molecules. The uncertainty was expressed in the form of the standard error calculated from multiple trials.

SmFRET Trajectory Analysis. We developed MatLab scripts to record and analyze the manually selected transition from smFRET trajectories because the currently available smFRET analyzing programs tend to ignore the fast (<5 s) transit state changes in some of the DNA constructs. A total of 300−600 individual molecules of each DNA construct from two or more independent experiments were initially, manually categorized to ensure the molecular dynamic behavior was consistent across different imaging areas and experiments. The detailed molecule behavior analysis was performed by incorporating more than 200 individual molecules of each DNA construct. The FRET value and time of each transition were manually assigned by the user. The recorded manually selected FRET values were then plotted against the mean FRET value calculated between two transitions. Most of the manually selected and calculated FRET values were >95% consistent. However, in the cases of fast transit states that lasted for <5 s, the manually reported FRET values better reflect the maximum FRET fluctuation of the transit states.

https://dx.doi.org/10.1021/acs.biochem.0c00434
Biochemistry XXXX, XXX, XXX−XXX

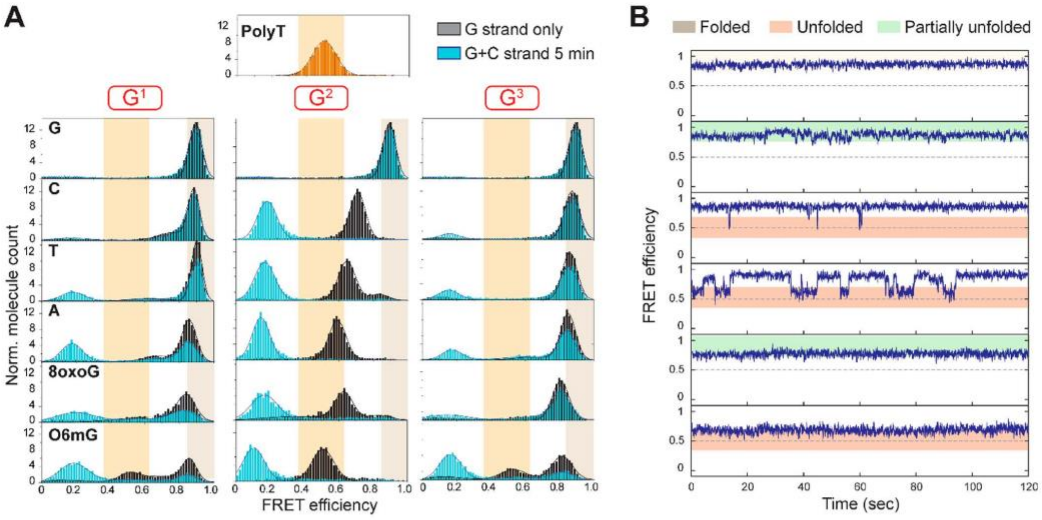

Figure 2. Structural disruption is dependent on both base and position. (A) FRET histograms of each DNA construct before (gray) and after (cyan) incubation for 5 min with the complementary C strand $(CCCTAA)_4$. High FRET converts to low FRET upon annealing as an indicator of accessibility. (B) Sample single-molecule traces of a telomeric construct harboring an 8oxoG at the G^1 position displaying the three major types of molecular behavior.

The transition behavior analysis was designed to screen through each smFRET trajectory and identify the lowest FRET value each molecule had encountered during the 120 s recording time or before photobleaching. The fraction of molecules exhibiting different molecular behaviors was estimated by a bootstrapping procedure that randomly sampled 200 traces from each construct and repeats 200 times. Both manually selected and calculated mean FRET values of each transition were analyzed with bootstrap and generated a similar result. The data reported herein are based on the manually selected FRET values. The fraction and reported error of each population were obtained from the medium and confidential interval of 95% from the bootstrapping results.

Telomerase Binding Assay. The single-molecule pull-down (SiMPull) assay for telomerase binding was performed on the same TIRF microscope at room temperature as smFRET. Mouse monoclonal IgM against hTERT (LS-B95) was purchased from LifeSpan Biosciences. The antibody was labeled with Alexa-647 C5 maleimide (Thermo Fisher) at a 1:35 molar ratio in PBS and 100 mM sodium bicarbonate on ice for 1 h and purified by Bio-Gel P6 columns in Tris buffer, as described previously.[50] Biotinylated mouse anti-FLAG monoclonal antibody M2 at a 1:100 dilution (F9291, Sigma) was immobilized in the imaging chamber via biotin–neutravidin interaction as described above. The imaging chamber was washed with telomerase reaction buffer (TRB) containing 50 mM Tris-HCl (pH 8), 50 mM KCl, and 1 mM $MgCl_2$. The cell lysate containing human telomerase (1:50 dilution in TRB) was added to the antibody-coated surface and incubated for 20 min at room temperature. Subsequently, 10 nM no-biotin Cy3-labeled partial duplex DNA was applied to the chamber and incubated for 20 min. Unbound DNA was washed away with TRB, which was immediately followed by adding the Alexa-647-conjugated hTERT antibody (1:5000 dilution) to the chamber. The imaging chamber was first washed with TRB and then with imaging buffer containing 0.5% glucose, 10 mM Trolox, 1 mg/mL glucose oxidase, 4 μg/mL catalase, and the same salts as TRB [50 mM Tris-HCl (pH 8), 50 mM KCl, and 1 mM $MgCl_2$]. Thirty or more movies were recorded for each chamber with sequential excitation with a 532 nm green laser (for Cy3-labeled DNA) and a 641 nm red laser (for the Alexa 647-labeled antibody). The colocalization of the Cy3 and Cy5 signal under sequential excitation was analyzed with a MatLab script to give the binding ratio of DNA-bound telomerase to the overall telomerase signal. Each DNA construct had been tested at least three times on different dates and normalized to the mean binding ratio of the R3 DNA construct, to give the mean telomerase binding fraction and standard error between repeats. The specificity of the antibodies against telomerase was confirmed as described previously.[50]

Telomerase Extension Assay. The telomerase extension assay was slightly modified from the previous protocol.[49,50,54] Briefly, telomerase was eluted from the beads with 2 times the bead volume of a mix consisting of 250 μg/mL 3× FLAG peptide (Sigma-Aldrich) in 1× telomerase buffer and 150 mM KCl. The bead slurry was incubated for 30 min at 4 °C with mixing, and telomerase in the supernatant was collected using Mini Bio-Spin Chromatography columns (Bio-Rad). The same cell lysate used in our SiMPull assay was employed in the extension assay. *In vitro* reaction mixtures (20 μL) with oligonucleotide primers (1 μM) contained telomerase reaction buffer, 0.3 μM of 3000 Ci/mmol [α-^{32}P]dGTP (PerkinElmer), and a cellular dNTP (Thermo Fisher) concentration mix of 37 μM dTTP, 24 μM dATP, 29 μM dCTP, and 5.2 μM dGTP. Reactions were started by adding 3 μL of an immunopurified telomerase eluent, incubated for 1 h at 37 °C, and then terminated by adding 2 μL of 0.5 M EDTA and heat inactivated for 20 min at 65 °C. An 18-mer radio end-labeled

https://dx.doi.org/10.1021/acs.biochem.0c00434
Biochemistry XXXX, XXX, XXX−XXX

oligonucleotide was added as a loading control (LC) (8.0 fmol) to the inactivated reaction mixtures prior to purification with an Illustra MicroSpin G-25 column (GE Healthcare). Radiolabeling of LC was performed in a 20 μL reaction mixture containing 10 pmol of oligonucleotide, 1× T4 PNK buffer (NEB), 2 μL of 3000 Ci/mmol [γ-^{32}P]ATP (PerkinElmer), and 10 units of T4 PNK (NEB), and the mixture was incubated for 60 min at 37 °C followed by heat inactivation at 65 °C for 20 min. An equal volume of loading buffer [94% formamide, 0.1× Tris-borate-EDTA (TBE), 0.1% bromophenol blue, and 0.1% xylene cyanol] was added to the reaction eluent from the G-25 spin column. The samples were heat denatured for 10 min at 100 °C, loaded onto a 10% denaturing acrylamide gel (7 M urea and 1× TBE), and electrophoresed for 70 min at a constant of 38 W. Samples were imaged using a Typhoon phosphorimager (GE Healthcare). The relative telomerase activity was quantitated using ImageQuant and normalized to the loading control as described previously.[49,55,56]

RESULTS

Oxidative and Alkylation Base Lesions Cause Greater Structural Disruption Than Mutations. We designed a series of 16 DNA constructs containing four repeats of TTAGGG with five types of modifications at the three terminal guanine positions. First, we examined if the single site oxidative and alkylation base lesions, and mutations caused by these lesions, change the structure of the telomeric DNA. We substituted three guanines at the 3′ end individually with 8oxoG, O6mG, A, T, or C. All DNA constructs share the same 18 bp nontelomeric double-stranded stem. The 24-mer telomeric oligonucleotide is written as $(TTAGGG)_3$-$TTAG^1G^2G^3$, in which G^1−G^3 represent the three guanine positions replaced by a lesion or mutation, followed by Cy3 at the 3′ end. The annealed 18-mer oligonucleotide has a Cy5 at the 5′ end that FRET pairs with Cy3 and a biotin conjugated at the 3′ end for immobilization to a neutravidin-coated single-molecule surface (Figure 1B and Table S1). We probed the formation of G4 by FRET.[19,32,38]

We used a physiologically relevant potassium concentration (100 mM KCl)[57] to capture FRET images and built the FRET histogram by compiling more than 4000 FRET values collected from 20 fields of view, thus representing the ensemble average FRET of all DNA molecules. The FRET histograms for all 16 DNA constructs displayed diverse patterns depending on the type of chemical modifications and their positions (Figure 2A, black). We also obtained a FRET histogram of a 25-mer polythymine (polyT) as an unstructured control, which yields a single peak centered at 0.5 FRET (Figure 2A, top orange histogram). The FRET histogram of the unmodified $(TTAGGG)_4$ DNA (4R) has a single peak centered at 0.9 (Figure 2A, top left, black histogram), which is consistent with a tightly folded G4 structure.[32]

The constructs that harbor a point mutation (A, C, or T) at the G^1 or G^3 position all show a major high FRET peak similar to unmodified 4R, conferring minimal disruption in the folded G4 structure (Figure 2A). The only minor exception to this pattern is A in the G^1 position that induces an additional lower FRET shoulder (23 ± 2% at 0.68 FRET calculated from the area under the Gaussian fit), suggesting a small fraction of molecules fold into a slightly altered (more open) conformation or undergo conformational dynamics. By contrast, all modifications at the G^2 position induce a FRET peak shift to substantially lower values, signifying a higher degree of G4 disruption than modification at the other two positions. This is consistent with previous reports that the middle G position, denoted G^2, is the most critical base for G4 thermal stability.[6,42] When 8oxoG or O6mG was placed at position G^1 or G^3, the histograms displayed significant deviations from the G4 folded peak. 8oxoG at G^1 and G^3 positions induced broadening of the major high-FRET peak, which spread over to the mid-FRET range. Such shoulders become much more pronounced by O6mG substitution at both G^1 and G^3 positions that generate 30−40% of the peak transitioning to the mid-FRET range, reflecting a significant degree of disrupted G4 structure. The 0.5 mid-FRET peak induced by O6mG at all positions indicates that the degree of unfolding matches that of the unstructured polyT.

Taken together, our data suggest that at the G^1 and G^3 positions, the base lesions cause significant structural distortions while point mutations induce only minor or insignificant structural alterations. Quantification of the high-FRET and mid-FRET shifts reveals a general rank order for the extent of G4 disruption as O6mG > 8oxoG ≥ A > T > C at the G^1 and G^3 positions. This order likely arises from the size and chemical property of the substituted bases; the smaller pyrimidines can fit into the space of a missing guanine, while the purine and lesions cause both steric hindrance and interrupted hydrogen bonds. We observe extensive unfolding arising from modification of the central guanine, G^2, in agreement with previous CD and UV melting studies.[6,7,41] All FRET histograms of the G^2-substituted constructs exhibit a complete disappearance of high-FRET peaks, and the concomitant appearance of mid-FRET peaks, emphasizing the maximal perturbations induced by G^2 modifications (Figure 2A). Interestingly, the magnitude of the FRET peak shift of the mutant constructs follows a similar order of A (0.6) > T (0.65) > C (0.71), expressed as the main FRET peak center values. The G4 destabilization of human telomeric DNA caused by A or T substitution is consistent with previous reports.[58,59] O6mG at the G^2 position causes the strongest structure disruption among all of the constructs. Indeed, the FRET histogram of the O6mG substitution almost overlaps with the polyT histogram, which indicates the O6mG at the G^2 construct behaves as unstructured ssDNA.

Lesion Position Determines the Accessibility of Damaged Telomeric DNA. Having mapped the structural disruptions by the base modifications, we next tested the accessibility of all of the DNA constructs by applying a complementary strand $(CCCTAA)_4$ that we termed the "C strand". As shown previously, the C strand completely anneals to the G4 strand as evidenced by a single low-FRET peak when the C strand is added in a 200-fold molar excess.[32,49,50] The cyan histograms in Figure 2A were collected after the addition of 10 nM C strand for 5 min (100 mM KCl). The appearance of a low-FRET peak at 0.2 indicates the formation of a long 24 bp duplex, $(TTAGGG)_4/(CCCTAA)_4$, which can form only when the C strand anneals to unfolded G4. Therefore, the FRET shift to 0.2 represents the openness or accessibility of the folded structure.[32] Under our experimental condition, the unmodified 4R displayed negligible (~8%) annealing while the G^2 lesion and mutant constructs all showed 100% accessibility to the C strand (Figure 2A, cyan), which is consistent with our previous report.[50] Interestingly, the G^1 and G^3 lesion and mutant constructs exhibited varying degrees of accessibility depending on the type of base substitution, ranging from

https://dx.doi.org/10.1021/acs.biochem.0c00434
Biochemistry XXXX, XXX, XXX−XXX

~15% (C at G^3) to ~90% (O6mG at G^1), as quantified in Figure 4C (gray bars). The C strand accessibility of both G^1- and G^3-modified constructs roughly follows the same trend of O6mG (89% and 68%) > 8oxoG (50% and 24%) ≥ A (50% and 35%) > T (35% and 35%) > C (17% and 14%); the numbers in parentheses indicate accessibility induced by G^1 and G^3 modification, respectively. More interestingly, while unmodified 4R remained inaccessible to the C strand (~11%), all constructs with G^1 and G^3 lesions or mutations reached 84−95% accessibility after 2 h (see Table S2). This likely reflects the slow rate of G4 conformational dynamics when the chemical modification or mutation is at the first or last position of the GGG sequence. This effect correlates with the smaller degree of G4 disruption caused by G^1 and G^3 modifications and further emphasizes the position-dependent effect of the DNA lesions and mutations in telomeric G4.

To further examine C strand accessibility, we measured the C strand annealing kinetics by collecting time lapse FRET histograms after C strand addition. All of the G^2-substituted constructs completely annealed to the C strand within 3 min with a half-time ($t_{1/2}$) ranging from 0.5 min (O6mG and 8oxoG) to 0.6 min (A), 0.7 min (T), and 0.8 min (C) (Figure S2 and Table S2). O6mG and 8oxoG substitution at G^1 or G^3 generated lower reaction rates of 2−5 min ($t_{1/2}$), while T and A mutations at G^1 and G^3 resulted in rates of 5−9 min ($t_{1/2}$). Interestingly, the C mutations showed the slowest annealing rates of 25 ± 3 min (G^1) and 73 ± 4 min (G^3). The fast and complete annealing observed with all of the G^2 substitutions is expected on the basis of the structural destabilization caused by disrupting the central G-quartet, resulting in high accessibility (Figure 2A). However, the varying degree of accessibility obtained for G^1 and G^3 substitutions is more subtle and difficult to rationalize. Therefore, we sought to examine the conformational dynamics that may persist in differently folded states for each construct. We hypothesized that the accessibility of a telomeric overhang relies on (1) the reduction of global G4 compactness or (2) the dynamic conformational fluctuations (unfolding−refolding transitions) that expose DNA bases to the C strand. To test the first hypothesis, we plotted the C strand accessibility against the center of the major FRET peak or the area of the minor shoulder of each construct. This showed a poor correlation with C strand accessibility (Figure S3). This lack of correlation indicates that the reduction of global compactness is likely not the main reason for the high accessibility of damaged or mutated telomeric DNA.

The Dynamic Unfolding Population Contributes to Telomeric DNA Accessibility. We tested the second hypothesis raised above by analyzing the real-time smFRET trajectories of all of the DNA constructs. As demonstrated previously, the 4R construct displays a steady high FRET.[50] By contrast, all of the G^2 mutant and lesion constructs exhibit two-step FRET fluctuations oscillating between their major peak FRET value (0.5−0.7) and high FRET of 0.8−0.9 (Figure S1). On the other hand, the G^1 or G^3 position variants exhibit a complicated pattern of conformational dynamics from unfolded ssDNA (FRET value of polyT), intermediate FRET states, to a fully folded G4 state (Figure S1). Interestingly, all of the lesions and mutations at G^1 or G^3 induced similar FRET states, albeit distributed differently (Figure S1). The main difference between various bases at the same position is the distribution of dynamic patterns. To quantify conformational dynamics, we focused on the most "unfolded" state of a molecule, which is represented by the lowest-FRET state observed in a smFRET trace, and classified the smFRET traces into three categories: folded [stable high-FRET traces without fluctuation, similar to G4 (Figure 2B, gray area)], unfolded [traces that visit the unfolded 0.5 FRET state (Figure 2B, red area)], and partially unfolded [all other traces with steady FRET interspersed with transitions above 0.6 (Figure 2B, green area)]. This classification disregards the ability of refolding in the dynamic traces and simply focuses on the maximum unfolded level of each trace.

A summary of the FRET state classification as the fractional distribution of folded (black), partially unfolded (green), and unfolded (red) populations is shown in Figure 3A. As

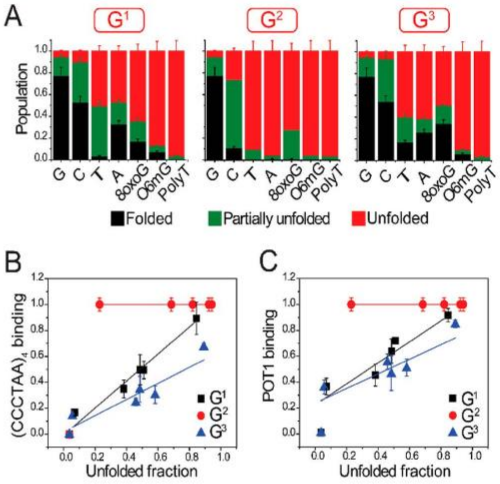

Figure 3. Complementary strand and POT1 binding reflect the structural instability of the telomeric G-quadruplex. (A) FRET state classification as the fractional distribution of folded (black), partially unfolded (green), and unfolded (red) populations. (B and C) Plots of the fraction of single-molecule traces displaying dynamic FRET or steady unfolded state (FRET < 0.6) vs the fraction of molecules bound to $(CCCTAA)_4$ or POT1, respectively.

expected, the G^2 modifications led to almost entirely unfolded or partially unfolded molecules. One exception is the G^2 to C mutation that displays a larger population of partially unfolded molecules, possibly due to the G:C base pair stabilizing the partially folded conformation. For the G^1 or G^3 substitutions, the abundance of unfolded or partially unfolded populations roughly follows the order O6mG > 8oxoG ≥ A > T > C, as seen before. To check if the molecules undergoing dynamic folding and unfolding transitions may allow for C strand annealing, we plotted the fraction of dynamic molecules against the fraction of C strand annealed molecules. This plot showed a linear correlation for both the G^1 and G^3 constructs (Figure 3B, black and blue, respectively), suggesting that the dynamic conformational state gives rise to C strand accessibility for constructs with G^1 and G^3 modifications. By contrast, the G^2 modifications induced complete accessibility regardless of the conformational state of the construct (Figure 2B, red), likely due to the high degree of G-quartet disruption. The X-ray crystallography and NMR structures of telomeric G4 show that potassium ions in the central cavity interact with

https://dx.doi.org/10.1021/acs.biochem.0c00434
Biochemistry XXXX, XXX, XXX−XXX

eight oxygen atoms from two layers of G-quartets.[33,60] In our constructs, the base lesions or mutations at the G^1 and G^3 positions prevent formation of the top or bottom G-quartet but allow the other two consecutive layers of the G-quartet to be held together by one potassium ion. The G^2 position modifications, however, interfere with the central G-quartet, leading to depletion of potassium ions and thereby disrupting all G-quartet layers. Therefore, while the 0.6−0.75 FRET states in G^1- and G^3-modified constructs represent partially unfolded states that are inaccessible to the C strand, the same 0.6−0.75 FRET states in G^2 constructs may represent looser structures that allow the C strand to anneal.

POT1 Binding Requires Structural Dynamics or Unfolding. We next asked if all of the modified constructs differ in POT1 accessibility. POT1 is a unique shelterin component that specifically binds to the single-stranded telomeric overhang.[15,16,52] In our earlier study, we reported that POT1 cannot unfold and bind to the stably folded G4 formed in 100 mM KCl, while POT1 can access a G4 with a single 8oxoG at the G^2 position.[50] We tested accessibility by applying POT1 (100 nM) to the constructs. POT1 binding shifts the smFRET histogram peak to a lower FRET value (0.4) (Figure S4). The FRET histograms collected 5 min after the addition of POT1 exhibited a trend highly similar to that of C strand accessibility (Figure S4). Accordingly, the plot of the dynamically unfolded fraction against the fraction of POT1 bound molecules also displays a linear correlation for the G^1 and G^3 constructs (Figure 3C). The O6mG constructs showed the highest bound fraction (~100%), followed by 8oxoG constructs rendering 70−90% bound. Similarly, A and T mutations showed 50−100% binding to POT1, while the C mutation displayed 10−50% binding (Table S2 and Figure S4). These data imply that the "unfolded" conformation is also responsible for binding of POT1 to constructs with damage or mutations at G^1 and G^3. Again, the G^2 modifications all led to complete binding of POT1, consistent with a high degree of structural disruption. It is possible that binding of POT1 to the constructs with base substitutions was also affected by the mutated sequence, which reduces the availability of the minimum POT1 binding site.[61,62] Nevertheless, the similarity between the POT1 and C strand correlation plots suggests that they both access their binding target passively, rather than actively invading the folded G4 structure. In both plots, the lowest accessibility point at the bottom left corner is the unmodified 4R construct (Figure 3B,C), which remains folded into a G4 without yielding accessibility to POT1 and C strand.

The binding kinetics of POT1 measured in the same way as for C strand annealing revealed that 100% of POT1 binding occurred within 3 min, with binding half-times, $t_{1/2}$, ranging from 0.1 min (O6mG and 8oxoG) to 0.2 min (A and T) to 0.3 min (C) (Figure S4). The O6mG substitution at G^1 and G^3 yielded the shortest binding half-time ($t_{1/2}$ of ~1 min) compared to those of 8oxoG ($t_{1/2}$ ~ 2 min) and mutants ($t_{1/2}$ ~ 2−5 min). As expected, the binding half-times obtained for the modified G^1 and G^3 constructs were generally longer than for modified G^2 constructs (Figure S4).

Base Lesions but Not Mutations Promote Telomerase Binding and Extension Activity. We previously showed that 8oxoG in the G^2 position of a telomeric G4 enhances telomerase extension activity.[49,50] To test if this stimulation depends on lesion position, we performed single-molecule pull-down (SiMPull) assays with all of the constructs tested above (Figure 4A). Briefly, the SiMPull assay entails the application

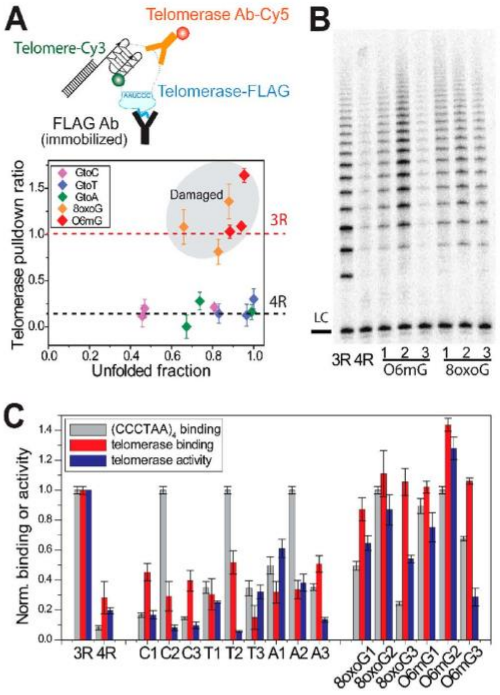

Figure 4. 8oxoG and O6mG lesion at any of the terminal guanines that promotes telomerase binding. (A) Single-molecule pull-down experiment and a plot of normalized telomerase binding vs the percent of single-molecule traces displaying an unfolded state (FRET < 0.6). Error bars represent the SD from three or more telomerase binding assays. (B) Telomerase activity on substrates containing a base lesion. 3R and 4R represent DNA constructs with three and four (TTAGGG) repeats, which serve as unfolded and folded G-quadruplex controls, respectively. Numbers indicate the position of G modification. (C) Normalized C strand binding fraction, telomerase binding, and telomerase activity obtained from C strand annealing, single-molecule pull-down, and *in vitro* telomerase activity assays, respectively. The number after each mutated or modified base indicates the position.

of lysate from mammalian cells that overexpress FLAG-tagged human telomerase to the single-molecule slides coated with an anti-FLAG antibody.[32,49,50,53] We confirmed the pull-down efficiency by adding a fluorescently (Alexa 647) labeled anti-telomerase antibody. We applied telomeric constructs (10 nM) labeled with Cy3 without biotin to the telomerase-bound surface and performed a dual excitation detection to capture both signals arising from telomerase (Alexa 647) and the bound DNA substrate (Cy3). The relative binding affinity of each construct for telomerase was calculated from the colocalization efficiency (i.e., ratio of the overlapping fluorophore signal in DNA-bound telomerase over total telomerase Alexa647 only signal). Each value was normalized against the unfolded positive control, 3R, which consists of three repeats of TTAGGG (Figure 4A, red dashed line). The tightly folded 4R (G4) showed the lowest level of binding to telomerase (Figure 4A, black dashed line) as reported previously.[50,63] Surprisingly, every construct that harbors a

https://dx.doi.org/10.1021/acs.biochem.0c00434
Biochemistry XXXX, XXX, XXX−XXX

lesion, 8oxoG or O6mG, in the G^1–G^3 position, uniformly displayed a very high binding affinity for telomerase, even exceeding the level of the 3R control (Figure 4A, gray area). By contrast, all of the T, A, and C mutations displayed extremely low levels of binding to telomerase, regardless of the mutation position (Figure 4A, bottom).

Plotting the telomerase binding affinity against the unfolded fraction of each telomeric construct shows that all G^1–G^3 constructs fall into two groups (Figure 4A). One group consists of the lesion-containing constructs (Figure 4A, gray oval) that exhibit a strikingly high telomerase binding level regardless of the status of the unfolded population. The second group consists of all of the point mutation constructs that uniformly show an unexpectedly low level of telomerase binding, matching the level seen in the highly folded 4R construct (Figure 4A, black dashed line), regardless of the degree of unfolding. Such an all-or-none pattern between the lesion and mutant constructs is in contrast to C strand and POT1 binding, which are proportional to the structural disruption of the telomeric construct. The uniformly low level of binding of telomerase to all constructs with mutations in G^1–G^3 clearly indicates that the mutations generate a mismatch with the telomerase RNA template, thereby lowering the base pairing capability. By contrast, 8oxoG and O6mG, although chemically modified, maintain the guanine base and may cause less disruption of the base pairing with the telomerase RNA template. On the basis of these unexpected observations, we posit that unlike the C strand and POT1, telomerase can actively disrupt partially unfolded G4 structures and exhibits high sequence selectivity.

We next performed *in vitro* primer extension assays to measure telomerase activity on all of the DNA constructs tested above. The telomerase extension products appeared as well-distinguished bands in the gel, demonstrating the addition of hexameric repeats. As shown in Figure 4B, the telomeric substrates harboring 8oxoG or O6mG at the G^1 and G^2 positions were elongated to lengths similar to those of 3R, suggesting that telomerase can extend a damaged telomeric substrate with similar processivity. We quantified the extension products and plotted with the telomerase binding and C strand accessibility values (Figure 4C). Overall, the telomerase binding and extension activity show a high level of correlation. Exceptions are the G^3-8oxoG and G^3-O6mG constructs that show low extension activity despite a high telomerase binding level (Figure 4B), clearly indicating the importance of the terminal guanine for extension. This agrees well with our previous finding and work from others that the incorporation of 8oxoG from the cellular dNTP pool terminates telomerase extension.[49,64] We also noticed a mild discrepancy between telomerase binding and activity for the constructs with A mutations at G^1 and G^2, which show a low level of telomerase binding, but intermediate levels of telomerase activity (55% and 38%) (Figure 4C and Figure S5). This may be explained by telomerase tolerating a purine-pyrimidine mismatch, which partially compensates for the lower level of telomerase binding. On the other hand, an A mutation at G^3 has ~45% telomerase binding but <10% telomerase activity, which resembles the pattern for 8oxoG and O6mG at G^3. Taken together, these results suggest that either an incorrect or damaged base can inhibit further extension when incorporated at the end of a telomere.

8oxoG at G^1 or G^3 Causes Partial Unfolding of the Telomeric DNA That Allows Telomerase to Engage. Our previous and current findings corroborate a model that accessibility of telomeric DNA to external factors such as a C strand and POT1 depends on the structural status (i.e., any modification that unlocks the folded G4 structure can increase the accessibility depending on the extent of the disruption). Nevertheless, telomerase binding does not follow this order as demonstrated by the constructs with 8oxoG at G^1 and G^3, which are largely inaccessible to the C strand but attain 100% telomerase binding (Figure 4A). To further examine a possible rearrangement of the DNA conformation that may not be visible in our current design, we prepared alternatively labeled DNA FRET constructs that provide a better resolution of G4 conformations.[38,50] The Cy5 dye was relocated away from the end of the duplex to a phosphate between the fourth and fifth base from the 5′ end (Top4.5) (Figure 5A). This new

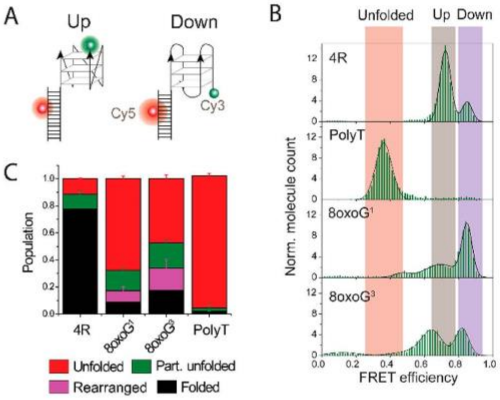

Figure 5. 8oxoG at G^1 and G^3 induces subtle conformational changes that allow telomerase to engage. (A) DNA construct design with an alternative dye position. The Cy5 dye is at the phosphate group between the fourth and fifth bases from the 5′ end (Top4.5). (B) FRET histogram of undamaged DNA and constructs with 8oxoG at G^1 or G^3 displaying up (gray), down (purple), and unfolded populations (orange). (C) Distribution of single-molecule traces observed with the alternative (Top4.5) Cy5 dye position. The molecules with subtle conformational changes (magenta), which were not detectable with the original Cy5 position, may allow telomerase binding to transiently unfolded molecules. Error bars represent the standard error obtained from randomized sampling process of trace distributions.

configuration enables us to distinguish between different G4 conformations as demonstrated by the smFRET histogram of undamaged 4R splitting into one dominant peak at 0.7 FRET (80%) and a minor peak at 0.85, while polyT has a single peak at 0.35 (Figure 5B).

In the Top4.5 FRET constructs, the G^1-8oxoG and G^3-8oxoG substitutions display a different pattern of FRET histograms. While the G^1-8oxoG construct shows a dominant FRET peak at the lower value, 0.7 with a small shoulder, the G^3-8oxoG construct produces slightly shifted FRET peaks at 0.65 and 0.8 with similar peak sizes (Figure 5B). It is difficult, and not our intention, to distinguish which FRET peak corresponds to which particular G4 conformer, because our FRET construct can report only on the distance between the 5′ and 3′ ends of the $(TTAGGG)_4$ sequence. In Top4.5, all of the G4 conformations that have the same relative orientation

https://dx.doi.org/10.1021/acs.biochem.0c00434
Biochemistry XXXX, XXX, XXX−XXX

between the first and fourth TTAGGG repeat may have a similar FRET value. Therefore, parallel and hybrid-1 G4 [both first and fourth repeats have the same 3′ to 5′ orientation ("up" in Figure 5A)] as well as antiparallel and hybrid-2 [fourth strand has the opposite 3′ to 5′ orientation ("down" in Figure 5A)] will be in one FRET peak. This bias might be explained by an 8oxoG preference for the *syn* conformation as reported in a recent NMR study.[7] While the smFRET assay cannot define the precise G4 structure, it can reveal structural dynamics caused by the lesion. We performed analysis of single-molecule trajectories with the same algorithm used in the previous analysis with the adjusted FRET cutoff values. In addition to the previous categories of folded, partially unfolded, and unfolded, we assigned the additional fluctuating FRET transitions between the two FRET states as "rearranged" (Figure 5C and Figure S6). The fraction of the rearranged population (purple in Figure 5C) is calculated from the difference between the partial unfolded population obtained from the Top4.5 construct (brown in Figure S6) and the construct with the original Cy5 position (green in Figure S1). This "rearranged" population was not identified in the original dye position because the FRET fluctuation range was mixed with the rest of the partially unfolded species. Interestingly, the comparison between this FRET construct (Figure 5A) with the previous FRET construct (Figure 1B) reveals that the constructs with 8oxoG in both G^1 and G^3 positions undergo high levels of dynamic conformational exchange (Figure 5B). This was masked in the original FRET construct due to the dye locations, which were insensitive to this range of distance change (Figure 3A). Taken together, the increased population of molecules undergoing rearrangement (purple), partial unfolding (green), and unfolding (red) observed in both Top4.5 G^1-8oxoG and G^3-8oxoG constructs reveals a high degree of dynamics induced by both single-site lesions, which may contribute to the unusually high accessibility of telomerase.

Telomerase Binding Depends on an Open Telomeric Structure and Base Pairing with the RNA Template. Having shown that telomerase can bind to damaged telomeric DNA with the conformational rearrangement, we asked if the low level of telomerase binding to mutant telomeric DNA (Figure 4A) is due primarily to mismatches between the telomeric primer and the telomerase RNA template. To test this, we moved the mutation to an internal, second repeat (R2) location such that the structural disruption is induced while allowing for correct base pairing with the telomerase RNA template (Figure 6A). We observed that the constructs with a G to T mutation at G^1 and G^2 positions in the R2 repeat produce FRET histograms and dynamic trace distributions similar to the terminal repeat T mutations (Figure 6A and Figure S7). Consistently, the accessibilities of the C strand and POT1 to constructs in both the second (R2) and terminal (R4) repeats were also comparable, confirming the same degree of structural disruption induced by both mutant positions (Figure S8A,B). Strikingly, the level of binding of telomerase to the R2 mutants reached 100%, dramatically higher than that of the corresponding mutation in the terminal repeat of R4 (Figure S8C). Likewise, the telomerase extension activity of all C, T, and A mutations at G^1 and G^2 positions in R2 was substantially enhanced (Figure 6B,C), revealing recovered extension activity by all six R2 mutants. This result strongly indicates that telomerase extension activity is greatly enhanced when the G4 structure is disrupted, yet recovery of

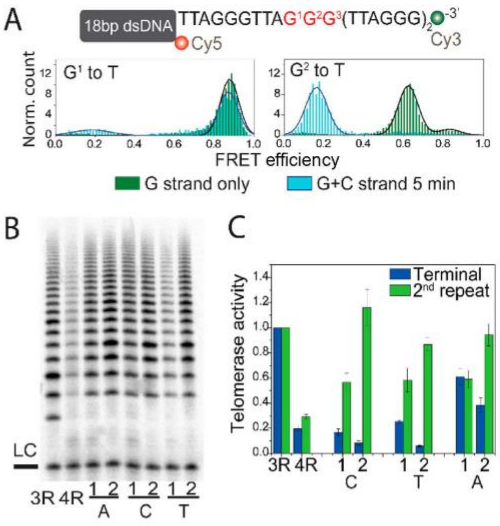

Figure 6. Mutations at the upstream TTAGGG induce conformational changes that allow telomerase to engage. (A) FRET histogram of T mutations at G^1 and G^2 of the second TTAGGG repeat alone (green) or upon C strand addition (light blue). (B) Gel image of the telomerase activity assay for constructs with the indicated base mutation at G^1 and G^2 of the second TTAGGG repeat. (C) Quantified telomerase activity from constructs with mutations at G^1 and G^2 of the second and terminal repeats. The telomerase activity of terminal repeat mutant constructs (blue) was extracted from Figure 4C and is shown here for comparison.

telomerase binding and extension activity requires correct base pairing between the telomeric overhang and RNA template. In other words, mutations can have a significant impact up- or downregulating telomerase activity in a manner that is highly dependent on position.

■ DISCUSSION

The G-quadruplex (G4) is a common noncanonical secondary structure that forms in telomeric single-stranded overhangs, yet the physiological role of this structure in telomeres remains ambiguous. Studies of G4-stabilizing ligands and G4-destabilizing base modifications suggest G4 might play a regulatory role in telomere integrity.[49,65,66] Many structural studies reported that base modifications disrupt the hydrogen bonding between guanines and, therefore, destabilize the G4 formed in telomeric overhangs.[5−7,41,42] In this study, we systematically tested at the single-molecule level the effects on the structural dynamics of two common DNA lesions, 8oxoG and O6mG, and all possible point mutations, C, T, and A, at the three terminal guanine positions of telomeric DNA overhangs. We took advantage of single-molecule resolution to confirm the formation of unimolecular structure in all of the constructs, because ensemble assays cannot distinguish bimolecular G4 from unimolecular G4.[41,42] We further discerned whether multiple conformations and structural dynamics coexist in molecules sharing the exact same base sequence and chemical configuration. Using our newly developed smFRET analytical tool, we categorized >100000 smFRET trajectories into different classes of dynamic

https://dx.doi.org/10.1021/acs.biochem.0c00434
Biochemistry XXXX, XXX, XXX−XXX

Scheme 1. (A) Lesions in an Overhang May Induce Telomerase Activation, and (B) a Base Modification Lesion Might Induce a Long-Term "Unlocking" Effect in the Telomere

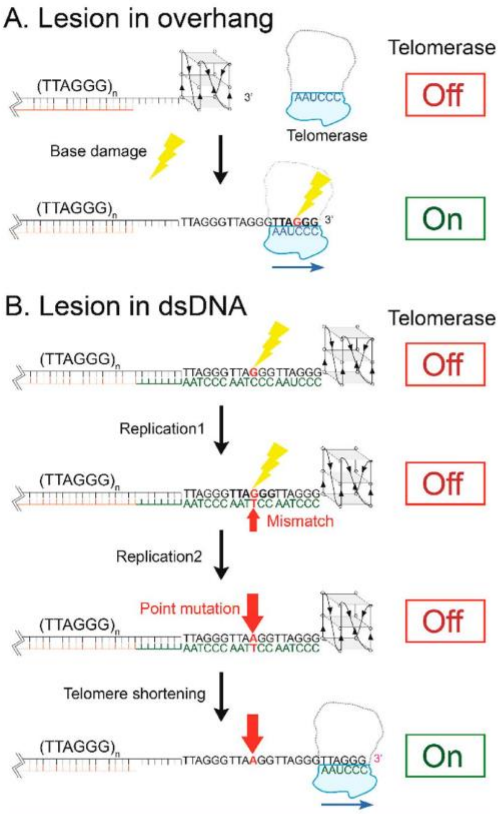

conformational changes based on the most unfolded state (lowest FRET value) each single molecule experienced. The FRET values of the unstructured polyT and stably folded G4 were used as markers for unfolded and fully folded G4, respectively. Our data reveal that DNA lesions and mutations shift the distribution of the unfolded, partially folded, or fully folded G4 conformations, to varying extents. Our single-molecule approach reveals how base modifications that affect Hoogsteen hydrogen bonding alter the dynamics of G4 structure, in addition to causing the conformational changes shown by NMR and CD approaches.[5−7,41,42]

Our results strongly support the conclusion from earlier studies that modification of guanines in telomeric overhang disrupts and destabilizes the G4 structure,[6,42] which is most pronounced when the central guanine (G^2) is modified or mutated.[6] We also showed that lesions and mutations at G^1 and G^3 cause a G4 structural distortion that differs from the undamaged 4R. This result is consistent with a recent NMR study that shows that G4 with 8oxoG at the central guanine (G^2) prefers a different strand orientation from 8oxoG at the other two guanines (G^1 and G^3).[7] Interestingly, our new data reveal that this position-dependent effect extends to all of the modified guanines and mutations we tested, although the extent of G4 disruption and the corresponding accessibility vary with the type of modification. Our results suggest that the structural disruption caused by lesions and mutations might be a general phenomenon arising from any base changes in the telomeric overhang GGG runs.

Using our new method of classifying structural dynamics, we discovered two general rankings that affect the strength of G4 structure disruption independently: (1) $G^2 > G^3 \geq G^1$, and (2) O6mG > 8oxoG ≥ A > T > C. This trend of different guanine positions can be explained by the shared potassium ion shown in the X-ray crystal structure.[33,67] Losing or misaligning one guanine reduced the number of oxygens that interact with the K^+ between adjacent G-quartets. Guanine lesions or mutations at either end, G^1 or G^3, allow the other two G-quartets to form and be stabilized by one shared K^+, while losing a guanine in the central G-quartet makes it unable to hold the K^+ between G-quartets. The differences observed among various base modifications can be explained by steric hindrance and electrostatic repulsion that interfere with Hoogsteen base pairing. Such effects will be more prominent with larger purines than pyrimidines. In addition, the smallest distortion caused by cytosine substitution may arise from the Watson−Crick base pairing with the guanine that may stabilize G4. In contrast, substitution with adenine or modified guanines not only eliminates the proper electron donor and acceptor needed for Hoogsteen base pairing but also repels the other three guanines from the G-quartet, perturbing sugar puckering and further disrupting G4 structure. It is worth noting that reports[68,69] show telomeric G4 in buffer containing K^+ is kinetically more stable and is less accessible than the G4 in Na^+. Throughout our study, we used 100 mM K^+, which is similar to the intracellular environment and physiologically relevant. At this K^+ concentration, G4 is stable and undergoes very few conformational changes. However, we found the base lesions and mutations can still unfold this stable G4, which is reported to be a poor telomerase substrate.[61] We reason this destabilization effect and the consequential increase in telomerase accessibility would not be as pronounced in a low-K^+ or no K^+ environment.

Remarkably, the correlation between structural disruption and telomeric DNA accessibility did not apply for telomerase binding and extension activity. First, all lesions led to a high level of telomerase binding regardless of the damage positions. In addition, our results suggest that telomerase can gain access to weakly folded structures that POT1 or the C strand cannot bind, suggesting an active unfolding mechanism of telomerase. Despite the chemical base changes, telomerase may engage with the damaged guanine that can base pair with the RNA template in telomerase. The binding and extension of telomerase were correlated in all cases except for 8oxoG and O6mG at the G^3 position, which showed reduced activity due to the lesions acting as terminating bases.[49,64] In contrast, all mutations (except A in the terminal repeat) showed greatly diminished telomerase binding and extension activity. We tested two possible reasons: structural distortion versus imperfect base pairing. Our data support the second scenario. First, all of the G^2 mutant constructs have high accessibility to the C strand, arguing against the structural disruption explanation. Second, the detrimental effects of mismatches were confirmed by relocating the mutation to an upstream repeat (R2). A construct with structural disruption lacking a

https://dx.doi.org/10.1021/acs.biochem.0c00434
Biochemistry XXXX, XXX, XXX−XXX

mismatch with the RNA template was sufficient to fully recover telomerase binding and activity, implicating the imperfect base pairing as the primary cause.

Importantly, our findings provide evidence for a longer-lasting and inheritable consequence of telomeric base damage. First, when a lesion occurs at the telomeric overhang, it can disrupt G4 structure, allowing telomerase to access the 3′ end and triggering telomerase extension activity, which can lead to oncogenic consequences in premalignant cells (Scheme 1A). The damaged base positioned upstream after several cycles of TTAGGG addition can destabilize the G4 structure forming in the DNA product between contacts with the telomerase catalytic site and the anchor site that resides in the TEN domain,[70] which prevents DNA dissociation and enhances telomerase processivity. This hypothesis is supported by a report that proposed nascent telomeric DNA folding in the product can trigger product dissociation.[71] Moreover, unless repaired, 8oxoG and O6mG lesions arising in the extended overhang, or in the duplex telomeric region, can cause mutations upon C strand fill-in or replication of the complementary C-rich strand, respectively. For example, O6meG will mispair with T during replication and cause a G to A mutation in the G-rich strand. In other words, base lesions in the duplex can be converted to point mutations within telomere DNA. The mutation may reach the overhang through telomere erosion if telomerase is absent or inhibited, and thereby disrupt G4 formation and enable telomerase extension. Therefore, DNA lesions in the telomeres that are converted to mutations may upregulate telomerase activity after rounds of cell replication (Scheme 1B). In summary, our biophysical studies reveal that DNA lesions and consequent mutations can promote or inhibit telomerase activity depending on where the base modification arises.

■ ASSOCIATED CONTENT

Supporting Information

The Supporting Information is available free of charge at https://pubs.acs.org/doi/10.1021/acs.biochem.0c00434.

List of oligonucleotides, table of binding kinetics, and extra figures of data (PDF)

■ AUTHOR INFORMATION

Corresponding Author

Sua Myong − *Thomas C. Jenkins Department of Biophysics, Johns Hopkins University, Baltimore, Maryland 21218, United States; Physics Frontier Center (Center for Physics of Living Cells), University of Illinois, Urbana, Illinois 61801, United States;* orcid.org/0000-0001-9098-3423; Email: smyong@jhu.edu

Authors

Hui-Ting Lee − *Thomas C. Jenkins Department of Biophysics, Johns Hopkins University, Baltimore, Maryland 21218, United States*

Samantha Sanford − *Department of Environmental and Occupational Health, University of Pittsburgh Graduate School of Public Health and University of Pittsburgh Medical Center Hillman Cancer Center, Pittsburgh, Pennsylvania 15261, United States*

Tapas Paul − *Thomas C. Jenkins Department of Biophysics, Johns Hopkins University, Baltimore, Maryland 21218, United States*

Joshua Choe − *Thomas C. Jenkins Department of Biophysics, Johns Hopkins University, Baltimore, Maryland 21218, United States*

Arindam Bose − *Department of Environmental and Occupational Health, University of Pittsburgh Graduate School of Public Health and University of Pittsburgh Medical Center Hillman Cancer Center, Pittsburgh, Pennsylvania 15261, United States*

Patricia L. Opresko − *Department of Environmental and Occupational Health, University of Pittsburgh Graduate School of Public Health and University of Pittsburgh Medical Center Hillman Cancer Center, Pittsburgh, Pennsylvania 15261, United States*

Complete contact information is available at: https://pubs.acs.org/10.1021/acs.biochem.0c00434

Author Contributions

S.S. and T.P. contributed equally to this work. The manuscript was written through contributions of H.-T.L., T.P., P.L.O., and S.M. The experiment was performed by H.-T.L., T.P., S.S., and J.C. All authors have given approval to the final version of the manuscript.

Funding

This work was supported by Grant R01 CA 207342-01A1 (all members of the Myong and Opresko laboratory) and Grant R35 ES030396 to P.L.O.

Notes

The authors declare no competing financial interest.

■ ACKNOWLEDGMENTS

The authors thank Dr. Taekjip Ha for helpful discussion about telomere G-quadruplexes. The authors especially appreciate Ms. Olivia Yang's help in developing the MatLab script used for semiautomatic analysis of smFRET trajectories. The authors thank Xander Orenstein for assistance with POT1 purification.

■ ABBREVIATIONS

G4, G-quadruplex; smFRET, single-molecule Förster resonance energy transfer; SiMPull, single-molecule pull-down.

■ REFERENCES

(1) Cadet, J., and Wagner, J. R. (2013) DNA base damage by reactive oxygen species, oxidizing agents, and UV radiation. *Cold Spring Harbor Perspect. Biol. 5*, a012559.

(2) Lindahl, T. (1993) Instability and decay of the primary structure of DNA. *Nature 362*, 709−715.

(3) Lipscomb, L. A., Peek, M. E., Morningstar, M. L., Verghis, S. M., Miller, E. M., Rich, A., Essigmann, J. M., and Williams, L. D. (1995) X-ray structure of a DNA decamer containing 7,8-dihydro-8-oxoguanine. *Proc. Natl. Acad. Sci. U. S. A. 92*, 719−723.

(4) Singh, S. K., Szulik, M. W., Ganguly, M., Khutsishvili, I., Stone, M. P., Marky, L. A., and Gold, B. (2011) Characterization of DNA with an 8-oxoguanine modification. *Nucleic Acids Res. 39*, 6789−6801.

(5) Cheong, V. V., Heddi, B., Lech, C. J., and Phan, A. T. (2015) Xanthine and 8-oxoguanine in G-quadruplexes: formation of a G.G.X.O tetrad. *Nucleic Acids Res. 43*, 10506−10514.

(6) Vorlickova, M., Tomasko, M., Sagi, A. J., Bednarova, K., and Sagi, J. (2012) 8-oxoguanine in a quadruplex of the human telomere DNA sequence. *FEBS J. 279*, 29−39.

(7) Bielskute, S., Plavec, J., and Podbevsek, P. (2019) Impact of Oxidative Lesions on the Human Telomeric G-Quadruplex. *J. Am. Chem. Soc. 141*, 2594−2603.

(8) Takahashi, S., Kim, K. T., Podbevsek, P., Plavec, J., Kim, B. H., and Sugimoto, N. (2018) Recovery of the Formation and Function of Oxidized G-Quadruplexes by a Pyrene-Modified Guanine Tract. *J. Am. Chem. Soc. 140*, 5774−5783.
(9) Kamiya, H., Miura, K., Ishikawa, H., Inoue, H., Nishimura, S., and Ohtsuka, E. (1992) c-Ha-ras containing 8-hydroxyguanine at codon 12 induces point mutations at the modified and adjacent positions. *Cancer Res. 52*, 3483−3485.
(10) Kamiya, H., Murata-Kamiya, N., Koizume, S., Inoue, H., Nishimura, S., and Ohtsuka, E. (1995) 8-Hydroxyguanine (7,8-dihydro-8-oxoguanine) in hot spots of the c-Ha-ras gene: effects of sequence contexts on mutation spectra. *Carcinogenesis 16*, 883−889.
(11) Cooke, M. S., Evans, M. D., Dizdaroglu, M., and Lunec, J. (2003) Oxidative DNA damage: mechanisms, mutation, and disease. *FASEB J. 17*, 1195−1214.
(12) Drablos, F., Feyzi, E., Aas, P. A., Vaagbo, C. B., Kavli, B., Bratlie, M. S., Pena-Diaz, J., Otterlei, M., Slupphaug, G., and Krokan, H. E. (2004) Alkylation damage in DNA and RNA–repair mechanisms and medical significance. *DNA Repair 3*, 1389−1407.
(13) Bauer, N. C., Corbett, A. H., and Doetsch, P. W. (2015) The current state of eukaryotic DNA base damage and repair. *Nucleic Acids Res. 43*, 10083−10101.
(14) Cimino-Reale, G., Pascale, E., Battiloro, E., Starace, G., Verna, R., and D'Ambrosio, E. (2001) The length of telomeric G-rich strand 3′-overhang measured by oligonucleotide ligation assay. *Nucleic Acids Res. 29*, 35e.
(15) Palm, W., and de Lange, T. (2008) How shelterin protects mammalian telomeres. *Annu. Rev. Genet. 42*, 301−334.
(16) Baumann, P., and Cech, T. R. (2001) Pot1, the putative telomere end-binding protein in fission yeast and humans. *Science 292*, 1171−1175.
(17) Rodriguez, R., Muller, S., Yeoman, J. A., Trentesaux, C., Riou, J. F., and Balasubramanian, S. (2008) A novel small molecule that alters shelterin integrity and triggers a DNA-damage response at telomeres. *J. Am. Chem. Soc. 130*, 15758−15759.
(18) Abreu, E., Aritonovska, E., Reichenbach, P., Cristofari, G., Culp, B., Terns, R. M., Lingner, J., and Terns, M. P. (2010) TIN2-tethered TPP1 recruits human telomerase to telomeres in vivo. *Mol. Cell. Biol. 30*, 2971−2982.
(19) Hwang, H., Buncher, N., Opresko, P. L., and Myong, S. (2012) POT1-TPP1 regulates telomeric overhang structural dynamics. *Structure 20*, 1872−1880.
(20) Kawanishi, S., and Oikawa, S. (2004) Mechanism of telomere shortening by oxidative stress. *Ann. N. Y. Acad. Sci. 1019*, 278−284.
(21) Oikawa, S., Tada-Oikawa, S., and Kawanishi, S. (2001) Site-specific DNA damage at the GGG sequence by UVA involves acceleration of telomere shortening. *Biochemistry 40*, 4763−4768.
(22) Rhee, D. B., Ghosh, A., Lu, J., Bohr, V. A., and Liu, Y. (2011) Factors that influence telomeric oxidative base damage and repair by DNA glycosylase OGG1. *DNA Repair 10*, 34−44.
(23) Yarosh, D. B. (1985) The role of O6-methylguanine-DNA methyltransferase in cell survival, mutagenesis and carcinogenesis. *Mutat. Res., DNA Repair Rep. 145*, 1−16.
(24) Rasouli-Nia, A., Sigbhat-Ullah, Mirzayans, R., Paterson, M. C., and Day, R. S., 3rd. (1994) On the quantitative relationship between O6-methylguanine residues in genomic DNA and production of sister-chromatid exchanges, mutations and lethal events in a Mer- human tumor cell line. *Mutat. Res., DNA Repair 314*, 99−113.
(25) Morin, G. B. (1989) The human telomere terminal transferase enzyme is a ribonucleoprotein that synthesizes TTAGGG repeats. *Cell 59*, 521−529.
(26) Cristofari, G., and Lingner, J. (2006) Telomere length homeostasis requires that telomerase levels are limiting. *EMBO J. 25*, 565−574.
(27) Blasco, M. A. (2005) Telomeres and human disease: ageing, cancer and beyond. *Nat. Rev. Genet. 6*, 611−622.
(28) Zhu, X., Han, W., Xue, W., Zou, Y., Xie, C., Du, J., and Jin, G. (2016) The association between telomere length and cancer risk in population studies. *Sci. Rep. 6*, 22243.
(29) Lei, M., Zaug, A. J., Podell, E. R., and Cech, T. R. (2005) Switching human telomerase on and off with hPOT1 protein in vitro. *J. Biol. Chem. 280*, 20449−20456.
(30) de Lange, T. (2005) Shelterin: the protein complex that shapes and safeguards human telomeres. *Genes Dev. 19*, 2100−2110.
(31) Ray, S., Bandaria, J. N., Qureshi, M. H., Yildiz, A., and Balci, H. (2014) G-quadruplex formation in telomeres enhances POT1/TPP1 protection against RPA binding. *Proc. Natl. Acad. Sci. U. S. A. 111*, 2990−2995.
(32) Hwang, H., Kreig, A., Calvert, J., Lormand, J., Kwon, Y., Daley, J. M., Sung, P., Opresko, P. L., and Myong, S. (2014) Telomeric overhang length determines structural dynamics and accessibility to telomerase and ALT-associated proteins. *Structure 22*, 842−853.
(33) Parkinson, G. N., Lee, M. P., and Neidle, S. (2002) Crystal structure of parallel quadruplexes from human telomeric DNA. *Nature 417*, 876−880.
(34) Dai, J., Punchihewa, C., Ambrus, A., Chen, D., Jones, R. A., and Yang, D. (2007) Structure of the intramolecular human telomeric G-quadruplex in potassium solution: a novel adenine triple formation. *Nucleic Acids Res. 35*, 2440−2450.
(35) Phan, A. T., Kuryavyi, V., Luu, K. N., and Patel, D. J. (2007) Structure of two intramolecular G-quadruplexes formed by natural human telomere sequences in K+ solution. *Nucleic Acids Res. 35*, 6517−6525.
(36) Schultze, P., Hud, N. V., Smith, F. W., and Feigon, J. (1999) The effect of sodium, potassium and ammonium ions on the conformation of the dimeric quadruplex formed by the Oxytricha nova telomere repeat oligonucleotide d(G(4)T(4)G(4)). *Nucleic Acids Res. 27*, 3018−3028.
(37) Burge, S., Parkinson, G. N., Hazel, P., Todd, A. K., and Neidle, S. (2006) Quadruplex DNA: sequence, topology and structure. *Nucleic Acids Res. 34*, 5402−5415.
(38) Tippana, R., Xiao, W., and Myong, S. (2014) G-quadruplex conformation and dynamics are determined by loop length and sequence. *Nucleic Acids Res. 42*, 8106−8114.
(39) Lee, J. Y., Okumus, B., Kim, D. S., and Ha, T. (2005) Extreme conformational diversity in human telomeric DNA. *Proc. Natl. Acad. Sci. U. S. A. 102*, 18938−18943.
(40) Ambrus, A., Chen, D., Dai, J., Bialis, T., Jones, R. A., and Yang, D. (2006) Human telomeric sequence forms a hybrid-type intramolecular G-quadruplex structure with mixed parallel/antiparallel strands in potassium solution. *Nucleic Acids Res. 34*, 2723−2735.
(41) Zhao, A., Zhao, C., Tateishi-Karimata, H., Ren, J., Sugimoto, N., and Qu, X. (2016) Incorporation of O(6)-methylguanine restricts the conformational conversion of the human telomere G-quadruplex under molecular crowding conditions. *Chem. Commun. (Cambridge, U. K.) 52*, 1903−1906.
(42) Mekmaysy, C. S., Petraccone, L., Garbett, N. C., Ragazzon, P. A., Gray, R., Trent, J. O., and Chaires, J. B. (2008) Effect of O6-Methylguanine on the Stability of G-Quadruplex DNA. *J. Am. Chem. Soc. 130*, 6710−6711.
(43) Johnson, J. E., Smith, J. S., Kozak, M. L., and Johnson, F. B. (2008) In vivo veritas: using yeast to probe the biological functions of G-quadruplexes. *Biochimie 90*, 1250−1263.
(44) Maizels, N. (2006) Dynamic roles for G4 DNA in the biology of eukaryotic cells. *Nat. Struct. Mol. Biol. 13*, 1055−1059.
(45) Macrae, I. J., Zhou, K., Li, F., Repic, A., Brooks, A. N., Cande, W. Z., Adams, P. D., and Doudna, J. A. (2006) Structural basis for double-stranded RNA processing by Dicer. *Science 311*, 195−198.
(46) Huppert, J. L. (2008) Hunting G-quadruplexes. *Biochimie 90*, 1140−1148.
(47) Lipps, H. J., and Rhodes, D. (2009) G-quadruplex structures: in vivo evidence and function. *Trends Cell Biol. 19*, 414−422.
(48) Biffi, G., Tannahill, D., McCafferty, J., and Balasubramanian, S. (2013) Quantitative visualization of DNA G-quadruplex structures in human cells. *Nat. Chem. 5*, 182−186.
(49) Fouquerel, E., Lormand, J., Bose, A., Lee, H. T., Kim, G. S., Li, J., Sobol, R. W., Freudenthal, B. D., Myong, S., and Opresko, P. L.

https://dx.doi.org/10.1021/acs.biochem.0c00434
Biochemistry XXXX, XXX, XXX−XXX

(2016) Oxidative guanine base damage regulates human telomerase activity. *Nat. Struct. Mol. Biol. 23*, 1092−1100.
(50) Lee, H. T., Bose, A., Lee, C. Y., Opresko, P. L., and Myong, S. (2017) Molecular mechanisms by which oxidative DNA damage promotes telomerase activity. *Nucleic Acids Res. 45*, 11752−11765.
(51) Sowd, G., Lei, M., and Opresko, P. L. (2008) Mechanism and substrate specificity of telomeric protein POT1 stimulation of the Werner syndrome helicase. *Nucleic Acids Res. 36*, 4242−4256.
(52) Lei, M., Podell, E. R., and Cech, T. R. (2004) Structure of human POT1 bound to telomeric single-stranded DNA provides a model for chromosome end-protection. *Nat. Struct. Mol. Biol. 11*, 1223−1229.
(53) Hwang, H., Opresko, P., and Myong, S. (2015) Single-molecule real-time detection of telomerase extension activity. *Sci. Rep. 4*, 6391.
(54) Hwang, H., and Myong, S. (2014) Protein induced fluorescence enhancement (PIFE) for probing protein-nucleic acid interactions. *Chem. Soc. Rev. 43*, 1221−1229.
(55) Latrick, C. M., and Cech, T. R. (2010) POT1-TPP1 enhances telomerase processivity by slowing primer dissociation and aiding translocation. *EMBO J. 29*, 924−933.
(56) Zaug, A. J., Podell, E. R., Nandakumar, J., and Cech, T. R. (2010) Functional interaction between telomere protein TPP1 and telomerase. *Genes Dev. 24*, 613−622.
(57) Andersen, O. S. (2013) *Cellular electrolyte metabolism*, Springer, New York.
(58) Pedroso, I. M., Duarte, L. F., Yanez, G., Burkewitz, K., and Fletcher, T. M. (2007) Sequence specificity of inter- and intramolecular G-quadruplex formation by human telomeric DNA. *Biopolymers 87*, 74−84.
(59) Tomaško, M., Vorlíčková, M., and Sagi, J. (2009) Substitution of adenine for guanine in the quadruplex-forming human telomere DNA sequence G3(T2AG3)3. *Biochimie 91*, 171−179.
(60) Bao, H. L., Liu, H. S., and Xu, Y. (2019) Hybrid-type and two-tetrad antiparallel telomere DNA G-quadruplex structures in living human cells. *Nucleic Acids Res. 47*, 4940−4947.
(61) Zaug, A. J., Podell, E. R., and Cech, T. R. (2005) Human POT1 disrupts telomeric G-quadruplexes allowing telomerase extension in vitro. *Proc. Natl. Acad. Sci. U. S. A. 102*, 10864−10869.
(62) Loayza, D., Parsons, H., Donigian, J., Hoke, K., and de Lange, T. (2004) DNA binding features of human POT1: a nonamer 5′-TAGGGTTAG-3′ minimal binding site, sequence specificity, and internal binding to multimeric sites. *J. Biol. Chem. 279*, 13241−13248.
(63) Zahler, A. M., Williamson, J. R., Cech, T. R., and Prescott, D. M. (1991) Inhibition of telomerase by G-quartet DNA structures. *Nature 350*, 718−720.
(64) Aeby, E., Ahmed, W., Redon, S., Simanis, V., and Lingner, J. (2016) Peroxiredoxin 1 Protects Telomeres from Oxidative Damage and Preserves Telomeric DNA for Extension by Telomerase. *Cell Rep. 17*, 3107−3114.
(65) Moye, A. L., Porter, K. C., Cohen, S. B., Phan, T., Zyner, K. G., Sasaki, N., Lovrecz, G. O., Beck, J. L., and Bryan, T. M. (2015) Telomeric G-quadruplexes are a substrate and site of localization for human telomerase. *Nat. Commun. 6*, 7643.
(66) Yaku, H., Murashima, T., Miyoshi, D., and Sugimoto, N. (2012) Specific binding of anionic porphyrin and phthalocyanine to the G-quadruplex with a variety of in vitro and in vivo applications. *Molecules 17*, 10586−10613.
(67) Luu, K. N., Phan, A. T., Kuryavyi, V., Lacroix, L., and Patel, D. J. (2006) Structure of the human telomere in K+ solution: an intramolecular (3 + 1) G-quadruplex scaffold. *J. Am. Chem. Soc. 128*, 9963−9970.
(68) Wang, Z. F., Li, M. H., Hsu, S. T., and Chang, T. C. (2014) Structural basis of sodium-potassium exchange of a human telomeric DNA quadruplex without topological conversion. *Nucleic Acids Res. 42*, 4723−4733.
(69) Siebenmorgen, T., and Zacharias, M. (2017) Origin of Ion Specificity of Telomeric DNA G-Quadruplexes Investigated by Free-Energy Simulations. *Biophys. J. 112*, 2280−2290.
(70) Nguyen, T. H. D., Tam, J., Wu, R. A., Greber, B. J., Toso, D., Nogales, E., and Collins, K. (2018) Cryo-EM structure of substrate-bound human telomerase holoenzyme. *Nature 557*, 190−195.
(71) Jansson, L. I., Hentschel, J., Parks, J. W., Chang, T. R., Lu, C., Baral, R., Bagshaw, C. R., and Stone, M. D. (2019) Telomere DNA G-quadruplex folding within actively extending human telomerase. *Proc. Natl. Acad. Sci. U. S. A. 116*, 9350−9359.

https://dx.doi.org/10.1021/acs.biochem.0c00434
Biochemistry XXXX, XXX, XXX−XXX

Appendix G Practice makes progress

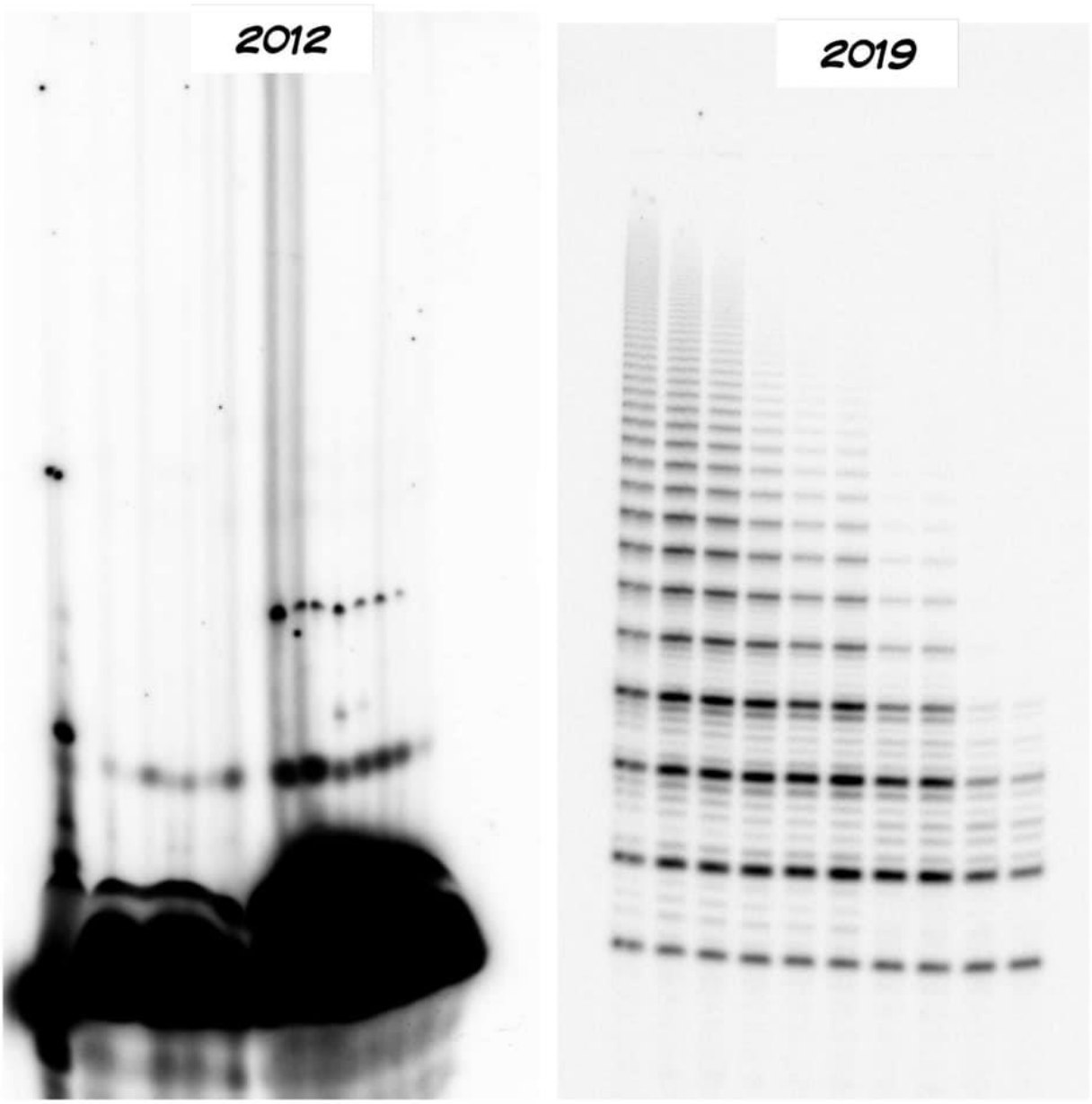

Figure 27. "Practice doesn't make perfect! Practice makes progress!" – Wise words by Cami Opresko. Direct telomerase assays from 2012 vs. 2019.

Bibliography

1. Muller, H. The remaking of chromosomes. *Collecting Net* **13**, 181-198 (1934).

2. McClintock, B. Cytological observations of deficiencies involving known genes, translocations and an inversion in Zea mays. *Missouri Agricultural Exp. Station Res. Bull.* **163**, 1-30 (1931).

3. Hayflick, L. & Moorhead, P.S. The serial cultivation of human diploid cell strains. *Exp Cell Res* **25**, 585-621 (1961).

4. Watson, J.D. Origin of concatemeric T7 DNA. *Nat New Biol* **239**, 197-201 (1972).

5. Olovnikov, A.M. A theory of marginotomy. The incomplete copying of template margin in enzymic synthesis of polynucleotides and biological significance of the phenomenon. *J Theor Biol* **41**, 181-90 (1973).

6. Blackburn, E.H. & Gall, J.G. A tandemly repeated sequence at the termini of the extrachromosomal ribosomal RNA genes in Tetrahymena. *J Mol Biol* **120**, 33-53 (1978).

7. Szostak, J.W. & Blackburn, E.H. Cloning yeast telomeres on linear plasmid vectors. *Cell* **29**, 245-55 (1982).

8. Greider, C.W. & Blackburn, E.H. Identification of a specific telomere terminal transferase activity in Tetrahymena extracts. *Cell* **43**, 405-13 (1985).

9. de Lange, T. Shelterin: the protein complex that shapes and safeguards human telomeres. *Genes Dev* **19**, 2100-10 (2005).

10. Hockemeyer, D., Daniels, J.P., Takai, H. & de Lange, T. Recent expansion of the telomeric complex in rodents: Two distinct POT1 proteins protect mouse telomeres. *Cell* **126**, 63-77 (2006).

11. Wu, L. et al. Pot1 deficiency initiates DNA damage checkpoint activation and aberrant homologous recombination at telomeres. *Cell* **126**, 49-62 (2006).

12. Bianchi, A. et al. TRF1 binds a bipartite telomeric site with extreme spatial flexibility. *EMBO J* **18**, 5735-44 (1999).

13. Nishikawa, T. et al. Solution structure of a telomeric DNA complex of human TRF1. *Structure* **9**, 1237-51 (2001).

14. Lei, M., Podell, E.R. & Cech, T.R. Structure of human POT1 bound to telomeric single-stranded DNA provides a model for chromosome end-protection. *Nat Struct Mol Biol* **11**, 1223-9 (2004).

15. Wang, F. et al. The POT1-TPP1 telomere complex is a telomerase processivity factor. *Nature* **445**, 506-10 (2007).

16. Takai, K.K., Hooper, S., Blackwood, S., Gandhi, R. & de Lange, T. In vivo stoichiometry of shelterin components. *J Biol Chem* **285**, 1457-67 (2010).

17. Moyzis, R.K. et al. A highly conserved repetitive DNA sequence, (TTAGGG)n, present at the telomeres of human chromosomes. *Proc Natl Acad Sci U S A* **85**, 6622-6 (1988).

18. Greider, C.W. & Blackburn, E.H. A telomeric sequence in the RNA of Tetrahymena telomerase required for telomere repeat synthesis. *Nature* **337**, 331-7 (1989).

19. Chen, J.L. & Greider, C.W. Determinants in mammalian telomerase RNA that mediate enzyme processivity and cross-species incompatibility. *EMBO J* **22**, 304-14 (2003).

20. Theimer, C.A., Blois, C.A. & Feigon, J. Structure of the human telomerase RNA pseudoknot reveals conserved tertiary interactions essential for function. *Mol Cell* **17**, 671-82 (2005).

21. Shefer, K. et al. A triple helix within a pseudoknot is a conserved and essential element of telomerase RNA. *Mol Cell Biol* **27**, 2130-43 (2007).

22. Lai, C.K., Miller, M.C. & Collins, K. Roles for RNA in telomerase nucleotide and repeat addition processivity. *Mol Cell* **11**, 1673-83 (2003).

23. Qi, X. et al. RNA/DNA hybrid binding affinity determines telomerase template-translocation efficiency. *EMBO J* **31**, 150-61 (2012).

24. Chen, J.L., Blasco, M.A. & Greider, C.W. Secondary structure of vertebrate telomerase RNA. *Cell* **100**, 503-14 (2000).

25. Tycowski, K.T., Shu, M.D., Kukoyi, A. & Steitz, J.A. A conserved WD40 protein binds the Cajal body localization signal of scaRNP particles. *Mol Cell* **34**, 47-57 (2009).

26. Venteicher, A.S. et al. A human telomerase holoenzyme protein required for Cajal body localization and telomere synthesis. *Science* **323**, 644-8 (2009).

27. Laprade, H. et al. Single-Molecule Imaging of Telomerase RNA Reveals a Recruitment-Retention Model for Telomere Elongation. *Mol Cell* **79**, 115-126 e6 (2020).

28. Nakamura, T.M. et al. Telomerase catalytic subunit homologs from fission yeast and human. *Science* **277**, 955-9 (1997).

29. Lingner, J. et al. Reverse transcriptase motifs in the catalytic subunit of telomerase. *Science* **276**, 561-7 (1997).

30. Nguyen, T.H.D. et al. Cryo-EM structure of substrate-bound human telomerase holoenzyme. *Nature* **557**, 190-195 (2018).

31. Mitchell, M., Gillis, A., Futahashi, M., Fujiwara, H. & Skordalakes, E. Structural basis for telomerase catalytic subunit TERT binding to RNA template and telomeric DNA. *Nat Struct Mol Biol* **17**, 513-8 (2010).

32. Gillis, A.J., Schuller, A.P. & Skordalakes, E. Structure of the Tribolium castaneum telomerase catalytic subunit TERT. *Nature* **455**, 633-7 (2008).

33. Jurczyluk, J. et al. Direct involvement of the TEN domain at the active site of human telomerase. *Nucleic Acids Res* **39**, 1774-88 (2011).

34. Holt, S.E. et al. Functional requirement of p23 and Hsp90 in telomerase complexes. *Genes Dev* **13**, 817-26 (1999).

35. Venteicher, A.S., Meng, Z., Mason, P.J., Veenstra, T.D. & Artandi, S.E. Identification of ATPases pontin and reptin as telomerase components essential for holoenzyme assembly. *Cell* **132**, 945-57 (2008).

36. Xi, L. & Cech, T.R. Inventory of telomerase components in human cells reveals multiple subpopulations of hTR and hTERT. *Nucleic Acids Res* **42**, 8565-77 (2014).

37. Xin, H. et al. TPP1 is a homologue of ciliate TEBP-beta and interacts with POT1 to recruit telomerase. *Nature* **445**, 559-62 (2007).

38. Houghtaling, B.R., Cuttonaro, L., Chang, W. & Smith, S. A dynamic molecular link between the telomere length regulator TRF1 and the chromosome end protector TRF2. *Curr Biol* **14**, 1621-31 (2004).

39. Ye, J.Z. et al. TIN2 binds TRF1 and TRF2 simultaneously and stabilizes the TRF2 complex on telomeres. *J Biol Chem* **279**, 47264-71 (2004).

40. Nandakumar, J. et al. The TEL patch of telomere protein TPP1 mediates telomerase recruitment and processivity. *Nature* **492**, 285-9 (2012).

41. Schmidt, J.C., Dalby, A.B. & Cech, T.R. Identification of human TERT elements necessary for telomerase recruitment to telomeres. *Elife* **3**(2014).

42. Steitz, T.A. DNA polymerases: structural diversity and common mechanisms. *J Biol Chem* **274**, 17395-8 (1999).

43. Wu, R.A., Upton, H.E., Vogan, J.M. & Collins, K. Telomerase Mechanism of Telomere Synthesis. *Annu Rev Biochem* **86**, 439-460 (2017).

44. Wang, H. & Blackburn, E.H. De novo telomere addition by Tetrahymena telomerase in vitro. *EMBO J* **16**, 866-79 (1997).

45. Greider, C.W. Telomerase is processive. *Mol Cell Biol* **11**, 4572-80 (1991).

46. Damm, K. et al. A highly selective telomerase inhibitor limiting human cancer cell proliferation. *EMBO J* **20**, 6958-68 (2001).

47. Robart, A.R. & Collins, K. Investigation of human telomerase holoenzyme assembly, activity, and processivity using disease-linked subunit variants. *J Biol Chem* **285**, 4375-86 (2010).

48. Wang, H., Gilley, D. & Blackburn, E.H. A novel specificity for the primer-template pairing requirement in Tetrahymena telomerase. *EMBO J* **17**, 1152-60 (1998).

49. Robart, A.R. & Collins, K. Human telomerase domain interactions capture DNA for TEN domain-dependent processive elongation. *Mol Cell* **42**, 308-18 (2011).

50. Wu, R.A. & Collins, K. Human telomerase specialization for repeat synthesis by unique handling of primer-template duplex. *EMBO J* **33**, 921-35 (2014).

51. Berman, A.J., Akiyama, B.M., Stone, M.D. & Cech, T.R. The RNA accordion model for template positioning by telomerase RNA during telomeric DNA synthesis. *Nat Struct Mol Biol* **18**, 1371-5 (2011).

52. Yang, W. & Lee, Y.S. A DNA-hairpin model for repeat-addition processivity in telomere synthesis. *Nat Struct Mol Biol* **22**, 844-7 (2015).

53. Collins, K. & Greider, C.W. Tetrahymena telomerase catalyzes nucleolytic cleavage and nonprocessive elongation. *Genes Dev* **7**, 1364-76 (1993).

54. Patrick, E.M., Slivka, J.D., Payne, B., Comstock, M.J. & Schmidt, J.C. Observation of processive telomerase catalysis using high-resolution optical tweezers. *Nat Chem Biol* **16**, 801-809 (2020).

55. Latrick, C.M. & Cech, T.R. POT1-TPP1 enhances telomerase processivity by slowing primer dissociation and aiding translocation. *EMBO J* **29**, 924-33 (2010).

56. Hwang, H., Buncher, N., Opresko, P.L. & Myong, S. POT1-TPP1 regulates telomeric overhang structural dynamics. *Structure* **20**, 1872-80 (2012).

57. Hegde, M.L. et al. Oxidative genome damage and its repair: implications in aging and neurodegenerative diseases. *Mech Ageing Dev* **133**, 157-68 (2012).

58. Lonkar, P. & Dedon, P.C. Reactive species and DNA damage in chronic inflammation: reconciling chemical mechanisms and biological fates. *Int J Cancer* **128**, 1999-2009 (2011).

59. Mao, X., Gu, C., Chen, D., Yu, B. & He, J. Oxidative stress-induced diseases and tea polyphenols. *Oncotarget* **8**, 81649-81661 (2017).

60. Reuter, S., Gupta, S.C., Chaturvedi, M.M. & Aggarwal, B.B. Oxidative stress, inflammation, and cancer: how are they linked? *Free Radic Biol Med* **49**, 1603-16 (2010).

61. Zou, Y., Sfeir, A., Gryaznov, S.M., Shay, J.W. & Wright, W.E. Does a sentinel or a subset of short telomeres determine replicative senescence? *Mol Biol Cell* **15**, 3709-18 (2004).

62. Fumagalli, M. et al. Telomeric DNA damage is irreparable and causes persistent DNA-damage-response activation. *Nat Cell Biol* **14**, 355-65 (2012).

63. von Zglinicki, T., Saretzki, G., Ladhoff, J., d'Adda di Fagagna, F. & Jackson, S.P. Human cell senescence as a DNA damage response. *Mech Ageing Dev* **126**, 111-7 (2005).

64. d'Adda di Fagagna, F. et al. A DNA damage checkpoint response in telomere-initiated senescence. *Nature* **426**, 194-8 (2003).

65. Maciejowski, J. & de Lange, T. Telomeres in cancer: tumour suppression and genome instability. *Nat Rev Mol Cell Biol* **18**, 175-186 (2017).

66. de Lange, T. Shelterin-Mediated Telomere Protection. *Annu Rev Genet* **52**, 223-247 (2018).

67. Barnes, R.P., Fouquerel, E. & Opresko, P.L. The impact of oxidative DNA damage and stress on telomere homeostasis. *Mech Ageing Dev* **177**, 37-45 (2019).

68. Artandi, S.E. et al. Telomere dysfunction promotes non-reciprocal translocations and epithelial cancers in mice. *Nature* **406**, 641-5 (2000).

69. Shay, J.W. Role of Telomeres and Telomerase in Aging and Cancer. *Cancer Discov* **6**, 584-93 (2016).

70. Kim, N.W. et al. Specific association of human telomerase activity with immortal cells and cancer. *Science* **266**, 2011-5 (1994).

71. Cifuentes-Rojas, C. & Shippen, D.E. Telomerase regulation. *Mutat Res* **730**, 20-7 (2012).

72. Broccoli, D., Young, J.W. & de Lange, T. Telomerase activity in normal and malignant hematopoietic cells. *Proc Natl Acad Sci U S A* **92**, 9082-6 (1995).

73. Vinagre, J. et al. Frequency of TERT promoter mutations in human cancers. *Nat Commun* **4**, 2185 (2013).

74. Huang, D.S. et al. Recurrent TERT promoter mutations identified in a large-scale study of multiple tumour types are associated with increased TERT expression and telomerase activation. *Eur J Cancer* **51**, 969-76 (2015).

75. Kinde, I. et al. TERT promoter mutations occur early in urothelial neoplasia and are biomarkers of early disease and disease recurrence in urine. *Cancer Res* **73**, 7162-7 (2013).

76. Wang, N. et al. TERT promoter mutation as an early genetic event activating telomerase in follicular thyroid adenoma (FTA) and atypical FTA. *Cancer* **120**, 2965-79 (2014).

77. Akincilar, S.C. et al. Long-Range Chromatin Interactions Drive Mutant TERT Promoter Activation. *Cancer Discov* **6**, 1276-1291 (2016).

78. Kyo, S., Takakura, M., Fujiwara, T. & Inoue, M. Understanding and exploiting hTERT promoter regulation for diagnosis and treatment of human cancers. *Cancer Sci* **99**, 1528-38 (2008).

79. Stern, J.L., Theodorescu, D., Vogelstein, B., Papadopoulos, N. & Cech, T.R. Mutation of the TERT promoter, switch to active chromatin, and monoallelic TERT expression in multiple cancers. *Genes Dev* **29**, 2219-24 (2015).

80. Huang, F.W. et al. Highly recurrent TERT promoter mutations in human melanoma. *Science* **339**, 957-9 (2013).

81. Horn, S. et al. TERT promoter mutations in familial and sporadic melanoma. *Science* **339**, 959-61 (2013).

82. Bell, R.J. et al. Cancer. The transcription factor GABP selectively binds and activates the mutant TERT promoter in cancer. *Science* **348**, 1036-9 (2015).

83. Whitaker, A.M., Schaich, M.A., Smith, M.R., Flynn, T.S. & Freudenthal, B.D. Base excision repair of oxidative DNA damage: from mechanism to disease. *Front Biosci (Landmark Ed)* **22**, 1493-1522 (2017).

84. Kanvah, S. et al. Oxidation of DNA: damage to nucleobases. *Acc Chem Res* **43**, 280-7 (2010).

85. Simic, S.V.J.a.M.G. One-electron redox potentials of purines and pyrimidines. *Journal of Physical Chemistry* **90**, 974-978 (1986).

86. Sekiguchi, M. & Tsuzuki, T. Oxidative nucleotide damage: consequences and prevention. *Oncogene* **21**, 8895-904 (2002).

87. Freudenthal, B.D. et al. Uncovering the polymerase-induced cytotoxicity of an oxidized nucleotide. *Nature* **517**, 635-9 (2015).

88. von Zglinicki, T. Oxidative stress shortens telomeres. *Trends Biochem Sci* **27**, 339-44 (2002).

89. Oikawa, S. & Kawanishi, S. Site-specific DNA damage at GGG sequence by oxidative stress may accelerate telomere shortening. *FEBS Lett* **453**, 365-8 (1999).

90. Wang, Z. et al. Characterization of oxidative guanine damage and repair in mammalian telomeres. *PLoS Genet* **6**, e1000951 (2010).

91. Fouquerel, E. et al. Oxidative guanine base damage regulates human telomerase activity. *Nat Struct Mol Biol* **23**, 1092-1100 (2016).

92. Aeby, E., Ahmed, W., Redon, S., Simanis, V. & Lingner, J. Peroxiredoxin 1 Protects Telomeres from Oxidative Damage and Preserves Telomeric DNA for Extension by Telomerase. *Cell Rep* **17**, 3107-3114 (2016).

93. Bessman, M.J., Frick, D.N. & O'Handley, S.F. The MutT proteins or "Nudix" hydrolases, a family of versatile, widely distributed, "housecleaning" enzymes. *J Biol Chem* **271**, 25059-62 (1996).

94. Fujikawa, K. et al. The oxidized forms of dATP are substrates for the human MutT homologue, the hMTH1 protein. *J Biol Chem* **274**, 18201-5 (1999).

95. Fujikawa, K., Kamiya, H., Yakushiji, H., Nakabeppu, Y. & Kasai, H. Human MTH1 protein hydrolyzes the oxidized ribonucleotide, 2-hydroxy-ATP. *Nucleic Acids Res* **29**, 449-54 (2001).

96. Mo, J.Y., Maki, H. & Sekiguchi, M. Hydrolytic elimination of a mutagenic nucleotide, 8-oxodGTP, by human 18-kilodalton protein: sanitization of nucleotide pool. *Proc Natl Acad Sci U S A* **89**, 11021-5 (1992).

97. Tsuzuki, T. et al. Spontaneous tumorigenesis in mice defective in the MTH1 gene encoding 8-oxo-dGTPase. *Proc Natl Acad Sci U S A* **98**, 11456-61 (2001).

98. Patel, A. et al. MutT Homolog 1 (MTH1) maintains multiple KRAS-driven pro-malignant pathways. *Oncogene* **34**, 2586-96 (2015).

99. Rai, P. et al. Continuous elimination of oxidized nucleotides is necessary to prevent rapid onset of cellular senescence. *Proc Natl Acad Sci U S A* **106**, 169-74 (2009).

100. Rai, P. et al. Enhanced elimination of oxidized guanine nucleotides inhibits oncogenic RAS-induced DNA damage and premature senescence. *Oncogene* **30**, 1489-96 (2011).

101. Gad, H. et al. MTH1 inhibition eradicates cancer by preventing sanitation of the dNTP pool. *Nature* **508**, 215-21 (2014).

102. Huber, K.V. et al. Stereospecific targeting of MTH1 by (S)-crizotinib as an anticancer strategy. *Nature* **508**, 222-7 (2014).

103. Dong, L. et al. Echinacoside induces apoptotic cancer cell death by inhibiting the nucleotide pool sanitizing enzyme MTH1. *Onco Targets Ther* **8**, 3649-64 (2015).

104. Ahmed, W. & Lingner, J. PRDX1 and MTH1 cooperate to prevent ROS-mediated inhibition of telomerase. *Genes Dev* **32**, 658-669 (2018).

105. Greider, C.W. Telomerase activity, cell proliferation, and cancer. *Proc Natl Acad Sci U S A* **95**, 90-2 (1998).

106. Dikmen, Z.G. et al. In vivo inhibition of lung cancer by GRN163L: a novel human telomerase inhibitor. *Cancer Res* **65**, 7866-73 (2005).

107. Frink, R.E. et al. Telomerase inhibitor imetelstat has preclinical activity across the spectrum of non-small cell lung cancer oncogenotypes in a telomere length dependent manner. *Oncotarget* **7**, 31639-51 (2016).

108. Salloum, R. et al. A molecular biology and phase II study of imetelstat (GRN163L) in children with recurrent or refractory central nervous system malignancies: a pediatric brain tumor consortium study. *J Neurooncol* **129**, 443-451 (2016).

109. Thompson, P.A. et al. A phase I trial of imetelstat in children with refractory or recurrent solid tumors: a Children's Oncology Group Phase I Consortium Study (ADVL1112). *Clin Cancer Res* **19**, 6578-84 (2013).

110. Chiappori, A.A. et al. A randomized phase II study of the telomerase inhibitor imetelstat as maintenance therapy for advanced non-small-cell lung cancer. *Ann Oncol* **26**, 354-62 (2015).

111. Pascolo, E. et al. Mechanism of human telomerase inhibition by BIBR1532, a synthetic, non-nucleosidic drug candidate. *J Biol Chem* **277**, 15566-72 (2002).

112. Bashash, D., Ghaffari, S.H., Mirzaee, R., Alimoghaddam, K. & Ghavamzadeh, A. Telomerase inhibition by non-nucleosidic compound BIBR1532 causes rapid cell death in pre-B acute lymphoblastic leukemia cells. *Leuk Lymphoma* **54**, 561-8 (2013).

113. Holec, A.D., Mandal, S., Prathipati, P.K. & Destache, C.J. Nucleotide Reverse Transcriptase Inhibitors: A Thorough Review, Present Status and Future Perspective as HIV Therapeutics. *Curr HIV Res* **15**, 411-421 (2017).

114. Engelman, A. & Cherepanov, P. The structural biology of HIV-1: mechanistic and therapeutic insights. *Nat Rev Microbiol* **10**, 279-90 (2012).

115. Smith, R.L., de Boer, R., Brul, S., Budovskaya, Y. & van Spek, H. Premature and accelerated aging: HIV or HAART? *Front Genet* **3**, 328 (2012).

116. Cohen, J. & Torres, C. HIV-associated cellular senescence: A contributor to accelerated aging. *Ageing Res Rev* **36**, 117-124 (2017).

117. Strahl, C. & Blackburn, E.H. The effects of nucleoside analogs on telomerase and telomeres in Tetrahymena. *Nucleic Acids Res* **22**, 893-900 (1994).

118. Strahl, C. & Blackburn, E.H. Effects of reverse transcriptase inhibitors on telomere length and telomerase activity in two immortalized human cell lines. *Mol Cell Biol* **16**, 53-65 (1996).

119. Hukezalie, K.R., Thumati, N.R., Cote, H.C. & Wong, J.M. In vitro and ex vivo inhibition of human telomerase by anti-HIV nucleoside reverse transcriptase inhibitors (NRTIs) but not by non-NRTIs. *PLoS One* **7**, e47505 (2012).

120. Lewis, W., Day, B.J. & Copeland, W.C. Mitochondrial toxicity of NRTI antiviral drugs: an integrated cellular perspective. *Nat Rev Drug Discov* **2**, 812-22 (2003).

121. Apostolova, N., Blas-Garcia, A. & Esplugues, J.V. Mitochondrial toxicity in HAART: an overview of in vitro evidence. *Curr Pharm Des* **17**, 2130-44 (2011).

122. Trifunovic, A. et al. Premature ageing in mice expressing defective mitochondrial DNA polymerase. *Nature* **429**, 417-23 (2004).

123. Gomez, D.E., Armando, R.G. & Alonso, D.F. AZT as a telomerase inhibitor. *Front Oncol* **2**, 113 (2012).

124. Faraj, A. et al. Effects of beta-L-3'-azido-3'-deoxythymidine 5'-triphosphate on host and viral DNA polymerases. *Antiviral Res* **47**, 97-102 (2000).

125. Yegorov, Y.E. et al. Reverse transcriptase inhibitors suppress telomerase function and induce senescence-like processes in cultured mouse fibroblasts. *FEBS Lett* **389**, 115-8 (1996).

126. Tejera, A.M., Alonso, D.F., Gomez, D.E. & Olivero, O.A. Chronic in vitro exposure to 3'-azido-2', 3'-dideoxythymidine induces senescence and apoptosis and reduces tumorigenicity of metastatic mouse mammary tumor cells. *Breast Cancer Res Treat* **65**, 93-9 (2001).

127. Jeng, K.S., Sheen, I.S. & Jeng, W.J. Azidothymidine treatment of hepatocellular carcinoma in rats: an in vivo study of telomerase inhibition. *Hepatogastroenterology* **58**, 2091-6 (2011).

128. Mender, I., Gryaznov, S., Dikmen, Z.G., Wright, W.E. & Shay, J.W. Induction of telomere dysfunction mediated by the telomerase substrate precursor 6-thio-2'-deoxyguanosine. *Cancer Discov* **5**, 82-95 (2015).

129. Karran, P. & Attard, N. Thiopurines in current medical practice: molecular mechanisms and contributions to therapy-related cancer. *Nat Rev Cancer* **8**, 24-36 (2008).

130. Yuan, B. & Wang, Y. Mutagenic and cytotoxic properties of 6-thioguanine, S6-methylthioguanine, and guanine-S6-sulfonic acid. *J Biol Chem* **283**, 23665-70 (2008).

131. Daehn, I., Brem, R., Barkauskaite, E. & Karran, P. 6-Thioguanine damages mitochondrial DNA and causes mitochondrial dysfunction in human cells. *FEBS Lett* **585**, 3941-6 (2011).

132. Zhang, F., Fu, L. & Wang, Y. 6-thioguanine induces mitochondrial dysfunction and oxidative DNA damage in acute lymphoblastic leukemia cells. *Mol Cell Proteomics* **12**, 3803-11 (2013).

133. Karlseder, J., Broccoli, D., Dai, Y., Hardy, S. & de Lange, T. p53- and ATM-dependent apoptosis induced by telomeres lacking TRF2. *Science* **283**, 1321-5 (1999).

134. Takai, H., Smogorzewska, A. & de Lange, T. DNA damage foci at dysfunctional telomeres. *Curr Biol* **13**, 1549-56 (2003).

135. Zhang, G. et al. Induction of Telomere Dysfunction Prolongs Disease Control of Therapy-Resistant Melanoma. *Clin Cancer Res* **24**, 4771-4784 (2018).

136. Sengupta, S. et al. Induced Telomere Damage to Treat Telomerase Expressing Therapy-Resistant Pediatric Brain Tumors. *Mol Cancer Ther* **17**, 1504-1514 (2018).

137. Zeng, X. et al. Administration of a Nucleoside Analog Promotes Cancer Cell Death in a Telomerase-Dependent Manner. *Cell Rep* **23**, 3031-3041 (2018).

138. Longley, D.B., Harkin, D.P. & Johnston, P.G. 5-fluorouracil: mechanisms of action and clinical strategies. *Nat Rev Cancer* **3**, 330-8 (2003).

139. de Lange, T. How telomeres solve the end-protection problem. *Science* **326**, 948-52 (2009).

140. Pickett, H.A. & Reddel, R.R. Molecular mechanisms of activity and derepression of alternative lengthening of telomeres. *Nat Struct Mol Biol* **22**, 875-80 (2015).

141. Flynn, R.L. et al. Alternative lengthening of telomeres renders cancer cells hypersensitive to ATR inhibitors. *Science* **347**, 273-7 (2015).

142. Parks, J.W. & Stone, M.D. Coordinated DNA dynamics during the human telomerase catalytic cycle. *Nat Commun* **5**, 4146 (2014).

143. Kocak, H. et al. Hoyeraal-Hreidarsson syndrome caused by a germline mutation in the TEL patch of the telomere protein TPP1. *Genes Dev* **28**, 2090-102 (2014).

144. Schaich, M.A. et al. Mechanisms of nucleotide selection by telomerase. *Elife* **9**(2020).

145. Powers, K.T. & Washington, M.T. Analyzing the Catalytic Activities and Interactions of Eukaryotic Translesion Synthesis Polymerases. *Methods Enzymol* **592**, 329-356 (2017).

146. Beard, W.A., Shock, D.D., Batra, V.K., Prasad, R. & Wilson, S.H. Substrate-induced DNA polymerase beta activation. *J Biol Chem* **289**, 31411-22 (2014).

147. Schneider, C.A., Rasband, W.S. & Eliceiri, K.W. NIH Image to ImageJ: 25 years of image analysis. *Nat Methods* **9**, 671-5 (2012).

148. Cristofari, G. & Lingner, J. Telomere length homeostasis requires that telomerase levels are limiting. *EMBO J* **25**, 565-74 (2006).

149. Cristofari, G. et al. Low- to high-throughput analysis of telomerase modulators with Telospot. *Nat Methods* **4**, 851-3 (2007).

150. Traut, T.W. Physiological concentrations of purines and pyrimidines. *Mol Cell Biochem* **140**, 1-22 (1994).

151. Ahluwalia, G. et al. Initial studies on the cellular pharmacology of 2',3'-dideoxyinosine, an inhibitor of HIV infectivity. *Biochem Pharmacol* **36**, 3797-800 (1987).

152. Johnson, M.A. & Fridland, A. Phosphorylation of 2',3'-dideoxyinosine by cytosolic 5'-nucleotidase of human lymphoid cells. *Mol Pharmacol* **36**, 291-5 (1989).

153. Hsu, G.W., Ober, M., Carell, T. & Beese, L.S. Error-prone replication of oxidatively damaged DNA by a high-fidelity DNA polymerase. *Nature* **431**, 217-21 (2004).

154. Tomlinson, C.G. et al. Two-step mechanism involving active-site conformational changes regulates human telomerase DNA binding. *Biochem J* **465**, 347-57 (2015).

155. Loayza, D., Parsons, H., Donigian, J., Hoke, K. & de Lange, T. DNA binding features of human POT1: a nonamer 5'-TAGGGTTAG-3' minimal binding site, sequence specificity, and internal binding to multimeric sites. *J Biol Chem* **279**, 13241-8 (2004).

156. Zaug, A.J., Podell, E.R., Nandakumar, J. & Cech, T.R. Functional interaction between telomere protein TPP1 and telomerase. *Genes Dev* **24**, 613-22 (2010).

157. Kaul, Z., Cesare, A.J., Huschtscha, L.I., Neumann, A.A. & Reddel, R.R. Five dysfunctional telomeres predict onset of senescence in human cells. *EMBO Rep* **13**, 52-9 (2011).

158. Bertram, J.G., Oertell, K., Petruska, J. & Goodman, M.F. DNA polymerase fidelity: comparing direct competition of right and wrong dNTP substrates with steady state and pre-steady state kinetics. *Biochemistry* **49**, 20-8 (2010).

159. Hockemeyer, D. & Collins, K. Control of telomerase action at human telomeres. *Nat Struct Mol Biol* **22**, 848-52 (2015).

160. Collins, K. Ciliate telomerase biochemistry. *Annu Rev Biochem* **68**, 187-218 (1999).

161. Chen, Y., Podlevsky, J.D., Logeswaran, D. & Chen, J.J. A single nucleotide incorporation step limits human telomerase repeat addition activity. *EMBO J* **37**(2018).

162. Hardy, C.D., Schultz, C.S. & Collins, K. Requirements for the dGTP-dependent repeat addition processivity of recombinant Tetrahymena telomerase. *J Biol Chem* **276**, 4863-71 (2001).

163. Koag, M.C., Jung, H. & Lee, S. Mutagenic Replication of the Major Oxidative Adenine Lesion 7,8-Dihydro-8-oxoadenine by Human DNA Polymerases. *J Am Chem Soc* **141**, 4584-4596 (2019).

164. Hernandez-Sanchez, W. et al. A non-natural nucleotide uses a specific pocket to selectively inhibit telomerase activity. *PLoS Biol* **17**, e3000204 (2019).

165. Maciejewska, A.M., Lichota, K.D. & Kusmierek, J.T. Neighbouring bases in template influence base-pairing of isoguanine. *Biochem J* **369**, 611-8 (2003).

166. Robinson, H. et al. 2'-Deoxyisoguanosine adopts more than one tautomer to form base pairs with thymidine observed by high-resolution crystal structure analysis. *Biochemistry* **37**, 10897-905 (1998).

167. Kamiya, H. & Kasai, H. Formation of 2-hydroxydeoxyadenosine triphosphate, an oxidatively damaged nucleotide, and its incorporation by DNA polymerases. Steady-state kinetics of the incorporation. *J Biol Chem* **270**, 19446-50 (1995).

168. Bukowska, A.M. & Kusmierek, J.T. Miscoding properties of isoguanine (2-oxoadenine) studied in an AMV reverse transcriptase in vitro system. *Acta Biochim Pol* **43**, 247-54 (1996).

169. Hidaka, K. et al. Specificity of mutations induced by incorporation of oxidized dNTPs into DNA by human DNA polymerase eta. *DNA Repair (Amst)* **7**, 497-506 (2008).

170. Ling, Y.H., Nelson, J.A., Cheng, Y.C., Anderson, R.S. & Beattie, K.L. 2'-Deoxy-6-thioguanosine 5'-triphosphate as a substrate for purified human DNA polymerases and calf thymus terminal deoxynucleotidyltransferase in vitro. *Mol Pharmacol* **40**, 508-14 (1991).

171. Schaich, M.A., Smith, M.R., Cloud, A.S., Holloran, S.M. & Freudenthal, B.D. Structures of a DNA Polymerase Inserting Therapeutic Nucleotide Analogues. *Chem Res Toxicol* **30**, 1993-2001 (2017).

172. Bohon, J. & de los Santos, C.R. Effect of 6-thioguanine on the stability of duplex DNA. *Nucleic Acids Res* **33**, 2880-6 (2005).

173. Gomez, D., Kassim, A. & Olivero, O. Preferential incorporation of 3'-azido-2',3'-dideoxythymidine (azt) in telomeric sequences of cho cells. *Int J Oncol* **7**, 1057-60 (1995).

174. Olivero, O.A. & Poirier, M.C. Preferential incorporation of 3'-azido-2',3'-dideoxythymidine into telomeric DNA and Z-DNA-containing regions of Chinese hamster ovary cells. *Mol Carcinog* **8**, 81-8 (1993).

175. Torres, R.A. & Lewis, W. Aging and HIV/AIDS: pathogenetic role of therapeutic side effects. *Lab Invest* **94**, 120-8 (2014).

176. Mender, I. et al. Telomerase-Mediated Strategy for Overcoming Non-Small Cell Lung Cancer Targeted Therapy and Chemotherapy Resistance. *Neoplasia* **20**, 826-837 (2018).

177. Qian, W. et al. Chemoptogenetic damage to mitochondria causes rapid telomere dysfunction. *Proc Natl Acad Sci U S A* **116**, 18435-18444 (2019).

178. Tomlinson, C.G., Sasaki, N., Jurczyluk, J., Bryan, T.M. & Cohen, S.B. Quantitative assays for measuring human telomerase activity and DNA binding properties. *Methods* **114**, 85-95 (2017).

179. Lee, H.T. et al. Position-Dependent Effect of Guanine Base Damage and Mutations on Telomeric G-Quadruplex and Telomerase Extension. *Biochemistry* (2020).

180. Stefl, R., Spackova, N., Berger, I., Koca, J. & Sponer, J. Molecular dynamics of DNA quadruplex molecules containing inosine, 6-thioguanine and 6-thiopurine. *Biophys J* **80**, 455-68 (2001).

181. Jain, A., Liu, R., Xiang, Y.K. & Ha, T. Single-molecule pull-down for studying protein interactions. *Nat Protoc* **7**, 445-52 (2012).

182. Diolaiti, M.E., Cimini, B.A., Kageyama, R., Charles, F.A. & Stohr, B.A. In situ visualization of telomere elongation patterns in human cells. *Nucleic Acids Res* **41**, e176 (2013).

183. Song, M.G., Bail, S. & Kiledjian, M. Multiple Nudix family proteins possess mRNA decapping activity. *RNA* **19**, 390-9 (2013).

184. Yu, Y. et al. Proliferating cell nuclear antigen is protected from degradation by forming a complex with MutT Homolog2. *J Biol Chem* **284**, 19310-20 (2009).

185. Yang, S.K. et al. A common missense variant in NUDT15 confers susceptibility to thiopurine-induced leukopenia. *Nat Genet* **46**, 1017-20 (2014).

186. Kakuta, Y. et al. NUDT15 R139C causes thiopurine-induced early severe hair loss and leukopenia in Japanese patients with IBD. *Pharmacogenomics J* **16**, 280-5 (2016).

187. Yang, J.J. et al. Inherited NUDT15 variant is a genetic determinant of mercaptopurine intolerance in children with acute lymphoblastic leukemia. *J Clin Oncol* **33**, 1235-42 (2015).

188. Matsuoka, K. NUDT15 gene variants and thiopurine-induced leukopenia in patients with inflammatory bowel disease. *Intest Res* (2020).

189. Valerie, N.C. et al. NUDT15 Hydrolyzes 6-Thio-DeoxyGTP to Mediate the Anticancer Efficacy of 6-Thioguanine. *Cancer Res* **76**, 5501-11 (2016).

190. Zhang, X., Mar, V., Zhou, W., Harrington, L. & Robinson, M.O. Telomere shortening and apoptosis in telomerase-inhibited human tumor cells. *Genes Dev* **13**, 2388-99 (1999).

191. Iwabuchi, K., Bartel, P.L., Li, B., Marraccino, R. & Fields, S. Two cellular proteins that bind to wild-type but not mutant p53. *Proc Natl Acad Sci U S A* **91**, 6098-102 (1994).

192. Beigel, J.H. et al. Remdesivir for the Treatment of Covid-19 - Preliminary Report. *N Engl J Med* (2020).

193. de Wit, E. et al. Prophylactic and therapeutic remdesivir (GS-5734) treatment in the rhesus macaque model of MERS-CoV infection. *Proc Natl Acad Sci U S A* **117**, 6771-6776 (2020).

194. Pruijssers, A.J. et al. Remdesivir Inhibits SARS-CoV-2 in Human Lung Cells and Chimeric SARS-CoV Expressing the SARS-CoV-2 RNA Polymerase in Mice. *Cell Rep*, 107940 (2020).

195. Grein, J. et al. Compassionate Use of Remdesivir for Patients with Severe Covid-19. *N Engl J Med* **382**, 2327-2336 (2020).

196. Hoover, S. & Striker, R. Thiopurines inhibit bovine viral diarrhea virus production in a thiopurine methyltransferase-dependent manner. *J Gen Virol* **89**, 1000-1009 (2008).

197. Hotchkiss, G., Pehrson, P.O., Larsson, S., Ahrlund-Richter, L. & Britton, S. Telomere loss in peripheral blood mononuclear cells may be moderately accelerated during highly active antiretroviral therapy (HAART). *J Acquir Immune Defic Syndr* **22**, 445-52 (1999).

198. Aladdin, H. et al. T-cell receptor excisional circles, telomere length, proliferation and apoptosis in peripheral blood mononuclear cells of human immunodeficiency virus-infected individuals after 18 months of treatment induced viral suppression. *Scand J Immunol* **57**, 485-92 (2003).

199. Wolthers, K.C. et al. T cell telomere length in HIV-1 infection: no evidence for increased CD4+ T cell turnover. *Science* **274**, 1543-7 (1996).

200. Detels, R. et al. The multicenter AIDS Cohort Study, 1983 to. *Public Health* **126**, 196-8 (2012).

201. Rickabaugh, T.M. et al. The dual impact of HIV-1 infection and aging on naive CD4 T-cells: additive and distinct patterns of impairment. *PLoS One* **6**, e16459 (2011).

202. Kimura, M. et al. Measurement of telomere length by the Southern blot analysis of terminal restriction fragment lengths. *Nat Protoc* **5**, 1596-607 (2010).

203. Aviv, A., Valdes, A.M. & Spector, T.D. Human telomere biology: pitfalls of moving from the laboratory to epidemiology. *Int J Epidemiol* **35**, 1424-9 (2006).

204. Roth, A., Harley, C.B. & Baerlocher, G.M. Imetelstat (GRN163L)--telomerase-based cancer therapy. *Recent Results Cancer Res* **184**, 221-34 (2010).

205. Ding, X. et al. BIBR1532, a Selective Telomerase Inhibitor, Enhances Radiosensitivity of Non-Small Cell Lung Cancer Through Increasing Telomere Dysfunction and ATM/CHK1 Inhibition. *Int J Radiat Oncol Biol Phys* **105**, 861-874 (2019).

206. Zhang, G. & Shay, J.W. Inducing rapid telomere irreparable damage in telomerase-expressing cancers. *Oncotarget* **9**, 35803-35804 (2018).

207. Reyes-Uribe, P. et al. Exploiting TERT dependency as a therapeutic strategy for NRAS-mutant melanoma. *Oncogene* **37**, 4058-4072 (2018).

208. Su, Z. et al. Telomerase mRNA-transfected dendritic cells stimulate antigen-specific CD8+ and CD4+ T cell responses in patients with metastatic prostate cancer. *J Immunol* **174**, 3798-807 (2005).

209. Vetsika, E.K. et al. Immunological responses in cancer patients after vaccination with the therapeutic telomerase-specific vaccine Vx-001. *Cancer Immunol Immunother* **61**, 157-168 (2012).

210. Shaw, V.E. et al. Current status of GV1001 and other telomerase vaccination strategies in the treatment of cancer. *Expert Rev Vaccines* **9**, 1007-16 (2010).

211. Zhang, Q. et al. Effective gene-viral therapy for telomerase-positive cancers by selective replicative-competent adenovirus combining with endostatin gene. *Cancer Res* **64**, 5390-7 (2004).

212. Nemunaitis, J. et al. A phase I study of telomerase-specific replication competent oncolytic adenovirus (telomelysin) for various solid tumors. *Mol Ther* **18**, 429-34 (2010).

213. Teng, G. et al. Combined antitumor activity of the nitroreductase/CB1954 suicide gene system and gamma-rays in HeLa cells in vitro. *Mol Med Rep* **14**, 5164-5170 (2016).

214. Xiao, Z. et al. Telomerase: a target for therapeutic effects of curcumin and a curcumin derivative in Abeta1-42 insult in vitro. *PLoS One* **9**, e101251 (2014).

215. Moorhouse, A.D. et al. Stabilization of G-quadruplex DNA by highly selective ligands via click chemistry. *J Am Chem Soc* **128**, 15972-3 (2006).

216. Shin-ya, K. et al. Telomestatin, a novel telomerase inhibitor from Streptomyces anulatus. *J Am Chem Soc* **123**, 1262-3 (2001).

217. Lagah, S. et al. RHPS4 G-quadruplex ligand induces anti-proliferative effects in brain tumor cells. *PLoS One* **9**, e86187 (2014).

218. Waki, K. et al. Establishment of functional telomerase immortalized human hepatocytes and a hepatic stellate cell line for telomere-targeting anticancer drug development. *Cancer Sci* **101**, 1678-85 (2010).

219. Drygin, D. et al. Anticancer activity of CX-3543: a direct inhibitor of rRNA biogenesis. *Cancer Res* **69**, 7653-61 (2009).

220. Marchbanks, C.R. Drug-drug interactions with fluoroquinolones. *Pharmacotherapy* **13**, 23S-28S (1993).

221. Miller, K.D. et al. A phase II study of weekly oral methotrexate and zidovudine (AZT) in advanced adenocarcinoma of the pancreas and hepatocellular carcinoma. *Invest New Drugs* **14**, 207-12 (1996).

222. Morgan, R.J., Jr. et al. Phase I study of cisdiamminedichloroplatinum in combination with azidothymidine in the treatment of patients with advanced malignancies. *Cancer Chemother Pharmacol* **51**, 459-64 (2003).

223. Lennard, L. Clinical implications of thiopurine methyltransferase--optimization of drug dosage and potential drug interactions. *Ther Drug Monit* **20**, 527-31 (1998).

224. Otterness, D. et al. Human thiopurine methyltransferase pharmacogenetics: gene sequence polymorphisms. *Clin Pharmacol Ther* **62**, 60-73 (1997).

225. Mender, I. et al. Telomere Stress Potentiates STING-Dependent Anti-tumor Immunity. *Cancer Cell* (2020).

226. Lei, M., Podell, E.R., Baumann, P. & Cech, T.R. DNA self-recognition in the structure of Pot1 bound to telomeric single-stranded DNA. *Nature* **426**, 198-203 (2003).

227. Lei, M., Zaug, A.J., Podell, E.R. & Cech, T.R. Switching human telomerase on and off with hPOT1 protein in vitro. *J Biol Chem* **280**, 20449-56 (2005).

228. Wang, F. & Lei, M. Human telomere POT1-TPP1 complex and its role in telomerase activity regulation. *Methods Mol Biol* **735**, 173-87 (2011).

229. Schmidt, J.C., Zaug, A.J. & Cech, T.R. Live Cell Imaging Reveals the Dynamics of Telomerase Recruitment to Telomeres. *Cell* **166**, 1188-1197 e9 (2016).

230. Laprade, H. et al. Single-Molecule Imaging of Telomerase RNA Reveals a Recruitment-Retention Model for Telomere Elongation. *Mol Cell* (2020).